# A and $K_s^0$ Production in Au+Au Collisions at 1.23A GeV

Dissertation zur Erlangung des Doktorgrades der Naturwissenschaften

vorgelegt beim Fachbereich Physik der Johann Wolfgang Goethe-Universität in Frankfurt am Main

> von Timo Scheib aus Offenbach am Main

> > Frankfurt 2017 (D30)

vom Fachbereich Physik der Johann Wolfgang Goethe-Universität als Dissertation angenommen.

# Dekan:

Prof. Dr. Owe Philipsen

# **Gutachter:**

Prof. Dr. Joachim Stroth Prof. Dr. Christoph Blume

# Datum der Disputation: 24.05.2017

# Abstract

In April and May 2012 data on Au+Au collisions at beam energies of  $E_{\rm kin} = 1.23$ A GeV were recorded with the High Acceptance Di-Electron Spectrometer, which is located at the GSI Helmholtz Center for Heavy Ion Research in Darmstadt, Germany. At this beam energy all hadrons containing strangeness are produced below their elementary production threshold. The required energy is not available in binary NN collisions but must be provided by the system e.g. through multi-particle interactions or medium effects like a modified in-medium potential (e.g. KN/ $\Lambda$ N potential). Thus, a high sensitivity to these medium effects is expected in the investigated system.

The baryon-dominated systems created in relativistic heavy-ion collisions (HIC) at SIS18 energies reach densities of about 2-3 times ground state density  $\rho_0$  and may be similar to the properties of matter expected in the inner core of neutron stars. It is in particular the behavior of hadrons containing strangeness, i.e. kaons  $(K^{+/-}, K_s^0)$  and hyperons  $(\Lambda, \Xi^-)$ , and their potentials in the dense medium which may have severe implications on astrophysical objects and processes. As ab-initio calculations of quantum chromodynamics (QCD) cannot be performed rigorously on the lattice at finite baryo-chemical potentials due to the fermion sign problem, effective descriptions have to be used in order to model properties of dense systems and the involved particles. The only way to access the in-medium potential of strange hadrons above nuclear ground state density  $\rho_0$  is by comparing data from relativistic HIC to such effective microscopic models. Up to now, not much data on neutral kaons and  $\Lambda$  hyperons are available from heavy collision systems close to their NN production threshold. These two electromagnetically uncharged strange hadrons are in particular well suited to study their potential in a dense nucleon-dominated environment as their kinematic spectra are not affected by Coulomb interactions.

After an elaborate improvement of tracking algorithms and a careful event cleaning procedure, in total 2.1 x 10<sup>9</sup> Au+Au events were analyzed containing the 0 - 40% most central events. The investigated strange hadrons  $\Lambda$  and  $K_s^0$  are identified via their weak decays into p- $\pi^-$  and  $\pi^+$ - $\pi^-$  respectively. The relatively large mean decay lengths enable an analysis based on constraints on the decay topology which allows to distinguish between the decay and the primary vertex in order to suppress combinatorial background to the invariant mass spectrum. The data is then analyzed multi-differentially as a function of rapidity y, reduced transverse mass  $m_t - m_0$  and four centrality classes in steps of 10%. For the 0 - 40% most central collisions multiplicities of  $Mult_{tot} = (3.97 \pm 0.06^{stat} \pm 0.06^{sys}_{Cut} \pm 0.04^{sys}_{Extrapol}) \times 10^{-2}$  for  $\Lambda$  hyperons and of  $Mult_{tot} = (1.54 \pm 0.03^{stat} \pm 0.05^{sys}_{Cut} \pm 0.15^{sys}_{Extrapol}) \times 10^{-2}$  for  $K_s^0$  mesons were determined. The inverse slope parameters at mid-rapidity  $T_{\text{eff}}$  of  $93\pm2\pm4$  for  $\Lambda$  and  $97\pm1\pm2$  for  $K_s^0$  agree within uncertainties. For both particles, a more than linear rise of the mean multiplicity is observed with centrality which is in agreement with measurements by former experiments at higher energies. This indicates that the strength of the rise is only weakly proportional to the excess energy.

The experimental data are compared to predictions from three state-of-the-art hadronic transport models: IQMD (c8), HSD (711n) and UrQMD (3.4). All three are semi-classical models simulating HIC on an event-by-event basis. The investigated transport models can be grouped in two relevant fractions: on one side, the HSD and IQMD transport models with a repulsive KN potential of 40 MeV at nuclear ground state density  $\rho_0$  increasing linearly with density as well as an attractive  $\Lambda N$  potential which scales with 2/3 of the strength of the NN potential. On the other side, there is the UrQMD code which employs higher-lying  $\Delta$  and N<sup>\*</sup> resonances but neither includes a repulsive KN nor an attractive NN/AN potential. It is shown, that no model describes all observables at once and that no observable can be described unambiguously by all models. Results from the HSD and IQMD transport models may give the impression that a repulsive KN potential is necessary to describe particle kinematics ( $p_t$  spectra), yet, at least partially UrQMD calculations can (over)compensate the effect of the potential via particle production through intermediate resonances but fails to reproduce the scaling of the yields with centrality. On the other hand,  $p_t$  spectra of  $\Lambda$  are best described by the UrQMD model. The ambiguities in three out of four observables for each investigated particle hamper conclusions on the KN/AN potential and more model-to-data comparison on additional observables are important to rule out further ambiguities.

Observing a null result within the attempt to reconstruct the multi-strange  $\Xi^-$  hyperon, which would be produced about 840 MeV below its elementary threshold, an upper limit on the production yield can be determined. This limit is derived by using the Feldman-Cousins approach, which is purely based on the statistics of the selected data sample. The confidence interval is chosen to include 99.7% (corresponding to  $3\sigma$ ) of the hypothetical signal providing an upper limit of  $M_{\rm FC} < 2.32 \times 10^{-3}$ , being in agreement with former  $\Xi^-$  measurements and transport predictions. Considering the upper production limit, a maximum boundary on the ratio of  $\Xi^-$  to  $(\Lambda + \Sigma^0)$  hyperons is derived to be  $N_{\Xi^-}/N_{\Lambda+\Sigma^0} < 5.8 \times 10^{-2}$ .

# Inhaltsangabe

Im April und Mai 2012 nahm das an der GSI/Darmstadt am SIS18-Beschleuniger befindliche High Acceptance Di-Electron Spectrometer Daten von Au+Au Kollisionen bei einer Strahlenergie von  $E_{kin} = 1,23A$  GeV auf. Bei dieser Strahlenergie läuft die Produktion aller Seltsamkeitenthaltenden Hadronen unterhalb ihrer individuellen Nukleon-Nukleonschwelle ab, was eine Produktion in binären Kollisionsprozessen unmöglich macht und daher indirekt durch das sie umgebende Medium bewerkstelligt werden muss. Bei letzteren könnte es sich beispielsweise um modifizierte Teilcheneigenschaften in dichter Kernmaterie oder die Akkumulation von Energie durch mehrfache Wechselwirkungen handeln. Die unter diesen Bedingungen produzierten Hadronen eignen sich daher besonders als Sonden der Hochdichtephase des Systems, da die Produktion in dieser Phase maximal sensitiv auf die erwähnten sekundäre Produktionsprozesse ist.

Relativistische Schwerionenkollisionen (HIC) im SIS18-Energiebereich erlauben die Erzeugung von Systemen hadronischer Materie mit bis zu dreifacher Grundzustandsdichte  $\rho_0$ , wie sie beispielsweise im Inneren von Neutronensternen auftreten könnte. Da diese Zustände mit Hilfe der Quantenchromodynamik (QCD) bei endlichen Dichten nicht präzise berechnet werden können, muss auf effektive Beschreibungen dichter Systeme und der darin befindlichen Teilchen zurückgegriffen werden. Diese effektiven Modelle liefern Vorhersagen für Schwerionenexperimente und dienen umgekehrt der weiteren Präzisierung dieser theoretischen Beschreibungen und derer Anfangsbedingungen. Im Speziellen das Verhalten Seltsamkeit-enthaltender Teilchen wie Kaonen ( $K^{+/-}$ ,  $K_s^0$ ) und Hyperonen ( $\Lambda$ ,  $\Xi^-$ ) und deren Potentiale in dichter Materie könnte weitreichende Konsequenzen für astrophysikalische Prozesse sowie Objekte und deren Struktur haben.

Relativistische HIC bieten die einzige Möglichkeit das Potential seltsamer Teilchen in Materie oberhalb der Grundzustandsdichte zu untersuchen, indem experimentelle Daten mit effektiven mikroskopischen Modellen verglichen werden. Die Datenlage um neutrale Kaonen und  $\Lambda$ Hyperonen, produziert in Schwerionenkollisionen unterhalb der elementaren Schwelle, ist bis heute rar. Diese beiden elektrisch neutralen seltsamen Hadronen eignen sich insbesondere um das Potential in dichter Nukleon-dominierter Umgebung zu untersuchen, da ihre kinematischen Spektren nicht durch Coulomb-Wechselwirkung überlagert werden.

Nach einer für das vorliegende System notwendigen Verbesserung der Spurrekonstruktionsalgorithmen und einer sorgfältigen Ereignisselektion wurden insgesamt 2, 1 x 10<sup>9</sup> Au+Au Reaktionen analysiert, welche die 0 – 40% zentralsten Ereignisse enthalten. Die untersuchten seltsamen Hadronen  $\Lambda$  und  $K_s^0$  werden über ihre schwachen Zerfälle in p- $\pi^-$  bzw.  $\pi^+$ - $\pi^-$  im Endkanal nachgewiesen. Die relativ großen mittleren Zerfallslängen ermöglichen eine Analyse basierend auf deren Zerfallstopologie, bei der der Reaktions- vom Zerfallsvertex unterschieden und zur Unterdrückung des kombinatorischen Untergrunds zum invarianten Massenspektrum verwendet werden kann. Die Daten werden anschließend differentiell als Funktion der Rapidität, reduzierten transversalen Masse  $m_t - m_0$  sowie in vier Zentralitätsklassen in Schritten von 10% ausgewertet. Es wurden Multiplizitäten für die 0 - 40% zentralsten Kollisionen von  $Mult_{tot} = (3,97 \pm 0,06^{stat} \pm 0,06^{sys}_{Cut} \pm 0,04^{sys}_{Extrapol}) \times 10^{-2}$  für  $\Lambda$  Hyperonen und von  $Mult_{tot} = (1,54 \pm 0,03^{stat} \pm 0,05^{sys}_{Cut} \pm 0,15^{sys}_{Extrapol}) \times 10^{-2}$  für  $\Lambda^0$  Mesonen ermittelt. Die inversen Steigungsparameter bei Midrapidität  $T_{eff}$  von  $93\pm2\pm4$  für  $\Lambda$  und  $97\pm1\pm2$ für  $K_s^0$  stimmen innerhalb der Unsicherheiten überein. Für beide Teilchen wird ein mehr als linearer Anstieg der Produktionsrate mit zunehmender Anzahl der Partizipanten, und somit der Zentralität, beobachtet. Dieser Anstieg ist in Übereinstimmung mit den Ergebnissen früherer Experimente bei höheren Energien, was den Schluss nahe legt, dass die Stärke des Anstiegs nur eine schwache Abhängigkeit von der Exzessenergie aufweist.

Im Anschluss werden die experimentellen Daten mit Vorhersagen dreier State-of-the-Art Transportmodelle verglichen: IQMD (c8), HSD (711n) und UrQMD (3.4). Die untersuchten Transportmodelle lassen sich grob in zwei Gruppen unterteilen: Auf der einen Seite stehen die Modelle HSD und IQMD mit einem repulsiven KN Potential von 40 MeV bei Grundzustandsdichte  $\rho_0$  und linearem Anstieg mit zunehmender Dichte, sowie einem attraktiven  $\Lambda$ N Potential, das mit 2/3 relativ zur Stärke des NN Potentials skaliert. Auf der anderen Seite befindet sich UrQMD, welches in der verwendeten Version weder mittlere NN Potentiale noch KN/ $\Lambda$ N Potentiale beinhaltet. Es zeigt sich, dass kein Modell in der Lage ist alle Observablen simultan zu beschreiben und keine Observable übereinstimmend von allen Modellen beschrieben werden kann. Die Ergebnisse der HSD und IQMD Transportmodelle legen nahe, dass ein repulsives KN Potential notwendig ist um die Teilchenkinematik ( $p_t$ -Spektren) widerzugeben, jedoch ist UrQMD zumindest teilweise in der Lage diesen Effekt des Potentials durch die Produktion über intermediäre Resonanzenanregung zu kompensieren. Die Uneindeutigkeit der Vorhersagen (für je drei von vier Observablen pro Teilchen) macht den weiteren Versuch der Extraktion von KN bzw.  $\Lambda$ N Potentialen unmöglich.

Weiterhin wurde der Versuch unternommen, das  $\Xi^-$  Hyperon zu rekonstruieren, welches zwei seltsame Quarks enthält und bislang noch nicht derart weit unterhalb seiner NN-Schwelle (-840 MeV) nachgewiesen wurde. Die Beobachtung eines Nullresultats veranlasste die Bestimmung einer oberen Produktionsgrenze. Diese Grenze wird mit Hilfe der Feldman-Cousins Methode, welche rein auf der Statistik der vorliegenden Datenprobe basiert, ermittelt. Hierfür wird ein Konfidenzintervall gewählt, das 99,7% (entsprechend  $3\sigma$  einer Normalverteilung) des hypothetischen Signals umfasst, was zu einer oberen Grenze von  $M_{\rm FC} < 2, 32 \times 10^{-3}$  führt. Das Resultat ist in Übereinstimmung mit früheren Untersuchungen zur Rekonstruktionsfähigkeit von HADES sowie mit Vorhersagen des UrQMD-Transportmodells. Unter der Annahme der ermittelten oberen Produktionsgrenze lässt sich weiterhin ein maximales Verhältnis von  $\Xi^-$  zu  $\Lambda + \Sigma^0$ Hyperonen von  $N_{\Xi^-}/N_{\Lambda+\Sigma^0} < 5, 8 \times 10^{-2}$  bestimmen.

# Contents

Al	bstrac	t		i	
In	haltsa	ingabe		iii	
Co	ontent	ts	v		
1	Intro	oductio	n to Strange Particle Production in HIC	1	
	1.1	Strong	ly Interacting Hadronic Matter	1	
		1.1.1	Phenomenology of Quantum Chromodynamics	1	
		1.1.2	Phases of Hadronic Matter	2	
		1.1.3	Experimental Access to Strongly Interacting Matter: Heavy-Ion Collisions	4	
		1.1.4	Mapping the QCD Phase Diagram	6	
		1.1.5	Equation of State for Nuclear Matter	8	
	1.2	Particl	e Production in HIC at few GeV/u	12	
		1.2.1	Strange Particle Production	13	
		1.2.2	Production Mechanisms in Matter Created in HIC	14	
	1.3	Hadro	n Properties in Dense Baryonic Matter and QCD Models	18	
		1.3.1	Chiral Symmetry	19	
		1.3.2	Chiral Symmetry Breaking	20	
		1.3.3	Strangeness in Nuclear Matter	21	
		1.3.4	Melting of the Quark Condensate and Modification of Hadron Properties	24	
		1.3.5	Cloudy Bag Model	25	
	1.4		etical Models: Access to Properties of Dense Matter	26	
		1.4.1	Dynamical Evolution – Kinetic Transport Models	27	
		1.4.2	Thermal Particle Production – Statistical Models	32	
	1.5		of-the-Art: Results from Previous Experiments	34	
		1.5.1	Observables	34	
		1.5.2	KaoS	35	
		1.5.3	FOPI	36	
		1.5.4	HADES	37	

2	Higł	і Ассер	tance Di-Electron Spectrometer	41
	2.1	Physic	s Motivation and Technical Requirements	41
	2.2	Techni	cal Components	43
		2.2.1	Tracking System: Magnetic Spectrometer	43
		2.2.2	META Detectors	46
		2.2.3	Start- and Veto-Detector	49
		2.2.4	Segmented Gold Target	50
		2.2.5	Forward Wall	51
		2.2.6	Lepton Identification	52
		2.2.7	Central Trigger System and Data Acquisition	53
3	Ever	nt Selec	tion and Track Reconstruction	55
	3.1	Beam	Time Facts and Numbers	55
	3.2	Data P	Processing and Quality Assessment	55
	3.3	Stabili	ty of Detector Systems	57
	3.4	Event	Characteristics	58
		3.4.1	Event Vertex Reconstruction	58
		3.4.2	Event Selection	60
		3.4.3	Centrality Selection	62
	3.5	Track	Reconstruction	63
		3.5.1	Segment Reconstruction	65
		3.5.2	MDC-META Detector Matching	71
		3.5.3	Momentum Reconstruction	71
	3.6	Particl	e Identification	75
		3.6.1	Reconstruction of Charged Particles	75
		3.6.2	Reconstruction of Decayed Particles	80
	3.7	Start T	Time Determination and Recalculation	82
	3.8	Match	ing Simulation and Data	83
		3.8.1	Event Generators	84
		3.8.2	Detector Modeling: GEANT	84
		3.8.3	MDC Time Cuts	84
		3.8.4	Modeling $\delta$ -electron Contributions in Simulation	86
4	Reco	onstruc	tion of $K^0_s, \Lambda$ and $\Xi^-$	91
	4.1		Selection	91
	4.2	Recon	struction of Weakly Decaying Hadrons	101
		4.2.1	Single Particle Identification	101
		4.2.2	Pair Analysis	104
	4.3	Accep	tance and Efficiency Correction	130
		4.3.1	Acceptance Determination	134
		4.3.2	Detector and Reconstruction Efficiency	135
		4.3.3	Decay Curve	
	4.4	Search	for the Cascade	140

		4.4.1	Search for Rare Signals	140	
		4.4.2	Decay Topology and Cut Value Estimation	141	
5	-		al Results	147	
	5.1	$\Lambda$ Prod	uction		
		5.1.1	Transverse Mass Spectra		
		5.1.2	Rapidity Density and Inverse Slope Distributions		
		5.1.3	Centrality-differential Analysis	156	
	5.2	$K_s^0$ Pro	duction		
		5.2.1	Transverse Mass Spectra	159	
		5.2.2	Rapidity Density and Inverse Slope Distributions	159	
		5.2.3	Centrality-differential Analysis	164	
	5.3	Upper ]	Limit on $\Xi^-$ Production $\ldots$	166	
	5.4	Summa	ary of Investigated Particle Production in Au+Au	171	
6	Disc	ussion		173	
	6.1	Ensem	ble of Reconstructed Strange Hadrons in Au+Au	174	
	6.2	Compa	rison of $K_s^0$ and $\Lambda$ Production Yields to World Data	178	
	6.3	Compa	rison to Transport Model Calculations	180	
		6.3.1	Particle Production Yields and Centrality Dependence	180	
		6.3.2	Rapidity Density Distribution	181	
		6.3.3	Transverse Momentum Spectra	186	
		6.3.4	What can be concluded from comparisons to transport models?	189	
	6.4	Compa	rison to Statistical Hadronization Model	194	
	6.5	Chemic	cal vs. Kinetic Freeze-out Temperatures	195	
	6.6	Compa	rison of the Upper Production Limit of $\Xi^-$ to World Data $\ldots \ldots \ldots$	196	
Su	mma	ry		199	
Zu	samn	nenfassı	ing	205	
Α	Supi	olement	al Material	211	
Lis	st of F	igures		217	
Lis	List of Tables 22.				
Bil	bliogr	aphy		225	

# Chapter 1

# **Introduction to Strange Particle Production in HIC**

# **1.1 Strongly Interacting Hadronic Matter**

# 1.1.1 Phenomenology of Quantum Chromodynamics

In the early 70's deep-inelastic electron-proton collisions shed light on a more fundamental structure of protons replacing the thought of point-like nucleons in the core of atoms. Today the inner structure of these objects is known to be built up of quarks q, antiquarks  $\bar{q}$  and gluons g, socalled partons, which are described by the field theory of quantum chromodynamics (QCD). An important property of QCD is the confinement of strongly interacting partons which only occur in bound states [1]. The strong binding is represented by the charge of QCD that each parton carries – its color. All bound states are color-neutral and can be subdivided into the groups of baryons (qqq) and mesons ( $q\bar{q}$ ). They are color neutral, meaning that they have zero net color charge. The force carriers of the strong interaction are the gluons which themselves carry color charge and hence not only interact with quarks but also with other gluons. This is one of the major differences to quantum electrodynamics where the electrically uncharged photons cannot directly interact with each other.

A hadronic state has a significantly higher mass than the sum of the quark masses it consists of. This can be understood in a simplified, phenomenological picture by making use of Heisenberg's uncertainty principle which states that

$$\Delta x \Delta p \ge \hbar. \tag{1.1}$$

This means that the two quantities position x and momentum p cannot be determined with arbitrary precision. In an extended system like a hadron, consisting of color-charged particles, nature will ensure color neutrality and hence keep its partons as localized as possible. In the case of a nucleon, containing only the light quarks u and d, the volume is experimentally well constrained and can be approximated by a sphere with radius 1 fm. Considering 1.1 this results in a lower limit for a constituent quarks momentum of  $p \approx 200$  MeV/c. According to Einstein's relativistic equation

$$E = \sqrt{(m_0 c^2)^2 + (pc)^2} \tag{1.2}$$

and by neglecting the small u and d quark masses, the total energy and hence the mass of the three confined constituents can be determined to amount roughly to  $600 \text{ MeV/c}^2$  which explains already 2/3 of the actual nucleon mass by dynamical generation. A more involved QCD-based justification of why hadrons carry much higher masses than their constituents follows in section 1.3.

A formal prediction of QCD is the inverse dependence of the strong coupling on the energy density. Contrary to quantum electrodynamics (QED), the coupling constant  $\alpha_s$  of strong interaction is inversely proportional to the energy. The coupling of quarks and gluons becomes asymptotically weaker with increasing energy transfer resulting in vanishing coupling strength between color charged particles in the limit of high energy transfers or small distances. A deconfinement of hadronic matter in the limit of high energy densities is referred to as asymptotic freedom and may lead to a state of quasi-free quarks and gluons: the quark-gluon plasma (QGP) [2, 3, 4].

# **1.1.2** Phases of Hadronic Matter

The QGP state is assumed to have existed shortly after the big bang (up to  $10^{-6}s$ ) before the universe cooled down to energy densities where quarks and gluons formed bound states of hadronic matter. In figure 1.1 the two phases of QCD are indicated as a function of the two parameters temperature T in MeV<sup>1</sup> and baryo-chemical potential  $\mu_B^2$ . The latter one can be understood as a quantity describing the baryon to anti-baryon balance, thus having zero baryo-chemical potential correspond to an equal number of particles and anti-particles. With increasing values of  $\mu_B$  the net baryon number ( $N_{\rm B} - N_{\rm B}$ ) increases, resulting in finite net baryon densities.

To date still little is known about the QCD phase diagram, both experimentally as well as theoretically. The lower left part in the phase diagram, corresponding to low temperatures T and/or low baryo-chemical potential  $\mu_B$ , represents the region of hadronic matter which includes also our known atomic matter close to zero temperature at potentials of roughly  $\mu_B \approx 940$  MeV. This phase of hadronic matter is separated from the above mentioned phase of quark matter by a line indicating a phase transition. Lattice QCD calculations<sup>3</sup> predict a crossover phase transition at zero chemical potentials lattice QCD cannot be applied robustly to study the remaining parts of the phase diagram [7]. For this purpose effective models can be used which indicate a  $\mu_B$ -driven first-order phase transition at zero temperature [8, 9, 10]. Hence, from basic thermodynamic considerations this implies the existence of a critical point (CP) somewhere at finite baryo-chemical

2

<sup>&</sup>lt;sup>1</sup> kT at 298 K = 25.7 meV [5]

<sup>&</sup>lt;sup>2</sup> Generally speaking, a chemical potential  $\mu$  is a thermodynamical quantity describing the energy needed to add a particle with given quantum numbers to a system. The chemical potential is also given in units of electronvolt.

<sup>&</sup>lt;sup>3</sup> In lattice gauge theory the phase space is divided into little cells in which QCD can be solved non-perturbatively. In the limit of infinitely small cells and an infinitely large number of cells the continuum QCD is recovered.

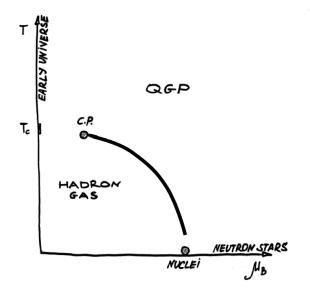


**Figure 1.1:** The phase diagram of QCD is described by the two parameters temperature T and baryo-chemical potential  $\mu_B$ . The hadronic phase at low to moderate T and  $\mu_B$  contains also the matter at nuclear ground state density. Due to the asymptotic freedom of QCD, a phase of deconfined quarks and gluons may be reached (QGP) with increasing temperatures and/or baryo-chemical potentials. At low  $\mu_B$  and moderate T a cross-over phase transition is predicted by Lattice QCD. A first-order phase transition would imply the existence of a critical point. Figure taken from [6].

potential and finite T before reaching the theoretically described cross-over region. At this point the two phases of a hadron gas and quark matter coexist. The search for such a point is focus of numerous experimental as well as theoretical investigations [11, 12].

The phase diagram can be linked to laboratories occurring in nature which are characterized by two limits:

- The limit of high temperature and low baryo-chemical potential reflects the conditions of the early universe shortly after the big bang, however, investigations by astrophysical means such as the measurement of radiation from cosmic micro-wave background (CMB) are limited to processes which have happened after the quark era had already ended.
- Vice versa, in the limit of low temperature and high net baryon densities a state of compressed nuclear matter will be created which may also occur in the core of neutron stars. Until today the innermost structure of these ultra-compact objects is unclear and various conceivable scenarios have been suggested such as strange particle or pion condensates, quark matter or hyperon stars [13, 14, 15, 16, 17, 18]. The large distance of neutron stars from earth strongly limits the amount of observables and makes investigations on their formation and structure complex. On the other hand, this lack of understanding implies that they are not well suited as laboratories to deduce information on the phases of hadronic matter. However, with the first detection of gravitational waves recently, this situation will certainly change in the future [19].

Due to the complexity of accessing the above mentioned laboratories, the only known possibility to study the various described phases of strongly interacting matter in terrestrial experiments is offered by heavy-ion collisions (HIC).

# **1.1.3 Experimental Access to Strongly Interacting Matter: Heavy-Ion Collisions**

The energy densities of quark matter believed to be necessary to create a QGP phase, may be reached in heavy-ion collisions. However, time scales for processes of the strong interaction are typically in the order of  $< 10^{-22}s$  making direct observations impossible. Instead, properties of matter can only be reconstructed from particles which are measured in active detector volumes nano- to microseconds later.

As can be seen from figure 1.1, access to a phase with quark degrees of freedom is achieved through an increase of temperature or net baryon densities, or both. These quantities can be controlled by the kinetic beam energy of the incident ions. Hence, the experimental approach to obtain such a phase by means of heavy-ion collisions can take various forms in terms of size and implementation of the accelerator. Furthermore, the beam energy is proportional to the number of newly produced particles through inelastic processes according to equation 1.2 which requires a dedicated apparatus in order to measure all or a subset of these particles. The detectors have to match the resulting particle rates, track densities etc. and differ in a variety of features depending on the particular physics case.

Large scale experiments at CERN<sup>4</sup> [20] in Geneva/Switzerland like the detectors ALICE<sup>5</sup> [21], ATLAS<sup>6</sup> [22] or CMS<sup>7</sup> [23] are fed by the world's largest particle collider LHC<sup>8</sup> [24]. The maximum kinetic beam energies reach up to few TeV per nucleon<sup>9</sup> resulting in extremely high temperatures and baryo-chemical potentials close to zero. The second largest particle accelerator RHIC<sup>10</sup> [25] is located at the BNL<sup>11</sup> [26] in Brookhaven/USA where the dedicated heavy-ion experiments STAR<sup>12</sup> [27] and PHENIX<sup>13</sup> [28] operate at high temperatures and low to moderate net baryon densities.

Compared to these accelerators, the ring accelerator SIS18<sup>14</sup> – where the HADES experiment is operating – is performing in the low beam energy regime of a few GeV per nucleon which results in high net baryon densities due to the increased stopping of the incoming nucleons [29].

The different stages of the space-time evolution of a symmetric heavy-ion collision are sketched in figure 1.2 and some of their important features with special emphasizes on the SIS energy regime are described in the following:

<sup>7</sup> Compact Muon Solenoid

- <sup>11</sup> Brookhaven National Laboratory
- <sup>12</sup> Solenoidal Tracker At RHIC
- <sup>13</sup> Pioneering High Energy Nuclear Interactions eXperiment

<sup>&</sup>lt;sup>4</sup> Conseil Européen pour la Recherche Nucléaire

<sup>&</sup>lt;sup>5</sup> A Large Ion Collider Experiment

<sup>&</sup>lt;sup>6</sup> A Toroidal LHC Apparatus

<sup>&</sup>lt;sup>8</sup> Large Hadron Collider

<sup>&</sup>lt;sup>9</sup> The maximum possible kinetic beam energy in a given accelerator depends on the mass of the accelerated particles.

<sup>&</sup>lt;sup>10</sup> Relativistic Heavy Ion Collider

<sup>&</sup>lt;sup>14</sup> SchwerIonen-Synchrotron 18 – The number is referring to the rigidity of the accelerator which can be understood as the resistance of a charged particle to the deflection induced by a magnetic field.

#### 1.1. STRONGLY INTERACTING HADRONIC MATTER

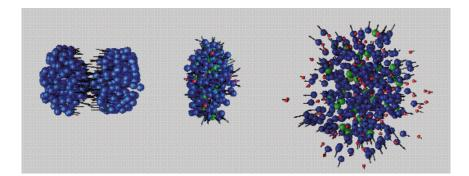


**Figure 1.2:** Stages of a central Au+Au collision obtained by an IQMD simulation at a beam energy of 2A GeV [30]. In the initial phase (left) the heavy-ions approach each other before the collision takes place where a high-density phase is created (center). Due to the pressure built up in the participant region, the system relaxes by expansion and cools down (right). The freeze-out is describing the point in time when all inelastic (chemical) and elastic (kinetic) interactions cease.

**Initial Phase** – Two Lorentz-contracted ions with N nucleons approach each other with a given impact parameter  $b^{15}$  before starting to overlap. A necessary condition for a reaction is that this impact parameter is smaller than two times the radius of the colliding nuclei.

**High-Density Phase** – At SIS energies, the nucleons cannot escape fast enough from the overlapping volume and a high-density region (fireball) is created where the nature of NN interactions is not well known. Nucleons involved in the collision are referred to as participants, those passing without interaction as spectators. At SIS energies the high-density phase is expected to be rather long-living and reaches its maximum density after about 10 - 20 fm/c. In the created matter collective many-body effects occur and properties of the constituents may undergo significant modifications (for details on in-medium modifications, see 1.3 and 1.3.3). For large systems and large enough NN cross-sections local equilibrium may be reached which would justify a description by thermodynamical observables like average temperatures and densities. In addition, a quark matter phase may be created [2, 4, 31]. An important quantity in this context is the nuclear stopping which quantifies to what extent the incoming nucleons are slowed down and thus remain in the reaction zone. The degree of stopping is larger in the SIS energy regime compared to RHIC or LHC energies.

**Expansion and Freeze-Out** – Due to the high pressure created in the collision zone the system will expand resulting in a fast reduction of temperature and density. In leading order this expansion is a spherically invariant, radial outward flow. Furthermore, the pressure gradient which drives the expansion strongly depends on the solid angle, hence a non-spherical flow pattern can be observed in non-central HIC and parametrized by Fourier coefficients  $v_n$  of n - th order [32, 33]. At SIS energies the passing time of the spectators is of the same order as the ex-

<sup>&</sup>lt;sup>15</sup> The impact parameter is the distance between the centers of two passing nuclei (or nucleons) perpendicular to their flight path.

pansion time of the fireball making interactions between hot (produced in the fireball) and cold (nucleons or light nuclei from spectators) matter likely [29].

After a certain relaxation time densities in the medium are sufficiently low that, first, all inelastic scattering processes and hence particle production cease: the so-called chemical freezeout occurs. From this point on the number of produced particles of a certain species will stay constant – except for resonance decays – and can be described by statistical models which will be discussed in section 1.4.2. Further expansion leads to a state where also elastic interactions stop which is referred to as kinetic freeze-out. After this point all relevant properties of particles like momentum and angular distributions will stay unchanged until they reach the detector<sup>16</sup>.

## **1.1.4** Mapping the QCD Phase Diagram

As pointed out previously, heavy-ion collisions constitute the only known experimental access to study the properties of matter under extreme conditions as they were present in our early universe or are realized in astrophysical objects such as neutron stars. In order to link experimental findings to the fundamental properties of such extreme states of matter theories and effective models have to be consulted. As discussed in the previous section, a HIC undergoes several steps during its temporal evolution with substantially distinct properties. This evolution rather corresponds to a trajectory in the QCD phase diagram with continuously changing temperature T and baryochemical potential  $\mu_B$ , as illustrated in figure 1.3. Plotted are the respective trajectories for a collision of Ar+KCl at  $E_{kin} = 1.76$ A GeV and for Au+Au at  $E_{kin} = 1.23$ A GeV – both systems have been measured with HADES - in the QCD phase diagram calculated with a coarse-graining approach based on the microscopic transport model UrQMD. In this quasi-macroscopical hybrid ansatz it is possible to connect the time evolution of a heavy-ion collision obtained from transport models (see section 1.4.1) with thermodynamical properties by dividing the system into little space-time cells. Bulk observables, such as temperature or density, are calculated for each cell and finally summed to obtain static properties of the full system. A detailed description of this model can be found in [34]. Similar realizations of this ansatz are presented in [35].

Purely macroscopic theories such as statistical hadronization models (SHM) [40], which will be discussed in 1.4.2, also provide access to the QCD phase diagram. In this picture, the particle production yields at chemical freeze-out obtained in a HIC are, in its simplest approach, described by the three thermodynamical observables temperature T, baryo-chemical potential  $\mu_B$ and the volume V. A fit of this model to the particle yields measured in experiment will provide a data point in the T- $\mu_B$  plane. In contrast to the previously described coarse-graining approach a time-evolutional description is not included in such a purely macroscopic static model. Figure 1.4 shows a systematic of data points obtained from various experimental sets of particle yields.

A very striking feature is that all points approximately line up on a curve connecting the experimental findings from low SIS up to the highest LHC energies, which calls for an inter-

<sup>&</sup>lt;sup>16</sup> In fact, a measuring process (e.g. identification via energy-loss or time-of-flight) by definition involves a change in particle properties, since a particle can only be detected when it interacts with the detector material. However, the detector is designed to keep these disturbances as small as possible. Furthermore, these mostly electromagnetic effects are well-known and observables can be corrected for. Sometimes, a complete stopping of a particle may even be the goal in order to identify it (calorimeters).

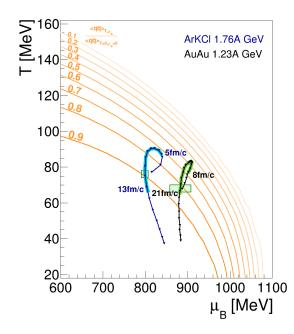
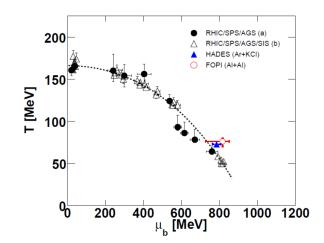


Figure 1.3: QCD phase diagram together with trajectories showing the evolution of a heavyion collision as a function of temperature Tand baryo-chemical potential  $\mu_B$  for two systems measured with HADES. The calculation is obtained from a UrQMD coarse-graining approach [34]. Indicated for each system are the times when the high-density phase starts and ends (blue band: Ar+KCl, green: Au+Au). The box indicates the chemical freeze-out points obtained from a statistical model fit to measured particle yields in the respective systems [36]. In case of Au+Au, the value is extracted including results from [37] and this thesis. Also indicated are the lines (orange) of constant expectation value for the quark condensate [38]. Figure taken from [39].

**Figure 1.4:** QCD phase diagram in the T- $\mu_B$  plane mapped with a statistical hadronization model (SHM). The data points are obtained from a THERMUS fit [41] to measured particle yields ranging from high-energy experiments down to SIS18 energies, where HADES is operating [40, 42, 43]. The points seem to line up on a common curve (dashed line) which indicates a SHM-based parametrization with a universal chemical freeze-out condition of  $\frac{\langle E \rangle}{\langle N \rangle} \approx 1$  GeV [42]. Figure taken from [44].



pretation of this common behavior. A first chemical freeze-out criterion in heavy-ion collisions was suggested to be the average energy per particle  $\frac{\langle E \rangle}{\langle N \rangle}$  which seems to be approximately unity independent of the beam energy and system size [45]. This means that, as soon as this quantity drops below a value of roughly one, all inelastic collisions in the hot and/or dense fireball cease and particle chemistry will remain constant if no further energy is put into the system. The dashed line in figure 1.4 indicates a parametrization based on the statistical hadronization model where this condition of  $\frac{\langle E \rangle}{\langle N \rangle} \approx 1$  GeV is fulfilled. Several alternative freeze-out criteria have been studied as well [42, 46, 47, 48].

As discussed in section 1.1.2, the assumption of a first-order phase transition together with the knowledge of having a cross-over at zero baryo-chemical potential imply a critical point in the QCD phase diagram. The search for this critical point where the phases would coexist and hence experimental observables may change drastically is addressed by various experiments. Programs dedicated to this search were conducted, e.g. the STAR beam energy scan [11].

For some phases predicted by theory it is questionable whether they are realized in nature and can be accessed with a heavy-ion collision. An example is the region where a superconducting phase may occur which requires extremely high baryo-chemical potentials  $\mu_B$  and rather low temperatures T [49, 50].

The question that has to be addressed in this context is how the "success" of these descriptions of complex many-body systems provided by (semi-)macroscopical models, where at least local equilibration is assumed, can be interpreted and to what extent conclusions on this apparent chemical equilibrium of the system created in a HIC can be drawn. This will be further discussed in section 1.5.4.

### **1.1.5** Equation of State for Nuclear Matter

Another way to describe a given state of a system in (local) thermal equilibrium on a macroscopic level in terms of bulk observables like pressure P, temperature T, density  $\rho$  or number of particles N is through its equation of state (EOS). The state of nuclear matter can be described by such an equation expressing the internal energy E of a system as a function of the variables temperature T and density  $\rho$ . When assuming an equilibrated state during the expansion of nuclear matter the center-of-mass energy of the reaction can be divided into a thermal internal energy  $E_{\rm th}$  and a compression energy  $E_{\rm C}$  term as follows:

$$E(\rho, T) = E_{\rm th}(\rho, T) + E_{\rm C}(\rho, T = 0) + E_0,$$

with  $E_0$  denoting the binding energy in the ground state which can be estimated to be  $E_0 \approx -16$  MeV/nucleon using the Bethe-Weizsäcker formula [51] for normal nuclear density  $\rho_0$ . Figure 1.5 shows the internal energy at zero temperature as a function of the relative density  $\rho/\rho_0$  which can be considered as the degree of compression of a system.

In a collision of heavy ions the thermal energy  $E_{\rm th}$  is translated into particle excitation or production via inelastic scattering processes. The compression energy  $E_{\rm C}$  results, as the name

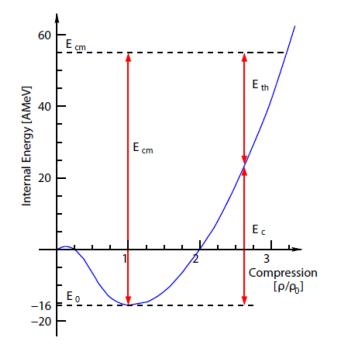


Figure 1.5: Internal energy per nucleon as a function of compression of nuclear matter [52]. The minimum is located at normal nuclear density  $\rho_0$ . At higher relative densities  $\rho/\rho_0$  the center-of-mass energy can be divided into a compressional  $(E_{\rm C})$  and a thermal  $(E_{\rm th})$  term.

suggests, in a compression of the matter and depends on the incompressibility modulus  $\kappa^{17}$  of the equation of state. The degree of stiffness of the equation of state is directly related to this quantity thus speaking of a soft for small and hard or stiff EoS<sup>18</sup> for high values of  $\kappa$ . The energy per nucleon in dense matter differs significantly depending on its stiffness. There have been many investigations indicating a soft EoS [53, 54, 55, 56, 57, 58]. However, this picture is challenged by more recent findings on flow data of charged particles in the SIS energy regime [59, 60] making conclusions on the stiffness of the equation of state still ambiguous.

The stiffness of the equation of state also plays an essential role for our understanding of astrophysical processes like supernovae explosions or the composition and structure of neutron stars. In the latter case the equation of state gives direct information on the maximum neutron star mass when using the Tolman-Oppenheimer-Volkov equation [61] and, vice versa, high-precision measurements of their mass can give crucial constraints on the range of values for the incompressibility  $\kappa$ . Measurements by [62] and [63] set a new upper limit on the maximum mass ( $< 2.03 \pm 0.04 M_{\odot}$  in [63]) of these ultra-dense objects challenging findings from HIC on the same observable ( $< 1.5 M_{\odot}$ ) [54, 64]. This observation lead to re-considerations about the inclusion of hyperons Y whose appearance in the interior of neutron stars is a possible scenario. This may indeed lead to a significant softening of the equation of state and hence a reduction of the maximum mass [65, 66, 67, 68] which seems to conflict with these new astronomical findings. However, in order to rule out this apparent conflict the behavior of hyperons in a dense environment, i.e. the strength of their interaction with nucleons and their resulting effective in-medium

<sup>&</sup>lt;sup>17</sup> The incompressibility is defined as the second derivative of the compression energy at  $\rho = \rho_0$  and describes the curvature of the equation of state at T = 0. A high value of  $\kappa$  describes a low compressibility of nuclear matter.

<sup>&</sup>lt;sup>18</sup> Soft matter will show less resistance to an external force compared to stiff matter.

potential YN has to be understood more precisely than it is constrained by experiments so far. Figure 1.6 shows the gravitational mass to radius relation for various scenarios obtained with the Quark-Meson Coupling (QMC) model [69] when including hyperons in the EOS showing the influence of several cut-offs of the  $\Lambda$  hyperon mass corresponding to different YN potentials. These calculations demonstrate that with a sufficiently repulsive  $\Lambda N$  potential agreement with the recent experimental results can be obtained.

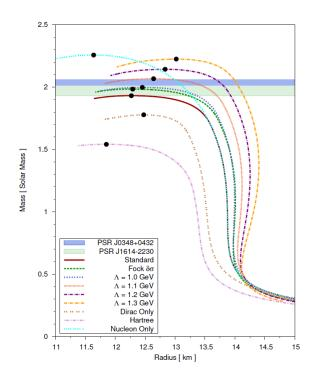


**Figure 1.6:** Gravitational mass to radius relation for neutron stars calculated with the QMC model [69] for various scenarios (lines) when including hyperons in the equation of state. The black points show the maximum mass of the corresponding calculation. Indicated as colored bars are also the experimentally observed maximum masses from [62] and [63]. Any EOS line which does not intersect with these observations has to be ruled out. Figure taken from [18].

The role of the potential between strange particles and nucleons and their dependence on density will be discussed in more detail in section 1.3 and will be the focus of the investigations within this thesis.

As addressed above, an equation of state describes bulk properties of an equilibrated system. However, the measurement of a heavy-ion collision and accordingly the detector observables are the result of an integral over all time scales of the system evolution and the assumption of global or even local equilibrium at SIS energies cannot be considered during most stages since the relaxation time which is needed for equilibration coincides with the lifetime of the interesting high-density phase. There exist experimental hints which indicate this incomplete equilibration even in central collisions [70, 71, 72]. Hence, in order to access all stages of the dynamic evolution and the full history of a HIC, a comparison to microscopic models is mandatory.

#### 1.1. STRONGLY INTERACTING HADRONIC MATTER

#### **Equation of State for Asymmetric Nuclear Matter**

In order to study properties of asymmetric nuclear matter the equation of state can be expressed in terms of the energy per nucleon as a function of baryonic density  $\rho$  and isposin<sup>19</sup> asymmetry  $\alpha$  [73, 74]:

$$E(\rho, \alpha) = E(\rho, \alpha = 0) + E_{sym}(\rho)\alpha^2 + \mathcal{O}(\alpha^2)$$

with

$$E_{\rm sym}(\rho) = \frac{1}{2} \left. \frac{\partial^2 E(\rho, \alpha)}{\partial \alpha^2} \right|_{\alpha=0} , \ \alpha = \frac{N-Z}{N+Z}$$

 $E_{\rm sym}$  denotes the symmetry energy term which is characterizing the isospin dependence of the equation of state and depends parabolically on the asymmetry parameter  $\alpha$ . It describes the difference in energy per nucleon between matter exclusively consisting of neutrons and isospin symmetric matter (Z = N).

Figure 1.7 shows the dependence of the symmetry energy on the relative nuclear density  $\rho/\rho_0$  of a system for calculations based on transport models, effective field theory, ab initio approaches and phenomenological density functionals. A clear divergence of the various calculations at supra-normal densities ( $\rho/\rho_0 \gg 1$ ) is visible.

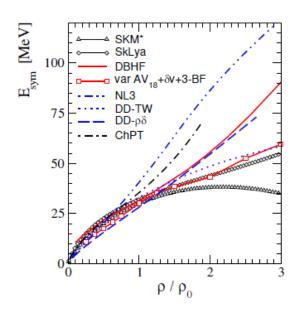


**Figure 1.7:** Symmetry energy as a function of relative baryon density for different model predictions. A strong divergence between various calculations is observed above 1-2 times  $\rho_0$ . Figure taken from [70].

In the region below nuclear saturation density  $\rho_0$  the symmetry energy term and the isospin dependence of nuclear forces is well constrained by various experiments operating in the Fermi

<sup>&</sup>lt;sup>19</sup> With respect to the strong interaction, protons and neutrons are considered to be the same particle ("nucleon") only differing in the so-called isospin quantum number. This formalism was introduced analogue to the spin quantum number which distinguishes between two different quantum states ("up" and "down") for otherwise identical electromagnetic particles. With the later discovered quarks being constituents of the nucleon, this formalism was extended onto quark level giving the two lightest quarks their names.

energy regime [75]. In order to constrain the behavior of the symmetry term towards high densities experimental probes in isospin-asymmetric matter at high baryon densities have to be studied. Ferini et al. [76] and others [57, 77, 78] predict the density dependence of the symmetry energy term to have significant influence on the yield of different isospin states of newly produced particles, thus making p/n,  $\pi^+/\pi^-$  and  $K^0/K^+$  valuable probes. Whereas the first observable cannot be considered in most experiments due to the challenge of measuring neutrons, the difficulty for the  $\pi^+/\pi^-$  ratio lies within the high absorption cross-sections of pions through nucleon resonances ( $N\pi \leftrightarrow \Delta$ ) inside the medium . In contrast to pions, kaons close to threshold have a large mean free path due to strangeness conservation (see 1.2.2) and hence do not suffer from secondary reabsorption processes like antikaons, however, charge exchange reactions of the type  $pK^+ \rightarrow nK^0$  do occur also in the kaon sector. Considering the symmetry energy term affecting the yield of neutral and positive kaons differently, their ratio becomes a suitable observable for the isospin dependence from the dense early stage of the collision where they are produced.

In the Au+Au collision system investigated in this thesis the density in the created medium is expected to be in the range of  $\rho/\rho_0 = 2 - 3$  where the deviation between the different models shown in figure 1.7 is already significant and therefore the sensitivity to the isospin dependence of the energy symmetry term may be given.

# **1.2** Particle Production in HIC at few GeV/u

In a collision of heavy-ions a high-density phase is created in which elastic and inelastic reactions take place. In the latter case kinetic energy of the projectile nucleons can be transformed into the mass of new particles corresponding to the famous equivalence of mass and energy, see equation 1.2.

As a consequence of energy and momentum conservation a necessary requirement for particle production in elementary collisions is that the total energy of both particles in the initial state is at least equal to the total rest energy of the particles in the final state. This energy is referred to as nucleon-nucleon (NN) threshold energy or elementary production threshold. If for example a pion – the lightest meson with a mass of  $140 \text{ MeV/c}^2$  – is produced in an elementary reaction as follows

$$NN \to NN\pi,$$
 (1.3)

an NN threshold energy in the center-of-mass system<sup>20</sup> of  $\sqrt{s} = 2.02$  GeV is needed. In order to produce heavier particles the kinetic beam energy  $E_{\rm kin}$  of the projectile has to be increased.

$$\sqrt{s} = \sqrt{(E_{0,\mathrm{P}})^2 + (E_{0,\mathrm{T}})^2 + (E_{\mathrm{kin},\mathrm{P}} + E_{0,\mathrm{P}}) \cdot 2E_{0,\mathrm{T}}}$$

with the energies at rest  $E_{0,P/T}$  of the projectile (P) and target (T) and the kinetic beam energy of the projectile  $E_{kin,P}$  [51].

 $<sup>\</sup>overline{}^{20}$  The energy  $\sqrt{s}$  available for particle production in the center-of-mass system of two colliding nucleons can be calculated via

In the investigated Au+Au beam time, which will be discussed in this thesis, the projectile energy is at  $E_{\rm kin} = 1.23$ A GeV corresponding to  $\sqrt{s} = 2.41$ A GeV in the center-of-mass system. As will be pointed out in the following, particles in heavy-ion collisions can be produced below their elementary threshold. Throughout this thesis this will be referred to as sub-threshold production.

### **1.2.1** Strange Particle Production

The additive quantum number strangeness S is a conserved quantity in the strong interaction. A strange quark s has the quantum number S = -1, its anti-particle  $\bar{s}$  carries S = +1 respectively<sup>21</sup>. Since the incident ions do not contain any strangeness, all detected particles carrying (anti-)strange quarks have to be newly produced. Due to the conservation of strangeness, each hadron containing a strange quark has to be produced together with another one carrying an anti-strange quark<sup>22</sup> such that the net strangeness quantum number adds up to zero:

$$N(s) - N(\bar{s}) = 0, \tag{1.4}$$

where  $N(s)/N(\bar{s})$  denote the number of strange/anti-strange quarks in a system. Thus for experimentally observed strange hadron yields in a heavy-ion collision around elementary threshold follows:

$$N(\underbrace{\Sigma^{+} + \Sigma^{-} + \Sigma^{0} + \Lambda + K^{-} + \bar{K}^{0}}_{N(s)}) - N(\underbrace{K^{+} + K^{0}}_{N(\bar{s})}) = 0.$$
(1.5)

In this strangeness balance equation only those hadrons are listed that contribute in leadingorder to strangeness production at SIS energies. The contribution of more rarely produced resonances such as  $\Sigma(1385)^{\pm}$  or multi-strange baryons with net strangeness |S| > 1 like  $\Xi^0(uss) / \Xi^-(dss)$  or  $\Omega(sss)$  can be neglected in this equation.

Because of the associative production, the occurrence of particles carrying the strange quark species  $(s/\bar{s})$  is rare at SIS energies compared to hadrons containing light quarks from the first family (u, d). The energetically most favorable production channel involving strangeness with the lowest threshold in nucleon-nucleon collisions is

$$NN \to N\Lambda K^+.$$
 (1.6)

Besides the positive kaon  $K^+$  ( $\bar{s}u$ ) a  $\Lambda$  (uds) hyperon – the lightest strange baryon – has to be produced. In order to conserve the baryon quantum number there also has to be a nucleon N

<sup>&</sup>lt;sup>21</sup> This rather confusing convention results from the fact that the kaon containing an antiquark was discovered first. This discovery lead to the introduction of the strangeness quantum number.

<sup>&</sup>lt;sup>22</sup> Another possibility is to have both quarks with net strangeness quantum number  $S \neq 0$  in a bound state. The  $s\bar{s}$  ground state is called  $\phi$  meson.

in the final state. The insignificantly heavier neutral kaon  $K^0$  is also produced together with a  $\Lambda$  hyperon resulting in approximately the same probability for this reaction. Although the negative kaon  $K^ (s\bar{u})$  is as heavy as the  $K^+$ , its production threshold is much higher than for the two previously mentioned reactions:

$$NN \to NNK^+K^-. \tag{1.7}$$

This again follows directly from strangeness conservation since due to the *s* quark in the negative kaon an  $\bar{s}$  quark is required which is present in the positive kaon. In order to guarantee the conservation of the baryon quantum number an additional nucleon in the final state makes this production much more expensive in terms of energy than 1.6.

Production channel	$\sqrt{s}_{ m thr}$ [A GeV]	$\sqrt{s}_{ m exc}$ [A GeV]		
$NN \to N\Lambda K^+$	2.55	-0.14		
$NN \rightarrow N\Lambda K^0$	2.56	-0.15		
$NN \to NK^+\Sigma$	2.62	-0.21		
$NN \rightarrow NNK^+K^-$	2.86	-0.45		
$NN \to NN\Phi$	2.9	-0.49		
$NN \to N \Xi^- K^{+/0} K^{+/0}$	3.25	-0.84		
$NN \to N\Omega^- K^+ K^+ K^+$	4.1	-1.69		
Center-of-mass energy $\sqrt{s}_{(Au+Au)} = 2.41 \text{A GeV}$				

**Table 1.1:** Production channels and thresholds of strange particles in nucleon-nucleon collisions. Indicated is also the center-of-mass energy available in the Au+Au collision system. The excess energy is defined as  $\sqrt{s}_{exc} = \sqrt{s}_{Au+Au} - \sqrt{s}_{NN}$ .

Table 1.1 gives a summary of the production channels for all strange particles and their thresholds in elementary nucleon-nucleon reactions which are compared to the beam energy available in the investigated Au+Au collision system.

# **1.2.2** Production Mechanisms in Matter Created in HIC

As listed in 1.1, all the NN thresholds for strange particles are above the center-of-mass energy in the Au+Au system that will be investigated in this thesis. However, a heavy-ion collision is a process involving many nucleons and is not restricted to one but involves multiple NN collisions. This implies that all measurements of hadrons carrying strangeness cannot merely be explained by primary elementary reactions inside the reaction zone but, instead, the production is realized by secondary or multi-step processes which are enabled in a high-density environment formed in a HIC thus making sub-threshold production possible.

#### 1.2. PARTICLE PRODUCTION IN HIC AT FEW GEV/U

Maybe even more importantly, the dense medium created in these collisions is a system at length scales where the quantum-mechanical nature of particle interactions cannot be ignored and the naive picture of a system with purely hadronic degrees of freedom becomes vague.

In the following, dominant mechanisms affecting strange particle production on hadronic level are listed:

- Fermi-momentum  $p_F$  This momentum is a consequence of the Pauli exclusion principle which implies that two identical fermions cannot populate the same quantum state. For that reason fermions in a many-fermion system are microscopically not at rest and can get additional momenta up to  $p_F = 270 \text{ MeV/c}^{2/23}$ .
- Accumulation of energy via multi-step processes This includes elastic scattering processes with other hadrons in the medium as well as inelastic collisions resulting in resonant intermediate states like the  $\Delta$  or  $N^*$  resonances.
- Strangeness exchange reactions The idea behind these reactions is that a strange quark from one hadron is exchanged with a light quark from another hadron [79, 80, 81]. In this way strangeness can first be produced in a NN reaction with low energy threshold and the formation of another hadron with higher threshold via exchange or recombination of constituent quarks becomes possible. Most prominent is the exchange channel π<sup>-</sup>(dū) + Λ(uds) → K<sup>-</sup>(sū) + n(udd) where in the first step a Λ baryon is produced together with a positive kaon which is energetically the most favorable channel<sup>24</sup> and which enables an indirect production of negative kaons. Strangeness exchange reactions will also be addressed in 1.3 and 1.5.
- Mass modification due to in-medium potentials Theoretical models predict a repulsive  $K^+$ -nucleon and an attractive  $K^-$ -nucleon potential resulting in an increase/decrease of the in-medium effective kaon mass respectively [82, 83, 84]. As a consequence, the energy threshold for the production of a negative kaon will be lowered<sup>25</sup>. Since the pseudoscalar mesons and hyperons are coupled via strangeness exchange mechanisms, the correct treatment of all in-medium potentials is crucial in theoretical descriptions, such as transport models, in order to obtain reasonable production yields. This turns out to be even more complicated when considering that the cross-sections for such exchange processes as a function of density are rather unknown. A more detailed description of medium potentials will be given in section 1.3.3.

<sup>&</sup>lt;sup>23</sup> As a consequence fermions close to absolute zero temperature are still moving with non-vanishing velocities.

<sup>&</sup>lt;sup>24</sup> Note, that the mentioned strangeness exchange channel results in a state with higher energy and is therefore an endothermic reaction. Nature will always favor the state in which the energy is minimized, however, combining this with the lowered effective in-medium potential of a negative kaon (see point 3) the energy in the final state may fall below the energy of the initial one.

<sup>&</sup>lt;sup>25</sup> At the same time the effective mass of a positive kaon would be increased. Since the negative kaon is most probably produced with a  $K^+$  this does not necessarily mean that the production threshold is effectively lowered. However, most models predict only a slight repulsion for kaons but a strong attraction for antikaons.

#### **Strange Particle Yields**

Despite the discussed processes enabling sub-threshold production in heavy-ion collisions it is clear that the production rates will rapidly drop when the beam energy falls below the elementary threshold. Figure 1.8 shows the dependence of strange particle as well as charged pion yields as a function of the center-of-mass energy of central Au+Au collisions, also referred to as excitation function.

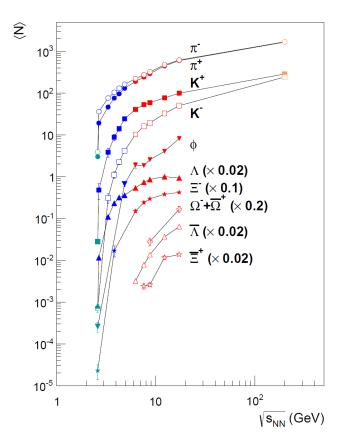


**Figure 1.8:** Excitation function of charged pions and strange particles. The data points indicate Pb+Pb and Au+Au measurements from experiments at SIS18 (green), AGS (blue), SPS (red) and RHIC (orange). The indicated HADES data points (full, green) are for the light Ar+KCl system. For a better overview, the hyperon yields are scaled down arbitrarily. [85, 86, 87, 88, 89, 90, 91, 92, 93, 94, 95, 96, 97]

The data points are a collection of several experiments at SIS18, AGS, SPS and RHIC. Strikingly, the availability of data below threshold is scarce. Concerning the SIS energy regime, so far only measurements for kaons,  $\phi$  mesons,  $\Lambda$  and  $\Xi^-$  hyperons from the light collision system Ar+KCl at 1.76A GeV by HADES could be added.

#### **Enhancement of (Multi-)Strange Particle Yields**

A model explaining (multi-)strange particle production in heavy-ion collisions is provided by the cloudy bag model [98, 99, 100], where quarks are contained in a hadronic bag which is surrounded by a meson cloud. Figure 1.9 (a) sketches a system of such baryonic bags each surrounded by a meson cloud at nuclear ground-state density. The space between the hadrons represents the QCD vacuum. Interactions may occur through overlapping meson clouds and thus meson exchange. An increase of the baryon density as shown in (b) consequently results in an increase of cloud-cloud (meson-meson) interactions with quarks, however, still being confined

#### 1.2. PARTICLE PRODUCTION IN HIC AT FEW GEV/U

inside the bag volume of single hadrons. At a certain threshold (energy) density a so-called "bag fusion" may occur (c), where the bags and meson clouds of different hadrons merge and then contain all constituent quarks within one larger bag where they can freely propagate, similar to the Fermi gas model. A more theoretical introduction on the cloudy bag model will follow in section 1.3.5.

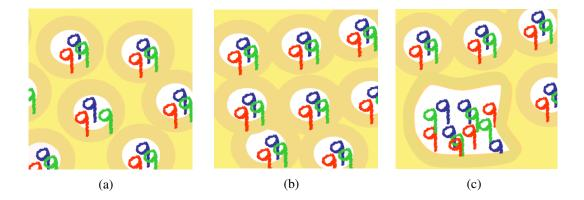


**Figure 1.9:** Three different scenarios for a hadronic system within the cloudy bag model: Shown are baryonic bags surrounded by meson clouds in a system (a) at ground state density, (b) of increased density with increased probability of cloud-cloud interactions and (c) of extremely dense baryonic matter where a bag-fusion may occur i.e. single hadronic bags merge to one large bag containing all constituent quarks. Figures taken from [101].

In a heavy-ion collision this fused system will merely consist of light u and d quarks. This implies that after the bag fusion the corresponding potential wells will be filled up to higher energy levels than in the initial hadrons. Hence for a sufficiently large fused bag, which can be obtained with increased baryon density, a transformation of light to strange quarks through the weak interactions may be energetically favored – a scenario as it may occur also in the core of neutron stars. This is, however, unlikely in a system created in a heavy-ion collision which is short-lived compared to the time scales of weak processes.

An alternative picture for (multi-)strange particle production is the following: a constituent quark from the fused bag may interact with a virtual  $s\bar{s}$  pair from the cloud, i.e. a u or d quark will coalesce with (or "knock out") the  $\bar{s}$  and form a  $K^+$  or  $K^0$  respectively. The remaining s quark might then populate the lowest state of the strange potential well. With increasing size of the fused bag and hence more constituent quarks within the bag volume, this knock-out process will have an enhanced probability to occur. If this is the case, two strange quarks will populate the same energy level and, due to their proximity in momentum space, may more likely end up in the same hadron. A requirement for such a process to happen is that the system lives long enough to establish a Fermi sea of quarks. According to theory, the lifetime of the dense phase is predicted to be rather high, ranging from 10 - 20 fm/c in the low energy regime and reaching its maximum at beam energies around 15 GeV/u [102], which would make particle production in heavy-ion collisions at SIS18 (and later SIS100) a perfect environment to investigate such mechanisms.

On hadron level, several other possibilities have been proposed to explain the observed enhancement of the  $\Xi^-$  yield, however, with rather moderate success. An increased attractive in-medium potential [103, 104, 105], similar to what was explained above for negative kaons, would have to reach rather unrealistic values [106].

Another source for cascade production may be strangeness recombination: two primary  $\Lambda$  hyperons are produced and then their quark content is exchanged such that a  $\Xi^-$  and a nucleon is formed, i.e.  $\Lambda\Lambda \to \Xi N$ , which was proposed to have an enhanced in-medium cross-section in [107]. Included and tested in transport codes [108] it was sufficient to explain the observed high  $\Xi/\Lambda$  ratio. Furthermore, an enhanced in-medium cross-section for anti-kaon induced cascade production ( $\bar{K}\Lambda \to \Xi\pi$ ) based on a coupled-channel calculation may be conceivable [109], however, in other calculations this process is calculated to be negligible [108].

When discussing possible effects enabling the production of such rare multi-strange hadrons, it is essential to take the sub-threshold  $\Xi^-$  measurement by HADES in the p+Nb collision system at 3.5 GeV into account [110]. Here the gap between the beam energy and production threshold is much smaller than in Ar+KCl. In p+A reactions the number of available options to explain the production is shrunk with respect to A+A systems since strong medium effects and multi-step processes are expected to be negligible. Whereas the cross-section for  $\Lambda\Lambda$  interactions is predicted to be significantly smaller, already a small contribution from the Fermi momentum of  $\approx 50$  MeV/c is sufficient to lift the energy above threshold. Another mechanism enabling the production would be a scattering of the projectile on correlated nucleons which may occur in a bound state (d,  $\alpha$ ) inside the target nucleus [111, 112]. This could also lift the available energy [110].

# **1.3 Hadron Properties in Dense Baryonic Matter and QCD Models**

As pointed out in the previous section, the above discussed phases of strongly interacting matter can be investigated by means of heavy-ion collisions. Different regions of temperature T and baryo-chemical potential  $\mu_B$  can be accessed by variation of beam energy.

In the energy regime of few GeV per nucleon, where the dominating hadronic degrees of freedom are the baryons, densities of approximately 2-3 times nuclear ground state density  $\rho_0$  and moderate temperatures of about 100 MeV can be reached. In such an environment meson production through excitation and decay of baryonic resonances plays a decisive role<sup>26</sup> [114, 115]. The system is rather long-lived and the conditions of increased density are predicted by transport models to reach a maximum at around 10 fm/c as can be seen from figure 1.10, which shows the time evolution of the macroscopic observables density  $\rho$ , temperature T and pion-chemical potential  $\mu_{\pi}$  for Au+Au collisions at 1.23A GeV calculated with a UrQMD coarse-graining approach [34, 116].

In a system of increased net-baryon density, hadron properties may change substantially and a profound understanding of NN as well as  $\pi N$  interactions is a necessary baseline before the

 $<sup>\</sup>overline{^{26}}$  In contrast, at energies exceeding 15A GeV, pion production dominates over baryon abundances [113].

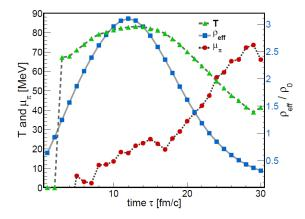


**Figure 1.10:** Time evolution of the macroscopic observables temperature T, effective baryon density  $\rho_{\rm eff}/\rho_0$  and pion-chemical potential  $\mu_{\pi}$  calculated for the collision center of Au+Au reactions at 1.23A GeV with the UrQMD coarse-graining approach. Maximum density and temperature of the system are reached at around  $\tau \approx 10$  fm/c. Figure taken from [34].

role of multi-particle processes and the physics of strange particles in this medium (KN, YN) can be addressed. An answer to the question how these in-medium modifications look like and to what extent they occur ultimately links the hadron properties observed in experiments to the fundamental properties of QCD. In the following a rather theoretic introduction is given on some concepts of QCD and how they might be linked by models to hadron properties in dense baryonic matter.

## **1.3.1** Chiral Symmetry

A fundamental concept of physics are symmetries: a system is referred to as symmetric when its properties do not change under transformation of some quantity. An intuitive example is that in a temporal symmetric system a repetition of an experiment at a later point in time will not change the physics outcome – more precisely: The laws of nature are invariant under time translations.

One of the symmetries of quantum chromodynamics is the chiral symmetry ( $\chi S$ ). The concept of chirality can be understood by first introducing helicity which is defined as the product of the spin and the momentum vector of a given particle, being either left-handed when pointing in opposite or right-handed when pointing in the same direction. The value of this quantity for a given particle depends on the reference frame, i.e. for non-zero masses there is always a reference frame in which the helicity of this particle will change its sign. This concept can be extended to the more abstract concept of chirality which also deals with right- and left-handed particles, but, in contrast to helicity, is a property independent of the mass of the particle and hence independent of the reference frame. A chirally symmetric particle (e.g. a fermion) is invariant under parity transformation<sup>27</sup>.

QCD can be considered a non-chiral theory which implies that the defining equation of motion, which is characterized by its Lagrangian  $\mathcal{L}$ , is invariant under chiral transformations. The transformation of chiral symmetry can be divided into a vector  $\Lambda_V$  and a axial-vector  $\Lambda_A$  part with the first one describing isospin rotations (e.g.  $\pi^- \to \pi^+$ ) and the second one a transformation (rotation) of particles into each other (e.g.  $\pi \to \sigma$ ). The corresponding axial and vector currents,

 $<sup>\</sup>overline{^{27}}$  A parity transformation describes the flip in the sign of one spatial coordinate.

which are invariant under chiral transformations in a chirally symmetric system, according to the Noether theorem, are conserved in the limit of vanishing quark masses<sup>28</sup>.

# 1.3.2 Chiral Symmetry Breaking

When bulk properties of a system change drastically and a phase transition takes place, this often involves a breaking process of a given symmetry. A spontaneously broken symmetry occurs when the defining Lagrangian  $\mathcal{L}$  respects the symmetry but the stable ground state – its vacuum state – breaks it<sup>29</sup>. The breaking of a symmetry in a phase transition system usually gives rise to an order parameter which describes the degree of order in the broken symmetry state and typically ranges from zero in one phase to non-zero in the other.

In the ground state of quantum chromodynamics at low temperatures and net baryon densities, i.e. the QCD vacuum<sup>30</sup>, quarks and gluons are confined. In this state the chiral symmetry of strong interaction is spontaneously broken  $(SB\chi S)$  which implies the formation of a nonvanishing expectation value of the chiral  $\langle \bar{q}q \rangle$  condensate as order parameter.

This spontaneous breaking of the chiral symmetry involves the existence of massless Goldstone bosons. When considering the SU(2) group with the two lightest quarks u and d, three pseudo-Goldstone bosons are involved:  $\pi^+, \pi^-$  and  $\pi^0$ . Pseudo, because an additional explicit breaking of chiral symmetry as a small scale perturbation is caused by the non-vanishing quark masses, hence the assumption of chiral symmetry has only approximate character which is indicated by the non-zero but still relatively small masses of the pions. Indeed, the most convincing evidence for the presence of  $SB\chi S$  in QCD are the experimentally well-known masses of the pseudoscalar mesons which are much lighter than the next heavier states, i.e. vector mesons like  $\rho$ . In the Lagrangian formalism the explicit breaking relates only to the axial vector current whereas the vector current is still conserved. The reason why the chiral symmetry can still be considered as approximately fulfilled is because the relevant energy scale of chiral symmetry breaking, i.e.  $\Lambda_{\chi} \approx 1$  GeV, is three orders of magnitude larger than the relatively small u and d quark masses.

Extending the SU(2) to the SU(3) sector by taking the strange quark into account, all eight pseudoscalar mesons ( $\pi^{\pm/0}$ ,  $\eta$ ,  $K^{\pm/0}$ ,  $\bar{K^0}$ ) of the quark model may be considered as Goldstone bosons. However, with this extension by the much more massive strange quark ( $m_s \approx 150$  MeV/c<sup>2</sup>) the contribution of explicit symmetry breaking becomes much more relevant and leaves the question open if the concept of chiral symmetry and its spontaneous breaking is still valid in the SU(3) group.

The spontaneously broken symmetry in the vacuum state and thus the formation of a  $\bar{q}q$  condensate is, besides others like the gluon condensate, responsible for the bulk of the mass in the ground state in QCD, i.e. the bound hadrons, and converts the light quarks into up to two orders of magnitude heavier confined constituents of baryons and mesons [57].

<sup>&</sup>lt;sup>28</sup> For a pedagogical review on the theory of chiral symmetry, see [117].

<sup>&</sup>lt;sup>29</sup> A more accurate formulation would be that the symmetry is rather hidden than broken since the underlying equations of motion contain the symmetry by definition.

<sup>&</sup>lt;sup>30</sup> In quantum field theories the vacuum state denotes the state of lowest possible energy.

### 1.3. HADRON PROPERTIES IN DENSE BARYONIC MATTER AND QCD MODELS 21

**Chiral Perturbation Theory** – At energies as high as at RHIC or LHC the strong coupling constant  $\alpha_s$  is sufficiently small to extract information on the dynamics of a system from the partition function of QCD perturbatively<sup>31</sup>. However, QCD becomes a non-perturbative theory in the limit of low energies as the coupling constant  $\alpha_s$  increases which means that perturbative methods cannot be applied. However, in this energy regime, where the SIS18 is operating, hadronic processes are dominated by pions due to their low mass and therefore observables can be expressed as an expansion in the pion mass and momenta which enables a perturbative treatment and is the basic concept of chiral perturbation theory (ChPT). This effective theory<sup>32</sup>, where the relevant degrees of freedom in the Lagrangian formalism are hadrons instead of short-scale quarks and gluons, is consistent with the (approximate) chiral symmetry of QCD, successfully describes the interaction between pseudoscalar mesons with baryons and allows a determination of the actual masses of the pseudoscalar mesons [118, 119].

The full Lagrangian of ChPT can be further reduced to an effective Lagrangian where nucleons and only a subset of mesons, e.g. kaons, become the relevant degrees of freedom and which can be treated perturbatively. This was shown to successfully describe the nature of KN interactions [57]. By using an effective Lagrangian a coupled channel problem can be avoided which occurs when many different species of interacting particles in a system are involved. A solution to such a problem is required for the equation of motion of each species separately but their coupling to each other by interaction terms and mean fields makes these calculations rather complex. These coupled channel problems are treated non-perturbatively and are addressed by various authors [120, 121, 122, 123, 124, 125].

More details on both, the effective treatment of strangeness in nuclear matter in the framework of ChPT as well as non-perturbative approaches like coupled channel dynamics, each considering chiral symmetry, follow in the subsequent section.

# **1.3.3** Strangeness in Nuclear Matter

The first formulation of a chiral Lagrangian to describe the interactions of kaons in nuclear matter was realized by Kaplan and Nelson [82, 84] and later used by many authors [120, 121, 122, 123, 124, 125, 126, 127, 128]. The Lagrangian in this formulation includes the baryon and pseudoscalar meson octets as degrees of freedom and involves the approximate chiral symmetry of QCD.

**Effective Chiral Lagrangian** – In order to avoid a coupled channel problem an effective chiral Lagrangian can be used. In case of a (anti)kaon-nucleon description, the interaction term in this formalism is divided into a vectorial and a scalar part, i.e. Weinberg-Tomozawa and Kaplan-Nelson terms respectively. The first is repulsive for kaons and attractive for antikaons whereas

<sup>&</sup>lt;sup>31</sup> When a mathematical problem cannot be solved exactly, there often exist so-called perturbative solutions where the basic problem is simplified/modified to a different problem to which an exact solution exists. Hence the original problem can be solved approximately. Not all problems can be extended such that a perturbative solution exists, which then requires a non-perturbative solution.

<sup>&</sup>lt;sup>32</sup> In an effective theory the fundamental degrees of freedom, i.e. the particles of the associated theory, are substituted by effective degrees of freedom relevant on higher length scales, e.g. using hadrons instead of quarks.

the latter is equally attractive for both, kaons and antikaons, and can be constrained by scattering experiments. However, in contrast to the experimentally well-studied  $\pi N$  scattering, the strength of the KN scattering in the Kaplan-Nelson term is relatively unknown and varies largely depending on the calculation [126, 129, 130, 131, 132].

**Mean Field Approach and Medium Potentials** – Since the treatment of a many-body problem is complex, it can be reduced to a one-body problem where e.g. kaons are propagated in a mean field generated by all surrounding nucleons. The application of the effective chiral Lagrangian in a mean field approximation enables a satisfying description of kaon dynamics and their mass shifts in nuclear matter as it was first calculated within the Nambu-Jona-Lasinio (NJL) model [83]. This treatment assumes the validity of the quasi-particle approximation, which will be discussed in more detail in 1.4.1 in the context of transport models. Figure 1.11 shows the charged kaon potentials as a function of density normalized to nuclear ground-state density obtained with the chiral mean field theory with and without various higher order corrections (lines) [133] as well as data extracted from  $K^+N$  scattering and from  $K^-$  atoms (shaded areas) [134] (For details on the calculations, see [57]).

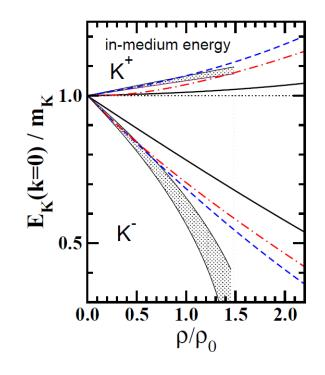


Figure 1.11: In-medium kaon energy normalized to the nominal kaon mass  $E_K/m_K$  as a function of density relative to nuclear groundstate density  $\rho/\rho_0$  for calculations of a repulsive kaon and attractive antikaon potential obtained in chiral mean-field theory with (MFT and without higher-order cor-ChPT+corr.) rections (MFT ChPT) [133] as well as from the mean-field quark-meson-coupling (QMC) model [135]. The bands indicate data on  $K^+N$ scattering and  $K^-$  atoms [134]. Kaons show an increase, antikaons a decrease of their inmedium energy with increasing density upon which all indicated calculations agree qualitatively. Figure taken from [57].

In the mean field ansatz for kaons in nuclear matter the Weinberg-Tomozawa term in the effective formalism of meson-nucleon interaction is responsible for a mass-splitting of  $K^+$  and  $K^-$  due to the breaking of the flavour SU(3) symmetry. Additional charge symmetry breaking, as it occurs in isospin asymmetric matter such as Au+Au, leads to a further splitting of the two isospin states into  $K^+$ ,  $K^0$  (kaons) and  $K^-$ ,  $\bar{K}^0$  (antikaons).

Calculations for the in-medium behavior of  $K^0$  at SIS energies give similar results as for  $K^+$  except for the absence of electromagnetic effects as higher-order corrections which makes neutral

kaons a good experimental probe for the kaon-nucleon potential when comparing to transport models<sup>33</sup>. Various of these comparisons have been performed consistently favoring an overall slightly repulsive kaon-nucleon potential [53, 136, 137, 138, 139, 140, 141], however, so far none of the available transport codes is able to describe all kaon observables simultaneously [57, 142]. A comparison of  $K_s^0$  observables to three different transport codes will be part of the investigations performed within this thesis.

In the hyperon sector in-medium properties have been calculated e.g. within the QCD sum rule ansatz [143, 144] where the (vector) self-energy<sup>34</sup> of the corresponding propagator<sup>35</sup> has been deduced to be 2/3 of the nucleon self-energy which shows reasonable agreement with experimental findings on hypernuclei formation [145, 146, 147] and on  $\Lambda$  hyperon flow [148, 149]. However, not much experimental constraints on the value of the YN potential are available. As stressed in 1.1.5, a more precise determination of the hyperon-nucleon potential may have severe implications on the equation of state and would hence improve our understanding of the neutron star structure.

A successful description of an interacting many-particle system in the mean field ansatz requires a proper treatment of in-medium scattering processes. Whereas a perturbative treatment for  $\pi N$  was demonstrated to give reasonable results [150], two-body scattering processes in the presence of resonances with non-negligible cross-sections make the quasi-particle approximation invalid and a non-perturbative solution becomes necessary. An example is the presence of the  $\Lambda(1405)$  resonance in the vicinity of the  $K^-p$  threshold which makes a perturbative ansatz in the  $K^-$  sector impossible. Figure 1.12 depicts schematically the antikaon coupling to hyperon resonances in the medium.

**Non-perturbative Coupled Channel Dynamics** – By solving the Bethe-Salpeter equation<sup>36</sup> the full two-body scattering amplitude and hence the coupled channel problem can be calculated non-perturbatively as it was done by several authors [120, 125, 151, 152, 153, 154]. In this relativistic covariant formalism not only the kaon/hyperon and nucleon degrees of freedom but, oppositely to the previously discussed effective mean field approach, also the other hadrons from the baryon and pseudoscalar meson octet are taken into account which is crucial for a proper next-to-leading order description of the KN/YN scattering.

For instance, this allows for a successful description of the  $\Lambda(1405)$  resonance which is dynamically generated when calculating the  $K^-p$  scattering amplitude with the physical kaon mass  $(m_K = 495 \text{ MeV/c}^2)$  and disappears when this mass is more and more reduced [120].

<sup>&</sup>lt;sup>33</sup> The  $K_s^0$  state is a superposition of a strange quark and antiquark, i.e.  $|d\bar{s} - s\bar{d}\rangle/\sqrt{2}$ . In order to obtain a  $K_s^0$  state containing an *s* quark, the  $\bar{s}$  must either be contained in an anti-hyperon or in another kaon, which would additionally require another baryon in the final state. Both channels are suppressed at energies close-to-threshold whereas a  $|d\bar{s}\rangle$  state is energetically favored as it can be produced in combination with a  $\Lambda$  hyperon. Hence the potential, driven by the  $\bar{s}$  quark content, can be approximately considered to be equal the one of positive kaons.

<sup>&</sup>lt;sup>34</sup> Self-energy describes the effective energy of a particle which is the result of all interactions with its surrounding particles.

<sup>&</sup>lt;sup>35</sup> A propagator can be considered as the probability amplitude of a particle to propagate from a space-point x to another y.

<sup>&</sup>lt;sup>36</sup> The Bethe-Salpeter equation is an equation in quantum field theory which describes the bound states of a twobody system, e.g. of a hydrogen atom or a meson.

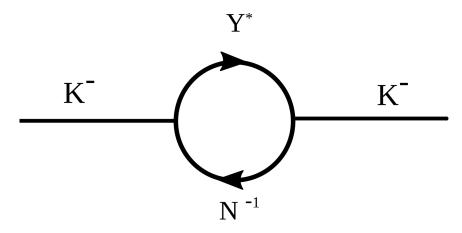


**Figure 1.12:** Feynman diagram of antikaons  $(K^-)$  coupling to hyperon resonance  $(Y^*)$  through nucleon-hole  $(N^{-1})$  excitation.

In the coupled channel approach in-medium properties are included by extending the Bethe-Salpeter equation systematically by quantum or effective many-particle effects like Pauli-blocking [123, 155], dressing of a particles propagator with self-energies or self-consistency etc. The impact of dressings of the corresponding propagators of  $\pi$ , N, K or Y on the respective interactions  $(NN, \pi N, NK, NY)$  are subject of various studies [153, 154, 156]. The dressing of N and Y propagators have been found to be of minor importance whereas in particular the coupling of the  $\pi$  meson to nucleon and  $\Delta$ -hole excitations in the medium strongly affects its properties and hence its dressing cannot be neglected. The inclusion effectively lowers the  $\pi\Lambda$  and  $\pi\Sigma$  thresholds which results in less attraction for the in-medium  $K^-$  potential [153, 154].

The antikaon in-medium potential calculated with coupled channel dynamics is predicted to be less attractive than obtained in the mean-field picture [123, 152]. This difference can be related to the antikaon in-medium spectral function<sup>37</sup> which is significantly modified by its coupling to the hyperon resonances in the medium. The complex and poorly known structure of the antikaon spectral function makes the validity of the quasi-particle approximation questionable.

# **1.3.4** Melting of the Quark Condensate and Modification of Hadron Properties

As described above, the order parameter related to spontaneous breaking of the chiral symmetry is the non-zero expectation value of the quark condensate in the QCD vacuum:  $\langle \bar{q}q \rangle \neq 0$ . This order parameter is expected to vanish when the chiral symmetry is restored and theoretical models like the Nambu-Jona-Lasinio model predict a decrease towards increasing temperature T and/or baryo-chemical potential  $\mu_B$ , also referred to as "melting". The chiral condensate  $\bar{q}q$  is predicted by this model to be reduced down to 80% of its vacuum value already at normal nuclear ground state density [157]. The dependence of the expectation value of the condensate  $\langle \bar{q}q \rangle$ 

<sup>&</sup>lt;sup>37</sup> A spectral function can be considered as a probability density function describing all possible states of a particle which can be occupied.

on temperature and baryo-chemical potential is shown in figure 1.3 for Polyakov-Quark-Meson model (PQM) calculations [6, 38].

A direct experimental access to the expectation value of the quark condensate is not known and hence a link has to be established, like e.g. the Gell-Mann-Oakes-Renner equation which relates the quark-antiquark condensate with the pion-nucleon sigma term [158].

In the mean field picture, the common dropping of the in-medium mass for kaons can be directly related to the Kaplan-Nelson term and can be interpreted in terms of a partial restoration of chiral symmetry. In coupled channel dynamics, it is difficult to differentiate between QCD vacuum effects and effects from many-body interactions and hence to pin down medium modifications.

## 1.3.5 Cloudy Bag Model

One way to describe the behaviour of quarks confined inside hadrons is realized within the MIT bag model from which hadron properties such as their mass, charge radii, magnetic moments or spectra have been deduced successfully in accordance with experimental observations [99, 159, 160, 161]. In this picture the dynamics of confined, relativistic quarks are calculated perturbatively within a static, spherical "bag" of volume V where they can move freely. The kinetic energy of the quarks generate a pressure, the bag constant B, which equals the pressure from the vacuum surrounding the bag as it is illustrated in figure 1.9.

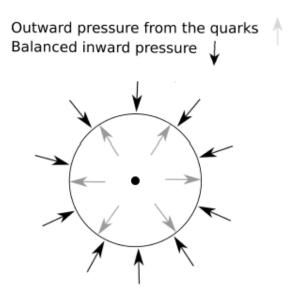


**Figure 1.13:** In the MIT bag model the dynamics of confined, relativistic quarks are calculated within a bag with volume V. The quarks are creating an outward pressure determined by the bag constant B which is equal to the inward pressure resulting from the vacuum which surrounds the bag. Figure taken from [162].

Despite its ability to fit the above mentioned properties of ground-state baryons and mesons reasonably well, there exist extensions to this model in order to provide more accurate descriptions and to include further effects. One of these extensions is the cloudy bag model: by introducing chiral symmetry, a pion cloud is formed which surrounds the bag and separates it from the vacuum as it is depicted in figure 1.9 (a).

The introduction of a pion field  $\phi$  solves the problem in the MIT description of non-vanishing axial currents which are carried by a quark to the surface of a hadron and which violates the conservation of the net flux. These currents at the surface of the bag can now be absorbed by a pion from the cloud and no axial flux will be lost.

At the same time the cloudy bag model provides a reasonable description of nucleon-nucleon interactions by meson exchange of two interfering meson clouds, consistent with the picture of NN interactions as it was first formulated by Yukawa already in the 1930s [163]. The impact of the pion cloud on the hadron properties can be controlled by modulating the strength of the pion field  $\phi^{38}$  and the radius R of the bag relative to the cloud, i.e. increasing the size of the bag implies a smaller size for the pion cloud and calls for stronger pion fields and vice versa [98, 99, 164]. Constraints on these parameters have to be obtained from experiment [165]. Best results are obtained for a rather large bag radius ranging from 0.8 - 1.1 fm and only moderate to weak pion field strength. An interesting consequence of such bag sizes would be that nucleons overlap in a nucleus and thus nuclear phenomena with quark degrees of freedom become relevant [164]. The pion field is implemented in the Lagrangian formalism of this model such that pion-quark interactions only occur at the surface of the bag. Pions from the cloud are able to penetrate the bag volume and can also be generated inside the bag, e.g. by residual forces between quark-antiquark pairs.

The cloudy bag model is able to describe many hadron properties with high precision. The inclusion of a pion cloud surrounding the MIT bag enables satisfactory predictions for pion-nucleon scattering, charge distributions, nucleon magnetic moment and axial form factor  $g_A$ , strong and EM decays of vector mesons which are all close to values obtained in experiment [99, 100, 166, 167].

Concerning the behaviour of hadrons, the leading order corrections made in the cloudy bag model are originating from the introduction of pions which is why the term "pion cloud" is often used. In a more general formulation the bags are surrounded by a meson cloud which also contains heavier mesons [168]. Compared to the light quark flavors the probability of having the much more massive  $s\bar{s}$ -pair is significantly lower. However, their occurrence in such a meson cloud may be relevant for rare strange particle production [169] at low beam energies as available at SIS18. This may have severe consequences on a high-density many-hadron system such as a heavy-ion collision. Possible implications for strangeness production were presented in section 1.2.2.

# **1.4 Theoretical Models: Access to Properties of Dense Matter**

An interpretation of the underlying fundamental physics processes of a heavy-ion collision can only be obtained by comparing experimental data to effective theoretical models. Theoretical models can be classified as either static or dynamic.

<sup>&</sup>lt;sup>38</sup> In the limit of vanishing pion field  $\phi \to 0$  the MIT bag model is regained.

A static model is time-invariant and describes a given state of a system in equilibrium where the most popular representatives are the statistical models which are based on stochastic probability distributions. Here, particle production is assumed to occur at chemical freeze-out and all possible final states of a heavy-ion collision are treated as a statistical ensemble. The success of these models in describing particle production yields in heavy-ion collisions ranges from top energies at LHC down to the SIS energy regime where the underlying assumption of global or even local equilibrium might not be fulfilled. The beauty of this model lies in its simplicity since the description only depends on few parameters. More details on statistical models follow in 1.4.2.

However, the physics observables investigated in experiment are the result of several possible effects occurring during various time steps of the evolution of a heavy-ion collision before kinetic freeze-out is reached. In order to understand and disentangle these effects, dynamical models describing the full evolution in time and space of a heavy-ion collision need to be consulted.

Hydrodynamical models provide a time-dependent description of the system. This quasimacroscopic ansatz treats the dynamic evolution of fluid cells instead of particles and was the first to describe successfully collective effects present in heavy-ion collisions. The hydrodynamical regime is only valid assuming an instantaneously and at least locally equilibrated system. Regarding the energy densities of a collision at SIS energies it is debatable if this condition is fulfilled. Furthermore, for a description of particles and their properties a transition from this macroscopic to a microscopic treatment (particlization) is needed, which involves even more model assumptions.

For this reason, microscopical approaches were developed where particles are propagated through phase space and the heavy-ion collision is described as a superposition of the individual NN collisions – these are the so-called kinetic transport models. A major focus of this work will lie on the comparison of data to various transport models and in the following their properties and differences will be explained in detail.

# **1.4.1** Dynamical Evolution – Kinetic Transport Models

The underlying assumption that all transport models have in common is the time-dependent propagation of N particles through space-time and their interaction with each other. Thus their fundamental degrees of freedom are the particles themselves, which can be strings, partons or hadrons, and this choice strongly depends on the kinetic beam energy. Heavy-ion collisions in the SIS energy regime are most successfully described by hadronic degrees of freedom because of the dominant role of resonance production. An overview of models applied in the few GeV energy regime and their relevant degrees of freedom as a function of center-of-mass energy are shown in figure 1.14.

**Transport equations of motion** – In its simplest form a point-like, classical particle N is moving on a straight trajectory within a given volume until it encounters another particle N. When a certain collision criterion for the two particles is fulfilled (e.g.  $\pi d^2 \leq \sigma_{tot}$ , where d denotes their impact parameter and  $\sigma_{tot}$  the total cross section) their momenta are changed randomly according to their free elementary cross-section. These cross-sections serve as model input and are taken

#### 28 CHAPTER 1. INTRODUCTION TO STRANGE PARTICLE PRODUCTION IN HIC

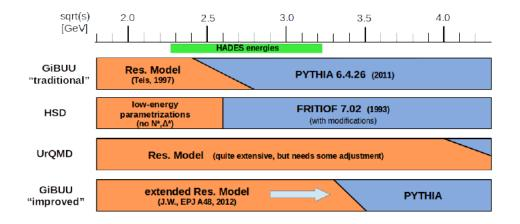


**Figure 1.14:** Region of validity of various transport models as a function of center-of-mass energy. The relevant degrees of freedom when describing a heavy-ion system strongly depends on the beam energy and can be switched in certain models. Figure taken from [170].

either from data or derived indirectly from models (e.g. OBE, additive quark model), detailed balance or isospin symmetry considerations.

A kinetic equation describing the propagation of particles in phase time and their interaction with another particle (two-body collisions) is the Boltzmann equation:

$$\left(\frac{\partial}{\partial t} + \vec{v}\nabla_{\vec{x}} + \frac{1}{m} \cdot \vec{F}\nabla_{\vec{v}}\right) f(\vec{x}, \vec{v}, t) = I_{\text{coll}},$$
(1.8)

with the single particle distribution function  $f(\vec{x}, \vec{v}, t)$ , a collision term  $I_{\text{coll}}$ , a diffusion term  $\vec{v}\nabla_{\vec{x}}$  and an external force term  $\frac{1}{m} \cdot \vec{F}\nabla_{\vec{v}}$ . The collision term  $I_{\text{coll}}$  includes decay and scattering cross sections as well as important input from microscopic theories e.g. quantum effects like Pauli blocking.

An exact solution of the Boltzmann equation is complicated hence there are various simplified descriptions valid under certain assumptions (e.g. Vlasov, Navier-Stokes, Fokker-Planck, Langevin). Examples for specific implementations of transport models are the VUU (Vlasov-Ueling-Uhlenbeck), BUU (Boltzmann-Ueling-Uhlenbeck) or HSD (Hadron String Dynamics) codes.

In the described ansatz many-body interactions or particle correlations (e.g. caused by quantummechanical effects like entanglement or formation of fragments) are not automatically included.

**Mean field description** – These effects resulting from many-body interactions are approximated by extending the transport model by an additional (external) mean field. This mean field influences all particles in exactly the same way independent of local fluctuations caused by each individual particle itself. Furthermore, Pauli blocking factors are introduced reducing the cross-sections for certain collisions. Thus transport models are still treating a one-body problem. For more details on the mean field description, see section 1.3.3.

29

Quasi-particle approximation and Off-shell transport – A basic requirement for a successful treatment of mean field dynamics involving classical equations of motion is the validity of the quasi-particle approximation (QPA) which assumes that the spectral strength of a particle is centered around its quasi-particle pole mass. In this ansatz the full spectral function (phase space distribution) of a particle is approximated by a weighted sum of N particles each described by a delta function with sharp position and momentum. This results in N quasi-particles which are propagated classically. The quality of this approximation – as well as the computation time - increases with the number of test-particles. The question arises if the validity of this picture is sustainable in heavy-ion collisions since the width of a particle's spectral function can suffer drastic changes inside a medium. If collisional broadening due to in-medium interactions is expected to be small or well-known, the QPA can be assumed to be justified. However, further (re-)absorption processes can occur leading not only to an increased width but to complex and poorly-known spectral distributions as in the case of negative kaons which experience a strong coupling to the  $\Lambda(1405)$  and  $\Sigma(1385)$  hyperons. The result on the corresponding spectral functions of kaons and antikaons in the medium as a function of momentum obtained with coupled channel calculations (see 1.3.3) are shown in figure 1.15 [57]. Clear modifications for the antikaon spectral function can be observed in the limit of low momenta where the QPA may not be valid any more. In such a case an on-shell<sup>39</sup> propagation of high momentum tails corresponding to such deeply bound states would violate energy and momentum conservation.

An ansatz to treat these contributions are off-shell dynamics where virtual particles are propagated without satisfying classical equations of motion [171, 172, 173]. However, a transition of the virtual particle to an on-shell state and hence its vacuum pole mass has to be well controlled, which is not straightforward [174]. Combined approaches of test-particles with reduced off-shell dynamics have also been developed [175, 176, 177, 178].

**Quantum Molecular Dynamics** – Alternatively to the one-body treatments (relying on the implementation of mean fields), molecular dynamics are a successful tool to simulate a many-body system such as a heavy-ion collision. The most extensively used class of many-body descriptions are the **Q**uantum Molecular Dynamics (QMD) transport models. Instead of a point-like treatment, the particles are considered as Gaussian density distributions in phase space. Though the particle propagation is still treated classically, the introduction of the smeared Gaussian wave-packets obeying the uncertainty principle leads to a smoother behaviour in terms of particle interactions and quantum effects. The phase space smearing manifests itself in an effective mean field for each n-body system without requiring a quasi-particle approach or parallel ensembles as in the Boltzmann approach enabling the treatment of heavy-ion collisions on an event-by-event basis. In the molecular dynamics approach a collision is taking place as soon as two wave-packets start to overlap. Since its basic implementation by Aichelin and coworkers, the QMD code has experienced several extensions by including isospin (IQMD - Isospin Quantum Molecular Dynamics) [179, 180], relativistic (RQMD - Relativistic Quantum Molecular Dynamics) [182] effects.

<sup>&</sup>lt;sup>39</sup> On-shell particles are not allowed to violate energy or momentum conservation, in contrast to an off-shell treatment.

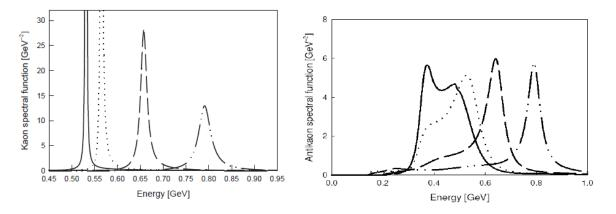


**Figure 1.15:** In-medium spectral functions for kaons (left) and antikaons (right) from coupled channel calculations for different momenta:  $p_K = 0$  (solid), 200 MeV (dotted), 400 MeV (dashed), 600 MeV (dash-dot-dot). In contrast to kaons, a strong modification and complex structure is obtained for antikaons with decreasing momenta. Figure taken from [57].

**Cross-sections** – For a successful description of particle production in transport models the input cross-sections are essential. Most suitably these cross-section are known from data of elementary collisions. However, in particular data on resonant particle production is scarce and therefore relies on parametrizations. Commonly used parametrizations in transport models are obtained from calculations by Tsushima et al. [183, 184] or from Li and Ko [185], but numerous other parametrizations are available [186, 187]. Evidently, this input to the model is based on many assumptions resulting in large uncertainties in the description. There is a trade-off between number of input cross-sections and uncertainty of individual cross-sections.

An additional uncertainty arises from the angular dependence of cross-sections which are – in contrast to reality – mostly assumed to be isotropic. Here again, transport models rely on experimental input in terms of data-driven parametrizations [188, 189]. Depending on the parametrization, the impact on the resulting phase space distribution can vary significantly [189]. However, these effects are often argued to be of minor importance in heavy-ion collisions and more relevant in elementary as well as p+A collisions.

**Sub-threshold Production** – In order to obtain reasonable statistics for rare processes, subthreshold particle production in transport models is calculated perturbatively [190, 191, 192]. This means that a particle is produced sub-threshold if kinematically allowed with a given probability in consideration of phase space and Pauli-blocking penalty factors. A perturbatively produced particle is then propagated virtually in parallel to the already ongoing dynamics feeling global bulk properties of the medium without affecting them itself – which is valid as long as their occurrence is rare. This makes in particular the description of multi-strange hadron production in transport models complicated as strangeness exchange mechanisms and interactions among strange particles may have significant impact on their yields [57]. **In-medium modification and Strangeness Production** – Along this line, another important aspect in treating sub-threshold production comes due to the fact that many of the input cross-sections are extracted from free scattering data. However, as discussed in section 1.3, particle properties may change significantly in the presence of a hot and dense medium. Therefore, a precise treatment of in-medium potentials in transport models is in particular crucial for sub-threshold production, not only because of the shift of production thresholds and hence the total yields, but also because of the resulting momenta of newly produced particles which are influenced by the vector field part in the relativistic mean field (RMF) description [193]. In the particular case of kaon production the inclusion of in-medium potentials will effectively enhance the kaon and lower the antikaon threshold. Due to the associated production of strangeness a shift of the kaon threshold is already introduced by the hyperon-nucleon ( $\Lambda$ ) potential. From the simple SU(3) flavor picture this is determined to be a factor 2/3 of the nucleon-nucleon field which is attributed to the reduced non-strange quark content (*uds* vs. *uud* / *udd*) [143, 144].

**Specific Implementations** – The comparison of the results from the data investigated in this thesis is focused on the one-body HSD model and the many-body treatments by IQMD and UrQMD whereby the latter one is operated in a cascade mode. Details about the specific implementations are described in the following, however, limited to the description in the SIS energy regime. Other transport models valid in this energy regime (GiBUU<sup>40</sup> [174], SMASH<sup>41</sup> [194]) are not considered within this thesis but hopefully in the further course of investigations on Au+Au data from HADES.

#### HSD

HSD is a one-body transport approach developed for a description of proton-nucleus and pionnucleus reactions as well as relativistic heavy-ion collisions covering a wide energy range from SIS up to RHIC energies which is achieved by switching degrees of freedom depending on the beam energy. This approach is using the test-particle approximation of a coupled set of relativistic transport equations for particles with in-medium self-energies. For the hadronic description the baryon octet and decuplet, the pseudo-scalar and vector meson nonets and selected higher resonances as well as their antiparticles are included. In-medium potentials can be added to the propagation of all hadrons. Baryons are propagated with momentum-dependent scalar and vector self-energies [195, 196]. The dominant production mechanism above  $\sqrt{s_{thr}} > 2.65$  GeV is via string-fragmentation. Cross-sections are either taken from experimental data or, whenever no data exists, estimated via detailed balance, from a coupled-channel approach based on a SU(3)invariant hadronic Lagrangian [108, 109], those of Tsushima et al. [183, 197] or as derived from [136, 198]. Additionally off-shell propagation of particles as described by Cassing and Juchem [175] can be added but contribute dominantly only in the negative kaon sector.

An extension to the HSD code is the parton-hadron-string dynamics model, short: PHSD. In the high-energy regime above beam energies of  $\approx 5$  GeV/c the defining degrees of freedom are

<sup>&</sup>lt;sup>40</sup> Giessen Boltzmann-Uehling-Uhlenbeck

<sup>&</sup>lt;sup>41</sup> Simulating Many Accelerated Strongly-interacting Hadrons – still in development

partons, i.e. quarks and gluons, instead of hadrons [199].

### IQMD

The IQMD code is an extension to the original QMD implementation. The main difference to the basic code is the inclusion of isospin dependent nuclear forces which impact the mean field and cross sections for binary scatterings. Additionally  $\Delta$  resonances as well as pions were added to the nucleons which makes this model in particular suitable for heavy-ion collisions up to 2A GeV and thus the SIS energy regime [136]. Same as for HSD, cross sections are either from experimental data, for reactions including unstable particles with finite widths as derived from [198] or, if unknown, estimated from reverse reactions (detailed balance).

## UrQMD

Another extension of the quantum molecular dynamics model is the ultra-relativistic treatment UrQMD [182]. As the most recent adaptation, it includes the largest set of baryons (including  $\Delta$ -,  $N^*$ - and hyperon resonances with masses up to 2.25A GeV) and mesons (including strange meson resonances)<sup>42</sup> and is applicable from SIS up to RHIC energies. The input cross-sections are mainly taken from experimental data [5] or estimated via the additive quark model, one-boson-exchange model, detailed balance or isospin symmetry [182, 186, 187, 201]. While production through annihilation processes ( $B + \overline{B} \rightarrow X$ ) or string excitations are not relevant in the SIS energy regime, all particles containing strangeness are produced via  $\Delta$ - or  $N^*$ - resonance excitations. Furthermore, strangeness exchange mechanisms as discussed in the previous section 1.2.2 are also implemented in the latest version. In contrast to IQMD, the UrQMD version used in this thesis is run in the cascade mode, i.e. the particles are treated point-like instead of using Gaussian wave packages. The used version of UrQMD does not include any mean field potentials, neither of NN nor of KN type.

To summarize, in this thesis three different implementations will be compared, which differ essentially in certain aspects. All three are semi-classical models simulating HIC on an event-by-event basis. While UrQMD produces particles at SIS energies in two-step processes via intermediate resonance excitations, in HSD and IQMD also direct production via two-to-three particle processes are included. In the presented version of UrQMD, neither mean field NN-potentials nor explicit K-/ $\Lambda$ -N potentials are included.

# **1.4.2 Thermal Particle Production – Statistical Models**

Compared to the dynamical description of heavy-ion collisions by transport models, statistical models represent in many aspects a rather contrary description. These kind of models provide a macroscopical (vs. microscopical) and static (vs. dynamic) description of the system which is assumed to be in thermal equilibrium. In contrast to transport theory, statistical models only need few parameters to successfully describe hadron multiplicities at chemical freeze-out. Vice versa, using experimental data on measured particle yields and fitting the relevant parameters of

 $<sup>\</sup>frac{42}{42}$  The full list can be found in [200].

the model – temperature T, baryo-chemical potential  $\mu_B$  and volume V – provides insight on the nature of the medium they originate from. The quality of reproducing experimental data may therefore be connected to the question of the degree of thermalization reached in a reaction.

#### **Ensemble Theory and Statistical Particle Production**

The description of a given system with volume V in statistical mechanics is performed within the ensemble theory introduced by Gibbs which is based on the ergodic hypothesis that the average over time is equal to the average over various ensembles. The system is described as a set of identical copies each of them representing a possible state following a given probability distribution. One distinguishes between three different types of ensemble:

**Micro-canonical Ensemble** (U, V, N) – the micro-canonical ensemble describes an isolated system where the number of particles N and total energy U are fixed.

**Canonical Ensemble** (T, V, N) – also describes a system with fixed number of particles N but unknown total energy. Instead the ensemble depends on the temperature T of the system keeping the average energy of various ensembles constant. The probability  $p_i$  to find a particle i in a certain micro state is proportional to

$$p_i \propto exp\left(\frac{-E_i}{kT}\right),$$

where k denotes the Boltzmann constant.

**Grand-canonical Ensemble**  $(T, V, \mu)$  – in this ensemble also the number of particles is not fixed anymore but conserved on average only by introducing a chemical potential  $\mu$ . Now the probability  $p_{i,q}$  for a particle occupying a given state in a system also depends on this potential as follows:

$$p_i \propto exp\left(\frac{-E_i + \mu_q}{kT}\right),$$

with q being the quantum number.

The grand-canonical (GC) ensemble has been proven to give an adequate description of hadron abundances in heavy-ion collisions in the limit of high temperature and/or large systemsize. As mentioned above, the system is fully described by a temperature T, volume V and chemical potentials – in the particular case of a HIC  $\mu_Q, \mu_B$  and  $\mu_S$  conserving the quantum numbers charge Q, baryon number B and strangeness S, respectively. In the GC ansatz the particle number density  $\rho_{i,q}$  for a particle i with quantum numbers  $\vec{q} = (Q_i, B_i, S_i)$  and their related chemical potentials  $\vec{\mu} = (\mu_Q, \mu_B, \mu_S)$  is proportional to

$$\rho_{i,q} \propto \int_0^\infty p^2 dp \ exp\left(\frac{-E_i + \vec{\mu}\vec{q}_i}{kT}\right).$$

In the recent decades statistical hadronization models have successfully reproduced particle yields from (ultra-)relativistic heavy-ion collisions by assuming sudden chemical freeze-out in a

thermally equilibrated system and they can be used as a tool to map the QCD phase diagram as described in section 1.1.4 [202, 203, 204, 205, 206].

However, for strange particle production at SIS energies, where the average multiplicity per event is much smaller than 1, a GC treatment overestimates the particle yields. In this case, the related quantum number cannot be controlled on average by a chemical potential anymore but has to be conserved exactly. This requirement of exact conservation is fulfilled in the canonical ansatz. As a result, strangeness at low energies is best described by a (strangeness-)canonical ensemble where only the strangeness quantum number is exactly conserved, leading to an additional phase space suppression for strange particle production, also referred to as (strangeness-) canonical suppression. Still, this canonical suppression was found to be insufficient when comparing to experimental data, thus a further suppression was required to fit the measured strange particle yields. A strangeness correlation volume  $V_C$ , parametrized by its radius  $R_C$ , was introduced which is smaller than the total fireball volume  $V_C < V$ . A particle carrying an *s* quark can only be produced when another particle containing an  $\bar{s}$  quark is found within the sub-volume  $V_C$ , thus an additional reduction of the available phase space for strangeness production is the consequence [204, 207, 208]. Independent of this correlation volume, alternative suppression parameters have been proposed [209] such as an undersaturation penalty factor  $\gamma_S$ .

# **1.5** State-of-the-Art: Results from Previous Experiments

### 1.5.1 Observables

As already pointed out in the previous sections, one of the major challenges in the investigation of the fundamental concepts of matter and particle properties results from the fact that the time and length scales of systems dominated by strong interactions are too small to allow direct measurements. First chance properties of particles have to be deduced indirectly with the help of theoretical models and from the quantities measured in the detector which are an integral over all time stages from the production process over its propagation through and modification by the medium including excitations, decays or elastic scattering until they finally reach the detector.

Selected detector observables of particles which can be linked by phenomenological models to theory as presented in section 1.4 are:

- **Yields** The integrated particle multiplicities which are measured in experiment. The rates are strongly influenced by in-medium potentials of the observed particles.
- Kinematics Transverse momentum and rapidity spectra reflect the kinematics of particles in pt y space. They combine contributions from collective effects such as radial or anisotropic flow, resonance production, final state interactions and in-medium potentials. The disentanglement of these effects and hence the interpretation of the spectra can be complex.
- Angular Distributions Anisotropies in the angular distribution of particles are a direct reflection of elliptic and higher-order flow effects as well as their in-medium potentials.

# 1.5.2 KaoS

The **Kaon Spectrometer KaoS** at SIS18 in Darmstadt was a first-generation experiment starting in 1991 which was designed to identify charged kaons in order to study e.g. the behavior of strangeness in dense nuclear matter. For particle identification and momentum measurement a double-focusing spectrometer consisting of a quadrupole and a dipole magnet was used. The setup is explained in detail in [210].

Within a few years the KaoS collaboration was able to measure and analyze the systems C+C (at 0.8, 1.0, 1.2, 1.5, 1.8 and 2A GeV), Ni+Ni (at 1.1, 1.5 and 1.93A GeV) and Au+Au (at 0.6, 0.8, 1.0, 1.135 and 1.5A GeV). The set of collision systems was particularly well suited to systematically study the different behavior of negative and positive kaons as a function of system size and beam energy. By studying the same system at decreasing beam energy it was possible for the first time to study the role of strange particle production close to and below threshold. An extensive review over the experimental results is given in [53, 211].

One of the major findings of the KaoS collaboration was that the production of charged kaons is coupled such that their observed yields show the same trend with varying system size which is derived from a constant  $K^-/K^+$  ratio as a function of collision centrality and system size. This was in particular surprising since the NN threshold for  $K^-$  lies significantly above the one for  $K^+$  production, as pointed out in section 1.2.2. A possible explanation for this observation was found by attributing a dominant role to the strangeness exchange mechanism as a source for  $K^{-}$  production presented in the previous section. Along the same direction, the inverse slope parameters of negative kaons were measured to be systematically below those of positive kaons, independent of system size and beam energy. It has been suggested that this difference can be interpreted as a result of different freeze-out times throughout the evolution of the collision system. A negative kaon created in such a strangeness exchange process will carry information of the heavy-ion collision from a later point in time where the system already cooled down through expansion. This will result in a smaller inverse slope parameter measured in experiment. A similar behavior of the inverse slope parameter of directly produced positive kaons and negative kaons created in strangeness exchange processes was supported by transport model calculations e.g. from IQMD [80]. The data of both these observations are presented in figure 1.16.

Another important result from the KaoS experiments was an estimate of the stiffness of the equation of state which was constrained through the measurements of positive kaon yields. The rise of the  $K^+$  multiplicity per nucleon M/A with the size of the collision system A as well as centrality dependent measurements of the  $K^+$  yield in Au+Au favor a rather soft equation of state with low values for the incompressibility factor  $\kappa$  ( $\approx 200$  MeV) when comparing to transport models [53]. However, these findings were challenged by recent measurements on the maximum neutron star mass [62, 63].

Due to the small geometrical acceptance of the kaon spectrometer no measurements on shortlived or neutral particles (e.g.  $K_s^0$ ,  $\Lambda$ ), which are reconstructed via their oppositely charged decay products, are available.

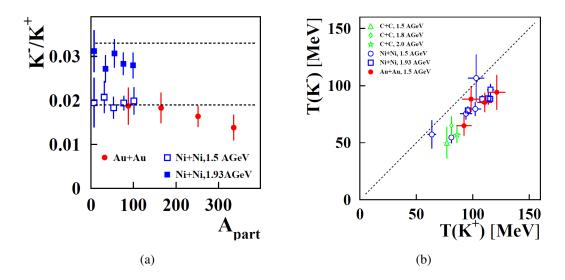


**Figure 1.16:** KaoS results: (a) constant ratio of negative to positive kaon yields as a function of  $A_{\text{part}}$  independent on the collision system. (b) Inverse slope parameter of negative vs. positive kaons. The inverse slope parameter for  $K^-$  is found to be systematically below the one of  $K^+$ , independent on system size and beam energy. Figures taken from [53].

# 1.5.3 FOPI

Another experiment at SIS18 dedicated to measure heavy-ion collisions was the FOPI detector system which started in the early 1990's. The abbreviation FOPI is referring to the high acceptance due to a coverage of nearly the full  $4\pi$  (*Four Pi*) solid angle. Over the years the FOPI collaboration was able to exploit light ( ${}^{40}Ca{}^{+40}Ca$ ), intermediate ( ${}^{58}Ni{}^{+58}Ni{}, {}^{96}Ru{}^{+96}Zr{}^{+96}Zr{}^{+96}Zr{}^{129}Xe{}^{+}CsI$ ) and up to heavy-ion systems ( ${}^{197}Au{}^{+197}Au$ ) encompassing in total 25 system energies (0.09A GeV (Au{}^{+}Au) to 1.93A GeV (Ca{}^{+}Ca)). These wide-range investigations are not only well-suited to study system size and energy dependence of physics observables from HIC but also to systematically constrain calculations from transport models which are ultimately configured to work globally in a certain energy regime independent of the considered system, observable and model implementation. The focus of the experimental program in the later years was put on investigations of properties of hot and dense matter and strangeness production in symmetric (e.g. Au{}^{96}Ru{}^{96}Zr{}), 213, 214].

In contrast to KaoS, the FOPI apparatus was able to reconstruct neutral particles decaying into charged particles giving access to a more extensive set of particles. This allows to compare our  $\Lambda$  and  $K_s^0$  results with the FOPI data. Along this line, it was also possible to reconstruct the  $\phi$  meson through its decay into  $K^+K^-$  (<sup>58</sup>Ni+<sup>58</sup>Ni). This measurement gave the first hint that a large fraction of negative kaons originate from this  $s\bar{s}$  state when approaching the elementary production threshold [215], which was later confirmed and studied in detail by the HADES collaboration (see next section). Recently, data from Ni+Ni and Al+Al collision systems on more involved investigations on the same observable were published by FOPI [216, 217].

## **1.5.4 HADES**

The High Acceptance Di-Electron Spectrometer is taking data at SIS18 since 2002. The full detector and its components will be explained in detail in chapter 2 and additionally a list of all beam times previous to the Au+Au collision system can be found in section 3.1. The second largest collision system measured with HADES was a beam of argon ions at a kinetic beam energy of  $E_{\rm kin} = 1.76$ A GeV incident on a KCl target which was recorded in 2005. In the following years it was possible to study a large set of strange particles produced in this system including, to name only a few, a multi-differential analysis of the  $\phi$  meson, the deeply sub-threshold measurement of the doubly-strange cascade  $\Xi^-$  and the determination of the  $\Sigma^{+/-}$  yields via a strangeness balance equation [36, 44, 218, 110, 137, 139, 219, 220].

Another unique reaction, that was studied extensively by the HADES collaboration, used a proton beam at  $E_{\rm kin} = 3.5$  GeV incident on a niobium <sup>93</sup>Nb target in 2008. Besides elementary collisions as a baseline, the investigation of pA collisions is a consequent intermediate step towards a complete understanding of heavy-ion collisions and for a reliable characterization of the underlying processes.

In the following, the major results are summarized and unsolved problems are presented, which will also be addressed in the investigation of the Au+Au collision system at 1.23A GeV.

#### How many $K^-$ originate from $\phi$ decays?

In the HADES Ar+KCl beam time it was not only possible to confirm indications from the FOPI collaboration that, close to threshold, a sizable fraction of negative kaons originate from  $\phi$  decays as well as to show that the  $\phi/K^-$  ratio rises significantly with decreasing beam energy [219]. HADES also succeeded for the first time to perform a differential analysis in terms of transverse mass and rapidity for the  $s\bar{s}$  state allowing to disentangle the inverse slope parameters of negative kaons coming from the mentioned decay and of those produced thermally together with a positive kaon. When correcting for this  $\phi$  feed-down the remaining inverse slope parameter agrees within uncertainties with the one for positive kaons. This result was challenging the previously established dominant role of the strangeness exchange mechanism which was deduced from the different inverse slope parameters of negative and positive kaons and attributed to their different freeze-out time in the evolution of the collision (see 1.5.2). This question is re-addressed for the Au+Au beam time in [37].

#### How to interpret the "success" of the statistical model?

The determined yields of all investigated hadrons could be compared to a statistical model addressing the question to which degree the production can be considered a purely statistical process in a thermalized system with a chemical freeze-out temperature  $T_{\rm chem}$  (for more details on statistical models, see 1.4.2). A fit of the statistical hadronization model in a strangeness canonical approach with the THERMUS software to the measured yields in the Ar+KCl collision system is presented in figure 1.17 showing a fair agreement with all strange particles, but the doubly-strange  $\Xi^-$  hyperon<sup>43</sup> [44].

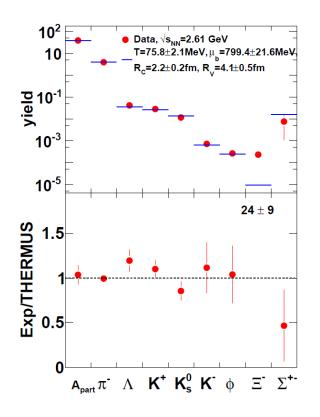


**Figure 1.17:** The upper plot shows measured hadron yields (red) from Ar+KCl collisions and the corresponding THERMUS fit values (blue bars) together with the obtained fit parameters. The lower plot shows the ratio of experimental data to the statistical model value. Figure taken from [44].

The success of statistical models in the low energy regime is still puzzling as statistical particle production is usually implicitly linked to thermalization and transport models predict that this equilibrium cannot be reached within the lifetime of a collision [136]. Furthermore, HADES has shown that a statistical model fit to elementary and p+Nb data gives similarly successful results [36] which leaves the question if or to which extent the fit quality sheds light on the degree of thermalization reached in such a heavy-ion collision system.

#### What is the catalyst for multi-strange particle production?

The measured  $\Xi^-$  yield exceeds the statistical model prediction by 1-2 orders of magnitude and many other models fail to describe this experimental observation [103, 104, 105, 221]. So far there are only two models which are able to reproduce the cascade yield [108, 222], however,

<sup>&</sup>lt;sup>43</sup> The cascade itself is excluded from the fit.

with rather different assumptions and conclusions. A back-of-the-envelope calculation illustrates the discrepancy: taking the measurement of singly-strange particles in the same system, the probability for the occurrence of producing an  $s\bar{s}$  in one event is of the order of  $P_{s\bar{s}} \approx 5 \cdot 10^{-2}$ . Assuming that these creation processes are independent, the probability to produce two strangeantistrange pairs is given by  $P_{s\bar{s}s\bar{s}} = P_{s\bar{s}}^2 \approx 2.5 \cdot 10^{-3}$ . The probability of producing a doublystrange cascade can be deduced from the measured cascade  $\Xi^-$  yield with  $P_{\Xi^-} + P_{\Xi^0} \approx 2 \cdot P_{\Xi} \approx$  $4 \cdot 10^{-4}$ , which also includes the  $\Xi^0$  that cannot be reconstructed with HADES. This number is roughly 5 times smaller than  $P_{s\bar{s}s\bar{s}}$ , which implies that in 20% of the cases where two strangeantistrange quark pairs are produced in an event, both *s* quarks end up in the same final state hadron [223]. A possible mechanism enabling such a process is the cloudy bag model, which was explained in section 1.3.5. However, the sub-threshold observation of the cascade already in the p+Nb system complements the  $\Xi^-$  observation in Ar+KCl and gives additional constraints on production mechanisms [110].

Future systematic high-precision measurements on sub-threshold cascade production in different systems at different energies will give further comprehensive insights. As a first step, it will be interesting to see whether the cascade can be reconstructed in the Au+Au system investigated in this thesis, where the production would occur even further below ( $\approx 800 \text{ MeV}$ ) its NN threshold than in Ar+KCl. With the higher track multiplicities leading to large combinatorial background the reconstruction in the significantly heavier Au+Au system will be a challenge, even when a similar enhancement is assumed.

#### What properties can be deduced from comparisons of experiment to transport models?

In the past, it has been demonstrated that many observables can be successfully described by transport models in which a basic assumption is the production of particles in binary collisions. Taking into account that the high-density phase ( $\rho > 2 \cdot \rho_0$ ) of a system created in a heavy-ion collision subsists only for a short time compared to its fully integrated space-time evolution, this success becomes less surprising since during most of the time the system is around ground state density and a description with hadronic degrees of freedom is appropriate, or one can deduce this from the success.

However, it is the phase of densities above 2-3 times ground state density which is of particular interest for the physics discussed here, which is expected to differ significantly from low-density systems and where the validity of a microscopic description with quasi-particles propagated through space-time is questionable. Whereas the formation time  $\Delta \tau_f^{44}$  for a hadronic state is of the order of 1 fm/c, the collision rates  $\Delta f_{\rm coll}^{-1}$  of hadrons can reach a few per fm/c in transport models which allows a violation of energy conservation of roughly  $\hbar/\Delta f_{\rm coll} \approx 200 - 500$  MeV, according to Heisenberg's equation 1.1. Hence, a relevant question with respect to strangeness production in a transport model ansatz is whether NN thresholds can play a decisive role with such high uncertainties in energy reached during the dense stage [223].

A question which can be addressed within the investigations of this thesis is the consistency of transport models. Discrepancies in their predictions may occur due to different model in-

<sup>&</sup>lt;sup>44</sup> The formation time describes the required time to form a full-sized hadron, i.e. when a state approaches its asymptotic wave function in the vacuum.

put such as cross-sections, however, the type of model (QMD vs (semi-)classical treatment) and technical implementation should not influence the outcome.

#### To what extent can in-medium potentials be constrained by HIC?

Particle properties at high baryon densities cannot be addressed directly by ab-initio calculations on the lattice due to the fermion determinant sign problem and therefore have to be modeled using effective Lagrangians. Relativistic heavy-ion collisions (HIC) provide a unique opportunity to constrain such models for densities larger than nuclear ground state density  $\rho_0$ . In particular kaons and  $\Lambda$  hyperons are promising probes of such collisions and have relevance for various astrophysical processes. As kaons contain an anti-strange quark, their coupling to baryons via formation of hyperon resonances is suppressed and they propagate in nuclear matter at ground state densities relatively free. One can estimate their mean free path in nuclear matter to be  $\lambda \approx 5$  fm by applying the low density approximation on the measured  $K^+$ -N cross-section. In the presented collision system  $K^{0,+}$  are produced below their free NN threshold with an excess energy of -150 MeV and can therefore not be formed directly in binary NN collisions. Hence, they are considered to be suitable messengers of the high density phase of such collisions.

Consequently, numerous works focused on kaons in this energy regime in the past. One of the most notable is the attempt to extract the equation of state (EOS) at densities exceeding nuclear ground state, based on the comparison of  $K^+$  multiplicity ratios from heavy (Au+Au) to light (C+C) collision systems to the same quantity obtained from microscopic transport models [54, 64, 224]. In addition, also the K-N potential has been frequently in the focus of investigations. Various model approaches based on chiral Lagrangians [151], one-boson-exchange models [193], the Nambu-Jona-Lasinio model [83] or coupled-channel calculations [225] predict an overall repulsive K-N potential. Most of the comparison of experimental data to microscopic models are also in favor of a repulsive K-N potential [53, 136, 137, 138, 139, 140, 141]. However, having no model describing all kaon observables consistently, no comprehensive picture emerged yet [57, 142].

A hyperons on the other hand are of peculiar interest as their presence and behavior influences the EOS itself. It has long been realized that inside neutron stars the appearance of hyperons via the weak interaction is possible and substantially softens the EOS [65, 66, 67, 68]. This leads to reduced upper limits for the maximum neutron star mass, which might induce conflicts [62, 63] with the recent observations of two solar mass neutron stars [18, 226]. Whether the appearance of hyperons inside a neutron star is energetically favorable depends on the strength of the Λnucleon potential, which is known to be attractive at ground state densities from hypernuclei formation [134]. However, the density dependence when approximating the potential in a meanfield description is uncertain [227]. Calculations based on the quark model in combination with a non-linear ω - σ model predict an attractive potential for densities below three times nuclear ground density but a repulsive potential for higher densities [228]. HIC collisions are the unique tool to study the Λ-N potential at high densities. However, data on Λ production from HIC at low energies are rare. While at SIS18 energies only data from medium-sized collision systems are available [44, 229], at AGS energies Λ production has been investigated in more details [230, 231, 232].

# Chapter 2

# **High Acceptance Di-Electron Spectrometer**

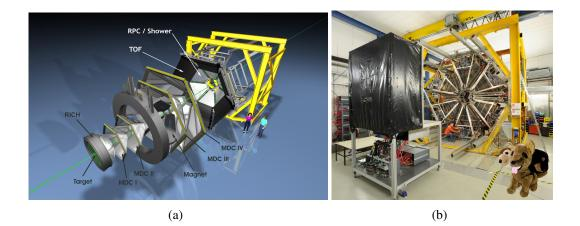


**Figure 2.1:** (a) Exploded view of the HADES setup. Indicated are the Mini-Drift Chambers (MDC) together with the superconducting magnet (ILSE) used for track reconstruction of charged particles, the Ring Imaging Cherenkov (RICH) and Pre-Shower detector for lepton identification as well as the RPC and TOF providing time-of-flight measurements. (b) Photograph of the backside of the detector in operational mode including the Forward wall.

# 2.1 Physics Motivation and Technical Requirements

The *High Acceptance Di-Electron Spectrometer* is located at the Schwerionen-Synchrotron (SIS) at GSI Helmholtzzentrum für Schwerionenforschung GmbH in Darmstadt and was first put into operation in October 2002. HADES has in particular been designed for an optimized detection of electron-positron pairs  $e^+-e^-$  from decays of the light vector mesons  $\rho$ ,  $\omega$  and  $\phi$  at SIS energies of 1-2A GeV. These vector mesons are excellent probes for an investigation of the high-density phase of a heavy-ion collision. Particularly the lifetime of the  $\rho$  meson is short enough to have vector meson decays mostly inside the dense medium and their dileptonic decay products carry this in-medium information almost undistorted to the detector since they are not affected by

Year	System	$E_{\rm kin}$ [A GeV]	Events (rec.) $[10^9]$
2002	C+C	2	0.25
2004	p+p	2.2	0.44
2004	C+C	1	0.495
2005	Ar+KCl	1.76	0.925
2006	d(n)+p	1.25	0.85
2007	p+p	1.25	1.7
2007	p+p	3.5	1.18
2008	p+Nb	3.5	4.21
2012	Au+Au	1.23	7.31
2014	$\pi^- + A$	0.5 - 1.57	0.38
2014	$\pi^- + p$	0.5 - 1.57	1.23
2018	Ag+Ag	1.6	_

**Table 2.1:** Overview of the past and upcoming collision systems and the corresponding beam energies investigated with HADES. Values taken from [233].

the strong interaction. A precise measurement of electron-positron pairs  $e^+-e^-$  gives the main constraints on the detector requirements:

- To study the decays of vector mesons into dielectrons the detector was optimized for a *high geometrical* e<sup>+</sup>-e<sup>-</sup> acceptance in the SIS energy regime, particularly to detect dielectrons at large solid angles which are emitted with large opening angles. The spectrometer covers about 80% in azimuthal and 18°-85° in polar direction. Detailed studies on the geometrical acceptance of e<sup>+</sup>-e<sup>-</sup> pairs as a function of mass and momentum can be found in [234]. For a detailed description of all detector components and a scheme of the setup, see section 2.2.
- Due to low production rates of the light vector mesons ρ and ω at SIS energies (< 10<sup>-3</sup> per reaction) and low branching ratios of the dileptonic decay channel (≅ 10<sup>-5</sup>) the number of recorded reactions has to be maximized. To achieve this goal, the data acquisition (DAQ) and the dead times of the detectors have to be optimized. For the Au+Au beam time an upgrade of the data acquisition was performed resulting in higher read-out rates which are necessary to cope with the higher bandwidth in this system.
- The background contribution to particle spectra from reactions not coming from the actual target but the detector material needs to be minimized by designs with low material budgets. Most importantly, the contribution from secondary  $e^+-e^-$  pairs coming from conversion processes has to be suppressed since they not only produce background in the dilepton mass spectrum, but also lead to higher occupancies in the detectors.

#### 2.2. TECHNICAL COMPONENTS

In addition, previous HADES experiments have demonstrated the strong hadron identification capabilities of the detector. In the following sections a special emphasis will be on the detector components which are relevant for the hadron reconstruction described in this thesis.

# 2.2 Technical Components

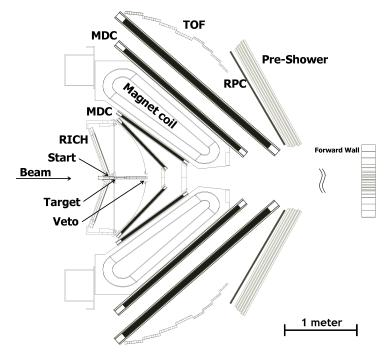


**Figure 2.2:** Schematic overview of a HADES cross-section showing the detector components. The beam is incident from the left on a segmented target (see 2.2.4) which is surrounded by the RICH detector (see 2.13). Start and veto detectors (see 2.2.3) are located in front of and behind the target. Two planes of mini drift chambers in front of and behind a superconducting magnet (see 2.2.1) are used for momentum reconstruction and identification of charged particles via energy-loss measurements. The META detectors RPC and TOF (see 2.2.2) are used for time-of-flight measurements.

# 2.2.1 Tracking System: Magnetic Spectrometer

The magnetic spectrometer consists of *Mini Drift Chambers* (MDC) and an *IronLess Superconducting Electromagnet* (ILSE). Combining these two components, traversing charged tracks and their momenta can be reconstructed.

#### Mini Drift Chambers – MDC

The setup contains 24 trapezoidal gas-filled mini drift chambers. Four planes of chambers are located downstream around the beam axis each divided into six sectors which are rotated by  $60^{\circ}$  with respect to each other, hence covering the full azimuthal angle of  $360^{\circ}$ . Two inner planes

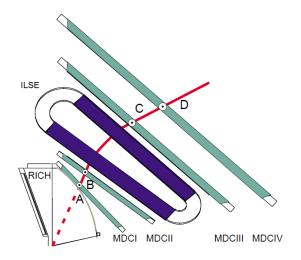
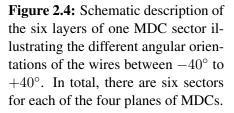
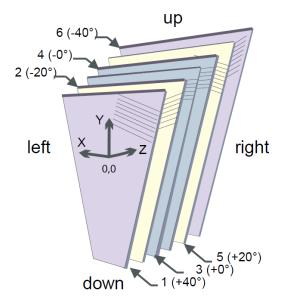


Figure 2.3: Schematic view of the magnetic spectrometer consisting of four planes of mini drift chambers (MDC I-IV) and the superconducting toroidal magnet (ILSE). A charged particle traversing the spectrometer ionizes the gas in the drift chambers. Its trajectory and momentum can be reconstructed via the measured hit points in the MDCs and its deflection caused by the magnetic field  $\vec{B}$  (see 3.5.3).

(MDC I and II) are located in front of and two outer planes (MDC III and IV) behind the magnet as illustrated in figure 2.3. The polar angle coverage ranges from  $\theta = 18^{\circ}$  to  $85^{\circ}$ .

Each of the 24 drift chambers has six layers, each equipped with parallel sense wires in different stereo angles with respect to each other as indicated in figure 2.4. With respect to the x-z plane in the sector reference system, the wires are inclined by  $\pm 40^{\circ}$  for the outermost over  $\pm 20^{\circ}$  to  $0^{\circ 1}$  for the innermost layers. This setup with differently oriented wires later allows to reconstruct the traversing point of a charged particle by projecting the fired wires onto a common plane for the determination of their intersection point, for details see section 3.5.3.





<sup>&</sup>lt;sup>1</sup> The wires for the two  $0^{\circ}$  layers are shifted by half a wire pitch with respect to each other.

#### 2.2. TECHNICAL COMPONENTS

For the Au+Au collision system the gas mixture of  $Ar/CO_2$  with a ratio of 70% to 30% was used for the first plane of chambers MDC I, whereas the other planes MDC II-IV were filled with 84% argon and 16% isobutane. Argon acts as a counting gas while the carbon dioxide and isobutane respectively were used as quenching gas, which serves as an absorber for UV radiation introduced by de-excitation of gas ions which increases the gas ionization and distorts the electric signal. As this effect is in the order of the ionization rate it cannot be neglected [234].

Essential for the conceptual design is a small area density. A total material budget of < 0.5% radiation length is realized by only 3-6 cm thick chambers and is necessary to minimize contributions from multiple scattering and from particles produced in secondary processes in the detector material which hamper the true signal. The main contribution here is the pair conversion where  $\gamma$  photons convert into dielectrons.

Figure 2.5 shows the mode of operation of one MDC drift cell. In a gas-filled drift chamber the gas atoms are ionized statistically along the trajectory of a charged traversing particle. By applying a voltage V the produced electron clusters are accelerated to an anode, also referred to as sense wires, whereas the resulting positive ions are accelerated to the cathodes. When the primary electrons reach sufficient energy to ionize more atoms in the gas an avalanche of secondary electrons is initiated. Due to this gas multiplication the read-out of short electric pulses becomes possible. The electric field strength and hence the acceleration of the created electrons increases strongly when approaching the anode wire.

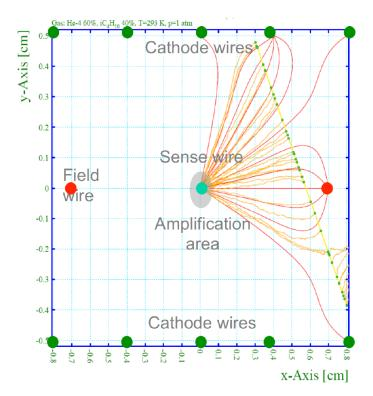


Figure 2.5: Schematic view of a charged particle traversing one MDC cell. A charged particle ionizes gas molecules statistically along its trajectory (green dots). The primary electrons are accelerated towards the anode wire (red lines) initiating an avalanche of secondary electrons few  $\mu$ m above the sense wire (gray area), inducing a signal [235].

Furthermore, the drift time of the electron cloud between the transit of the ionizing particle and the arrival of the electron cloud at the sense wire can be measured. With this drift time and the calculated drift velocity of electrons in the known gas, the minimum distance from the trajectory to the anode is deduced, which results in a high precision of the spatial resolution of about 100-200  $\mu$ m. This principle is explained in detail in section 3.5.1.4.

Another characteristic of charged particles traversing a medium (in this case the drift gas) is the specific energy-loss per unit path length dE/dx. This energy-loss is strongly correlated with the velocity/momentum of the particle and described by the Bethe-Bloch equation which is explained in section 3.6.1.2. The energy-loss is determined via the width of the measured signal in the drift chambers. The width is deduced from the time that the signal stays above an adjusted amplitude threshold which is referred to as *time over threshold* (*ToT*). This energy-loss information can be used for particle identification besides the time-of-flight measurement in the META detectors.

Together with the detected hit points in the drift chambers the momentum of the traversing particles can be reconstructed due to the transverse deflection of a charged particle induced by the magnetic field of the superconducting magnet ILSE which is described in the following subsection. The track and momentum reconstruction procedures are explained in section 3.5.

#### Magnet

The superconducting magnet ILSE is schematically depicted in figure 2.6. This magnet consists of six NbTi-coils which are located between the inner and outer drift chamber planes as indicated in figure 2.3. With a toroidal magnetic field geometry charged particles are deflected in polar direction leading to a curvature of the tracks allowing a momentum determination. Details of the momentum reconstruction are given in section 3.5.3. Since the performance of the electronic components of sub-detectors in the vicinity (RICH, MDC and TOF/RPC) must not be affected, the coil geometry was chosen to have minimum impact there. In addition the strength of the magnetic field was limited to have maximum intensity of 3.7 T at currents up to 3464 A on the coil surface decreasing down to 0.8 T in the center of a drift chamber sector. The magnetic coils are cooled with liquid helium down to 4.6 K in order to reach superconductivity.

### 2.2.2 META Detectors

The *Multiplicity Electron Trigger Array* (META) is located directly behind the last MDC plane IV. This detector system comprises the components used for time-of-flight measurement – a scintillator wall (TOF) and **R**esistive **P**late Chambers (RPC) – as well as the Pre-SHOWER detector, which will be discussed in section 2.2.6.

#### TOF

The time-of-flight detector TOF, shown in figure 2.7, is used for the measurement of the timeof-flight of a particle being an essential experimental quantity for particle identification as will be explained in section 3.6.1.1.

Like most components of the detector, the time-of-flight wall follows the trapezoidal geometry covering a polar angle from  $\Theta = 44^{\circ}$  to  $\Theta = 88^{\circ}$ . Same as for MDC planes the TOF detector consists of six sectors, each equipped with eight modules. Each of these modules again consists of eight plastic scintillator rods with a cross section of 20x20 mm<sup>2</sup> for the innermost 192 and

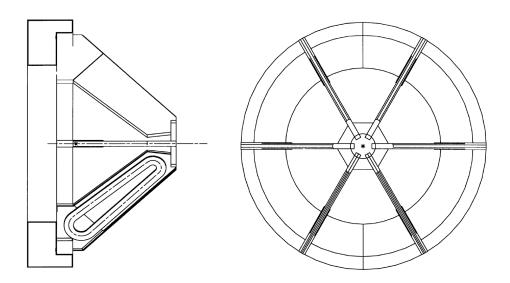


**Figure 2.6:** Technical drawing of the ironless, superconducting toroidal electromagnet ILSE, (left) side and (right) front view.

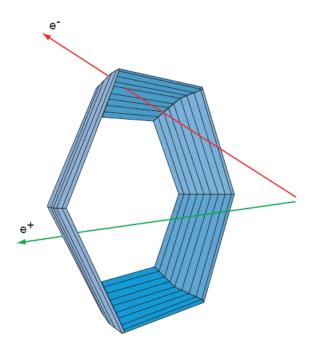


**Figure 2.7:** Schematic design of scintillator array of the time-of-flight wall TOF, covering polar angles from  $44^{\circ}$  to  $88^{\circ}$ .

 $30x30 \text{ mm}^2$  for the outermost 192 rods with lengths ranging from 1-2 m. Both ends of a rod are connected to photo multiplier tubes (PMT).

When a charged particle traverses the scintillator the atoms of its material get excited leading to photon emission by de-excitation back into the ground state. The emitted photons are multiplied by the PMTs and transformed into an electric signal. The intersection point of charged particles and the TOF wall is determined via the time difference of the two extracted signals at both ends of the rods at given length. The time signals on both sides determine the polar angle coordinate with a resolution of 2-3 cm whereas the azimuthal angle can be constrained with a resolution of 2.5 cm. A time resolution of up to 150 ps is achieved with this setup.

Furthermore, by measuring the amplitude of the read-out signal it is also possible to determine the energy-loss dE/dx of a charged particle analogue to the MDCs (see section 2.2.1).

#### RPC

The inner polar angle range from  $\Theta = 18^{\circ}$  to  $45^{\circ}$  is covered by six sectors of **R**esistive **P**late **C**hambers (RPC) (see figure 2.8). In 2008 the RPC replaced the TOFino detector which was similar to the TOF wall composed of scintillators but with significantly lower granularity. It is in particular the low polar angle region with high track densities reached in Au+Au collisions, resulting in high double hit probabilities, why this substitute was unavoidable. Each sector consists of 187 cells of three stacked aluminum electrodes separated by two glass plates in-between. Traversing charged particles ionize gas, which is located between the gaps of the plates, triggering an avalanche of electrons leading to a discharge. This detector provides an intrinsic time resolution below 73 ps, a transverse position resolution ranging from 22 to 42 mm depending on the cell width (see figure 2.8; variation along y-axis), a longitudinal position resolution of 8 mm with a detection efficiency for minimum ionizing particles of about 95%. The double hit probability in central Au+Au collisions reaches maximum 10% [236].

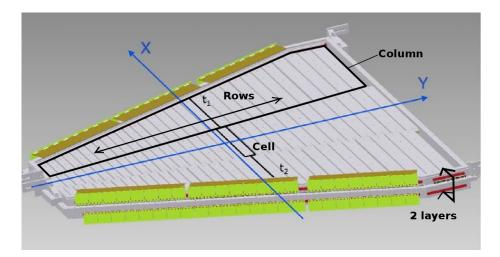


**Figure 2.8:** Technical drawing of one sector of resistive plate chambers covering polar angles from  $18^{\circ}$  to  $45^{\circ}$ . The RPC detector is used for time-of-flight measurements.

## 2.2.3 Start- and Veto-Detector

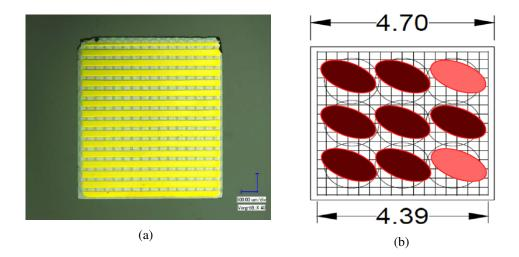


**Figure 2.9:** (a) Front view of the multi-strip start detector (module 1) showing the 16 monocrystalline diamond-based stripes. (b) During the Au+Au beam time the start detector was relocated nine times (indicated by the black rings) in order to minimize performance losses due to radiation damage. During one spill the beam is wandering within one ellipse.

As it will be discussed in section 3.6.1.1, the time-of-flight measurement provides the possibility to identify charged particles. Therefore, the particle production time  $t_0$  has to be determined, which is done by a start detector located in front of the reaction target. This production time  $t_0$  coincides with the point in time  $t_{coll}$  when the heavy-ion collision takes place from which the particles originate. Although there is a spatial displacement of the reaction vertex and the start detector position, as indicated in figure 2.10, the time measured in the start detector  $t_{start}$  coincides with  $t_{coll}$  within the precision of the particles time-of-flight  $t_{start} = t_{coll} = t_0$ .

The double-sided multi-strip start detector consists of monocrystalline diamond-based semiconductors and has a side length of 4.7 mm and a thickness of 50  $\mu$ m. Each of the two modules contains 16 stripes (in x- and y-direction). The time resolution of the start detector is about  $\Delta t = 50$  ps and the spatial resolution is sufficient to monitor the beam focusing. The elliptic beam spots on the start detector are schematically presented in figure 2.9 (b). Due to radiation damage its position had to be relocated nine times to guarantee high efficiency throughout the full Au+Au beam time. The efficiency of the  $t_0$  detector was determined to be above 95% [237].

The 100  $\mu$ m thick polycrystalline diamond veto detector is located 70 cm behind the 15-fold segmented Au target and is used to discard triggered reactions where no collision took place<sup>2</sup>. This anti-coincidence measurement as well as the dimensions of the start-target-veto system are sketched in figure 2.10.

<sup>&</sup>lt;sup>2</sup> Having measured an anti-coincidence does not necessarily mean that the triggered reaction actually was a relevant Au+Au reaction. Since the efficiency of the veto detector is limited to 95% [237], in up to 5% of the cases there will simply be no response even if a beam particle passed through.

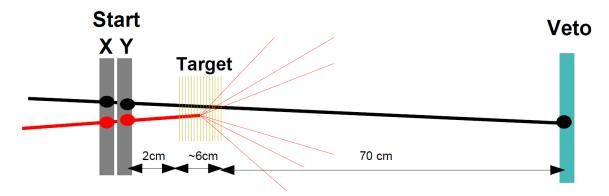
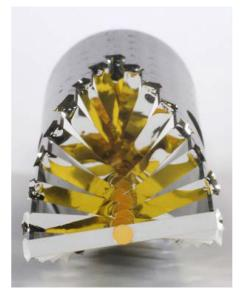


**Figure 2.10:** Scheme of the start and veto system. In the ideal case assuming 100% efficiency of all detectors, a beam particle is inducing a signal in the two modules of the start detector. If a reaction in the target takes place there is no response from the veto detector (red), if not, the beam particle will produce a hit in the veto detector as well (black). The signal in the start detector defines the start time  $t_{coll}$  of the reaction.

# 2.2.4 Segmented Gold Target

During the investigated beam time a 15-fold segmented Au-target was used. The distance between each of the gold disk segments is l = 4 mm, each with a radius of r = 1.5 mm and a thickness of  $d = 25 \ \mu$ m. The segments are mounted on thin kapton strips held by a carbon fibre tube. Figure 2.11 shows the front view of the full target.

**Figure 2.11:** Front view of the 15fold segmented gold target. Each target segment (golden disk) is fixed with a thin kapton strip to the carbon fiber tube.



One of the main requirements for the design of the target is to keep the conversion from  $\gamma$  radiation inside the target material into  $e^+-e^-$  pairs as low as possible, which is the reason for the segmentation. By maximizing the distance the contribution of conversion in the following segments can be neglected since the  $\gamma$  radiation typically leaves the target material with large

opening angles. Particularly in the case of gold this segmentation is inevitable since the conversion probability is proportional to the atomic number to the power of three ( $\propto Z^3$ )<sup>3</sup>. With  $Z_{Au} = 79$  this probability is approximately a factor 85 larger than for the second largest collision system measured with HADES so far ( $_{18}Ar+_{19}K_{17}Cl$ ). However, as the interaction rate is inversely proportional to the thickness of the target a compromise between these two quantities was found to be d=25  $\mu$ m.

## 2.2.5 Forward Wall

The forward hodoscope detector was installed in 2007 behind the HADES detector in the polar angle region of  $0.3^{\circ} < \Theta < 7.3^{\circ}$  which is not covered by any other detector component. It is orientated perpendicular to the beam axis and 7 m from the Au target. A schematic front view of the FW is shown in figure 2.12. It consists of 288 scintillator blocks varying in size. The main purpose of the FW hodoscope is to measure number and direction of reaction spectators and fragments from which the reaction plane and collision centrality can be deduced. The scintillator sizes are selected to ensure that a sufficient angular and spatial resolution is achieved to cope with different track densities. They range from 4 x 4 cm<sup>2</sup> for the innermost to 16 x 16 cm<sup>2</sup> for the outermost cells. Each cell has a thickness of 2.58 cm and is read-out by PMTs.

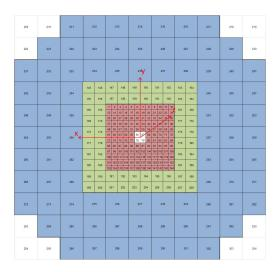


**Figure 2.12:** Front layout of forward hodoscope indicating the scintillator blocks surrounding the beam line [238]. The dimensions of the innermost scintillator blocks (red) are  $4 \times 4 \text{ cm}^2$ , followed by  $8 \times 8 \text{ cm}^2$  (green) and  $16 \times 16 \text{ cm}^2$  (blue) for the outermost cells.

$$\sigma(Z, E_{\gamma}) = Z(Z+1) \Big[ F_1(X) + F_2(X) \cdot Z + \frac{F_3(X)}{Z} \Big],$$

where  $E_{\gamma}$  denotes the incident gamma energy and  $X = ln(E_{\gamma}/m_ec^2)$ . The functions  $F_n$  are polynomials of fifth order and obtained from fits to experimental data in the range from  $1 \le Z \le 100$ .

<sup>&</sup>lt;sup>3</sup> The total cross section per atom for the conversion of a  $\gamma$  photon into an  $e^+$ - $e^-$  is given by the parametrization

## 2.2.6 Lepton Identification

#### RICH

Starting from the target in beam direction the *Ring Imaging Cherenkov* detector is the first detector in the HADES setup serving for dielectron identification purposes only. Figure 2.13 shows the cross section and indicates the working principle. When a charged particle traverses a medium of refraction index n = c/v < 1 with higher velocity than the speed of light in this medium, Cherenkov radiation is emitted under a certain opening angle with respect to the particle track. The resulting Cherenkov cone around its trajectory is reflected by the spherical mirror<sup>4</sup> and projected as a ring to a photon detector located in opposite direction.

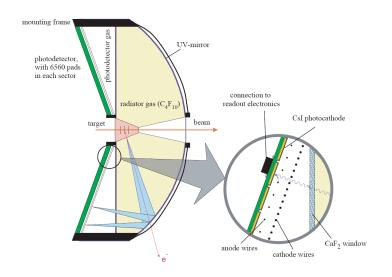


**Figure 2.13:** Schematic cross section of the RICH detector indicating the emitted Cherenkov light (blue areas) reflected on a UV-mirror and detected by a CsI photocathode.

The choice of the medium that the particle has to traverse with a given refraction index n determines the threshold in velocity/momentum for detection. In order to detect  $e^+-e^-$  pairs with momenta from 0.1 to 1.8 GeV/c the radiator gas  $C_4F_{10}$  was chosen. By using this gas, electrons can not only be separated from hadrons, but also from muons since they are significantly heavier than electrons.

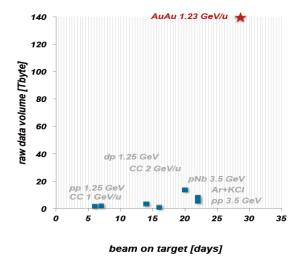
#### **Pre-Shower Detector**

The Pre-Shower detector is used for the identification of leptons with momenta above 300 MeV/c and is located behind the RPC detector hence covering the same polar angles. This detector is designed to distinguish between hadrons and leptons. Via bremsstrahlungs- and pair production processes electromagnetic showers are created which are almost exclusively triggered by relativistic electrons. The detector consists of trapezoidal wire chambers, where the electromagnetic showers are registered and lead converters, which have a thickness two times larger than the radiation length of electrons in lead. Each sector contains one module consisting of 1024 pads.

<sup>&</sup>lt;sup>4</sup> As all HADES detectors also the RICH mirror is divided into six sectors along the azimuth, four are made out of carbon and two out of glass.

#### 2.2. TECHNICAL COMPONENTS

With this conceptual design a characteristic relative energy-loss can be measured in the three wire planes which is different for leptons and hadrons. For more information, see [234].



### 2.2.7 Central Trigger System and Data Acquisition

**Figure 2.14:** Recorded data volume comparing different HADES beam times. The data volume recorded within the Au+Au beam time exceeds former beam times by roughly a factor of ten. Figure taken from [238].

To reduce the amount of collected insignificant data and the dead time between the recording of two collisions not all reactions are read-out. A multi-level trigger is defined which determines whether a reaction relevant for the HADES physics case, namely the potential production of vector mesons, took place. In the course of this thesis a triggered reaction will also be referred to as *event*.

The trigger in HADES is determined by the multiplicity of a reaction which is defined as the number of registered signals in the META detector and is anticorrelated with the impact parameter of the collision, which cannot be measured directly. Thus, this multiplicity is used for the classification of the collision centrality of an event, as will be discussed in more detail in section 3.4.3.

The trigger is divided into two levels – LVL1 and LVL2. In former beam times the first level was used to trigger reactions with a minimum centrality, whereas the second trigger selected events with potential lepton candidates. Since the average multiplicities in a LVL1 triggered Au+Au reaction are large enough to contain at least one lepton candidate, the LVL2 trigger became obsolete. In the Au+Au beam time two triggers were used, PT2 and PT3, both based on a minimum hit multiplicity in the TOF wall of 5 and 20 respectively.

In order to cope with the requirements of the Au+Au beam time, namely a factor ten higher data and event rates (see figure 2.14), the *data acquisition* (DAQ) was upgraded. The new DAQ system is based on about 500 modules with programmable logical blocks (FPGA<sup>5</sup>) which are controlled by one central module (CTS<sup>6</sup>). The major improvements are:

<sup>&</sup>lt;sup>5</sup> *Field Programmable Gate Array* 

<sup>&</sup>lt;sup>6</sup> Central Trigger System

- For the Au+Au collision system the new DAQ performs at data rates up to 8 kHz and 50% duty cycle. About 400 MByte/s are written to storage which corresponds to an improvement of roughly a factor 30.
- The electromagnetic noise produced by the read-out electronics in the sensitive front-end component of electronics was reduced significantly. This makes a reduction of signal detecting thresholds possible and allows DAQ and data transport from MDCs to run in parallel.
- A new user-friendly interface provides the user with online information about the status of all detector components.

Figure 2.14 shows the progress in recording data achieved due to the DAQ upgrade. For more information on the DAQ upgrade, see [239].

# Chapter 3

# **Event Selection and Track Reconstruction**

# **3.1 Beam Time Facts and Numbers**

In April and May 2012 the HADES experiment took for the first time data for a heavy collision system. Au-ions at a kinetic beam energy of  $E_{\rm kin} = 1.23$ A GeV were incident on a 15-fold segmented Au-target at rates of  $I_{\rm beam} = (1.2 - 1.5) \times 10^6 \, {\rm s}^{-1}$ . Events have been processed with data rates of 8 kHz and a 50% duty cycle. In total  $N_{\rm rec} = 7.31 \times 10^9$  events have been collected. Table 3.1 lists the most important specifications associated with the Au+Au beam time.

The readout was started by two multiplicity triggers based on the raw hit multiplicities in the TOF wall ( $Mult_{\text{TOF}}$ ), selecting semi-central to central ( $\approx 80\%$  with  $Mult_{\text{TOF}} > 20$ ) and peripheral to semi-central events ( $\approx 20\%$  with  $Mult_{\text{TOF}} < 20$ ) whereof only the first selection of events has been processed for this work. After a quality assessment of the detector performances, which were constantly monitored during data taking, further events were discarded, see section 3.2 and 3.3. A careful event cleaning procedure requiring selections on the reaction vertex and using the start-veto information will be described in section 3.4, which further improves the quality of selected events and reduces the number of analyzed reactions to the 0 - 40% most central collisions to  $N_{\text{evts}} = 2.12 \times 10^9$ . The full track reconstruction and particle identification will be introduced in 3.5 and 3.6 based on which a start time recalculation was conducted, which will be explained in 3.7. The procedure and necessary iterations to realistically model data and experimental setup in Monte Carlo simulations are presented in 3.8.

# **3.2 Data Processing and Quality Assessment**

The data acquisition, described in section 2.2.7, transports the triggered events and writes them to in total 101392 HLD files with an average number of 77000 reactions each. These files contain digitized detector signals of roughly 1.4 GB each and a unique number indicating the time of data taking with a time precision of one minute plus the number of the event builder<sup>1</sup> which

<sup>&</sup>lt;sup>1</sup> The server where the triggered data is sent to is called event builder. At this server different data streams are combined and then forwarded to permanent storage. In the Au+Au beam time in total eight event builders were used.

Projectile				
Projectile ions	$^{197}_{69+}$ Au			
Beam energy	$E_{\rm kin} = 1.23 {\rm A~GeV}$			
Beam intensity	$I_{\rm beam} = 1.2 - 1.5 \; {\rm x} \; 10^6 \; {\rm s}^{-1}$			
Target (section 2.2.4)				
Segments	15			
Segment distance	l = 4  mm			
Segment disc radius	r = 1.5  mm			
Density	$\rho = 19.32 \text{ g/cm}^3$			
Thickness	$d = 25 \ \mu \mathrm{m}$			
Interaction length	1.35%			
Data Acquisition (section 2.2.7)				
Av. Trigger rates	8 kHz			
Max. Data rates	$400 \text{ MByte } \cdot \text{s}^{-1} \text{ [239]}$			
Data volume	140 TByte			
Number of recorded events	$N_{\rm evts}=7.31 \ge 10^9$			
<b>Event Characteristics (0-40%)</b> (section 3.4)				
Number of selected events	$N_{\rm evts} = 2.12 \ {\rm x} \ 10^9$			
Mean number of part. nucleons	$\langle A_{\rm part} \rangle = 190.9 \pm 8.7$			
Max. impact parameter	$b_{\rm max} = 9.18~{ m fm}$			

**Table 3.1:** Overview of beam time characteristics in Au(1.23A GeV) on Au measured with HADES in April/May 2012.

#### 3.3. STABILITY OF DETECTOR SYSTEMS

was used to store the file. With this unique ID the containing detector signals can be related to the performance of each detector component in operational mode via the data base management system Oracle. The performances of the subdetectors are monitored via the slow control system which saves settings and eventual malfunctions. By these means, further events can be sorted out.

A precise calibration of each sub detector system is necessary in order to extract physical observables like energy-loss, time-of-flight or momentum. A crucial requirement for a successful calibration is the exact measurement of all detector positions which is referred to as photometric alignment. Details of this procedure are given in [240].

After that, the HLD files are further converted to so called Data Summary Tapes (DST) with a total space on disk of 140 TByte. These DSTs contain fully reconstructed track candidates, including their momenta as well as further derivable physics observables relevant for an extensive analysis of the given heavy-ion system. In the following sections 3.3 and 3.4, further criteria on the event selection are described, which are partly based on fully reconstructed tracks. The reconstruction procedure converting detector hits into full tracks as well as the momentum determination will be described in section 3.5.

# **3.3** Stability of Detector Systems

During the four weeks of data taking a permanent fully efficient performance of each sub-detector cannot be guaranteed. A first data quality assessment (QA) based on the high voltages and drift time distributions in the drift chambers already showed significant and regular drops in sector 2 occurring during almost the complete beam time resulting in an exclusion of this angular region  $(240^{\circ} \le \phi \le 300^{\circ})$  from the analysis. Furthermore, the high voltage settings of the mini-drift chambers had to be readjusted once in MDCI and III and more than once in MDCII [241, 238] leading to different layer efficiencies and drift time distributions in the corresponding cells. Therefore, the respective layer efficiencies had to be determined individually based on MDC cluster hits resulting in a single efficiency per layer averaged over all cells<sup>2</sup>. For more details on this procedure, see [242, 238].

In order to track down further detector instabilities which passed the preliminary QA, the effects of the detector performance on fully reconstructed particle tracks are investigated. Therefore, the number of the most abundant reconstructed charged tracks, i.e. pions, protons and electrons, is investigated as a function of time. Figure 3.1 shows the count rates per event and sector for the calendar day 109 for negative pions identified via their velocity-momentum information as will be explained in section 3.6.1.1. Few but significant sector-dependent drops are observed, in this case particularly for sector 2. To guarantee a high quality data set with stable detector performance, for the further analysis all DST files are excluded, where at least one additional sector besides sector 2 shows a drop below a threshold determined to be 95% of the mean count rate of protons and/or pions per sector per day. These sector-dependent thresholds

<sup>&</sup>lt;sup>2</sup> Therefore, only events with moderate multiplicity per sector were considered in order to avoid biases from e.g. increasing double hit probabilities.

are indicated in figure 3.1 as dashed lines. After this pre-selection of data, an event cleaning procedure follows, which will be explained in the next section.

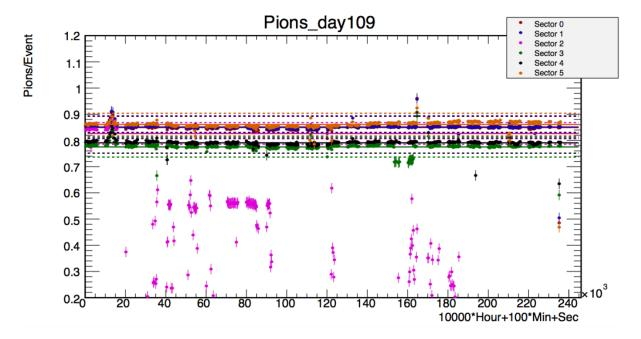


**Figure 3.1:** Mean count rate of identified negative pions per event and per sector as a function of beam time for calendar day 109. Each interval indicates one hour of a day resulting in 24 intervals. Significant drops are observed in few sectors leading to an exclusion of the containing files from the further analysis. The threshold for exclusion in a given sector is set to 95% of the mean count rate integrated over the complete day. Figure taken from [242].

# **3.4 Event Characteristics**

# 3.4.1 Event Vertex Reconstruction

In order to resolve each target segment separately a precise event vertex reconstruction is necessary. The resolution of the reconstructed event vertex, and hence its separation from secondary vertices, which are calculated for particles decaying outside the target region, is directly correlated with the suppression of combinatorial background. There are three iterations in order to determine the reaction vertex:

• Vertex via projection of clusters: In a first approximation the vertex segment is determined as described in 3.5.1.1. This iteration gives only a one-dimensional reconstruction of the vertex along the beam axis, however, with already a rather high efficiency of finding the correct segment.

#### 3.4. EVENT CHARACTERISTICS

- Vertex via inner segments: The second iteration is based on the reconstructed inner segments which are extrapolated back to the beam axis assuming straight lines. The resulting intersection points form a cluster in the region where the reaction took place. The geometrical center-of-gravity of the accepted points gives the interaction vertex.
- Vertex via reconstructed tracks: The last method gives the most precise event vertex calculation and is similar to the latter procedure but based on fully reconstructed tracks according to the Runge-Kutta procedure.

These methods are strongly correlated with the total multiplicity of an event making the reconstruction in the created high-track density environment rather precise. Furthermore, a triggered reaction does not necessarily mean that a pure Au+Au reaction took place. In few cases the beam particles can interact with the beam pipe or the start detector and hence geometrical constraints on the reconstructed vertex are made as will be described in the next section 3.4.2. The 15 reconstructed Au segments in the x-y plane in laboratory system are shown in figure 3.2.

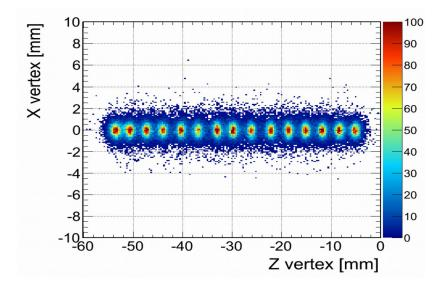


**Figure 3.2:** Reconstructed reaction vertices in the x-z plane. The 15-fold gold target segments are clearly visible.

Event Vertex in Simulation: The vertex position influences the geometrical acceptance of an event and hence has to be modeled properly in simulation in order to later successfully correct experimental data for acceptance. The reaction vertex of a particle generated in Pluto is arbitrarily chosen (x = y = z = 0) since the emission spectrum of particles is invariant under spacial translation. When the simulated particle is embedded into an event generated with the UrQMD model, in a first step, the target segment is randomly chosen (each segment with a probability of 1:15). Then, within this segment, the x-y-position is sampled according to a Gaussian parametrization of width  $\sigma = 1$  mm with a cut-off determined by the geometrical dimension of the segment (disc radius r = 1.5 mm). In z-direction, the position is sampled uniformly and the cut-off is determined by the thickness of a segment ( $d = 25 \mu$ m).

In case of simulated particles embedded into real data the actual vertex position is taken from the DST file, transported into the Pluto generator and tagged with the event sequence number. Later on this sequence number is needed to assure that the integrated sample of embedded data reproduces the full event vertex distribution, as can be seen in figure 3.2.

## 3.4.2 Event Selection

The recorded set of data does not solely contain reactions of Au+Au. The beam Au-ions also undergo interactions with materials besides the Au target, e.g. with the beam pipe or the diamond start detector. Furthermore, an overlay of multiple Au+Au reactions ambiguously assigned to one event (*pile-up events*) must be avoided to guarantee a clear classification of the investigated event. Hence, in order to assure a high purity of unique Au+Au collisions and a minimal contribution from background events, a careful event cleaning procedure has to be applied. Most of the false events are removed by using either selections on the reconstructed reaction vertex or information from the start-veto system.

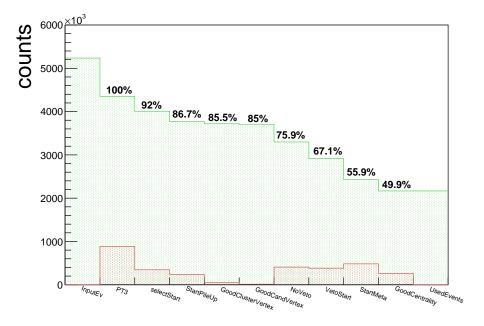


**Figure 3.3:** Number of events (green) after requiring event selection criteria as presented in the text, also plotted for each selection is the loss relative to the precedent criterion (red). The first bin (*InputEv*) contains the number of recorded events after a selection according to section 3.3 based on the sector-dependent investigation on the number of reconstructed charged tracks versus beam time, however, the starting point for the relative loss is the number of events after a PT3 trigger selection (*PT3*, 100%). The selection conditions are described in the text. The last bin indicates the number of events finally used for data analysis (*UsedEvents*) which correspond to roughly 50% of PT3 triggered data. This distribution is shown to demonstrate the relative loss and includes only data from one calendar day.

The event selection criteria are explained in the following. Most of the false events are removed by using either selections on the reconstructed reaction vertex or information from the start-veto system. The rejected fraction for each selection is displayed in figure 3.3. The indicated

#### 3.4. EVENT CHARACTERISTICS

loss in percent is determined relative to all PT3 triggered events ( $Mult_{\text{TOF}} > 20$ ), where all five sectors except sector 2 (see section 3.3) were performing stably:

- One hit in at least one of the two start modules and none in the veto detector was found (*selectStart*)<sup>3</sup>.
- Only one hit cluster was found in the start detector (*StartPileUp*) within  $-5 < t_0 < 15$  ns around the start time. Otherwise a potential reaction cannot be unambiguously assigned to one or the other start signal leading to wrong estimates of the time-of-flight of the detected particles.
- A selection on the reconstructed event vertex is made: The target extends from -65 < z < 0 mm. This selection is applied to make sure that the triggered reaction actually came from the Au-target and not e.g. from the start detector. Additionally at least two identified particles (*GoodCandVertex*) and one reconstructed track (*GoodClusterVertex*) each with a  $\chi^2$  greater than zero have to be found. The procedures have been described in the previous section 3.4.1.
- Events are excluded for which a veto hit within  $\Delta t = \pm 15$  ns around the measured start time was found (*NoVeto*). This reduces the probability of having another beam particle in a 30 ns time window<sup>4</sup>. Since the start detector has limited efficiency, it may happen that a beam particle caused a reaction in the target but none of the start modules responded to it. However, there could have been a start hit from another beam particle triggering a wrong start time for the reaction which would lead to wrongly calculated time-of-flights.
- Further events, where a start hit but no corresponding veto hit in a time window from 15 ns to 350 ns after  $t_0$  was found, are removed (*VetoStart*). This selection discards potential pile-up Au+Au collisions and accounts for the limited veto efficiency.
- Events, where a correlation between a late start hit and the META detectors in the time range from 80 ns to 350 ns after the triggered start time was found (*StartMeta*), are also rejected. The idea is similar to the previous one of avoiding pile-up events. The lower limit of 80 ns guarantees that all particles of an actual Au+Au event have reached one of the time-of-flight walls, whereas the upper limit of 350 ns is defined by the measuring range of the outermost drift chambers and was chosen to ensure that all signals of an actual Au+Au reaction are processed. Otherwise, the centrality determination could get polluted.
- Furthermore, in order to reduce the uncertainty on the mean number of participants  $\langle A_{\text{part}} \rangle$  only the 0 40% most central events are analyzed (*GoodCentrality*).

The listed exclusions finally lead to a high-quality data set of  $N_{\text{evts}} = 2.12 \text{ x } 10^9$  reactions which corresponds to roughly 50% of all PT3 triggered and 42% of all recorded events.

<sup>&</sup>lt;sup>3</sup> Assuming that the start-veto system works at 100% efficiency this would guarantee that a reaction inbetween start and veto detector took place (not necessarily Au+Au).

 $<sup>^4</sup>$  At least in 95% of the cases due to the also limited veto efficiency.

## **3.4.3** Centrality Selection

The properties of the created system and the resulting physical observables depend strongly on the centrality of the collision. The centrality can be e.g. characterized by the number of nucleons participating in the reaction  $A_{part}$  or the impact parameter b which is defined as the minimum transverse distance between their centers and is sketched in figure 3.4 (a). Intuitively, length scales of the impact parameter are in the order of the radius of a nucleus, i.e. femtometers, making a direct measurement of b rather impossible. The same holds true for  $A_{part}$ . An indirect way to estimate the centrality is via the Glauber model [243], where  $A_{part}$  and b can be related to the particle multiplicity which is a measurable quantity. By assuming that the number of produced particles rises monotonically with  $A_{part}$  towards more central collisions and thus decreasing impact parameter, the transverse energy  $E_t$  and the average number of charged particles  $N_{ch}$  can be estimated by performing Glauber Monte Carlo simulations as it was done within [233] for the Au+Au beam time. The simulated impact parameter distribution of a collision system can be used to determine the total reaction cross section.

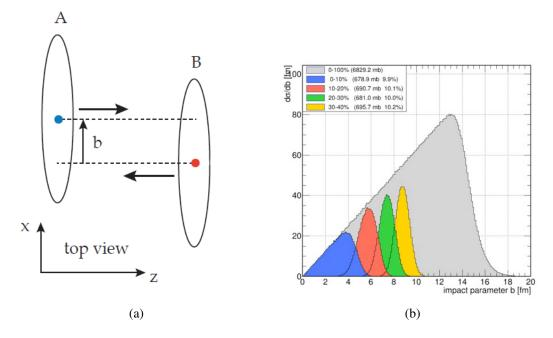


**Figure 3.4:** (a) Sketch of two colliding nuclei A and B in the x-z plane. The distance between their center-of-gravities (blue and red) in x-direction is defining the impact parameter b. Figure taken from [233]. (b) Impact parameter distribution for minimum bias Au+Au collisions (gray) at 1.23A GeV, as determined in [233]. Also indicated are the impact parameter distributions for the different centrality classes for 0-10% (blue), 10-20% (red), 20-30% (green) and 30-40% (yellow). Figure taken from [238].

 $N_{\rm ch}$  can then be determined by sampling the multiplicity distribution assuming a Gaussian distribution with mean  $\mu$  and sigma  $\sigma$  with:

$$N_{\rm ch} = \mu \cdot A_{\rm part} , \ \sigma = k \cdot \sqrt{\mu \cdot A_{\rm part}}.$$
 (3.1)

The parameters  $\mu$  and  $\sigma$  are obtained by performing a  $\chi^2$ -minimization procedure where an ensemble of simulated multiplicity distributions are compared to the experimental one. This procedure automatically takes the acceptance of the detector, and hence the PT3 triggered data set (TOF<sub>Mult</sub> > 20) used for this analysis, into account. The determined total cross section can then be grouped into several fractions corresponding to the centrality percentiles as listed in table 3.4 also showing further essential event characteristics extracted from the Glauber calculation. For more details on how the centrality classes were determined, see [233].

Figure 3.2 (b) shows the impact parameter distribution for minimum bias Au+Au collisions at 1.23A GeV as well as for each of the four different centrality classes used in this analysis. In order to reduce the uncertainty on the determined mean number of participants  $\langle A_{part} \rangle$  only the 40% most central events were analyzed.

Class [%]	$\langle A_{\rm part} \rangle$	$\langle b \rangle$ [fm]	$b_{\max}$ [fm]	$N_{\min}$	$N_{\rm max}$
0 - 10	$301\pm11$	3.14	4.6	160	250
10 - 20	$212\pm10$	5.70	6.5	121	160
20 - 30	$148\pm8$	7.38	7.95	88	121
30 - 40	$102\pm 6$	8.71	9.18	60	88

**Table 3.2:** Summary of the four centrality classes for 0 - 40% most central collisions in steps of 10% as estimated in [233] by using a Glauber Monte Carlo simulation. The classes can be related to the mean number of participants  $\langle A_{part} \rangle$  as well as the impact parameter *b* of a collision and to the hit multiplicities in the time-of-flight walls. The relative uncertainties of the mean number of participants decreases with increasing multiplicity and hence centrality.

## **3.5 Track Reconstruction**

When a charged particle traverses the active detector volume, for each of the four HADES drift chambers a high resolution track point and the direction of flight can be reconstructed. The two inner (MDC I/II) and outer (MDC III/IV) drift chamber planes are grouped respectively ("combined mode") assuming a straight track in between due to a vanishing magnetic field in this area. By interpolation of the corresponding hit points, this gives two track segments for a particle passing each of the four MDC planes: an inner and outer segment.

Figure 3.5 shows the flow chart for the full track and momentum reconstruction. Each of these steps will be explained in detail in the following subsections. The track segment reconstruction is done in two major steps: the cluster finder (green) and the segment fitter (blue), which are explained in subsection 3.5.1.2 and 3.5.1.4. In order to improve the resolution, not only the fired

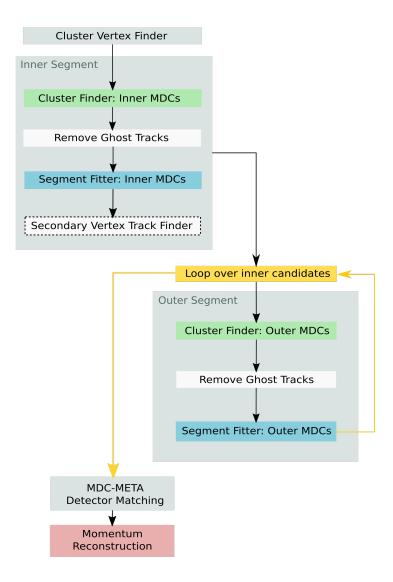


**Figure 3.5:** Flow chart of the track and momentum reconstruction. As a first iteration a preliminary vertex segment (3.5.1.1) is selected serving as vanishing point for the inner cluster finder (green; 3.5.1.2). In the next step fake track segments, so called ghost tracklets, can be largely removed (3.5.1.3). The remaining inner segments are fitted to the fired cells (blue; 3.5.1.4). An additional algorithm searches for inner segments corresponding to particles emitted from a secondary vertex (dashed; only used in latest version; 3.5.1.5). For each of the inner segments possible outer segments are searched and reconstructed including the same procedure as for the inner segments. The found outer segments are roughly matched to the META detector hits (3.5.2). As a last step the inner and outer segments are used to reconstruct the full track and thus the momentum (red; 3.5.3).

cells<sup>5</sup> but also the drift time information of the knocked-out electrons in the chamber gas is used (see figure 3.7). In the high track density environment created in central Au+Au collisions there is an enhanced probability of having fake track segments ("ghost tracklets") which are largely removed by an additional algorithm as will be described in 3.5.1.3. In the latest version of the Au+Au data set (gen9) a secondary vertex track finding algorithm (dashed) was introduced. This algorithm subsequently follows after the inner segment fitter and searches through the previously removed inner track segments under the hypothesis that they do not point back to the primary vertex. This method accounts for tracks which have not been emitted from the reaction vertex as it is the case for particles originating from weak decays (see 3.5.1.5). However, the analyzed data set presented in this thesis does not yet include this procedure.

With both segments given, a known magnetic field strength and by using an appropriate momentum determination algorithm the full particle track and its momentum can be reconstructed (red). Details follow in section 3.5.3.

## 3.5.1 Segment Reconstruction

The general concept is the following: When a charged particle passes a drift chamber several wires are fired based on the ionization of the gas in the chamber as explained in section 2.2.1. In order to find the particles point of intersection through the chamber all fired wires are projected onto a common plane.

## 3.5.1.1 Cluster Vertex Finder

In a first approximation the target segment is determined based on the projection quality of the wire distribution of MDCI and II. Therefore, the algorithm calculates the projection resolution for each segment which is used as a view point for the projection plane of the inner chambers. The segment with the best projection resolution (cluster size) and the largest amount of clusters, exceeding a certain threshold, is taken as the reaction vertex. In addition, the drift time information is used in order to shrink the projection volume and increase the resolution (the advantage of using the drift time information will be explained in section 3.5.1.4).

## 3.5.1.2 Candidate Search – Cluster and Segment Finder

There are two projection planes: one is located between MDC I/II and the other one between MDC III/IV as indicated in figure 3.6 (a).

**Cluster Finder Part I – Inner Segment**: Starting from the target cluster segment according to 3.5.1.1 as a view point, the volume of a drift cell is projected onto the common plane between the inner MDC planes I and II. The position of the projection plane is chosen such that the transverse elongations of all drift cell projections from the two MDC planes are equal. An example how this projection of drift cells can look like in a low track density environment is shown in figure 3.6 (b) where three dominant intersection points can be observed. In order to improve the

<sup>&</sup>lt;sup> $\overline{5}$ </sup> Throughout this section the terms *drift cell* and *wire* are used equivalently.

spatial resolution, the drift time information is used additionally. Figure 3.7 shows schematically this concept and the impact on the spatial elongation when involving the drift time information.

If several wire projections cross each other a local maximum emerges reaching values up to 12 – one entry for each layer of the two planes. The local maximum is also referred to as cluster. If the number of entries (cluster amplitude) exceeds a certain event-dependent threshold (typically  $N_{\rm thr} \geq 9$  in Au+Au, depends on the total number of fired wires in the corresponding event) the cluster is accepted.

Connecting the local maximum in the projection plane with the target point results in two intersection points in MDCI and II respectively which by interpolation gives the inner segment.

**Cluster Finder Part II – Outer Segment:** The search for wire clusters in the outer drift chambers MDC III and IV follows the same principle with the difference that the target cannot be used as view point for the projection. Instead the intersection point of the inner segment with a virtual plane centered in the region of maximum magnetic field – the so called kick plane (see section 3.5.3) – is used. This kick plane approximates the continuous influence of the magnetic field on the charged particle by a one-point momentum deflection.

The cluster finder for the outer drift chambers is done for each intersection point of the inner segment with the kick plane individually and provides the outer segment.

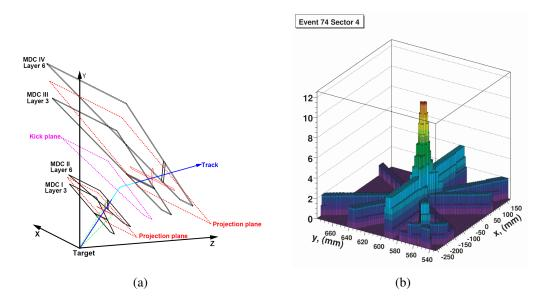


**Figure 3.6:** (a) Schematic view of the segment finding process in the four MDC planes. The intersection point of the extrapolated inner segment with the kick plane serves as view point for the cluster finding algorithm of the outer segment following the same principle as for the inner segment finder. For details, see text. (b) Projection of fired cells in the x-y plane. In this example, a clear local maximum emerges as a cluster. If the number of entries exceeds a certain event-dependent threshold the cluster is accepted. Figures taken from [244].

## 3.5.1.3 Removal of Ghost Tracks

Because of wrongly fired wires due to noise or ambiguous cluster assignments, the cluster finding algorithm may lead to a non-negligible contribution of false segments, so called ghost tracks or tracklets, which occur in particular in the finding process of inner segments where the track densities are higher than in the outer parts of the detector.

By evaluating global patterns of the reconstructed track segments, the ghost tracks have been found to show a rather distinct behavior with respect to the true clusters, which are:

- Smaller average cluster amplitudes.
- Smaller average number of unique wires (contributing to this cluster only).
- Larger average number of wires participating in real clusters.
- Smaller average cluster size.

Thus, the ghost tracks are identified with these signatures removing in case of the inner segment  $\approx 45\%$  and for the outer segment 68% fakes while losing in both cases only up to 0.1% real tracks [245].

#### 3.5.1.4 Segment Fitter

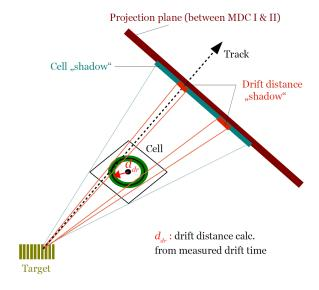


**Figure 3.7:** Scheme to visualize the improvement in projection resolution when using the measured drift time information of the electrons knocked-out by a traversing charged particle (dashed line) in the chamber gas. Compared to a projection of the full cell (teal) the drift time information significantly shrinks the projection volume onto the common plane between the drift chamber planes (red). The drift time measurement can be translated to a drift distance of the electrons with a Garfield simulation resulting in a ring with radius  $d_{\rm dr}$ . The width of the ring (green) results from the precision of the drift time measurement.

The spatial and angular resolution of the candidates achieved by using the previously explained method alone cannot cope with the necessary precision in particular for the high occupancies in Au+Au reactions. Therefore, the obtained segments are fitted to the fired drift cells by using additionally the measured drift time to reduce the projection volume. This  $\chi^2$ -minimization gives a quality parameter which can be retrieved on analysis level. Figure 3.7 depicts schematically the impact on the projection quality when using the drift time information. In order to translate the measured drift times into the distance of a particle trajectory to the sense wire in a drift cell a Garfield<sup>6</sup> simulation is used, where each drift cell is modeled in two dimensions and the trajectory can be described by its impact angle  $\theta$  and the minimum distance to the anode wire  $d_{\min}$ . A functional of the form  $t_{\text{drift}} = f(d_{\min}, \theta)$  can be derived.

The straight segments obtained from the cluster finder are fitted to the drift time information obtained from the fired cells. For the fitting a functional F for the i drift cells of a segment is defined in time space:

$$F = \sum_{i} \frac{(t_{\text{drift}}^{i} + t_{\text{off}} - t_{\text{TDC}}^{i})^{2}}{(\Delta t_{\text{TDC}}^{i})^{2}} \cdot w_{i}$$
(3.2)

and minimized with

 $t_{
m drift}$  – Drift time from Garfield model  $t_{
m off}$  – Time-of-flight of particle from target to drift chamber  $t_{
m TDC}$  – Drift time measured by TDC ( $t_{
m measured} - t_{
m wire}$ )  $w_i$  – Weighting constant (Tukey weight)  $\Delta t_{
m drift}$  – Error of drift time measurement by TDC.

The errors of the drift time measurement  $\Delta t_{\text{drift}}$  are determined from a Garfield simulation. For more details see [235]. In order to improve in particular efficiency and resolution for low momentum tracks, a pre-fit algorithm is preceding the segment fitter routine [246].

## 3.5.1.5 Secondary Vertex Track Finder

After the inner segment finder an additional iteration over all removed wires which were not used in the reconstructed inner segments is performed. In contrast to the inner segment finder, this algorithm is not based on the assumption that the particle is emitted from the primary vertex and hence accounts for secondary vertex decays. This algorithm [245] was first performed in the latest generation of DST production, i.e. *gen9*, and could not yet be included in this analysis. The procedural steps are listed in the following complemented by figure 3.8 displaying the scheme of this routine to support a better understanding:

- 1. Select wires not used in fitted segments.
- 2. Search for a combination of two crossing wires, one in MDCI (green) and another one in MDCII (blue), with a minimum angle of  $\geq 40^{\circ}$  between them<sup>7</sup>.

<sup>&</sup>lt;sup>6</sup> Garfield is the name of a software developed at CERN to simulate two- and three-dimensional drift chambers.

<sup>&</sup>lt;sup>7</sup> In the Au+Au beam time, the crossing wire combinations for MDCII are only allowed in a window of  $\pm 5$  wires around the cell crossed by a line connecting the target to the cluster point of two crossing wires in MDCI. This constraint was made to reduce large computing times due to high event multiplicities resulting in large combinatorics for this algorithm.

- 3. Assume a straight line intersecting with the found clusters of these two pairs of crossing wires (red line).
- Search all wires crossed by this line and accept if the number of fired cells per MDC plane is N<sub>x</sub> ≥ 7.
- 5. Perform segment fitter equivalently to section 3.5.1.4.
- 6. Add segment to list of reconstructed inner segments (marked as *off-vertex*) and add wires to list of fitted wires.
- 7. Repeat 1-6 until no more candidates are found.

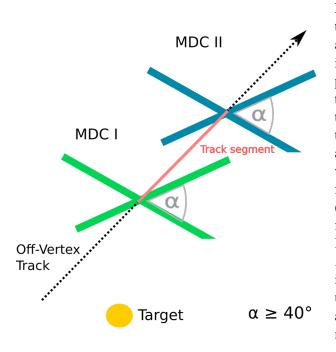
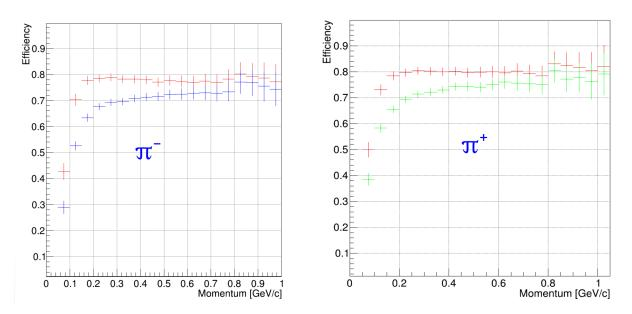
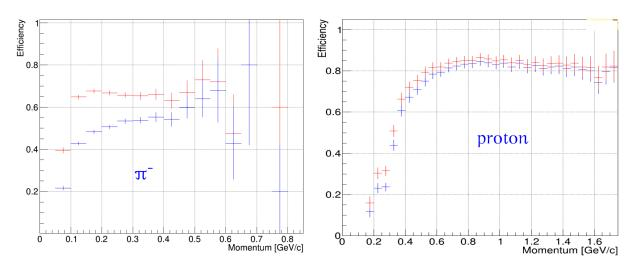


Figure 3.8: Scheme to visualize the routine for the secondary vertex track finder. In order to account for tracks (dashed black line) originating from a secondary vertex decay which do not point back to the target (yellow disc), an additional track finding routine is performed after the inner segment fitter. Therefore, a combination of two crossing wires, one in MDCI (green) and another one in MDCII (blue), are searched with a minimum angle of  $40^{\circ}$  inbetween. The found clusters are connected by a straight line (red line) providing a new segment, which is fitted to the fired cells as described in 3.5.1.4. If the number of fired cells per MDC plane is  $N_x \ge 7$ , the track segment is added to the list of inner segments, marked as off-vertex track. The used wires are added to the list of fitted wires and the routine is repeated until no more segments are found.

This additional procedure enhances the successful reconstruction of pions coming from a decay of neutral kaons by roughly 10-15%. For negative pions from  $\Lambda$  decays this number reaches even up to 30% whereas the improvement for protons is of the order of few percent. Figure 3.9 and 3.10 show the increase in track reconstruction efficiency for charged pions from  $K_s^0$  and  $\pi^-$ -proton pairs from  $\Lambda$  decays as obtained from a full MC simulation when using the described iteration. Although the increase of track reconstruction efficiency for protons originating from a primary  $\Lambda$  decay is rather moderate, the improvement for protons from  $\Lambda$  hyperons coming from  $\Xi^-$  decays may be more significant, since these protons have on average a larger distance of closest approach (DCA) when extrapolating to the primary vertex.



**Figure 3.9:** Monte Carlo simulation of track reconstruction efficiency as a function of pion momentum with (red) and without (blue/green) secondary vertex track finder for charged pions coming from  $K_s^0$  decays. An increase of successfully reconstructed charged pions ranging from 10 to 15% is achieved. The figures are taken from [247].



**Figure 3.10:** Monte Carlo simulation of track reconstruction efficiency as a function of momentum with (red) and without (blue) secondary vertex track finder for negative pions (left) and protons (right) coming from  $\Lambda$  decays. An increase of successfully reconstructed negative pions ranging up to 30% and protons of few percent is achieved. The figures are taken from [247].

#### 3.5.2 **MDC-META Detector Matching**

After the reconstruction and fitting of all outer segments a rough matching of their extrapolated trajectory to the registered META detector hits is performed resulting in a matching quality parameter  $\chi^2_{MM}$ . This quality parameter is defined as the deviation of the intersection point of the reconstructed track segment with the META hit dx-dy coordinates normalized to the associated uncertainties  $\sigma_x/\sigma_y$ :

$$\chi^2_{\rm MM} = \sqrt{\frac{dx^2}{\sigma_x} + \frac{dy^2}{\sigma_y}}.$$
(3.3)

In the Au+Au beamtime dy is determined by the geometry of the META detector cells, i.e. a track is matched to a hit if it points to a fired cell or deviates from this cell by a momentum dependent value which saturates at 4 mm for high momenta. For low momentum tracks this value is slightly higher in order to account for multiple scattering. This reduces equation 3.3 to:

$$\chi^2_{\rm MM} = \frac{dx}{\sigma_x}.$$
(3.4)

The distance of the extrapolated RK tracks to the hits in the META detectors dx is distributed Gaussian-like, as can be seen from figure 3.11 for minimum- (MIPS), intermediate- (MEPS) and maximum-ionizing (MAPS) particles<sup>8</sup>. In the rough matching process on DST level all combinations in a  $5\sigma$  window are accepted<sup>9</sup>. Figure 3.12 shows a schematic example of the explained matching procedure and the defining parameters.

A more detailed investigation on  $\chi^2_{\rm MM}$  and its correction in the TOF region for the Au+Au beam time can be found in [249] as well as a description of recalibration for "walk-effects" of the uncertainties  $\sigma_x$  in [37].

#### 3.5.3 **Momentum Reconstruction**

The momentum of a charged particle can be determined by its curvature when traversing a magnetic field. When a charge q propagates with velocity  $\vec{v}$  in a magnetic field  $\vec{B}$  the following relation applies for the Lorentz force:

$$\vec{F}_L = q(\vec{v} \times \vec{B}). \tag{3.5}$$

Due to this force the velocity  $\vec{v}$  and hence the momentum  $\vec{p}$  of the charged particle experiences a deflection perpendicular to  $\vec{v}$  and B. Integrating over the full path length s of the trajectory of the particle and by using equation 3.5, for the total momentum deflection  $\Delta \vec{p}_{tot}$  follows:

<sup>&</sup>lt;sup>8</sup> The width is inversely proportional to the energy loss. <sup>9</sup> The quality parameter  $\chi^2_{\rm MM}$  can be further constrained on the user level.

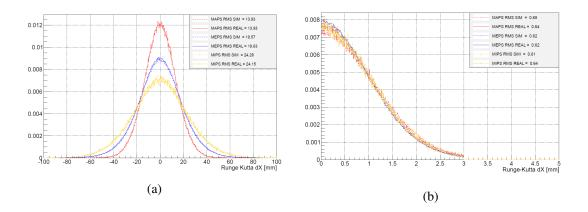


**Figure 3.11:** (a) Distance dx of extrapolated Runge-Kutta tracks to hits in the TOF detector for minimum- (MIPS, yellow), intermediate- (MEPS, blue) and maximum-ionizing (MAPS, red) pions and protons for data (solid) and simulation (dashed). The identified particles are grouped according to their velocity  $\beta$  and a track quality of  $\chi^2_{\rm RK} < 200$  is required. The data distributions are reasonably reproduced in simulation. (b) Distance dx of extrapolated Runge-Kutta tracks to hits in the TOF normalized to the calibrated width  $\sigma_x$ . The figures are taken from [248].

$$\Delta \vec{p}_{\text{tot}} = \vec{p}_{\text{out}} - \vec{p}_{\text{in}} = \int d\vec{p} = \int \vec{F} dt = \int q[\vec{v} \times \vec{B}] \, dt = -q \int \vec{B} \times d\vec{s}.$$
(3.6)

 $\vec{p}_{in}$  and  $\vec{p}_{out}$  denote the momenta before and after the deflection of the particle and are equal in their absolute value. Equation 3.6 shows that the deflection is in leading order independent of the momentum. Furthermore, the deflection angle  $\Delta\Theta$  between incoming and outgoing momentum can be deduced:

$$\sin\left(\frac{\Delta\Theta}{2}\right) = \frac{|\Delta\vec{p}_{\rm tot}|}{2|\vec{p}|},\tag{3.7}$$

with  $|\vec{p}| = |\vec{p}_{in}| = |\vec{p}_{out}|$ .

With the magnetic spectrometer, which consists of six magnetic coils and four planes of multi-wire drift chambers (see section 2.2.1), it is possible to reconstruct the momenta of traversing particles via three different methods with precisions of up to 1% [234]. Therefore, requirements are a precise knowledge of the magnetic field map that is obtained from *TOSCA*<sup>10</sup> simulations and the inner and outer track segments whose reconstruction was described in the previous section 3.5.

Besides the Runge-Kutta method used for the momentum determination in the Au+Au analysis, there are two other relevant procedures – the kick-track and the spline method:

<sup>&</sup>lt;sup>10</sup> TOSCA is an analysis package used for simulating three-dimensional electrostatic and magnetostatic fields.

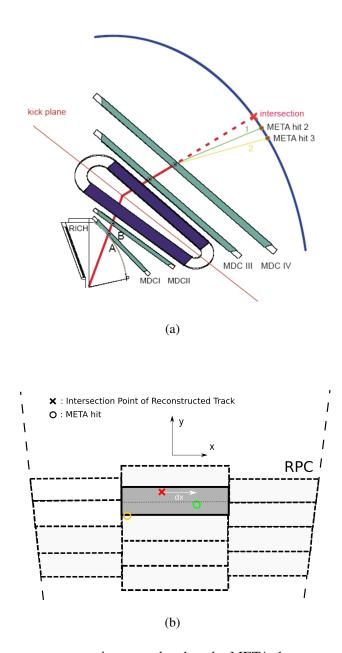


**Figure 3.12:** (a) The outer segment is extrapolated to the META detector assuming a straight line (dashed, red line) giving an intersection point in the corresponding detector cell. In this example two close-by hits were registered in the RPC (green and yellow line). Figure taken from [234]. (b) Corresponding RPC sector in *x*-*y* coordinates. One META hit (green) is slightly closer to the intersection point of the extrapolated outer track segment (red cross) than the other one (yellow) in dx. With respect to dy, both hits are accepted since the green one is inside the cell, the yellow one rather close to the border of the cell (dy < 4 mm). The distance dx defines the matching quality  $\chi^2_{\text{MM}}$ . When requiring a certain selection window on  $\chi^2_{\text{MM}}$ , the green hit will be chosen over the yellow one.

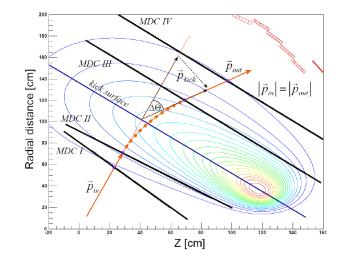


**Figure 3.13:** Sectional drawing of the magnetic spectrometer and the deflection of a particle experienced by the magnetic field. In the realistic case the particle trajectory indicated by the orange line gets deflected in the full magnetic field area, also inbetween the MDC planes I/II and III/IV respectively. The kick-track method neglects this continuous deflection, instead a one-point deflection at the kick surface is assumed. Also the spline procedure only describes a stepless deflection between MDC II and III. The most accurate is provided by the Runge-Kutta method where the particle trajectory is reconstructed iteratively by solving the equation of motions with variable step size. Figure taken from [234].

- For the kick-track procedure the simplifying assumption is made that the track gets deflected at one single point in polar direction at the kick surface that is indicated in figure 3.13. The intersection point of the straight inner track segment extrapolated to the kick surface together with a hit in the META detector provide the angular deflection  $\Delta\Theta$ . By using the simulation software GEANT (see section 3.8.2) the absolute value of the momentum  $|\vec{p}|$  can be calculated for a given total momentum deflection  $\Delta\vec{p}_{tot}$  and angular deflection  $\Delta\Theta$  via equation 3.6. For a more detailed discussion on this procedure see [234].
- The significantly higher momentum resolution is obtained with the spline method. Here the equation of motion is solved at several points in the region between MDC II and III as indicated by the orange dots in figure 3.13. The determined momentum is used later on as initial value for the Runge-Kutta procedure. This method as well as the above mentioned kick-track procedure neglect the penetration of the magnetic field in the region of the inner and outer segments. This approximation of straight track segments is not exact which leads to non-negligible uncertainties in the momentum reconstruction in particular for low momenta and makes a consideration of the more precise Runge-Kutta method necessary. For more details of the spline-method see [234].
- The Runge-Kutta method is a mathematical, multi-step process for an iterative solution of initial value problems and was developed by Carl Runge and Martin Wilhelm Kutta. This method solves numerically the equations of motion for the Lorentz force. Based on the

## 3.6. PARTICLE IDENTIFICATION

momentum determined via the spline-method a next track point can be extrapolated and thus the particle trajectory can be reconstructed recursively. A smaller point-to-point step size results in a more precise track reconstruction, however, at the cost of computation time. This computation takes roughly one third of the fully integrated calculation time for DST production.

In the next step, the recursively determined trajectory is fitted to the measured hit points and the momentum is determined via an optimization procedure which is repeated up to eleven times and provides a  $\chi^2_{\rm RK}$  value. This parameter can later on be used as a requirement for track quality (see section 4.1). The Runge-Kutta method gives a precise reconstruction of the particle trajectory fully considering the presence of the magnetic field throughout the complete detector system. For more details, see [234].

It provides a more realistic description of effects like curly tracks, energy-loss of traversing particles or deflections of tracks in azimuthal direction close to the coils.

In the order specified the computation time for the methods increases but on the other hand results in an improved precision of the momentum reconstruction for a charged particle track.

# 3.6 Particle Identification

Reconstructed particle tracks can be assigned to a certain particle species via different methods. In case of HADES there are two relevant identification procedures for charged particles using either the time-of-flight information or the energy-loss in the drift chambers or both. Particles decaying before reaching the active detector volume can be reconstructed indirectly by identification of their charged decay products.

These identification methods are described in the following.

## **3.6.1 Reconstruction of Charged Particles**

## 3.6.1.1 Identification via Time-of-Flight and Momentum Measurement

For the identification of reconstructed particle tracks the correlation between the two measured observables momentum p and time-of-flight t is used.

The start time of a reaction  $t_0$  is provided by the start detector (see section 2.2.3) whereas one of the META detectors TOF or RPC (see section 2.2.2) gives the second time signal  $t_1$  resulting in the time-of-flight  $\Delta t = t_1 - t_0$  of a particle. Furthermore, the path length s of each particle trajectory is obtained from the track reconstruction via the Runge-Kutta method. The velocity  $\beta$  of a particle can then be determined via

$$\beta = \frac{v}{c} = \frac{\frac{s}{t}}{c} \tag{3.8}$$

as well as the relativistic Lorentz factor

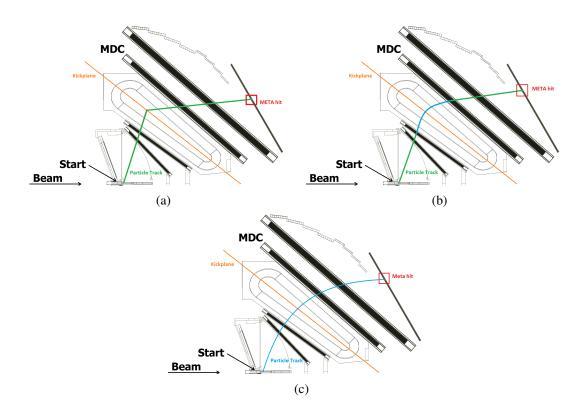


**Figure 3.14:** Schematic view of particle tracks reconstructed with the different methods described in the text. Whereas the kick-plane method (a) assumes a single-point deflection at a virtual plane in the center of the magnetic field, the spline method (b) iteratively reconstructs the curvature of a charged particle in the region between MDC II and III. The most precise reconstruction method is provided by the Runge-Kutta procedure (c) which accounts for the non-negligible intrusion of the magnetic field into the full detector system.

#### 3.6. PARTICLE IDENTIFICATION

$$\gamma = \frac{1}{\sqrt{1 - \beta^2}}.\tag{3.9}$$

As was pointed out in section 3.5.3, the Runge-Kutta method not only provides the path length s but in particular the momentum p of a track. Using 3.8 and 3.9 and by setting equal the lorentz force  $F_L$  and the centrifugal force  $F_Z$  the following relation between the mass-to-charge ratio m/q and the two measured observables velocity  $\beta$  and momentum p of a particle can be deduced:

$$\frac{m}{q} = \frac{p/q}{\beta\gamma c}.$$
(3.10)

Since the error of the time-of-flight measurement  $\Delta t$  for velocities close to the velocity of light c can lead to superluminal velocities ( $\beta > 1$ ), unphysical imaginary masses occur. To avoid this problem the square of the masses is calculated instead:

$$\frac{m^2}{q^2} = \frac{p^2/q^2}{\beta^2 \gamma^2 c^2}.$$
(3.11)

Figure 3.15 shows the characteristic velocity-momentum distribution in RPC (a) and TOF (b). There are clearly pronounced bands visible, indicating the different particle species. Most bands are well separated which is equivalent to a high purity in the particle identification and a low degree of misidentification. The plotted lines show the curves for different particles which are calculated by using equation 3.10. The determination of the graphical selection regions for particle identification is described in the appendix A.

Due to the higher time resolution in the RPC detector the identification has to be treated for both META detectors separately. The resulting mass distribution for charged particles is depicted in figure 3.16 for the RPC detector.

## 3.6.1.2 Identification via Specific Energy-Loss

Another possibility to identify charged particles is via their specific energy loss dE per unit path length dx in a traversed material, which can be measured in the mini-drift chambers MDC as well as in the TOF wall. The technical details of this measurement are described in subsection 2.2.1.

The dependency between the mean energy loss per unit path length  $\langle dE/dx \rangle^{11}$  and the velocity  $\beta$  of the traversing particle is described by the Bethe equation:

$$-\left\langle \frac{dE}{dx} \right\rangle = 4\pi N_A r_e^2 m_e c^2 z^2 \frac{Z}{A} \frac{1}{\beta^2} \left[ \frac{1}{2} ln \left( \frac{2m_e c^2 \beta^2 \gamma^2 T_{\text{max}}}{I^2} \right) - \beta^2 - \frac{\delta}{2} \right]$$
(3.12)

 $<sup>\</sup>frac{1}{11}$  An equivalent expression for energy loss per unit path length is stopping power.

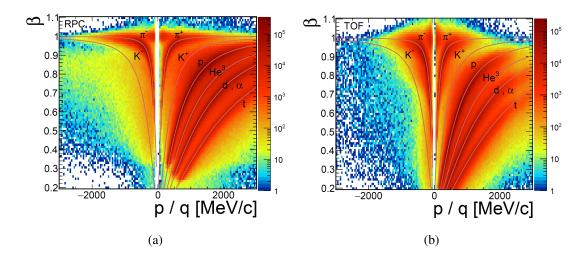


**Figure 3.15:** Velocity  $\beta$  as a function of momentum p over charge q for charged particles in (a) RPC and (b) TOF. Indicated as lines are the theoretically calculated curves for each particle species.

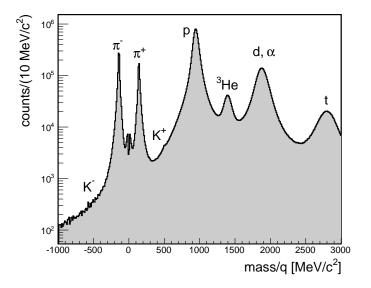


Figure 3.16: Mass spectrum of charged particles normalized to charge q in the RPC detector. Particle species can be identified by selecting a mass window around the expected nominal mass. Figure taken from [37].

## 3.6. PARTICLE IDENTIFICATION

with the variables:

 $N_A$  – Avogadro number = 6.0221415 x 10<sup>23</sup> mol<sup>-1</sup>,

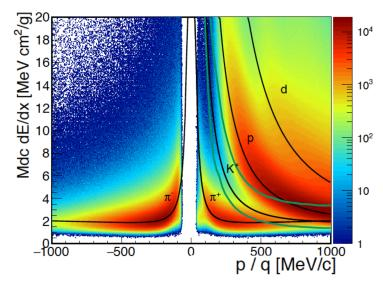
- $r_e$  Classical electron radius = 2.817940325 fm,
- $m_e$  Electron mass = 0.510998918 MeV,
  - z Atomic number of incident particle,
  - Z Atomic number,
  - A Atomic mass of absorber in  $g \text{ mol}^{-1}$ ,
  - I Characteristic ionization constant, depends on material in eV,
  - $\delta$  Density effect correction to ionization energy loss.

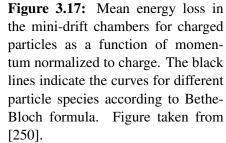
 $T_{\text{max}}$  denotes the maximum kinetic energy that can be transferred to an electron in a single collision and is given by:

$$T_{\rm max} = \frac{2m_e c^2 \beta^2 \gamma^2}{1 + 2\gamma m_e/M + (m_e/M)^2}$$

where M is the incident particle mass.

The energy loss per unit of distance of a particle that traverses a given material is dominated by its velocity  $\beta$ . Figure 3.18 shows the relation between the mean energy loss of a muon traversing copper as a function of its velocity  $\beta\gamma$ . Figure 3.17 shows the energy loss spectrum as a function of the momentum measured by the MDCs. Most prominently visible are the bands of the pions and protons. Indicated as a line are the calculated curves according to equation 3.12.





By applying a graphical two dimensional cut around this curve the corresponding particle species can be identified.

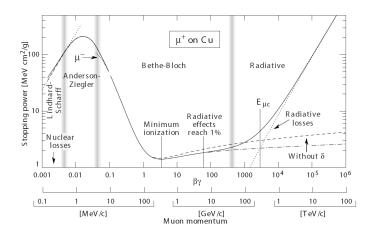


**Figure 3.18:** Stopping power for positive muons in copper as a function of  $\beta \gamma = p/Mc$ presented over nine orders of magnitude. The solid lines indicate the total energy loss per unit path length whereas the vertical bands separate regions of different approximations. The Bethe formula is applicable in the range from  $\beta \gamma \approx 0,04$  to  $\beta \gamma \approx 400$ . Figure taken from [5].

## **3.6.2 Reconstruction of Decayed Particles**

## 3.6.2.1 Invariant Mass

When a particle decays before reaching the detector it can only be reconstructed via its charged decay products, the so called daughter particles. If the daughter particles are identified according to 3.6.1 the masses  $m_1$  and  $m_2$  (and  $m_3...$ ) are set to the nominal value obtained from the PDG<sup>12</sup> [5] in order to avoid a propagation of experimental uncertainties like e.g. the time-of-flight measurement to the invariant mass spectrum. Furthermore, their momenta  $\vec{p}_{1,2}$  as well as the opening angle  $\Delta \theta_{12}$  between the tracks are determined by the Runge-Kutta procedure as described in 3.5.3. The square of the invariant mass  $M_{inv}^2$  is defined as the square of the sum of the decay particles four-momenta:

$$M_{inv}^{2} = (P_{1} + P_{2})^{2}$$
  
=  $(E_{1} + E_{2})^{2} - |\vec{p_{1}} + \vec{p_{2}}|^{2}$   
=  $E_{1}^{2} - |\vec{p_{1}}|^{2} + E_{2}^{2} - |\vec{p_{2}}|^{2} + 2E_{1}E_{2} - 2\vec{p_{1}}\vec{p_{2}}.$ 

By using the relativistic energy–momentum relation<sup>13</sup>, for the invariant mass  $M_{inv}$  of the mother particle follows:

$$M_{\rm inv} = \sqrt{(m_1^2 + m_2^2) + 2 \cdot \left(\sqrt{m_1^2 + (\vec{p}_1 c)^2} \sqrt{m_2^2 + (\vec{p}_2 c)^2} - |\vec{p}_1| |\vec{p}_2| c^2 \cos \theta_{1,2}\right)}.$$
 (3.13)

#### 3.6.2.2 Background estimation

The invariant mass is calculated in order to reconstruct particles decaying into charged particles before reaching the active detector volume. By summing over all combinations of identified

<sup>&</sup>lt;sup>12</sup> Particle Data Group

<sup>&</sup>lt;sup>13</sup>  $E^2 = p^2 c^2 + m^2 c^4$ 

charged particle pairs, an invariant mass spectrum is obtained which contains different contributions.

Consider a decay  $A \rightarrow B + C$ . The two daughter particles B and C may be particles of the same species but opposite electromagnetic charge. The identified particles B and C will show a correlation of their four-momenta in case they originate from the decay of particle A due to momentum and energy conservation. In the invariant mass spectrum these daughter pairs  $(B, C)_{signal}$  will emerge at the expected nominal mass of particle A and form the signal – smeared according to the width of the mother particle and due to a finite resolution of the detector. However, the particles B and C are not necessarily from the same mother particle A but can be uncorrelated which gives an additional contribution  $(B, C)_{uncorr}$  to the invariant mass spectrum. These pairs of uncorrelated particles do not underlie the constraints of energy and momentum conservation of an exclusive final state and hence populate the full phase space starting at a minimal value determined by the sum of their masses  $M_{\rm inv} = m_{\rm B} + m_{\rm C}$ . This contribution to the spectrum is called uncorrelated background. The identified particles B and C may also be correlated, yet classified as background which is referred to as correlated background  $(B, C)_{corr}$ . This occurs e.g. if they originate from a different mother particle which decays into the same final state (compare  $\Lambda$  and  $\Delta^0(1232)$  into  $p + \pi^-$ ) or as in the case of a  $\pi^0$  Dalitz decay, where two pairs of the same species (2 x  $e^+$ - $e^-$ ) originate from the same (grand-)mother ( $\pi^0$ ) but different intermediate particles (photons). For more details on the latter one, see [251]. Yet another contribution to the background comes due to misidentification, i.e. a particle D, representing another particle species, was by mistake identified as one of the daughter particles B or C.

An exact reproduction of the background will ideally leave only the signal contribution behind. There are several ways to model the background, which will be discussed in the following.

## **Sideband Method**

In the so called sideband method well-identified particles B of one species are combined with deliberately wrongly identified particles C of another species. Therefore, regions far aside a selected confidence interval around the expected mass region of particle C are selected which appear as "sidebands" in the spectrum. Since the candidates in these bands are unlikely to be the true particles C, this method will give an estimate on the background contribution to the invariant mass spectrum, however, under the assumption that the background shows a similar, continuous trend in the signal and the sideband region. The precision of this method increases with decreasing width of the signal.

## Like-Sign Method

For the like-sign method one of the daughter particles B or C is exchanged by its charge conjugate. Due to charge conservation these decays of particle A are strongly suppressed or impossible. This method approximates the contribution from uncorrelated background sources under the assumption that the contribution from correlated pairs of the same charge is negligible<sup>14</sup>. A caveat of this method is that the acceptance of the spectrometer for oppositely charged particles

<sup>&</sup>lt;sup>14</sup> Certainly, it is also possible to find pairs of the same electric charge in the final state. One example are decays of I = 3/2 resonances which can decay into two  $\pi^+$ .

is different leading to a distortion of the kinematic distribution compared to true pairs.

#### **Mixed-Event Technique**

Another method to construct the background in the invariant mass spectrum is the mixed-event technique. In this procedure the investigated particles B and C in the final state from different events are combined which are by definition uncorrelated. When the resulting invariant mass distribution (mixed-event spectrum) is subtracted from the one of daughter particles B and C of the same reaction (same-event spectrum), ideally only entries from correlated pairs remain including the desired signal of particle A. Since this technique offers a multitude of permutations exceeding the number of combinations of the like-sign method by far, the amount of statistics that can be obtained with this method are several orders above those of the same event spectrum. Therefore, the spectrum has to be normalized to the same-event spectrum before it can be subtracted. However, tight conditions for the mixing pairs have to be put on the classification of the events in order to guarantee similar kinematic properties. These constraints as well as the systematics of normalizing the spectra are described explicitly in the analysis section 4.2.2.

A crucial condition on the reconstructed background are high statistics in order to avoid the propagation of large uncertainties to the signal. This requirement is in favor of the mixed-event technique, where the statistics of the background can be increased arbitrarily.

## **3.7** Start Time Determination and Recalculation

The start time determination can be improved either by (re-)calibration of the start detector (walk correction, running means [252]) or by a recalculation based on fully reconstructed and identified tracks.

In the latter case the start time is recalculated as follows:

- 1. Particles are identified based on the  $\beta$ -p information (see section 3.6.1.1) and  $\beta$ -dE/dx (see section 3.6.1.2) simultaneously with a higher weight on the first correlation (60:40). A preliminary ID is assigned according to the smallest deviation.
- 2. Based on the identification hypothesis the time-of-flight of a particle is calculated according to  $\Delta t = \frac{s}{\beta c}$ . This gives a deviation to the measured start time of  $\Delta t_0 = \Delta t - t_{0,\text{start}}$ . The mean of this difference  $\langle \Delta t_0 \rangle$  for all particles but the selected one (in order to avoid a possible bias) in the event is calculated.
- 3. The new start time is calculated via  $t_{0,\text{new}} = t_{0,\text{start}} \langle \Delta t_0 \rangle$ .
- 4. The velocity  $\beta$  and mass m can be recalculated with the corrected  $t_{0,\text{new}}$ .

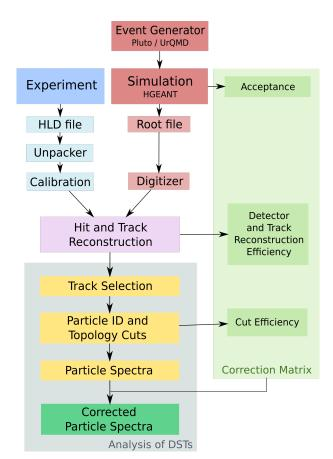
With this procedure the start time resolution can be improved up to  $\Delta t_0 = 31$  ps for most central events [236]. A more detailed description of the method can be found in [242].

## **3.8 Matching Simulation and Data**

A proper Monte Carlo (MC) simulation is an essential probabilistic baseline to complement the measured data and to fill the physical gaps which are either inaccessible by experiment or too complex to be directly calculable. To achieve the ultimate goal of properly correcting measured data for the limited acceptance and efficiency of a detector system a realistic modeling of particle production, kinematics and propagation through the active detector components as well as a precise mimic of their response characteristics is required.

After digitization, i.e. matching detector properties in simulation based on precise calibration of data, the files can be analyzed within the HYDRA framework which was developed for the HADES experiment following exactly the same steps as in the analysis of recorded data from experiment enabling a correction for limited acceptance and efficiency of the detector. The necessary steps are schematically depicted in figure 3.19 showing the analysis flow chart starting from experimental data taking and simulation.

Figure 3.19: Flow chart of the analysis scheme showing the required steps to obtain corrected particle spectra (teal). In order to correct the raw experimental data (blue) for acceptance and efficiency of the spectrometer, simulations (red) have to be used giving correction matrices (green) which are later folded with the raw particle spectra when analyzing the DSTs (yellow). For a proper correction of data, detector responses, i.e. hit and track reconstruction (purple), have to be mimicked in simulation via a digitization process (light red) based on calibrated data (light blue) as accurate as possible.



The approach of matching simulation to experimental data will be sketched in the following sections, starting with an overview of the event generators Pluto and UrQMD as well as GEANT, where the detector response is simulated. Then, crucial observables are discussed, which were found to require deeper investigations in order to achieve a satisfying matching.

## 3.8.1 Event Generators

Event generators are used to model heavy-ion collisions. The final-state particles created in such a Monte Carlo calculation can then be transported through a full detector response simulation (see 3.8.2).

## 3.8.1.1 Pluto

The simulation software Pluto is a Monte-Carlo event generator based on the data analysis software ROOT which was developed at CERN. It contains a multitude of libraries which were implemented in particular for (low-energy) heavy-ion as well as elementary collisions investigated with fixed-target experiments at arbitrarily selectable beam energies. Pluto includes the generation of particles assuming statistical emission from a thermal source or with any angular and momentum distribution as well as particle decays [253].

## 3.8.1.2 UrQMD

In contrast to Pluto, the microscopic transport model UrQMD provides the full space-time evolution of a heavy-ion reaction and is therefore ideally suited as event generator. For more information on UrQMD and transport models in general, see section 1.4.1<sup>15</sup>.

## 3.8.2 Detector Modeling: GEANT

HGeant is a simulation software based on the CERN software Geant 3.21 that can be used to define detector geometries, track particles injected from an event generator through the system<sup>16</sup> and to simulate hits in the active detector modules by modeling the underlying physical processes such as multiple scattering, deflection by magnetic fields or energy-loss in the drift chambers according to the Bethe-Bloch formula. The GCalor simulation package [GCalor] is used in the latest generation of simulated data complementing Geant.

In a next step these hits are digitized. These digitization processes are based on a precise calibration of real data and the properties of each detector system has to be modeled in simulation as accurate as possible in order to mimic the response characteristics of the real detector.

The following sections show the most important calibration procedures which were necessary to achieve a satisfying matching between simulation and experimental data.

## 3.8.3 MDC Time Cuts

For a realistic modeling of the detector performance and efficiencies in simulation contributions from background events, i.e. reactions which are not coming from Au+Au collisions, have to be identified and either excluded from data analysis by a proper event selection, which will be explained in 3.4, or mimicked in simulation.

<sup>&</sup>lt;sup>15</sup> In the used UrQMD version 3.3 deuterons and heavier fragments are not available.

<sup>&</sup>lt;sup>16</sup> In case of the presented analysis the generated particles decay within the HGeant simulation.

#### 3.8. MATCHING SIMULATION AND DATA

The main background sources are:

- Reactions of Au beam ions with other material than the Au target, e.g. beam pipe (Fe/C), target holder (kapton: C/N/O) or the diamond start detector (C).
- Pile-up events i.e. two or more Au+Au collision assigned to the same event.
- $\delta$ -electrons with energies of few MeV which are knocked-out by beam ions mainly from the target.

Besides their irrelevance to the investigated physics case (Au+Au reaction), the particles produced in such background events lead to additional loads in the sub-detector systems resulting in lower hit and in particular reconstruction efficiencies.

Figure 3.20 (a) shows the correlation in MDCI of the measured time-over-threshold  $ToT = t_2 - t_1$  versus  $t_1$ , where  $t_1$  denotes the time of a signal on a wire exceeding a given charge threshold (leading edge) and  $t_2$  the time after the signal falls again below this threshold (trailing edge).

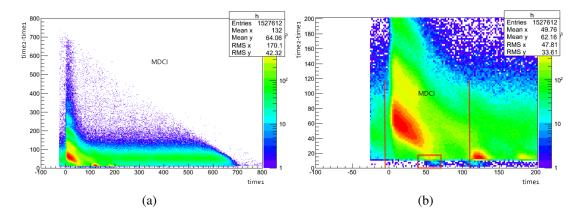
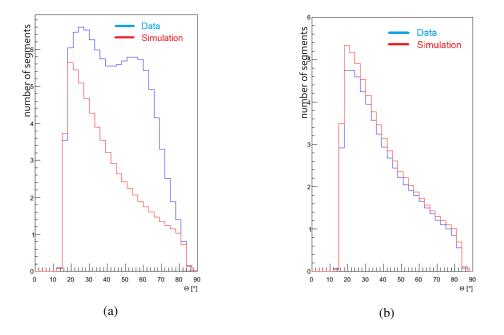


**Figure 3.20:** Time over threshold  $t_2 - t_1$  in inner MDCs before applying a time cut. As can be seen from figure (a), a continuous background contribution is visible over the full range of  $t_1$  (*time1*) for low time-over-thresholds up to 100 ns which can be attributed to  $\delta$ -electrons. The drift time distributions of electrons due to ionization by charged particles in the drift chambers can be precisely determined by Garfield simulations and hence give strong constraints on the allowed drift time window. On closer inspection, the zoom into the drift time region from -100 to 200 ns (b) reveals additional structures which could not be linked to any known systematic. Therefore, negative drift times as well as those above a value of 110 ns (red lines) and as indicated by the red box are excluded from further analysis. Figure taken from [238].

The drift time distributions of electrons due to ionization by charged particles in the drift chambers are well determined from Garfield simulations with precisions below 1% [235] and hence give strong constraints on the window in which drift times are expected in the investigated collision system. The regions outside this window (indicated in figure 3.20 (b) by red lines between  $-5 < t_1 < 110$  ns for MDCI) are excluded from the analysis as well as the region marked

by the box which cannot be reproduced in simulation by any known effect. These contaminating structures are found in all drift chamber planes and removed for analysis. The continuous band reaching time-over-thresholds values up to  $ToT \le 150$  ns appearing over the full range of drift times will be addressed in the following section 3.8.4.

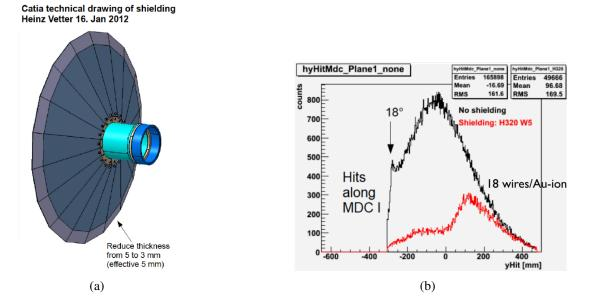
In figure 3.21 the corresponding number of reconstructed wire segments with and without excluding the described drift time regions are plotted showing a reasonable agreement between data and simulation after excluding the unphysical regions from analysis.



**Figure 3.21:** Number of reconstructed segments in MDCI in data (blue) and simulation (red) without (a) and with (b) MDC time cuts. A clear improvement when comparing the number of segments in data and simulation is obtained when the discussed selections on the drift time window are applied. Figure taken from [248].

## **3.8.4** Modeling $\delta$ -electron Contributions in Simulation

Whereas the first two sources of background can be significantly suppressed by an adequate event selection (3.4), the contribution from  $\delta$ -electrons cannot be removed on event basis and hence has to be adapted in simulation to reflect the background in data. To a certain extent these electrons with rather low opening angles can be absorbed by a polypropylen ( $C_3H_3$ ) shield which was installed before the beam time in 2011/12 exactly for this purpose. Figure 3.22 (a) shows a technical drawing of the  $\delta$ -electron shield. The wire hit distribution as obtained from simulation of the innermost drift chamber plane MDCI as a function of the y detector coordinate is plotted in figure 3.22 (b) and shows a significant reduction when the shield is installed in particular at low y corresponding to low polar angles, however, a complete suppression is not achieved. Due to their low energies of only few MeV they mainly affect the inner chambers MDCI+II.



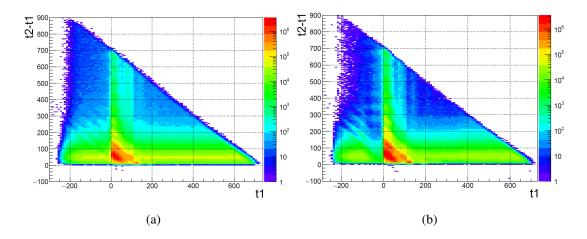
**Figure 3.22:** (a) Technical drawing of the  $\delta$ -electron shield which was installed in 2011/12 behind the target. (b) Simulated hit distribution as a function of y detector coordinate in innermost drift chamber plane MDCI with and without shielding. A clear reduction of the load in the low theta region (corresponding to low y) is obtained when introducing the  $\delta$ -electron shield. Figures taken from [254].

Figure 3.23 (a) shows again the correlation in MDCI of the time-above-threshold  $ToT = t_2 - t_1$  and  $t_1$ . The typically expected drift times in a triggered event in the two inner MDC planes ranges within  $0 < t_1 < 200ns$ . Figure (b) shows the same correlation after applying the event cleaning selection criteria (3.4) where a significant reduction of random correlations outside the triggered region of roughly one order of magnitude can be observed.

However, the cleaning procedure only slightly affects the dominant contribution from  $\delta$ electrons which can be found particularly at low  $T \circ T$  but over the full range of drift times  $t_1$ since these electrons are knocked-out independent of whether a Au+Au reaction takes place or not<sup>17</sup>. In order to account for this contamination, the contribution from  $\delta$ -electrons has to be modeled in the RICH and MDC digitizer in simulation in agreement with experimental data. In figure 3.24 (a) the loads in the MDCI sectors are presented showing a non-uniform distribution with respect to the azimuthal angle. The lower hit occupancy in sectors 2 and 5 can be related to the different material used in the RICH detector where in these two sectors the carbon mirrors were replaced by glass which has higher ( $\delta$ -)electron absorption rates.

The amount of  $\delta$ -electron is implemented iteratively to reproduce the hit distribution in the MDCs in a time region  $t_1 < 0$  ns which is chosen in order to exclude a correlation with the triggered event. In the RICH digitizer higher energy thresholds are set for the RICH sectors

<sup>&</sup>lt;sup>17</sup> A coincidence measurement of start and veto within the MDC measuring range (up to  $\approx 350$  ns) could be an access to remove further background events involving  $\delta$ -electrons. This, on the other hand, rejects also a large amount of Au+Au reactions reducing the total data set by additionally  $\approx 50\%$  [238].



**Figure 3.23:** Time over threshold  $t_2 - t_1$  as a function of drift time  $t_1$  in the innermost drift chamber MDCI before and after event cleaning according to 3.4. A significant reduction (one order of magnitude) of uncorrelated background is obtained when the event selection is applied. However, a high contribution from  $\delta$ -electrons emerging as constant band over the full drift time  $t_1$  range cannot be rejected and has to be modeled in a GEANT simulation. Figure taken from [238].

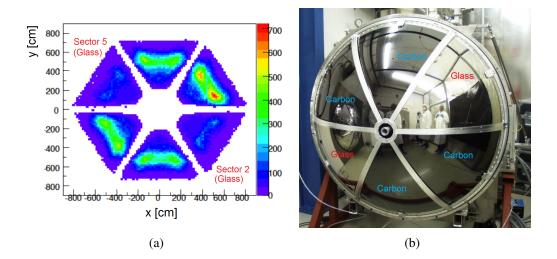


**Figure 3.24:** (a) MDCI hit distribution in the six sectors. The non-uniform distribution with respect to the azimuthal angle can be traced down to different materials used for the RICH sectors (b). The glass mirrors in the RICH detector used for sector 2 and 5 absorb more ( $\delta$ -)electrons resulting in different loads in the drift chambers. Figures taken from [248].

## 3.8. MATCHING SIMULATION AND DATA

with glass mirrors ( $E_{\delta}(SiO_4) > 4.5$  MeV) compared to those with carbon mirrors ( $E_{\delta}(C) > 2$  MeV) to account for different loads in the drift chambers. Figure 3.25 shows the improvement of matching efficiency of an MDCI layer (layer 4) in data and simulation before and after modeling the  $\delta$ -electron contribution.

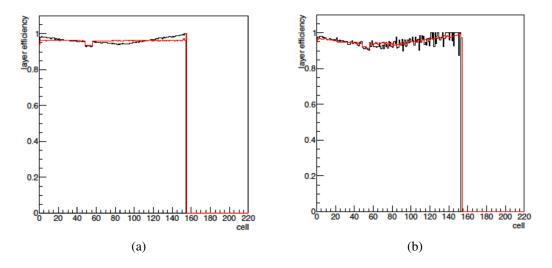


**Figure 3.25:** Comparison between data (black) and simulation (red) of wire efficiency as a function of cell number for layer 4 in MDCI before (a) and after (b) modeling  $\delta$ -electron contribution. Figures taken from [248].

The re-calibration of the specific energy loss measurement was also found to be essential and has been performed and described in detail within the investigations in [37].

# **Chapter 4 Reconstruction of** $K_s^0$ , $\Lambda$ and $\Xi^-$

The decay of strange particles through the weak interaction appears at rather long timescales thus allowing to distinguish their decay vertex (*secondary vertex*) from the primary one. This enables an analysis based on constraints (*cuts*) on their decay topology in order to significantly suppress combinatorial background in the invariant mass spectrum and hence to reduce the uncertainty on the extracted signal counts. The strange hadrons  $\Lambda$ ,  $K_s^0$  and  $\Xi^-$  investigated in this analysis can be reconstructed via their charged decay products which traverse the active HADES detector volume.

This chapter is structured as follows: Starting with the selected 0 - 40% most central events  $N_{\text{evts}} = 2.12 \times 10^9$ , a user-based track selection is made based on track quality parameters (4.1). For the reconstruction of the weakly decayed strange hadrons, their charged decay products have to be identified first (4.2.1), before the invariant mass spectrum can be calculated which is the starting point for the pair analysis (4.2.2). While more details on the investigation on single track properties can be found in [37], a strong focus is put on the decay topology of reconstructed off-vertex tracks. The section contains detailed investigations on the decay kinematics, background determination and suppression as well as a multi-differential analysis in terms of reduced transverse mass  $m_t - m_0$ , rapidity y and centrality C. The raw particle spectra have to be corrected for detector acceptance and efficiency in order to obtain their full production yields for which the Pluto software is used as event generator as well as a GEANT simulation to model a realistic detector response (4.3). The resulting corrected particle spectra are presented in the next chapter 5. The attempts to reconstruct the doubly-strange  $\Xi^-$  hyperon will be presented separately in the last section 4.4 of this chapter.

## 4.1 Track Selection

Starting point for the following discussion are the 0 - 40% most central events  $N_{\text{evts}} = 2.12 \text{ x} 10^9$ , which were selected according to a careful event cleaning procedure as presented in section 3.4.2. Each of these events contains reconstructed track candidates most of which share at least one track component. In order to sort out ambiguous tracks, a selection process based on a track quality parameters has to be undertaken.

In the case of hadron reconstruction, a particle track consists of an inner and an outer track segment as well as a hit in one of the META detectors<sup>1</sup>.

First, in order to guarantee a successful correction of data for acceptance and efficiency of the spectrometer, the distributions for each of the corresponding track components are compared to those in simulation.

Figure 4.1 shows the META hit distributions in the TOF (a) and RPC (b) detector for data (black) and simulation (red). Within the selected events, an average multiplicity in data of 38 and 88 is observed in TOF and RPC reaching up to 120 and 280 hits, respectively, indicating the significant difference in track densities for low compared high polar angles. A reasonable agreement between data and simulation is observed except in the high multiplicity tails, which cannot be reproduced in simulation. However, being 4-5 orders below the mean hit multiplicity, this deviation can be neglected. Figure 4.1 (c) displays the hit multiplicity distribution of RPC and TOF combined showing a good agreement between data and simulation.

Figure 4.2 shows the distribution for the number of reconstructed inner (a) and outer (b) track segments per event for data (black) and simulation (red). Both, the number of inner as well as outer segments can reach up to 600 per event with an average of 82. The simulation reproduces the shape of the distribution for data up to roughly 150 segments per event, however, fails at the high tails, leading to a roughly 15% lower mean value.

The track densities in the Au+Au collision system may lead to a large number of combinations for these three components which cannot always be combined to give a unique track. The four possibilities of ambiguously assigning these elements to the same track are sketched in figure 4.3. For one inner segment either multiple outer segments each with a unique (A) or a shared META hit (B) may be combined. Furthermore, a unique combination of inner and outer segment may not be unambiguously assigned to one META hit (C) or multiple unique tracks share a hit in one of the META detectors (D)<sup>2</sup>.

As can be easily understood, a strong dependence is observed of the number of shared components with centrality of a reaction. As can be seen from figure 4.4, for most central collisions, where the highest track densities occur, 40% of tracks share at least one inner (a), 31% an outer (b) and 35% a META hit (c). The probability of having ambiguous tracks in semi-peripheral events is lower, namely 19%, 19% and 13%, in the same order specified. In both cases, the number of shared segments and hits are rather well reproduced in simulation, however, slightly better in semi-peripheral collisions.

In the further course of analysis only unique tracks are used which do not share any MDC segment or META hit. Therefore, they have to be sorted qualitatively in order to make a decision which tracks will be rejected in case of ambiguities. The following quality parameters for a track or its components are available:

- $\chi^2_{\text{inner}}$ : Fit of inner segment to fired cells in MDC I and II (see 3.5.1.4).
- $\chi^2_{\text{outer}}$ : Fit of outer segment to fired cells in MDC III and IV (see 3.5.1.4).

<sup>&</sup>lt;sup>1</sup> The RICH information is only required in the dilepton analysis.

<sup>&</sup>lt;sup>2</sup> A combination of multiple inner with the same outer segment is not allowed.

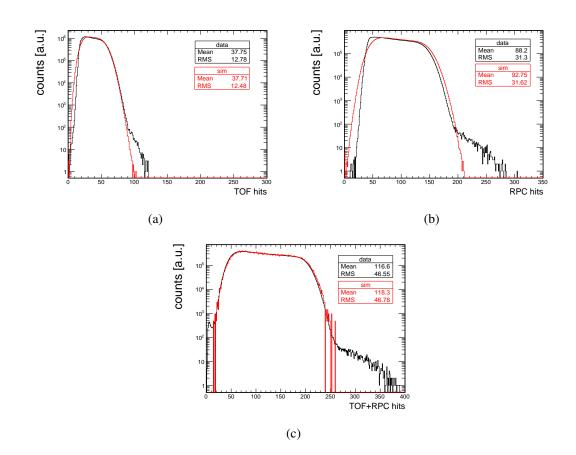


**Figure 4.1:** Hit multiplicity distributions separately in TOF (a) and RPC (b) in data (black) and simulation (red) for 0-40% most central collisions. The distributions in simulation are normalized to the number of entries in data to allow for a better comparison of the shape. The high multiplicity tails are not reproduced in simulation. A small discrepancy between data and simulation for low multiplicity events is observed in both cases. (c) Combined RPC and TOF multiplicity distribution indicating a good agreement between data and simulation.

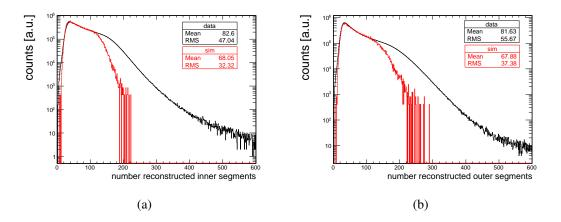


**Figure 4.2:** Number of inner (a) and outer (b) track segments per event for data (black) and simulation (red). The distributions in simulation are normalized to the number of entries in data to allow for a better comparison of the shape. Simulation reproduces the shape of the distribution for data in the region of most probable values, yet, misses the high tails.

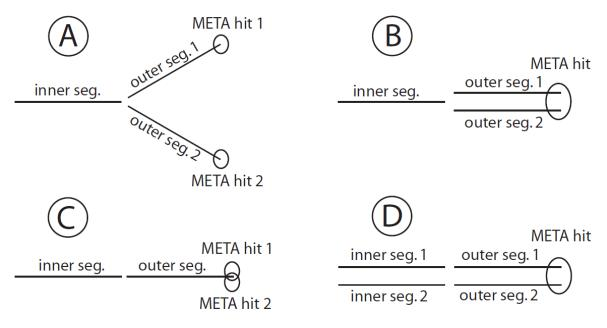


**Figure 4.3:** In case of the hadron analysis, in leading order four individual combinations to ambiguously assign the three track components inner/outer segment and META hit are possible. For each scenario, not only two but multiple ambiguous assignments may occur as well as combinations of these.

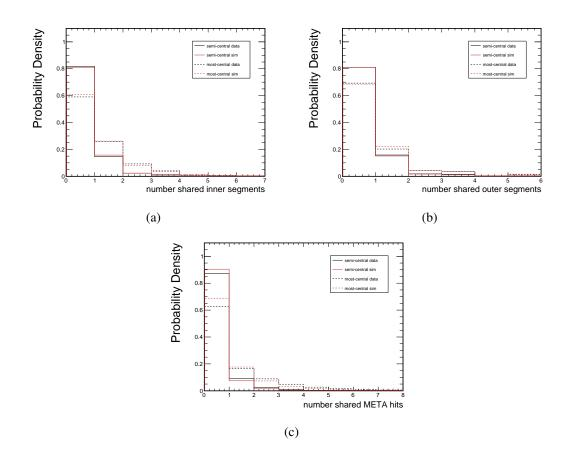


**Figure 4.4:** Probability density distributions of shared inner (a) and outer (b) segments as well as META hits (c) for track candidates for most central (dashed) and semi-peripheral (full) compared for data (black) and simulation (red). In most central collisions the probability of sharing an inner segment is about 40%, an outer segment 31% and a META hit 35%. The probability of having ambiguous tracks in semi-peripheral events is less, namely 19%, 19% and 13% in the same order specified. Simulation reproduces this behavior rather well, however, better in semi-central than in most central collisions.

- $\chi^2_{\rm RK}$ : Fit of reconstructed track to hit points (see 3.5.3).
- $\chi^2_{\rm MM}$ : Deviation of reconstructed track from META hit (see 3.5.2).

In the presented analysis all tracks from one event are sorted according to their Runge-Kutta matching quality  $\chi^2_{RK}$ . The track with the best quality is selected and the contained components are excluded for the next-best choice and so on, leading systematically to a set of unique tracks not sharing any track element.

Figure 4.5 shows again the number of shared components, now for selected track candidates according the described selection. The probability of sharing at least one inner segment (a) is reduced to 30%, for an outer segment (b) to 27% and for a META hit (c) to 26% in most central events. This implies, that the rejected tracks share on average more track components, than the tracks selected according the above described criterion.

The impact of a selection based on the described criterion is shown in figure 4.6 (a), which compares the mass spectrum for tracks passing this procedure (black) to the one for rejected tracks (blue). The mass spectrum for the selected tracks shows a significantly better mass resolution compared to the one based on the rejected tracks, where even protons and pions are barely visible. Figure 4.6 (b) shows a comparison between the same mass spectrum for the used tracks, now compared to simulation (red), showing a reasonable agreement<sup>3</sup>.

A discrepancy between data and simulation was found at the geometrical edges of the drift chambers leading to a sharp efficiency drop, as indicated in figure 4.7. Shown is the ratio of data and simulation in x-y coordinates of the intersection point of a reconstructed inner track segment with the two 40° layers of each drift chamber plane (upper left MDCI to lower right MDC IV). An enhancement of reconstructed tracks in data compared to simulation is observed in these areas, indicated by values well below unity. Therefore, a fiducial volume was selected, indicated by the boxes, such that only the regions inside the inner box are included in further analysis resulting on average in a better track quality.

The following list summarizes all constraints on the track selection applied in this hadron analysis:

- 1. A full track consists of an inner and an outer segment as well as a hit in one of the META detectors. These components cannot be shared by any other track within the event<sup>4</sup>.
- 2. Sector 2 (240° <  $\phi$  < 300°) is excluded<sup>5</sup> due to observed instabilities as discussed in section 3.3.
- 3. A fiducial volume accounting for the limited acceptance at the edges of the drift chamber sectors is selected<sup>6</sup>.

<sup>&</sup>lt;sup>3</sup> The discrepancy in the region particularly above the proton peak is because UrQMD does not contain any light nuclei such as deuterons or <sup>3</sup>He.

<sup>&</sup>lt;sup>4</sup> Used components will be marked with the flag *kIsUsed*.

<sup>&</sup>lt;sup>5</sup> getSector()==2

<sup>&</sup>lt;sup>6</sup> The tracks are marked with the flag *isAtAnyEdge*.

## 4.1. TRACK SELECTION

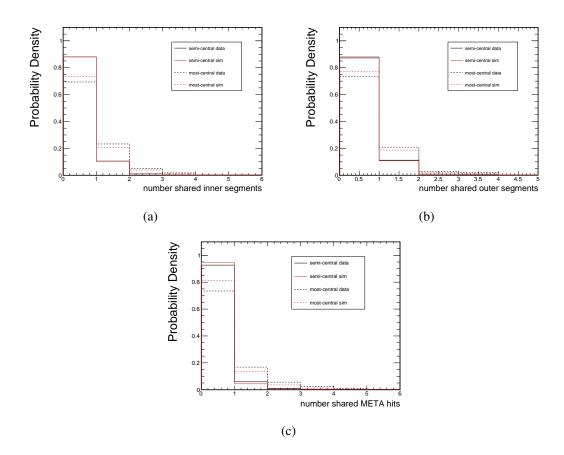


**Figure 4.5:** Probability density distributions of shared inner (a) and outer (b) segments as well as META hits (c) for selected track candidates (*kIsUsed*) for most central (dashed) and semi-peripheral (full) compared for data (black) and simulation (red). Compared to all track candidates (figure 4.4), the remaining tracks share less components. In most central collisions the probability of sharing an inner segment is about 30%, an outer segment 27% and a META hit 26%. The probability of having ambiguous tracks in semi-peripheral events is less, namely 12%, 13% and 10% in the same order specified. Simulation reproduces this behavior rather well, however, better in semi-central than in most central collisions.

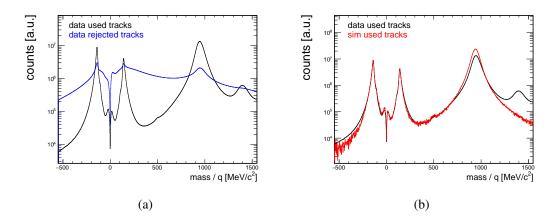
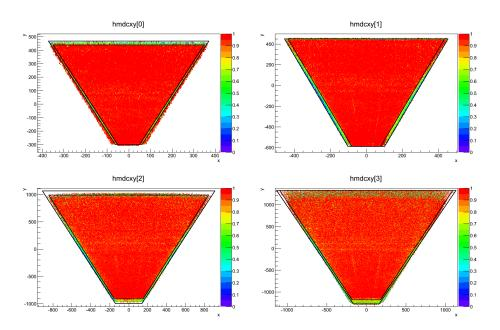


Figure 4.6: (a) Mass distribution of selected (black) and rejected (blue) track candidates according to the criteria described in the text. (b) Mass distribution of selected track candidates in data (black) and simulation (red). The distribution obtained from simulation is normalized to the data integral in the region around the positive pion mass (100 < m/q < 200).



**Figure 4.7:** Ratio of simulation to data in x-y coordinates of the intersection point of a reconstructed inner track segment with the two 40° layers of each drift chamber plane (upper left MDCI to lower right MDC IV). An enhancement of reconstructed tracks in data compared to simulation is observed in these areas, indicated by values well below unity. Therefore, a fiducial volume was selected, indicated by the boxes, such that only the regions inside the inner box are included in further analysis resulting on average in a better track quality. Plot taken from [238].

#### 4.1. TRACK SELECTION

- 4. The track is matched to META hits in absolute dx-dy values of the rods of TOF, respectively cells of RPC (4 mm in dy and  $3\sigma$  in dx, see section 3.5.2).
- 5. The  $\chi^2_{\text{inner}}$  minimization of the inner segment converged and hence has to be greater than zero.
- 6. A successful momentum reconstruction according to the Runge-Kutta procedure is required ( $\chi^2_{\rm RK} > 0$ ). Furthermore, a rough cut on the track quality is applied  $\chi^2_{\rm RK} < 1000$ . Figure 4.8 shows a comparison of the Runge-Kutta  $\chi^2$  distribution for data and simulation indicating a systematic difference. A tight cut on this quality parameter should hence be avoided in analysis.
- 7. A track is required to have a calculated velocity greater than zero ( $\beta > 0^7$ ) and a time-of-flight smaller than 60 ns.

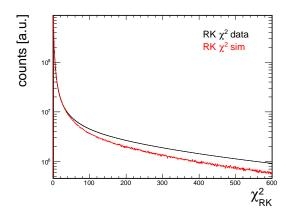


**Figure 4.8:** Runge-Kutta  $\chi^2$  distribution for charged particles in data (black) and simulation (red). A systematic deviation for the  $\chi^2$  distribution between data and simulation is observed, hence tight constraints on this quality parameter have to be avoided.

The weak selections 5-7 are applied rather to exclude unphysical tracks due to a wrong termination in the track segment reconstruction,  $\chi^2$  minimization or matching algorithms.

Figure 4.9 shows the number of track candidates before (a) and after all the previously mentioned selections (b) were applied for data (black) and simulation (red) leading to a significant reduction of available tracks after the full selection. Regarding the mean of the distribution, there are 45 tracks reaching multiplicities up to 110 per event. A fair agreement is observed when comparing to simulation where a mean track multiplicity of 48 is obtained. Figure 4.9 (c) shows the multiplicity distribution for tracks with a minimum distance of closest approach of 5 mm with respect to the primary vertex. All tracks, which will be selected in the further course of analysis, fulfill this requirement due to the characteristic decay topology of the investigated strange hadrons. Except for the high multiplicity tail being 4-6 orders below the mean rates, the distribution is well reproduced in simulation.

<sup>&</sup>lt;sup>7</sup> The velocity  $\beta$  is set to -1 for erroneous time-of-flight measurements  $\Delta t < 0$ .

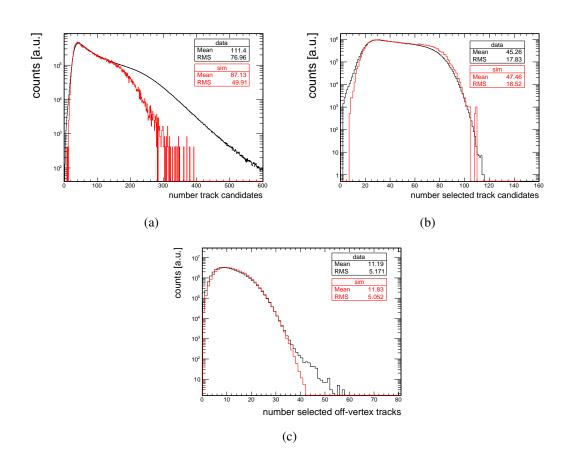


**Figure 4.9:** Track candidate distribution in data (black) and simulation (red) before (a) and after (b) all listed track selection criteria. The difference is mainly induced by rejecting tracks sharing at least one of the three track components in hadron analysis (*kIsUsed*). The decision which tracks are excluded is based on their Runge-Kutta matching quality  $\chi^2_{\rm RK}$ . (c) Track candidate distribution for tracks with a minimum distance of closest approach of 5 mm to the primary vertex. A reasonable agreement is observed.

# 4.2 **Reconstruction of Weakly Decaying Hadrons**

The strange hadrons under investigation are the singly-strange  $\Lambda$  hyperon and  $K_s^0$  meson as well as the much rarer produced doubly-strange  $\Xi^-$  baryon<sup>8</sup>. Some of their characteristics are summarized in table 4.1.

Considering the fact that these three particle species decay via the weak interaction their mean lifetimes are sufficiently high, such that a large fraction decays well outside the primary vertex region enabling an analysis based on geometrical selections on their decay topology. Most of them decay before reaching the first drift chamber plane allowing to track their charged decay products in the detector which is necessary for their reconstruction<sup>9</sup>.

The next section of this chapter describes the identification process of the decay products, which is common for all three strange particles, followed by the reconstruction of  $\Lambda$  and  $K_s^0$ . The investigation on the much less abundant  $\Xi^-$  hyperon will be presented separately in section 4.4.

	Λ	$K_s^0$	[ <u>+</u> ]
Composition	$ uds\rangle$	$\left  d \bar{s} \right\rangle + \left  \bar{d} s \right\rangle / \sqrt{2}$	$ dss\rangle$
Mass [MeV/c <sup>2</sup> ]	1115.68	497.65	1321.71
<i>cτ</i> [cm]	7.89	2.68	4.91
$\sqrt{s_{ m exc}}$ [GeV]	-0.14	-0.14	-0.84
Final State	$p+\pi^-$	$\pi^+ + \pi^-$	$p$ + $\pi^-$ + $\pi^-$
Corresponding BR [%]	63.9	69.2	63.9

**Table 4.1:** Overview of properties of  $\Lambda$ ,  $K_s^0$  and  $\Xi^-$ . Listed are quark composition, mass, mean decay length  $c\tau$ , excess energy  $\sqrt{s_{\text{exc}}} = \sqrt{s_{\text{Beam}}} - \sqrt{s_{\text{NN}}}$ , decay particles occurring in the investigated final state and the corresponding branching ratio for this channel.

## 4.2.1 Single Particle Identification

The three investigated hadrons are identified by calculating the invariant mass of their charged decay products which have to be identified first. As can be read of table 4.1, only three different particle species occur in their final states: positive pions  $\pi^+$ , negative pions  $\pi^-$  and protons p.

<sup>&</sup>lt;sup>8</sup> For historical reasons the  $\Xi^-$  baryon is also called 'Cascade' due to its cascade-like decay topology.

<sup>&</sup>lt;sup>9</sup> For the longest living of the three investigated hadrons, the  $\Lambda$  hyperon, roughly one out of 100 million reach MDCI (minimum distance from last target segment to chamber  $d_{\min} \approx 40$  cm) assuming an average momentum of p = 1500 MeV/c.

In contrast to the analysis of charged particles emitted from the primary reaction vertex, in the presented secondary vertex analysis the decay products are identified via a selection on their mass instead of using the correlation between beta and momentum as described in 3.6.1.1. The reconstructed momentum and hence the calculated velocity of charged particles are determined under the assumption that the production occurs in the target. As this is not the case for particles originating from a weak decay of a massive hadron, the velocity is underestimated and hence the reconstructed mass shifted towards higher values. By calculating the path length of the mother particle this effect can be corrected for. However, in order to avoid a bias which was observed when using the beta-momentum correlation for particle identification, only moderate selections on the particle mass are applied. This results in an enhancement of uncorrelated background due to misidentification but can be compensated by a well controlled background determination and suppression, see 4.2.2.

The procedure determining the graphical cuts as a function of velocity  $\beta$  and momentum p can be found in the appendix A.

### **Pion Identification**

The pion is the second-most abundant hadron occurring in heavy-ion collisions at SIS energies. There exist three different isospin states:  $\pi^+(u\bar{d})$ ,  $\pi^-(\bar{u}d)$  and  $\pi^0(\frac{1}{\sqrt{2}}(u\bar{u} - d\bar{d}))$ . With a mass of 139.57 MeV/c<sup>2</sup> and 134.98 MeV/c<sup>2</sup> respectively the charged and the neutral pions are the lightest of all hadrons. The  $\pi^{\pm}$  mesons decay with a branching ratio of BR = 99.99% into a  $\mu^{\pm}-\nu_{\mu}$  pair but due to their relatively long mean decay length of  $c\tau = 7.8$  m the majority is directly measurable in the HADES drift chambers.

Figure 4.10 shows the mass times charge distribution for all charged particles in the mass region where (a) negative and (b) positive pions are expected for data (black) and simulation (yellow) which show a reasonable agreement. In the following analysis, pions are selected in a mass window  $0 < |m| < 300 \text{ MeV/c}^2$ , indicated by the arrows, where the rate has already dropped by 2 - 3 orders with respect to the maximum of the distribution. Furthermore, loose cuts on the track quality parameters  $\chi^2_{\text{RK}} < 400$  and  $\chi^2_{\text{MM}} < 3$  are applied.

### **Proton Identification**

Heavy-ion collisions at SIS energies are baryon-dominated. The most abundant charged particle is the proton  $p(|uud\rangle)$  which is the lightest baryon with a mass of  $m = 938.27 \text{ MeV/c}^2$ . At these energies protons are not produced in the collision process but originate from the target and beam ions<sup>10</sup>.

Figure 4.11 shows the mass times charge distribution of protons for data (black) and simulation (yellow). The lines indicate the selection region of  $700 < m < 1200 \text{ MeV/c}^2$ . The light nuclei with the next-higher mass-to-charge ratio is He<sup>3</sup> ( $\approx 1410 \text{ MeV/c}^2$ ) whose signal is also visible in the same figure on the right side of the proton peak. The light nuclei will give a significant background contribution deteriorating the purity of proton identification. Since UrQMD does not contain deuterons or other nuclei a rather moderate agreement is observed and the background to the proton signal cannot be reproduced in simulation. In order to test a possible bias

<sup>&</sup>lt;sup>10</sup> A direct production would require an anti-proton, i.e.  $pp \rightarrow ppp\bar{p}$ , which is rather expensive in terms of energy.

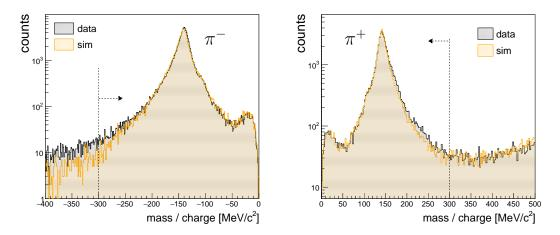


**Figure 4.10:** Mass over charge distribution from -400 to  $0 \text{ MeV/c}^2$  (left) and 0 to  $500 \text{ MeV/c}^2$  (right) for charged particles from experimental data (black) and simulation (yellow). The distribution from simulation is normalized to the integral of the distribution in data. A dominant peak is observed at the expected mass ( $139.57 \text{ MeV/c}^2$ ) for negative and positive pions. The dashed lines indicate the position where the mass cut is applied. Furthermore, in both cases the mass is required to be greater than zero. The small contamination from dielectrons was found to be negligible in the secondary vertex analysis.

on the acceptance and efficiency correction, the mass window is widened to 600 < m < 1300 MeV/c<sup>2</sup>. Furthermore, loose cuts on the track quality parameters  $\chi^2_{\rm RK} < 400$  and  $\chi^2_{\rm MM} < 3$  are applied. Details on the systematic investigations on particle identification are presented when discussing the results in chapter 5. Table 4.2 summarizes the applied cuts on the mass spectra as well as on track quality parameters for the identification of pions and protons.

	$\pi^{\pm}$	p
mass [MeV/c <sup>2</sup> ]	0 < m < 300	700 < m < 1200
momentum [MeV/c]	$0$	$0$
$\chi^2_{ m RK}$	< 400	< 400
$\chi^2_{ m MM}$	< 3	< 3

**Table 4.2:** Overview of selections used for identification of charged particles from which the strange hadrons  $\Lambda$ ,  $K_s^0$  and  $\Xi^-$  are reconstructed.

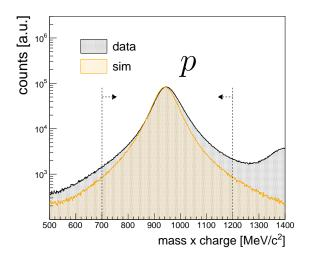


**Figure 4.11:** Mass over charge spectra from 500 to 1400 MeV/ $c^2$  for experimental data (black) and simulation (yellow). The distribution from simulation is normalized to the integral of the spectrum in data. A dominant peak is observed at the expected mass of the proton (938.27 MeV/ $c^2$ ). The dashed lines indicate the position where the mass cuts are applied. Due to the absence of deuterons and other nuclei in UrQMD, the distribution in simulation is not reproducing experimental data.

### 4.2.2 Pair Analysis

### 4.2.2.1 Decay Topology

As discussed in section 3.6.2.1, the invariant mass can be calculated from the four-momenta of the daughter tracks and thus depends on their three-momenta, opening angle and masses<sup>11</sup>. Figure 4.12 shows the invariant mass spectra for p- $\pi^-$  (a) and  $\pi^+$ - $\pi^-$  (b) pairs.

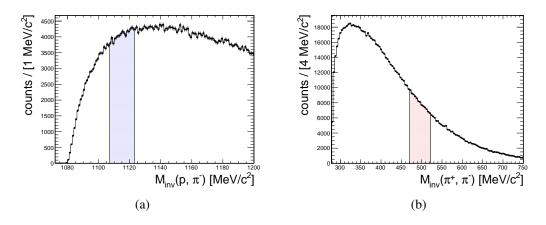


**Figure 4.12:** Invariant mass spectra of  $p - \pi^-$  (a) and  $\pi^+ - \pi^-$  (b) without applying any topology cuts. The colored area indicates the expected signal region estimated in a  $2\sigma$  region around the nominal mass value taken from the PDG [5] as listed in table 4.1. The widths are based on the expected detector resolution as obtained from simulation:  $\sigma_{\Lambda} \approx 2.5 \text{ MeV/c}^2$  and  $\sigma_{K_s^0} \approx 8 \text{ MeV/c}^2$ , see figures A.6 in the appendix A.

<sup>&</sup>lt;sup>11</sup> The masses of identified particles are set to their nominal value in order to avoid a propagation of the uncertainty of the mass.

In order to reduce the contribution of uncorrelated pairs to the invariant mass spectrum topological selections are applied. These selections put constraints on the decay topology of the weakly decaying hadrons and are intended to sort out uncorrelated rather than correlated pair candidates which will improve the signal-to-background ratio. The subsequently listed parameters are constrained in the further analysis. For illustration the decay topology is sketched in figure 4.13 exemplarily for the  $\Lambda$  hyperon decay:

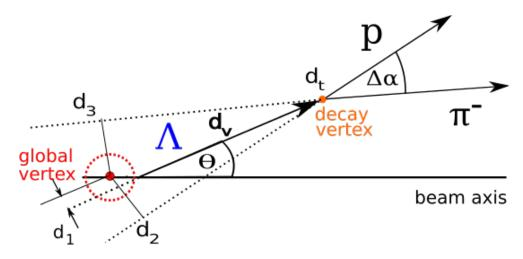


**Figure 4.13:** Two-dimensional sketch of the  $\Lambda$  hyperon decay topology. The  $\Lambda$  track is reconstructed via the charged decay products p and  $\pi^-$ . The decay vertex is determined from their distance of closest approach (DCA). Several requirements can be set in order to suppress contributions from uncorrelated daughter pairs: distance between primary and secondary vertex  $(d_v)$ , distance of the primary vertex and the proton and pion respectively  $(d_{2,3})$ , DCA between daughter tracks  $(d_t)$ , DCA of the mother trajectory to the primary vertex  $(d_1)$ . In addition, a minimum opening angle cut is applied  $(\Delta \alpha)$ .

- $d_v$ : Lower limit on the distance of primary vertex to the decay vertex of the mother particle. By applying this selection criterion the relatively long lifetimes of the particles decaying via the weak interaction are taken into account and hence a decay outside the primary reaction vertex is guaranteed. Only if this "off-vertex" condition is precedent, it is reasonable to relate the following requirements to the decay topology of a weakly decaying hadron.
- $d_1$ : Upper limit on the distance of closest approach (DCA) of the mother track to the primary vertex of the collision. This constraint guarantees that the reconstructed mother particle is pointing to the reaction vertex where it is assumed to be emitted from.
- $d_t$ : Upper limit on the minimum distance between the two decay particles. The daughters have a common vertex if they originate from the same decay.
- $d_2$  and  $d_3$ : Lower limit on the distance between the primary vertex and the track of the respective daughter particle extrapolated back to the target. Since the two daughter particles are emitted under a certain opening angle  $\Delta \alpha$  (Q-value, see 4.2.2.2) their tracks are pointing away from the primary vertex ("off-vertex" tracks).

- $\Delta \alpha$ : Minimum value for the opening angle of the two daughters. This limitation sorts out close pairs which cannot be resolved in the first drift chambers. This requirement is important for the matching quality of the background determined via the mixed-event procedure, which will be discussed in section 4.2.2.3.
- $z_{\text{decay}} > z_{\text{prim}}$ : In a fixed-target experiment the decay vertex of a particle has to be located downstream in the hemisphere behind the target. z denotes the beam axis coordinate.<sup>12</sup>

The topology parameters are strongly correlated which can be understood intuitively from the sketch of the decay topology in figure 4.13. As an example, figure 4.14 shows the modification of the  $d_v$  distribution – the minimum distance of primary to secondary vertex – with and without applying the remaining cuts as listed in table 4.3 as they will be used later on in the analysis. A way to access a first estimation of the cut values will be explained in section 4.2.2.4.

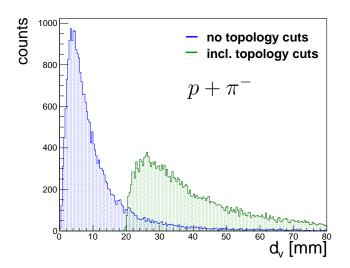


**Figure 4.14:**  $d_v$  distribution with (green) and without (blue) topology cuts applied for  $p + \pi^-$  pairs. The cuts on the remaining parameters are taken from table 4.3.

### **4.2.2.2** Characteristics of Decay Kinematics: $\Lambda$ vs. $K_s^0$

In the investigated Au+Au collision system the most abundant particles are protons which are, with a multiplicity of  $\approx 100$ , roughly a factor 10 more abundant than negative pions. As a consequence, the combinatorial background in the invariant mass distribution of  $\Lambda$  candidates is significantly higher than in the reconstruction of neutral kaons  $K_s^{0\ 13}$ . Hence, in order to obtain a similar signal-to-background ratio, stronger constraints on the decay kinematics are required in the  $\Lambda$  relative to the  $K_s^0$  analysis resulting in lower topology cut efficiencies.

<sup>&</sup>lt;sup>12</sup> Tracks are reconstructed as vectors which are infinitely extended in space. The decay vertex is defined via the intersection point of the two daughter tracks. So technically this vertex can be calculated to be in front of the target ( $z_{\text{decay}} < z_{\text{prim}}$ ).

<sup>&</sup>lt;sup>13</sup> This results on average in a factor 10 higher combinatorics for  $\Lambda$  (100 times 10 combinations) than  $K_s^0$  (10 times 10).

The decay of the  $\Lambda$  hyperon and the  $K_s^0$  meson share qualitatively the same topology. However, the kinematics differ in few details resulting in quantitatively different treatments.

The mean decay length  $c\tau$  of neutral kaons is approximately a factor 3 smaller than for the  $\Lambda$  hyperon (see table 4.1). This property is straightly reflected in the mean value of parameter  $d_v$  which has direct impact on  $d_2$  and  $d_3$ .

One major difference is the Q-value of the two decays<sup>14</sup>. If the sum of the rest masses of the daughters decreases, there is more kinetic energy available to be distributed to the daughter hadrons, leading to larger opening angles on average among them, which is directly correlated with  $d_2$  and  $d_3$  as can be easily understood from figure 4.13. The Q-values for the investigated decays are

$$Q(\Lambda \to \pi^- p) = 38.7 \,\mathrm{MeV}$$

and

 $Q(K_s^0 \to \pi^- \pi^+) = 218.3 \text{ MeV}.$ 

Thus, on average the opening angle between the pion daughters from the  $K_s^0$  decay will be larger which is depicted in figure 4.15 (a) comparing the opening angle distributions for the daughter particles from the investigated  $\Lambda$  and  $K_s^0$  decay channels as obtained from MC simulations. The mean of the broader distribution for decays of  $K_s^0$  mesons is significantly above the one for  $\Lambda$  hyperons which has severe impact on the decay vertex resolution. For illustration, the impact of the opening angle on the decay vertex resolution is sketched in figure 4.16. The decay vertex is calculated as the intersection point of the reconstructed charged tracks. Since the tracks have a limited resolution this intersection point can be considered to be an overlap area which variates in size depending on their opening angle. From this considerations, the decay vertex resolution of the  $K_s^0$  mesons is expected to be higher than for  $\Lambda$  hyperons, however, the interplay between several effects e.g. polar angle, Lorentz boost, multiple scattering and momentum distributions make a rigorous conclusion difficult. For a deeper understanding, multi-differential studies have to be performed.

Another important kinematic difference is the following: the final state proton has only a slightly smaller mass than its mother particle  $(m_p/m_\Lambda \approx 0.84)$ . According to energy and momentum conservation its direction of flight is almost congruent with the one of the  $\Lambda$  hyperon resulting in a higher probability of having protons at low  $\theta$  angles compared to pions from a  $K_s^0$  decay  $(m_\pi/m_{K_s^0} \approx 0.28)$ . Figure 4.15 (b) shows the distribution of protons coming from  $\Lambda$  (blue) and positive pions from  $K_s^0$  (red) decays as obtained from MC simulations. Due to the described decay kinematics, protons are emitted dominantly at low  $\theta$  angles where the reconstruction efficiency is smaller due to higher track densities, whereas the positive pions show a rather broad

$$Q = (m_{\rm A} - (m_{\rm B} + m_{\rm C})) \cdot c^2, \tag{4.1}$$

<sup>&</sup>lt;sup>14</sup> For a decay of particle A into its daughter particles B and C the Q-value is defined as

where  $m_{A,B,C}$  are the rest masses of the particles. The Q-value is also referred to as the reaction energy and is positive for exothermic and negative for endothermic reactions.

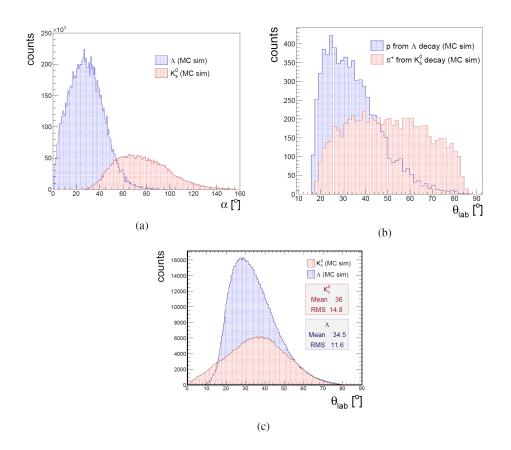


**Figure 4.15:** (a) Opening angle distribution between decay products of  $\Lambda$  (blue) and  $K_s^0$  (red) generated in a MC simulation with Pluto. The opening angles of  $\pi^- - \pi^+$  pairs from  $K_s^0$  decays are on average much larger than for  $\pi^- - p$  from  $\Lambda$  which has a direct impact on the resolution of the reconstructed decay vertex. (b)  $\theta$  distribution for protons from  $\Lambda$  (blue) and positive pions from  $K_s^0$  (red) decays generated in a MC simulation. (c)  $\theta$  distribution of  $\Lambda$  hyperons (blue) and  $K_s^0$  mesons, also generated in MC simulations. Due to the higher mass, the  $\Lambda$  experiences a stronger Lorentz boost resulting on average in an increased emission at low  $\theta$  angles than for  $K_s^0$ . This is indicated by the lower mean and RMS of the distribution for  $\Lambda$  compared to  $K_s^0$ .

distribution<sup>15</sup>. Furthermore, the significantly heavier  $\Lambda$  experiences a stronger Lorentz boost than the  $K_s^0$  meson. Hence,  $\Lambda$  hyperons have a higher probability of being emitted at low  $\theta_{lab}$  angles than  $K_s^0$  mesons, as can be seen from figure 4.15 (c), which is indicated by the lower values for the mean and the RMS of the  $\theta_{lab}$  distribution for  $\Lambda$  hyperons compared to  $K_s^0$  mesons as obtained from MC simulations. This increases the probability even more of having protons from  $\Lambda$  decays in the region of high track densities.

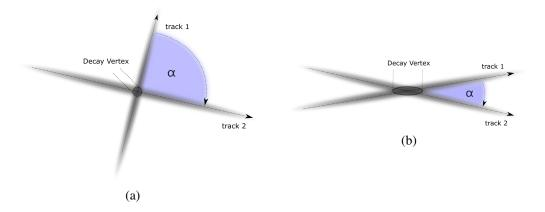


**Figure 4.16:** The decay vertex of a particle can be determined as the intersection point of the two reconstructed charged particles. The resolution of the decay vertex depends strongly on the momentum resolution (indicated by shaded area around track) and the opening angle  $\alpha$  which underlines the importance of a precise tracking algorithm. Compared to large opening angles (a), particles emitted with small  $\alpha$  have a larger overlap area for a given momentum resolution (b) resulting in a worse decay vertex resolution.

### 4.2.2.3 Background Determination

In section 3.6.2.2, the different techniques for the reconstruction of uncorrelated background were described with special emphasis on the mixed-event technique which is used in this analysis. Since two different events can have strikingly different properties a random combination may not give a realistic reproduction of the background. In the following, the investigated requirements on the conditions for the mixing of two events are listed:

• **Detector Performance:** The performance of the detector is not continuous over the beam time due to different high voltage settings, trips, missing modules caused by radiation damage etc. which may directly affect the quality of track reconstruction. Therefore, only candidates from events with comparable performance are mixed. This can be achieved by pairing particles from the same file where the event recording times differ typically only within few minutes.

<sup>&</sup>lt;sup>15</sup> The distribution looks similar for negative pions from  $K_s^0$  decays.

- Centrality: The phase space distribution may depend on the event multiplicity, however, investigations on the shape of the mixed-event distribution indicated a negligible sensitivity even when mixing most central with semi-peripheral collisions. The disagreement is below 1% indicating that no strong condition on this event class is necessary.
- Event Vertex: The different gold target segments measure in total a length of 60 mm. A Au+Au reaction in the first segment will occupy the detector components at different polar angles than the exact same reaction would e.g. in the last segment resulting in a different phase space distribution. In order to guarantee that the impact of the constraints on the decay topology are similar for the mixed and same event distributions only reactions are combined which are close in space  $(d_{\rm EV} < 10 \text{ mm})^{16}$ . However, investigations have shown that the discrepancies of the shape of the mixed-event spectrum when mixing events with varying relative distance of their reaction vertices  $\Delta d_{\rm EV}$  do not exceed few percent.
- Opening Angle: The products of a decay are emitted under a certain opening angle. For small opening angles the hit point distance in the first plane of drift chambers may be smaller than the detector granularity resulting in a decreasing probability for a successful reconstruction of close pairs. For obvious reasons, this effect cannot occur when two particles from different events are combined since they are reconstructed independently. This results in an enhancement in the region of low opening angles for the distribution obtained for mixed events compared to same event pairs. Hence, low opening angles are excluded from analysis (Δα > 15°).
- Event Plane Angle: In case of presence of flow in a collision system it is preferable to group the events according to the event plane angle  $\Psi_{EV}$ . However, no significant impact on the shape of the invariant mass spectrum could be observed.

The contribution of misidentified charged particles to the same-event invariant mass spectrum can be considered to be the same as the one to the mixed-event spectrum and can hence be neglected.

### 4.2.2.4 Optimization of Selection Criteria and Signal Extraction

In order to find a first estimate on the cut value of the previously introduced topology parameters, Monte Carlo simulations are used. The distributions for the topology parameters of the simulated particle can then be compared to the ones obtained from experimental data. The investigated hadrons  $\Lambda$  and  $K_s^0$  are simulated in Pluto (see 3.8.1.1), embedded into events generated with UrQMD (1 per event), propagated through a full GEANT simulation where the decay takes place (see 3.8.2) and finally subjected to the full analysis chain as used for experimental data. By requesting their unique Monte Carlo ID, the distributions include exclusively the initially simulated strange hadrons.

<sup>&</sup>lt;sup>16</sup> Furthermore, the performance of the MDCs, in particular the first two planes of drift chambers, depend on the impact angles into the drift cells.

On the other hand, the topology parameter distributions in experimental data are calculated for all identified p- $\pi^-$  and  $\pi^+$ - $\pi^-$  pairs, respectively. Since the production of strange hadrons is rare, these pairs are most abundantly emitted from the primary instead of the secondary vertex and hence uncorrelated. Therefore, the distributions contain a large background fraction and only a small contribution comes from the actually investigated hadrons  $\Lambda$  and  $K_s^0$ . Hence, the experimental distributions can be considered as a background reference and compared to those obtained when retrieving the MC ID in order to estimate a minimum cut value starting from which the signal-to-background ratio will improve. The topology distributions for data and simulation in the case of  $\Lambda$  hyperons are shown in figure 4.17 and for  $K_s^0$  mesons in 4.18, respectively. The distribution in simulation is normalized to the integral of experimental data. As anticipated, the distributions differ significantly in data and simulation.

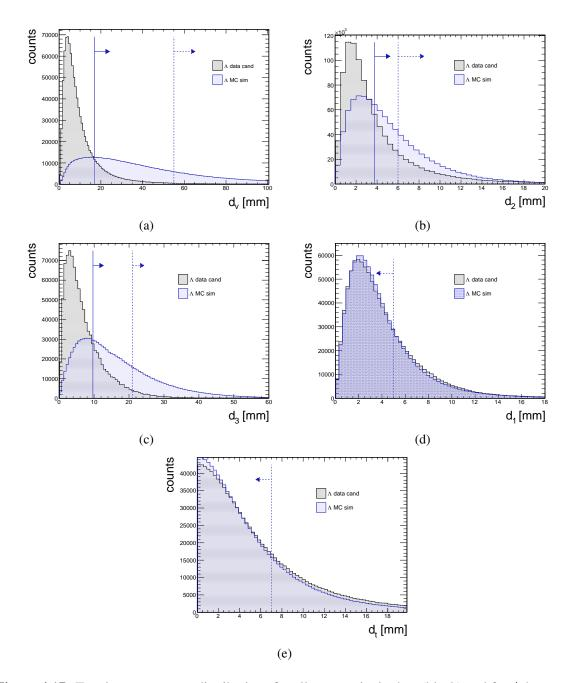
As a first approximation, an appropriate selection region would be, where the distributions obtained from simulation are enhanced over those from data. Such a selection may sort out more pairs emitted from the primary relative to the secondary vertex leading to an increase of the signal-to-background ratio in the invariant mass spectrum. However, this is a rather rough estimation as the value depends strongly on the normalization region. The regions where the distributions in simulation start to dominate over those from all pairs in data is indicated in the figures by solid lines. The description of the decay kinematics in simulation can be calculated rigorously and hence the cut values can be oriented to the indicated numbers in the distribution. However, in case of  $d_1$  and  $d_t$  (4.17, 4.18 (d) and (e)) this argument does not hold, since these DCA distributions are expected to increase towards low values for both, primary and secondary pair candidates, and are applied rather to sort out contributions from pairs coming from different vertices.

Figure 4.19 shows the invariant mass spectra for (a)  $\Lambda$  and (b)  $K_s^0$  candidates after applying topology cuts as indicated by the solid lines in figure 4.17 and 4.18 (a), (b) and (c) respectively (and the dashed lines in (d) and (e)). The applied cuts reduce background from uncorrelated pairs significantly such that a signal emerges exactly in the expected mass regions which was not observed in the invariant mass spectra containing all pairs, see figure 4.12.

However, for certain analysis it can be useful to further constrain the selection leading to even larger background suppression which makes the determination of the signal more precise. On the other hand, the more constraints are put on an analysis the larger the uncertainties for the efficiency corrections get. A trade-off has to be found favoring a minimization of the final systematic uncertainties. The dashed lines in 4.17 and 4.18 list the cut values which were actually selected for the final analysis which are an educated guess based on a high signal-to-background ratio (S/B) and a reasonable significance<sup>17</sup>. This is in particular crucial when performing a differential analysis where the background was found to be the dominating source for systematic uncertainties and which strongly depends on the investigated phase space region as will be explained in 4.2.2.6. The values used for analysis are summarized in table 4.3.

The topology cut efficiencies for the indicated values amount to 31% for  $\Lambda$  hyperons and 46% for  $K_s^0$  mesons. The lower efficiency in the  $\Lambda$  analysis is a result of the stronger constraints on

 $\frac{1}{17} Signif = \frac{S}{\sqrt{S+B}}$ 



**Figure 4.17:** Topology parameter distributions for all p- $\pi^-$  pairs in data (black) and for  $\Lambda$  hyperons generated in a MC simulation (blue). This comparison can be used to estimate the region where a cut on a topology parameter can be applied in order to suppress more background than signal in experimental data. The solid lines in (a), (b) and (c) indicate where the distribution from simulation starts to be enhanced over the one from data whereas the dashed lines indicate the actually used cut in the later analysis (the arrow indicates the region of accepted values). In distribution (d) and (e) only the analysis cut value is indicated by a dashed line. The distributions from simulation are normalized to the integral of the distribution in data.

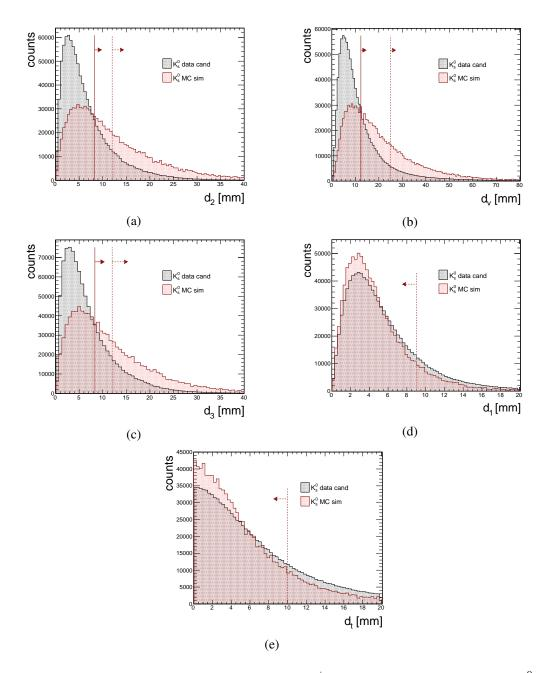


**Figure 4.18:** Topology parameter distributions for all  $\pi^+$ - $\pi^-$  pairs in data (black) and for  $K_s^0$  mesons generated in a MC simulation (red). This comparison can be used to estimate the region where a cut on a topology parameter can be applied in order to suppress more background than signal in experimental data. The solid lines in (a), (b) and (c) indicate where the distribution from simulation starts to be enhanced over the one from data whereas the dashed lines indicate the actually used cut in the later analysis (the arrow indicates the region of accepted values). In distribution (d) and (e) only the analysis cut value is indicated by a dashed line. The distributions from simulation are normalized to the integral of the distribution in data.

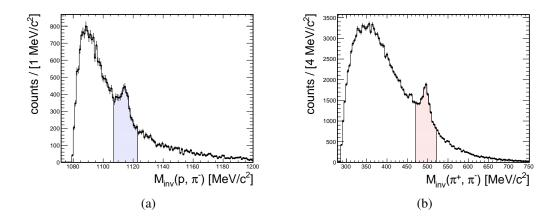


**Figure 4.19:** Invariant mass spectra of  $p-\pi^-$  (a) and  $\pi^+-\pi^-$  (b) when applying topology cuts as indicated in figure 4.17 and 4.18 (solid lines) for data obtained in a single day. The colored area indicates the expected signal region estimated in a  $2\sigma$  region around the nominal mass value. A clear peak emerges after suppressing a significant amount of background with selections on the decay kinematics.

	Λ	$K^0_s$
$d_v \text{ [mm]}$	> 65	> 24
$d_1 \text{ [mm]}$	< 5	< 8
$d_2 \text{ [mm]}$	> 8	> 12
$d_3  [mm]$	> 24	> 12
$d_t \text{ [mm]}$	< 6	< 9
$\Delta \alpha$ [°]	> 15	> 15

**Table 4.3:** Overview of topology cuts applied in the analysis of  $\Lambda$  and  $K_s^0$ . The topology cut efficiencies for the indicated values amount to 31% for  $\Lambda$  hyperons and 46% for  $K_s^0$  mesons.

the DCA parameters  $d_t$  and  $d_1$  improving the S/B ratio significantly as can be seen from figure 4.20. This reduces the overall secondary vertex cut efficiency in the  $\Lambda$  analysis from 45%, when applying the same DCA cuts as for the  $K_s^0$  reconstruction, down to 31% for the tighter values as listed in table 4.3. Due to the higher combinatorics in the  $\Lambda$  compared to the  $K_s^0$  reconstruction, the increasing S/B ratio is required in order to obtain similar uncertainties in both analysis. The choice will be benchmarked in terms of robustness of the applied acceptance and efficiency correction when calculating the mean lifetimes of the particles, see 4.3.3.

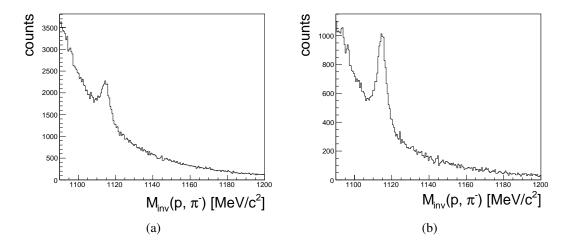


**Figure 4.20:** Invariant mass distribution of  $p-\pi^-$  pairs ( $\Lambda$ ) applying DCA cuts  $d_t$  and  $d_1$  as indicated in table 4.3 for (a)  $K_s^0$  mesons and (b)  $\Lambda$  hyperons. A significant improvement of the S/B to background ratio is observed requiring tighter cuts reducing the total secondary vertex cut efficiency in the  $\Lambda$  analysis from (a) 0.45 to (b) 0.31. The shown statistics correspond to roughly 1/30 of the full statistics.

Figure 4.21 shows the invariant mass distributions of  $\Lambda$  hyperons and  $K_s^0$  mesons integrated over the full phase space applying the cuts according to table 4.3. In total there are 71969 ± 268  $\Lambda$  hyperons and 109171 ± 330  $K_s^0$  mesons reconstructed with a signal-to-background ratio of  $S/B_{\Lambda} \approx 1$  and  $S/B_{K_s^0} \approx 1.8$  respectively. The signal is determined after subtraction of the mixed-event background (see section 4.2.2.3). The means extracted from a fit of a Gaussian distribution to the background-subtracted signal spectrum agree well with the expected invariant mass from the PDG [5]. The signal extraction will be discussed in more detail in the following.

#### Normalization

After having determined the background within the in section 4.2.2.3 mentioned classes, the invariant mass distribution for mixed events has to be normalized to the same-event spectrum. Therefore, both spectra are integrated in the same mass range and the ratio of integrated count rates is used to scale the mixed-event spectrum down to the same-event distribution. After normalization the background can be subtracted which ideally leaves the contribution of correlated pairs and hence the signal of the mother hadron behind.

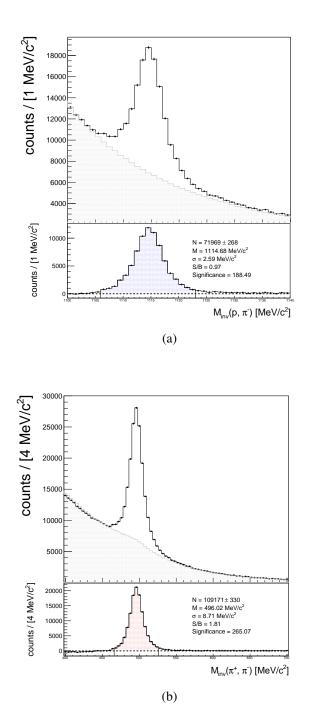


**Figure 4.21:** Upper part: Invariant mass spectra for  $\Lambda$  hyperons (a) and  $K_s^0$  mesons (b) for the 0 - 40% most central events after applying the topology cuts (see table 4.3) as used in the final analysis. The background as obtained from the mixed-event method is indicated in gray. Lower Part: After subtraction of the background in total a signal of  $\approx 72000 \Lambda$  hyperons and  $\approx 110000 K_s^0$  mesons remains. The error of the signal is calculated as  $\sqrt{S}$ . The significance is defined as  $Signif = \frac{S}{\sqrt{S+B}}$ .

For normalization the signal region has to be excluded when integrating the two spectra. Otherwise, if a signal contribution is available, the mixed-event spectrum overshoots the real background. A reasonable choice for normalization is at least  $3\sigma$  away from the expected mean of the signal obtained when assuming a Gaussian distribution. This would include only 0.27% of the actual signal.<sup>18</sup>

Certainly, the choice of normalization region is based on an educated guess: an exact reproduction of the background cannot be obtained over the full invariant mass range by the mixedevent method. Assuming a continuous trend of the background in the signal region, a normalization close to the signal will minimize effects from a systematic discrepancy of the background shape estimated via the ME technique. Furthermore, when normalizing at low invariant masses where the background contribution is largest, small differences in the shape will affect the tails, where the signals are mostly located in the presented analysis, much stronger.

Figure 4.22 shows the different regions used for background normalization. The sidebands indicated in 4.22 (a) and (b) are used as standard normalization in the  $\Lambda$  hyperon and  $K_s^0$  meson analysis whereas the wider windows in (c) and (d) are used as variation in order to estimate the systematic uncertainty of the background determination. The impact on the final particle spectra are discussed in chapter 5.

### Signal Extraction and Estimation of the Count Rate Uncertainty

After subtraction, the remaining signal is parametrized with a Gaussian fit function. The distribution is integrated in a  $3\sigma$  interval around the extracted mean  $\mu$  providing the count rate S with an uncertainty of  $\sqrt{S^{19}}$ .

### 4.2.2.5 Comparison of Data and Simulation

As already discussed in 3.8, the detector response has to be reproduced as accurately as possible in simulations. Every discrepancy on a cut variable between data and simulation may emerge as systematic uncertainty in the final results which are corrected for efficiency. In the presented secondary vertex analysis for rare strange particles, relatively low reconstruction efficiencies are dealt with ranging from 5 - 8% down to 0.2% which is mainly due to the applied topological constraints. By cutting on a certain variable, which is differently distributed in data as in simulation, the relative loss will also be different leading to a wrong correction of the measured data. Therefore, careful comparisons between simulated and measured data are made for quantities that are constrained in analysis. If the shape of a given variable is not reproduced in simulation,

<sup>&</sup>lt;sup>18</sup> For a variable drawn from a Gaussian random process the probability to lie outside  $\pm n \cdot \sigma$  around the mean  $\mu$  is called *p-value*. For example, the probability of a measurement following a Gaussian distribution lying outside  $\pm 1\sigma$  around the mean  $\mu$  is 32%, consistently 68% of data lie within  $1\sigma$ . The p-value for a given *n* can be calculated with error functions [255]. A  $5\sigma$  result with a *p*-value of  $5.7 \cdot 10^{-7}$  is called *discovery*.

<sup>&</sup>lt;sup>19</sup> For a given background normalization, the integral range has been widened to  $5\sigma$  showing no significant impact on S. In the calculation of the statistical uncertainty of the signal, the statistical error of the background is not included. The contribution of the background to the overall uncertainty is determined systematically by variation of the normalization region. Since the statistical and systematic uncertainty of the background are correlated, the inclusion of the statistical uncertainty to the signal uncertainty would result in an overestimation of the overall uncertainty.

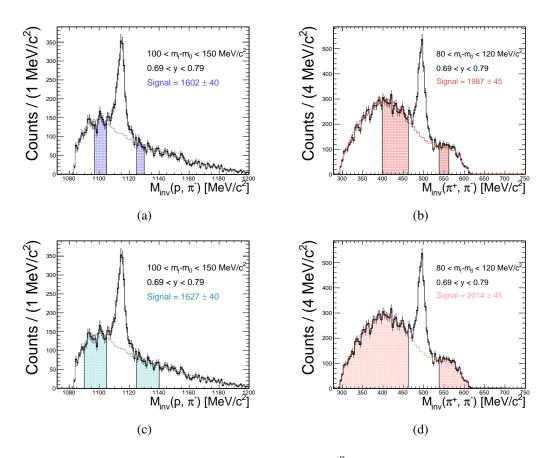


**Figure 4.22:** Invariant mass spectra of  $\Lambda$  (a), (c) and  $K_s^0$  (b), (d) candidates. The mixed-event spectrum is normalized to the integral of the same-event spectrum either in sidebands close to the signal (top row) or in widened sidebands (bottom row). The region of normalization is chosen to be at least  $3\sigma$  away from the signal region which includes only 0.27% of the signal when assuming a Gaussian-like signal distribution. The error of the signal is calculated as  $\sqrt{S}$ .

either cutting into this distribution should be avoided or the reason for the discrepancy needs to be found.

In figure 4.23 and 4.25, these comparisons are illustrated for the decay topology parameters for  $p-\pi^-$  and  $\pi^+-\pi^-$  pairs respectively. The distributions in simulation are obtained for pairs from events generated with the UrQMD model and are normalized to the full integral of data. As the strange hadron multiplicities are very small, their contribution to the distributions is negligible, in data as well as in simulation. A significant deviation will point towards systematic discrepancies in the description of the corresponding quantity in simulation. The shape of the distributions seems to be adequately reproduced in simulation, in particular for the decay topology cut quantities  $d_v$ , where the strongest constraints are applied, with a deviation of about 5-10% and 1-5%for  $\Lambda$  and  $K_s^0$  respectively. The opening angle  $\Delta \alpha$  distribution differs by roughly 2-5% and 5-10%. The distributions for  $d_2$  and  $d_3$  show a disagreement of maximum 15-20%, those for  $d_t$  and  $d_1$  overall agree within approximately 5-10%.

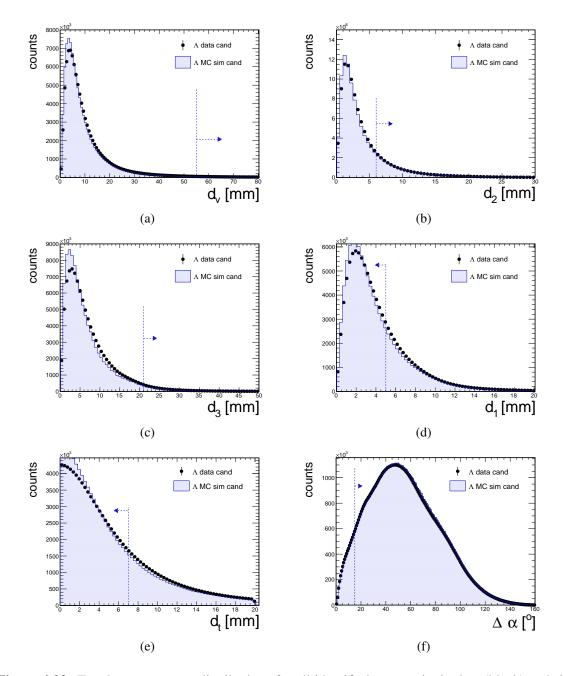
Figure 4.24 as well as 4.26 show the same comparisons between data and simulation, now for the track quality distributions. A systematic discrepancy is observed for the Runge-Kutta track quality parameter  $\chi^2_{\rm RK}$  which was already mentioned in section 4.1 and which was found to give a significant bias when applying constraints below roughly 200. A robust cut value was determined to be  $\chi^2_{\rm RK} < 400$  (for more details, see [37]).

A quantification of the level of agreement is difficult, since the distribution in simulation needs to be normalized to the data statistics. Depending on the region of normalization, the relative uncertainty can vary significantly. Hence, if the source for the discrepancy is unknown and cannot be attributed to a certain region in the distribution, a precise statement of the uncertainties is not possible here.

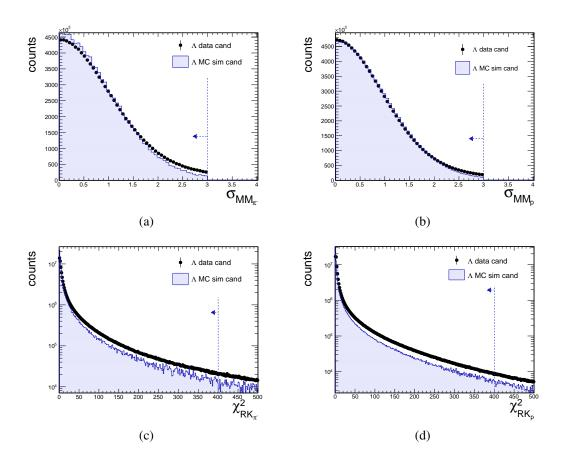
Furthermore, as explained in section 4.2.2.1, the secondary vertex parameters are highly correlated. Cutting into one distribution can have impact on another distribution, which might be different in simulation compared to data. For this reason and to get a more quantitative understanding of the agreement between measured and Monte-Carlo data further investigations on their relative efficiencies have to be conducted:

Figure 4.27 and 4.28 show the loss of signal counts in data (black) and simulation (blue/red) when applying topology cuts. The topology cuts directly affect the signal counts. If the relative loss of the signal differs when applying the same topology cut value in data and simulation, this hints at a systematic deviation in the description of the quantity that is constrained. In data, the signals are extracted as described in section 4.2.2.4, whereas in simulation the specific Monte Carlo ID is retrieved and the signal is integrated in the same range as in data. The signal for the loosest indicated cut value is used as reference, to which all subsequent signals with tighter constrained cuts are normalized to and which can hence be found at unity. For each figure all but one of the previously discussed cuts on the decay topology are set to the values as indicated in table 4.3. The remaining cut quantity is then varied (cut value indicated on x-axis) and the relative loss of signal counts compared for data and simulation. The dashed lines indicate the value to which the cut for the plotted quantity is set to in the final analysis.

A deviation exceeding statistical errors indicates systematic difference in data and simulation. However, considering that the signals are extracted without taking the systematic uncer-



**Figure 4.23:** Topology parameter distributions for all identified p- $\pi^-$  pairs in data (black) and simulation (blue). The distributions from simulation are normalized to the integral of those from experimental data. The selected parameters are constrained in analysis and therefore the shapes of their distributions are compared in order to check for eventual discrepancies between data and simulation. Overall, an adequate agreement is observed, in particular for  $d_v$ ,  $d_1$ ,  $d_2$  and  $\Delta \alpha$ .



**Figure 4.24:** Track quality parameter distributions for all identified p- $\pi^-$  pairs in data (black) and simulation (blue). The distributions from simulation are normalized to the integral of those from experimental data. The selected parameters are constrained in analysis and therefore the shapes of their distributions are compared in order to check for eventual discrepancies between data and simulation. A systematic discrepancy is observed for the Runge-Kutta track quality parameter  $\chi^2_{\rm RK}$  which was found to give a bias for the correction of data for acceptance and efficiency of the spectrometer. Hence, only a loose cut is applied ( $\chi^2_{\rm RK} < 400$ ).

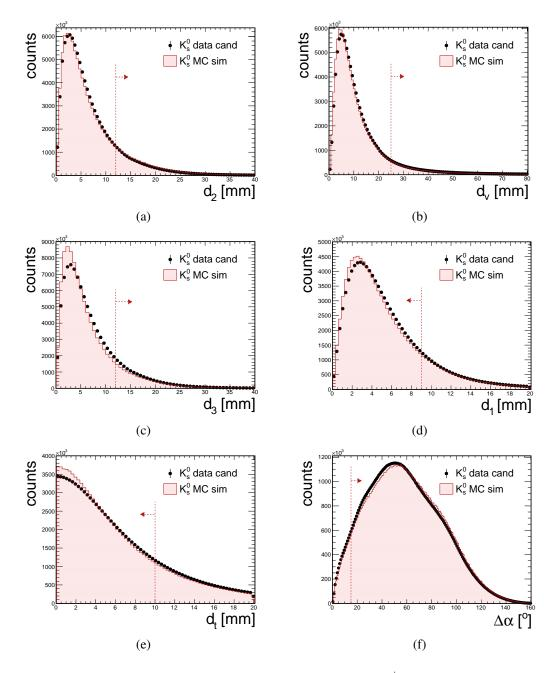
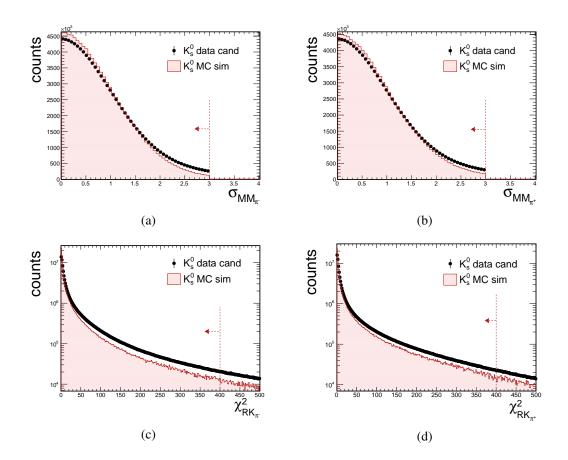
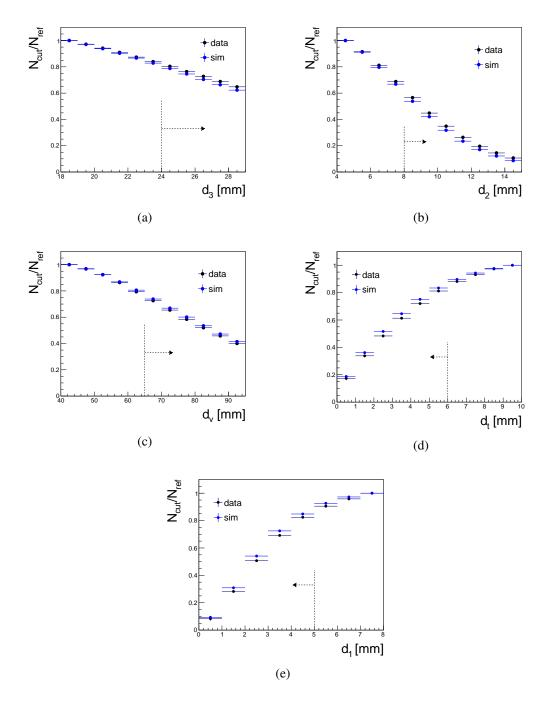


Figure 4.25: Topology parameter distributions for all identified  $\pi^+ \cdot \pi^-$  pairs in data (black) and simulation (red). The distributions from simulation are normalized to the integral of those from experimental data. The selected parameters are constrained in analysis and therefore the shapes of their distributions are compared in order to check for eventual discrepancies between data and simulation. Overall, a fair agreement is observed, in particular for  $d_v$ ,  $d_2$  and  $\Delta \alpha$ . The strongest deviation is observed for  $d_3$  at maximum 20%.



**Figure 4.26:** Track quality parameter distributions for all identified  $\pi^+ \cdot \pi^-$  pairs in data (black) and simulation (red). The distributions from simulation are normalized to the integral of those from experimental data. The selected parameters are constrained in analysis and therefore the shapes of their distributions are compared in order to check for eventual discrepancies between data and simulation. A systematic discrepancy is observed for the Runge-Kutta track quality parameter  $\chi^2_{\rm RK}$  which was found to give a bias for the correction of data for acceptance and efficiency of the spectrometer. Hence, only a loose cut is applied ( $\chi^2_{\rm RK} < 400$ ).



**Figure 4.27:** Relative loss of signal counts in experimental (data) and simulated (blue) data for the  $\Lambda$  hyperon as a function of different topology parameters. The signal for the loosest cut value (indicated on x-axis as leftmost for  $d_v$ ,  $d_3$ ,  $d_2$  and rightmost for  $d_1$ ,  $d_t$ ) is used as reference, to which all subsequent signals with tighter constrained cuts (corresponding cut value indicated on x-axis) are normalized to. For the remaining topology parameters the cut values according to table 4.3 are taken. The dashed line indicates the finally selected cut value for the plotted quantity and the arrow indicates the region of accepted values.

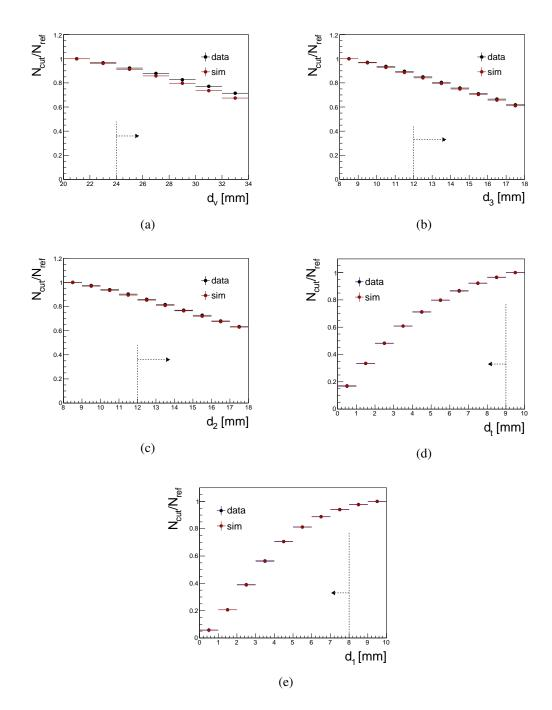


**Figure 4.28:** Relative loss of signal counts in experimental (data) and simulated (red) data for the  $K_s^0$  meson as a function of the different topology parameters. The signal for the loosest cut value (indicated on x-axis as leftmost for  $d_v$ ,  $d_3$ ,  $d_2$  and rightmost for  $d_1$ ,  $d_t$ ) is used as reference, to which all subsequent signals with tighter constrained cuts (corresponding cut value indicated on x-axis) are normalized to. For the remaining topology parameters the cut values according to table 4.3 are taken. The dashed line indicates the finally selected cut value for the plotted quantity and the arrow indicates the region of accepted values.

tainty from the background determination into account, an overall reasonable agreement can be confirmed.

A way to ultimately test the robustness of acceptance and efficiency correction are lifetime measurements which will be explained in section 4.3.3.

#### 4.2.2.6 Multi-differential Hadron Analysis

In order to investigate particle yields and kinematics the analysis is performed differentially in phase space as a function of the two kinematic variables rapidity y and reduced transverse mass  $m_t - m_0^{20}$ . Therefore, the particle yields are determined in  $n_{m_t} \ge n_y$  ( $n \in \mathbb{N}$ ) phase space bins and corrected differentially. The selected binning of phase space cells is listed in table 4.4 for the  $\Lambda$  and  $K_s^0$  analysis respectively. The choice for the size of the cells is based on statistical arguments requiring a reasonable amount of count rates in the bulk of cells in order keep statistical uncertainties under control.

		$m_t - m_0  [\text{MeV/c}^2]$	y
Δ	Range	[0, 600]	[0.09, 0.89]
	Bin Size	50	0.1
$K_s^0$	Range	[0, 600]	[0.09, 1.49]
	Bin Size	40	0.1

**Table 4.4:** Overview of differential phase space bins as a function of reduced transverse mass  $m_t - m_0$  and rapidity y used for  $\Lambda$  and  $K_s^0$  reconstruction.

#### **Invariant Mass Spectra**

Figure 4.29 and 4.30 show the invariant mass spectra of  $\Lambda$  and  $K_s^0$  obtained for the different transverse mass bins around mid-rapidity (0.69 < y < 0.79;  $y_{\text{mid}} = 0.74$ ) showing a clear signal for all  $m_t - m_0$  bins. A strong dependence of the count rates on  $m_t$  is observed increasing

<sup>20</sup> Taking the beam line as z axis, the rapidity y is defined as

$$y := \frac{1}{2} \ln \left( \frac{E + p_z c}{E - p_z c} \right) = \operatorname{artanh} \left( \frac{p_z c}{E} \right).$$

Equivalently is

$$y = \ln\left(\frac{E + p_z c}{m_t c^2}\right)$$
 with  $(m_t c^2)^2 := (mc^2)^2 + (p_x c)^2 + (p_y c)^2$ 

where  $m_t$  is the transverse mass. Hence energy and momentum can be rewritten as

$$E = m_t c^2 \cosh y , \quad p_z c = m_t c^2 \sinh y , \quad p_x c , \quad p_y c$$

rapidly at low values, reaching a maximum at low to intermediate  $m_t$  before slowly decreasing again towards higher values. The differential signal count rates are determined as described in 4.2.2.4 after subtraction of the background (dark area) from the invariant mass distribution. The background is normalized by default to the integral of the same-event spectrum in sidebands at  $1097.5 < M_{\rm inv} < 1105 \text{ MeV/c}^2$  and  $1125 < M_{\rm inv} < 1130 \text{ MeV/c}^2$  in case of  $\Lambda$  and  $400 < M_{\rm inv} < 460 \text{ MeV/c}^2$  and  $540 < M_{\rm inv} < 560 \text{ MeV/c}^2$  for the  $K_s^0$  analysis. After subtraction the signal is integrated in a  $3\sigma$  environment (indicated as colored areas) around the mean  $\mu$  as extracted from a Gaussian fit.

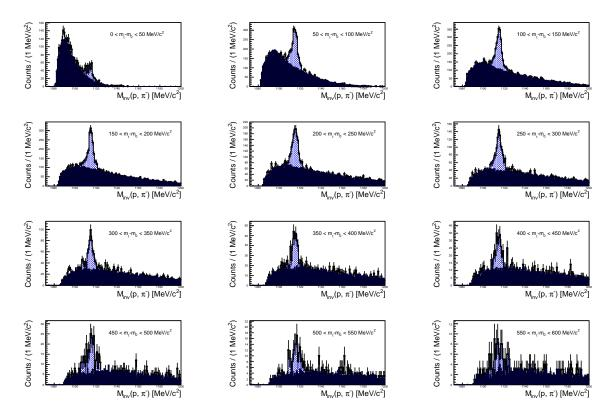


**Figure 4.29:** Invariant mass distributions for  $p \cdot \pi^-$  pairs at mid-rapidity ( $y_{\text{mid}} = 0.74$ ) as a function of reduced transverse mass in steps of  $m_t = 50 \text{ MeV/c}^2$ . The background (dark area) is normalized to the entries in sidebands around the expected signal region ranging from  $1097.5 < M_{\text{inv}} < 1105 \text{ MeV/c}^2$  and  $1125 < M_{\text{inv}} < 1130 \text{ MeV/c}^2$ . After background subtraction, the remaining distribution is fitted with a Gaussian function. The spectrum is then integrated  $3\sigma$  around the fitted mean which is indicated by the blue area.

The differential signal rates as a function of the full reduced transverse mass and rapidity range are presented in figure 4.31 showing in both cases,  $\Lambda$  (a) and  $K_s^0$  (b), a maximum in the backward hemisphere ( $y < y_{mid}$ ) at low to intermediate transverse masses.

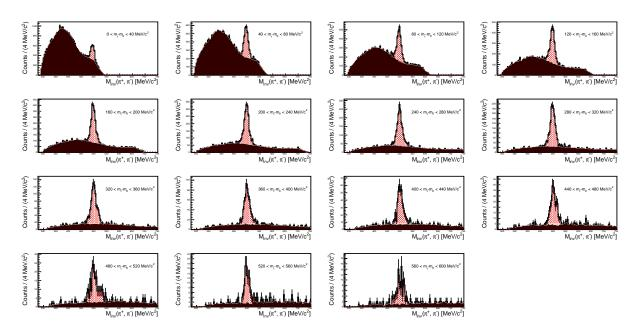
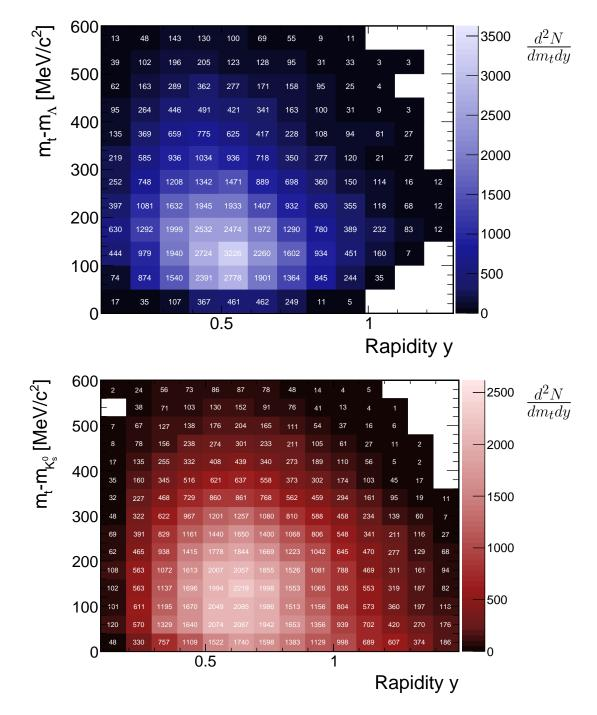


Figure 4.30: Invariant mass distributions for  $\pi^+ \cdot \pi^-$  pairs at mid-rapidity ( $y_{\rm mid} = 0.74$ ) as a function of transverse mass in steps of  $m_t = 40 \text{ MeV/c}^2$ . The background (dark area) is normalized to the entries in sidebands around the expected signal region ranging from  $400 < M_{\rm inv} < 460 \text{ MeV/c}^2$  and  $540 < M_{\rm inv} < 560 \text{ MeV/c}^2$ . After background subtraction, the remaining distribution is fitted with a Gaussian function. The spectrum is then integrated  $3\sigma$  around the fitted mean which is indicated by the red area.



**Figure 4.31:** Raw signal counts as a function of reduced transverse mass  $m_t - m_0$  and rapidity for  $\Lambda$  hyperons (top) and  $K_s^0$  (bottom) mesons. A maximum in the backward hemisphere ( $y < y_{mid} = 0.74$ ) at low to intermediate transverse masses for both particles is observed.

#### Signal-to-Background Ratio

The main contribution to the systematic uncertainties is the background (dark area) of uncorrelated pairs to the invariant mass spectrum. Its evolution and hence the S/B ratio and significance strongly depend on rapidity and transverse mass, as can be seen from the invariant mass spectra in figures 4.29 and 4.30, and therefore has to be well controlled. The uncertainty of the determined signal increases with the amount of background and hence with decreasing significance. Figure 4.32 shows the S/B ratio as a function of  $m_t - m_0$  and y. In both analysis a maximum towards high  $m_t$  in the backward hemisphere is observed. The ratio decreases towards forward-rapidities  $(y > y_{\text{mid}})$  and low transverse masses where most of the signal counts are located. Hence, it is in particular the latter region of low  $m_t$  where the propagation of background uncertainties to the signal has to be treated with care.

As one can easily understand, the background is not only a function of transverse mass and rapidity but also centrality. For an increasing event multiplicity the amount of background relative to signal counts is larger which is due to a different rise of combinatorics: Whereas the number of  $\Lambda/K_s^0$  hadrons increases with centrality (in leading order: signal  $\propto \langle A_{\text{part}} \rangle$ ), the same holds true for each of their two charged decay particles, however, combinatoric-wise this leads to a stronger increase for the background statistics (background  $\propto \langle A_{part} \rangle^2)^{21}$ . This dependence is illustrated in figure 4.33 and 4.34 showing a significant decrease for the signal-to-background ratio going from semi-central (upper left) to the 0 - 10% most central events (lower right) by a factor of roughly 2.5. The maxima of the corresponding distributions of  $\Lambda$  and  $K_s^0$  are set to the same value for all centralities to allow for an easier comparison<sup>22</sup>.

As demonstrated, the signal-to-background ratio is a function of transverse mass  $m_t$ , rapidity y and centrality  $\mathcal{C}$ :

### $f_{\mathrm{S/B}}(m_t, y, \mathcal{C}),$

hence, the same holds true for the systematic uncertainties of the extracted signal count rates. This requires a careful treatment of the normalization region of the mixed-event to the same-event spectrum. In particular the background contributions to the spectra at low transverse masses and towards more central collisions have to be well controlled and require individual normalization regions.

For an estimation of the systematic uncertainty of the background determination, the normalization range will be modified, as was explained in the previous section 4.2.2.4. The impact of the background uncertainty on the final results will be discussed in section 5.1.2.1 for the  $\Lambda$  and in section 5.1.2.1 for the  $K_s^0$  analysis.

#### 4.3 **Acceptance and Efficiency Correction**

Before results can be compared to other experiments or to theoretical models, experimental data has to be corrected for the imperfect detector acceptance and efficiency. Whereas the acceptance

<sup>&</sup>lt;sup>21</sup> As will be discussed in chapter 5, the results indicate a stronger rise of strange hadrons with centrality than pions, yet, the scaling is found to be well below  $\langle A_{\text{part}} \rangle^2$ . <sup>22</sup>  $S/B_{\text{max}}(\Lambda) = 14$  and  $S/B_{\text{max}}(K_s^0) = 40$ 

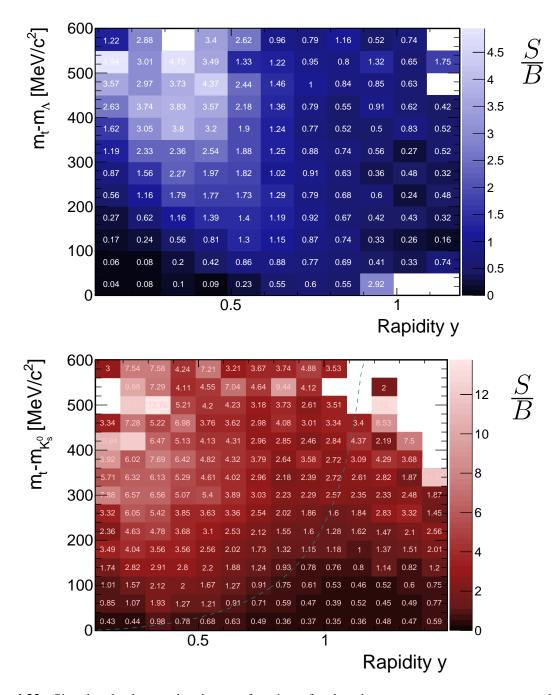


**Figure 4.32:** Signal-to-background ratio as a function of reduced transverse mass  $m_t - m_0$  and rapidity y for  $\Lambda$  hyperons (top) and  $K_s^0$  mesons (bottom). In both cases a maximum is observed towards high transverse masses in the rapidity backward-hemisphere ( $y < y_{mid}$ ). The ratio decreases towards high rapidities and low transverse masses.

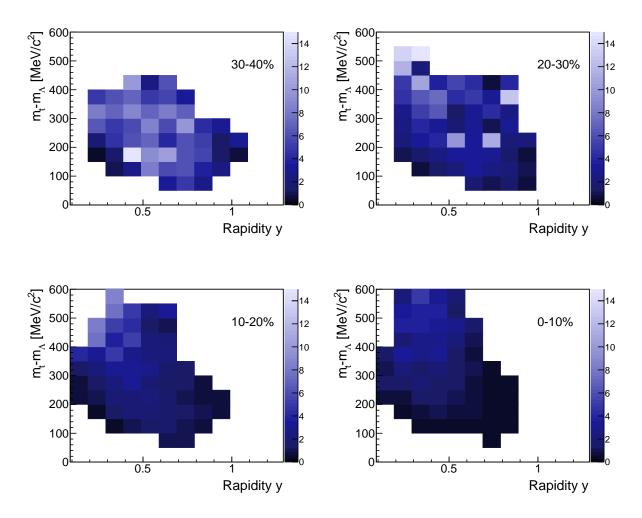


**Figure 4.33:** Signal-to-background ratio as a function of reduced transverse mass  $m_t - m_{\Lambda}$ , rapidity y and centrality C for  $\Lambda$  hyperons. For better comparison of the different centralities the maximum is set to the same value (= 15). A clear decrease of the S/B ratio is observed towards more central collisions due to increasing combinatorics of uncorrelated protons and pions.

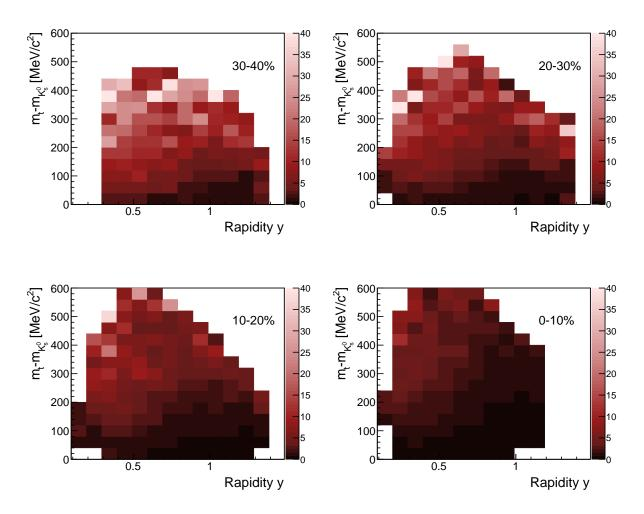


**Figure 4.34:** Signal-to-background ratio as a function of reduced transverse mass  $m_t - m_{K_s^0}$ , rapidity y and centrality C for  $K_s^0$  mesons. For better comparison of the different centralities the maximum is set to the same value (= 40). A clear decrease of the S/B ratio is observed towards more central collisions due to increasing combinatorics of uncorrelated positive and negative pions.

is referring to the pure geometry of a detector and describes whether a particle traverses its active volume or not, the latter one is more complex and can be subdivided into detector response, track reconstruction, particle identification and constraints applied in analysis like topology or track quality cuts.

The correction has to be estimated using a full MC simulation. The investigated strange hadrons  $\Lambda/K_s^0$  are therefore generated within the Pluto framework presented in section 3.8.1.1 and embedded into events generated with UrQMD (one particle per event). A realistic detector response is mimicked by subjecting the particle to a GEANT3 simulation as explained in 3.8.2. Here the particles decay and the geometrical acceptance can be determined via the charged decay products. By propagating the accepted particles through the same analysis chain as it is applied to real data a combined acceptance and efficiency correction factor  $\epsilon_{\text{combined}}$  can be calculated as

$$\epsilon_{\text{combined}}(m_t, y, \mathcal{C}) = \epsilon_{\text{acc}} \cdot \epsilon_{\text{reco}} = \frac{N_{\text{reco}}}{N_{\text{input}}}$$

where  $N_{\rm reco}$  denotes the number of signal counts determined from the invariant mass distribution of the two charged final state particles after all analysis steps and  $N_{\rm input}$  the number of initial input particles generated in Pluto. After retrieving the specific Monte Carlo ID of the input particle<sup>23</sup>, the signal distribution is fitted assuming a Gaussian distribution and integrated in a  $3\sigma$  environment around the extracted mean  $\mu$ , in order to account for the momentum dependent mass resolution of the detector<sup>24</sup>.

In contrast to what is often done in other pair analysis e.g for dileptons, the correction matrices are not determined by combining the single efficiencies of the decay products but directly for the  $\Lambda$  and  $K_s^0$  hadrons. This is due to the applied topology cuts which mostly depend on both daughter tracks and are highly correlated with respect to each other.

In the following sections the individual contributions to the full acceptance and efficiency are explained in more detail.

### 4.3.1 Acceptance Determination

Though the charged decay products are detected almost fully with respect to the azimuthal angle from  $\phi = 0^{\circ}$  to  $\phi = 360^{\circ}$ , the polar angle coverage ranges only from  $\theta = 18^{\circ}$  to  $\theta = 85^{\circ}$ .

The simulated particles decay in the GEANT simulation with a given branching ratio into the respective final state as listed in table 4.1. In this investigation a particle is considered as accepted if at least four layers in each MDC plane as well as one of the time-of-flight walls TOF or RPC were traversed. If both charged daughter particles fulfill this requirement, so does the mother hadron. For single tracks, in the limit of infinitesimal phase space cells, this would results in a particle either being accepted ( $\epsilon_{acc} = 1$ ) or not ( $\epsilon_{acc} = 0$ ). However, due to a finite size of phase space cells, the acceptance may reach values from zero to unity. By directly comparing the number of remaining particles via its detected decay products  $N_{acc}$  to the number of input particles generated in Pluto  $N_{input}$  the acceptance is determined:

<sup>&</sup>lt;sup>23</sup> ID<sub>Geant</sub> is 18 for  $\Lambda$  and 16 for  $K_s^0$ 

<sup>&</sup>lt;sup>24</sup> A systematic variation of the  $\sigma$  range did not reveal any significant impact on the final results.

$$\epsilon_{\rm acc}(m_t, y, \mathcal{C}) = \frac{N_{\rm acc}}{N_{\rm input}}.$$

Figure 4.35 shows the acceptance matrices for  $\Lambda$  and  $K_s^0$ .

# 4.3.2 Detector and Reconstruction Efficiency

Based on the number of accepted particles the detector and reconstruction efficiency  $\epsilon_{reco}$  is determined in the next step. This efficiency can be subdivided into several contributions which are listed in the following:

- $\epsilon_{det}$ : Digitization of individual efficiencies for each sub-detector in GEANT. The digitization parameters have to be adapted for each beam time since the performance of each sub-system depends strongly on occupancies, particle energies, applied voltages etc. This is mostly realized within the same data set or by using test beam data.
- $\epsilon_{tr}$ : Based on the digitized detector hits the same algorithms for track and momentum reconstruction as for data are applied as presented in section 3.5.
- $\epsilon_{\text{pid}}$ : Cuts applied for charged particle identification as explained in section 4.2.1.
- $\epsilon_{\chi}$ : Track quality parameters like Runge-Kutta  $\chi^2$  and META matching (section 4.1).
- $\epsilon_{sv}$ : A special focus is put on the secondary vertex cuts accounting for the decay kinematics. As pointed out in section 4.2, a satisfying gain in signal over background is achieved by applying cuts on the decay topology which in turn is the main contribution in reducing efficiency. The overall cut efficiencies for the in table 4.3 indicated values are 31% for  $\Lambda$ hyperons and 46% for  $K_s^0$ .

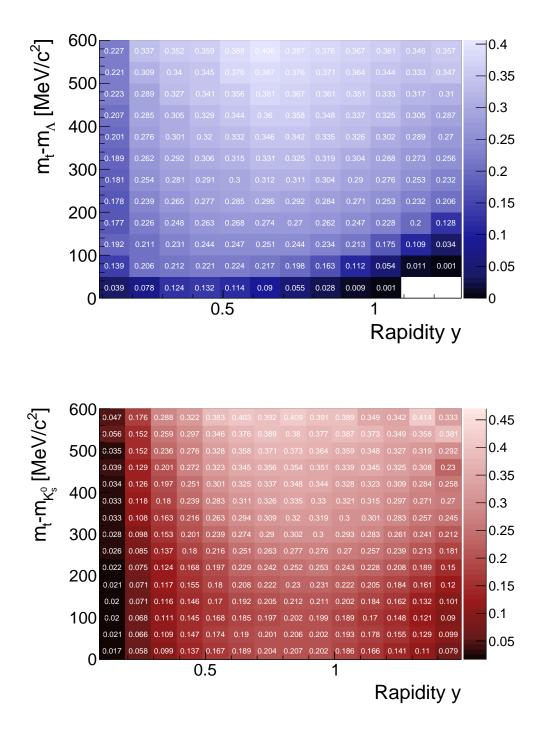
Most conveniently the total reconstruction efficiency  $\epsilon_{\text{reco}}$  is determined by calculating the ratio of the combined acceptance and reconstruction efficiency factor  $\epsilon_{\text{combined}}$  and the acceptance  $\epsilon_{\text{acc}}$  according to 4.3 and 4.3.1, respectively:

$$\epsilon_{\text{reco}}(m_t, y, \mathcal{C}) = \frac{\epsilon_{\text{combined}}}{\epsilon_{\text{acc}}}.$$

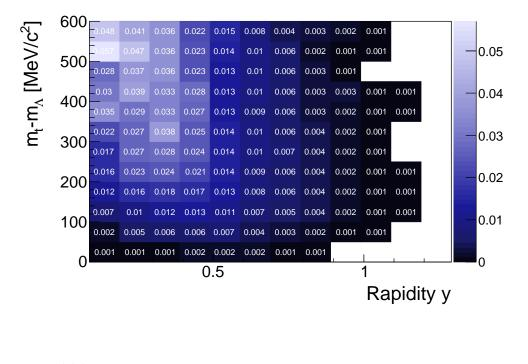
Figure 4.36 shows the reconstruction efficiency matrices for accepted  $\Lambda$  and  $K_s^0$ .

## 4.3.3 Decay Curve

A precise estimate of the impact of the decay topology constraints on the determined particle yields corrected for acceptance and efficiency are lifetime measurements. In contrast to the corrected particle yields and spectra, the mean lifetime is a system independent and well-measured quantity. By applying several sets of topology cuts for the  $\Lambda$  and  $K_s^0$  reconstruction the determined mean lifetimes should all agree with the expected value obtained from various independent measurements.



**Figure 4.35:** Acceptance  $\epsilon_{\rm acc}$  as a function of reduced transverse mass  $m_t - m_0$  and rapidity y for  $\Lambda$  (top) and  $K_s^0$  (bottom) as obtained from HGeant simulations. The highest acceptance is observed around mid-rapidity  $y_{\rm mid} = 0.74$  at rather high transverse masses.



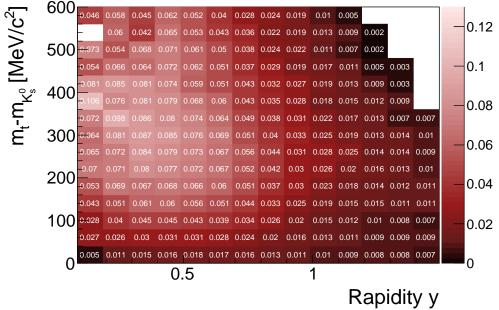


**Figure 4.36:** Detector and reconstruction efficiency  $\epsilon_{\text{reco}}$  as a function of reduced transverse mass  $m_t - m_0$  and rapidity y for accepted  $\Lambda$  (top) and  $K_s^0$  (bottom). This involves detector, tracking, particle identification, track quality and topology cut efficiencies.

Decaying particles follow the exponential decay law which is defined as:

$$N(t) = N_0 \cdot exp^{\frac{-t}{\tau}},\tag{4.2}$$

where  $N_0$  is the number of particles at t = 0 and  $\tau$  is the mean lifetime of the particle. N(t) gives for each point in time t the remaining number of particles. The time-of-flight  $\Delta t_{\text{lab}}$  of a relativistic particle P measured in the laboratory frame is given by:

$$\Delta t_{\rm lab} = \Delta t'_{\rm P} \cdot \gamma, \tag{4.3}$$

where  $\Delta t'_{\rm P}$  denotes the proper time of the particle and  $\gamma$  the relativistic Lorentz factor. The time-of-flight  $\Delta t_{\rm lab}$  of a particle can be calculated via the measured observables velocity  $\beta$  in the lab-frame and its decay length  $\Delta l$  which is the distance of the primary to the secondary vertex  $(d_v)$  introduced in section 4.2.2:

$$\Delta t_{\rm lab} = \frac{\Delta l}{\beta c}.\tag{4.4}$$

From equation 4.3 and 4.4 follows:

$$\Delta t'_{\rm P} = \frac{\Delta l}{\beta \gamma c} \tag{4.5}$$

which then gives with  $\beta \gamma c = |p|/m$ :

$$\Delta t'_{\rm P} = \frac{\Delta l \cdot m}{|p|},\tag{4.6}$$

with the absolute value of the measured momentum |p| and the nominal mass m of the particle. By plotting the number of reconstructed particles N(t) as a function of decay time  $\Delta t'_{\rm P}$  the function 4.2 can be fitted to the obtained decay curve which provides the two parameters  $N_0$  and the desired mean lifetime  $\tau$ .

As a proof of principle the mean lifetime is determined for particles generated in a Monte Carlo simulation where the mean lifetime  $\tau_{PDG}$  from the PDG was used as input. Here the exact values for momentum and decay length of the particle are provided by GEANT and the result for  $\tau_{fit}$  should be equal to the input  $\tau_{PDG}$  which is the case as shown in figure 4.37 (a) and 4.38 (a) for the  $\Lambda$  hyperon and  $K_s^0$  meson respectively.

For experimental data the count rates as a function of the decay time  $\Delta t'_{\rm P}$  are determined as described in 4.2.2.4 by subtracting the mixed-event background from the invariant mass spectra. The raw count rates are corrected for acceptance and efficiency as described in the previous section 4.3 yielding in the decay curve which is depicted in figure 4.37 (c) and 4.38 (c). Since there was no further estimation on the systematic uncertainties the mean lifetime was determined

138

in a region where the impact from the background uncertainty is minimized. Figures 4.37 (b) and 4.38 (b) show the S/B ratio times significance as a function of the decay time  $\Delta t'_{\rm P}$  showing a maximum indicated by colored areas. The mean lifetimes estimated in this region for the different topology cut sets are summarized in table 4.5.

	Λ	$K_s^0$	cut set
$ au_{ m exp}$ [ps]	$260.4\pm7$	$90.3 \pm 1$	default
	$284.5\pm6$	$84.8\pm1$	loose
	$251.1\pm9$	$93.3\pm1$	tight
$\langle  au_{ m exp}  angle$ [ps]	$265.3\pm10$	$89.5\pm3$	
$ au_{\mathrm{PDG}} \ [\mathrm{ps}]$	$263\pm2$	$89.6\pm2$	

**Table 4.5:** Mean lifetimes  $\tau_{exp}$  estimated from decay curves of  $\Lambda$  hyperons and  $K_s^0$  mesons compared to the PDG values  $\tau_{PDG}$  [5]. The mean lifetime was estimated for different sets of topology cut values, see table 4.6, leading to the mean lifetime  $\langle \tau_{exp} \rangle$ .

	Λ			$K_s^0$		
	default	loose	tight	default	loose	tight
$d_v [\mathrm{mm}]$	> 65	> 60	> 70	> 24	> 22	> 25
$d_1$ [mm]	< 5	< 6	< 5	< 8	< 8	< 7
<i>d</i> <sub>2</sub> [mm]	> 24	> 23	> 25	> 12	> 11	> 13
$d_3 \text{ [mm]}$	> 8	>7	> 9	> 12	> 11	> 13
$d_t \text{ [mm]}$	< 6	< 7	< 6	< 9	< 10	< 8

**Table 4.6:** Overview of variations of topology parameter values applied in the analysis of  $\Lambda$  and  $K_s^0$  in order to test systematic biases when correcting data for acceptance and efficiency. These variations have been tested for the final results (see chapter 5) and for the lifetime measurements presented in this section.

The discrepancies of the indicated values for different cut settings give an orientation on the magnitude of the uncertainty of the topology cuts, however, since the contribution from the background is neglected at this point any deeper conclusion is hampered. Taking the three different settings, a mean lifetime of  $265.3 \pm 12.7$  ps with a standard deviation of  $\sigma = 9.9$  ps for  $\Lambda$  hyperons and  $89.5 \pm 1.7$  ps with  $\sigma = 2.5$  for  $K_s^0$  mesons show a rather good agreement with the expected values  $263 \pm 2$  ps and  $89.6 \pm 1.6$  ps [5] respectively.

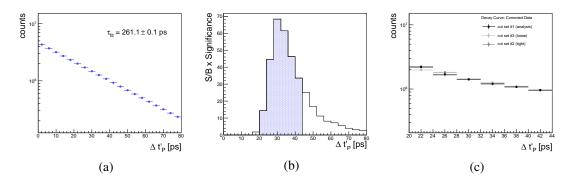


**Figure 4.37:** (a) Decay time distribution for  $\Lambda$  hyperons as obtained from MC simulation with a mean lifetime of  $\tau_{PDG} = 263 \pm 2$  ps. (b) S/B ratio times significance S/ $\sqrt{S+B}$  for the reconstructed  $\Lambda$  invariant mass distributions as a function of the decay time  $\Delta t'_P$ . The mean lifetime is determined in the colored area where the distribution reaches its maximum. (c) Decay time distribution for  $\Lambda$  hyperons from experimental data corrected for acceptance and efficiency for three different cut settings as listed in table 4.6. The values  $\tau_{exp}$  obtained by fitting the function 4.2 to data are summarized in table 4.5 and agree within statistical errors with the PDG value. The systematic uncertainties for the background determination are not considered here.

# 4.4 Search for the Cascade

# 4.4.1 Search for Rare Signals

As listed in table 4.1, the  $\Xi^-$  hyperon decays into a negative pion  $\pi^-$  and a  $\Lambda$  hyperon (BR $\approx$  100%) which then decays dominantly into a proton and  $\pi^-$  (BR= 63.9%). The strategy is similar to the singly-strange  $\Lambda$  hyperons and  $K_s^0$  mesons. The detected final state particles, in this case two negative pions and a proton, have to be identified as discussed in section 4.2.1. First, the invariant mass of proton and  $\pi^-$  pairs is calculated resulting in the mass spectrum for  $\Lambda$  candidates. The  $\Lambda$  hyperons are identified by a selection of  $2\sigma_{\text{Gauss}}$  around their nominal mass  $M_{\text{inv}} = 1115.68 \text{ MeV/c}^2$  where the width is assumed to be  $\sigma = 2.5 \text{ MeV/c}^2$  as estimated from the  $\Lambda$  analysis. In the next step, the  $\Lambda$  candidates are paired with another negative pion giving the invariant mass spectrum of  $\Xi^-$  candidates.

However, there are three major differences requiring an individual treatment of the  $\Xi^-$  reconstruction:

With an excess energy in the Au+Au system of √s<sub>exc</sub> ≈ -840 MeV (compared to ≈ -140 MeV for Λ/K<sup>0</sup><sub>s</sub>), the expected multiplicity of the cascade is significantly lower.

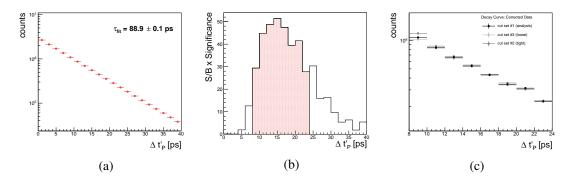


**Figure 4.38:** (a) Decay time distribution for  $K_s^0$  mesons as obtained from MC simulation with a mean lifetime of  $\tau_{PDG} = 89.6 \pm 1.6$  ps. (b) S/B ratio times significance  $S/\sqrt{S+B}$  for the reconstructed  $K_s^0$  invariant mass distributions as a function of the decay time  $\Delta t'_P$ . The mean lifetime is determined in the colored area where the distribution reaches its maximum. (c) Decay time distribution for  $K_s^0$  mesons from experimental data corrected for acceptance and efficiency for three different cut settings as listed in table 4.6. The values  $\tau_{exp}$  obtained by fitting the function 4.2 to data are summarized in table 4.5 and agree within statistical errors with the PDG value. The systematic uncertainties for the background determination are not considered here.

- As mentioned above, the cascade-like topology of doubly-strange Ξ<sup>-</sup> hyperons requires a detection of three final state particles, i.e. two negative pions and a proton. This results in roughly a factor 0.4-0.5 lower acceptance than for Λ hyperons (assuming an average acceptance for negative pions of 40 50%, as estimated from [37].).
- This also leads to a combinatoric which is approximately a factor 10 higher than in the Λ analysis (assuming ≈10 negative pions per event).

The listed items result in a significantly lower expected signal-to-background ratio requiring either a stronger suppression or a more precise determination of the background.

# 4.4.2 Decay Topology and Cut Value Estimation

Since the lifetime is large enough to resolve its decay vertex, constraints on the decay topology can be applied similar to those used for the  $\Lambda$  and  $K_s^0$  reconstruction (see section 4.2.2). However, due to its two-step decay, the topology can be extended by few parameters as shown in figure  $4.39^{25}$ :

d<sub>v1/v2</sub>: Lower limit on the distance of primary vertex to the decay vertex of the mother particle. This criterion is applied for Ξ<sup>-</sup> and Λ. Since the Λ hyperon in this case is not emitted from the primary vertex but originates from a Ξ<sup>-</sup> decay, the parameter d<sub>v2</sub> is expected to be larger on average than in the Λ hyperon analysis as described in section 4.2.2.

 $<sup>^{25}</sup>$  Note, that only the main differences to the single-decay topology are listed.

- d<sub>2,3,4,5</sub>: Lower limit on the distance between the primary vertex and the respective decay tracks extrapolated back to the target. In this case the proton and the pion are emitted further away from the primary vertex and hence the quantities d<sub>2,3</sub> are larger on average. When originating from a Cascade decay the Λ hyperon is not necessarily pointing to the primary vertex anymore. However, since the Λ mass is close to the Ξ<sup>-</sup> mass (m<sub>Λ</sub>/m<sub>Ξ</sub> ≈ 84%) the DCA of Λ to the primary vertex d<sub>5</sub> is still small.
- $\Delta\beta$ : Minimum value for the opening angle of the two daughters. This limitation sorts out close pairs which cannot be resolved in the first drift chambers.
- z<sub>dv(Λ)</sub> > z<sub>dv(Ξ)</sub> > z<sub>prim</sub>: Regarding the beam axis z, the vertices must have the indicated order.

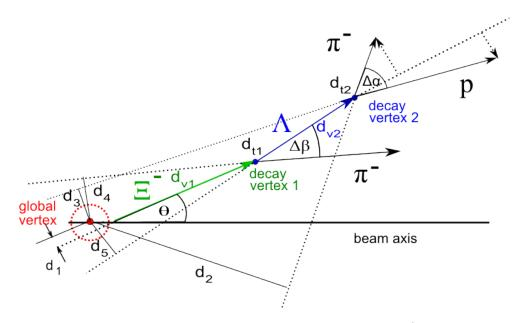


**Figure 4.39:** Topology of the doubly-strange  $\Xi^-$  hyperon decaying into  $\Lambda$  and  $\pi^-$  (BR $\approx 100\%$ ). The  $\Lambda$  hyperon then decays into p and  $\pi^-$ , as was depicted in figure 4.13. Cuts on the topology can be oriented to the values obtained for the  $\Lambda$  decay, yet, slight adaptations accounting for the different kinematics have to be made, see text for details.

In order to estimate the cut values, again, the same strategy as for  $\Lambda$  and  $K_s^0$  can be pursued (see section 4.2.2.4).  $\Xi^-$  hyperons are generated in Pluto, subjected to a full GEANT simulation including its decay and finally propagated through the full analysis chain as used for data. By retrieving their unique Monte Carlo ID, the obtained parameter distributions include exclusively contributions from the generated hadron. On the other hand, the distributions in experimental data are calculated for all identified  $\Lambda^0 - \pi^-$  pairs which are most abundantly emitted from the primary instead of a secondary vertex. Hence, they contain a large background fraction and, if at all, only a small contribution comes from the rarely produced  $\Xi^-$  hadrons. The latter distributions from uncorrelated pairs can hence be considered as a background reference and compared to the

142

#### 4.4. SEARCH FOR THE CASCADE

parameter distributions obtained when retrieving the MC ID in order to estimate a minimum cut value starting from which the signal-to-background ratio will improve.

Figure 4.40 shows the topology parameter distributions for all  $\Xi^-$  candidates in data and for  $\Lambda$  hyperons generated in a MC simulation (green) originating from a  $\Xi^-$  decay. The solid lines indicate where the distribution from simulation starts to be enhanced over the one from data whereas the dashed lines indicate the actually used cut in the later analysis. In order to give an impression on the differences of the decay topology for  $\Lambda$  hyperons originating from a  $\Xi^-$  decay compared to those thermally emitted from the reaction zone, the distributions for the latter ones are generated in a MC simulation and also plotted (blue). A clear difference to  $\Lambda$  hyperons from  $\Xi^-$  decays can be observed for the "off-vertex" parameters  $d_{v2}$ ,  $d_2$  and  $d_3$ .

Figure 4.40 shows the topology parameter distributions for all  $\Xi^-$  candidates in data and for generated  $\Xi^-$  hyperons thermally emitted from the primary vertex (green). The solid lines indicate where the distribution from simulation starts to be enhanced over the one from data whereas the dashed lines indicate the actually used cut in the later analysis. The arrows indicate the region of accepted values.

Certainly, this estimation is rough and only gives a lower limit for the cut values. Tighter constraints are chosen, particularly for the "off-vertex" parameters  $d_{v1/2}$ ,  $d_2$ ,  $d_3$ ,  $d_4$  and  $d_5$ , to obtain a stronger relative loss of background compared to signal counts.

An alternative strategy would be to loosely constrain the discussed parameters in order to maintain signal statistics, however, this means to rely on a very precise background determination, which can be argued based on the systematic uncertainties observed in the  $\Lambda$  analysis.

The default cut values are listed in table 4.7. The resulting invariant mass distribution will be presented in the next chapter 5. Table 4.8 shows the variation values of the topology parameters used for the determination of systematic uncertainties.

$\Lambda$ from $\Xi^-$	decay	$\Xi^-$ decay		
$d_{\mathrm{v2}}  [\mathrm{mm}]$	> 55	$d_{\rm v1}$ [mm]	> 14	
$d_5 \; [mm]$	< 6	$d_1  [mm]$	< 6	
$d_2 [mm]$	> 21	$d_4 \; [mm]$	> 8	
$d_3 [{ m mm}]$	> 5	$d_{\mathrm{t1}}$ [mm]	< 6	
$d_{\mathrm{t2}}$ [mm]	< 6	$\Delta\beta$ [°]	> 15	
$\Delta \alpha$ [°]	> 15			

**Table 4.7:** Overview of topology parameter values applied in the analysis of  $\Xi$  hyperons.

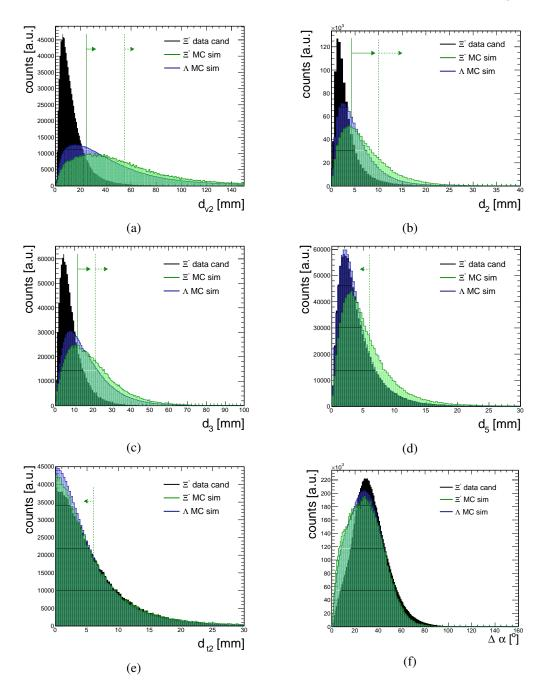


**Figure 4.40:** Topology parameter distributions for all identified  $\Lambda$ - $\pi^-$  pairs in data (black) and for  $\Lambda$  hyperons originating from a decay of primary  $\Xi^-$  hyperons generated in a MC simulation (green). This comparison can be used to estimate the region where a cut on a topology parameter can be applied in order to suppress more background than signal in experimental data. The solid lines indicate where the distribution from simulation starts to be enhanced over the one from data whereas the dashed lines indicate the actually used cut in the later analysis. For comparison  $\Lambda$  hyperons generated in a MC simulation originating from the primary reaction zone are also plotted (blue) where a clear difference to  $\Lambda$  hyperons from  $\Xi^-$  decays can be observed for the "off-vertex" parameters  $d_{v2}$ ,  $d_2$  and  $d_3$ . The distributions from simulation are normalized to the integral of the distribution in data. The arrows indicate the region of accepted values.

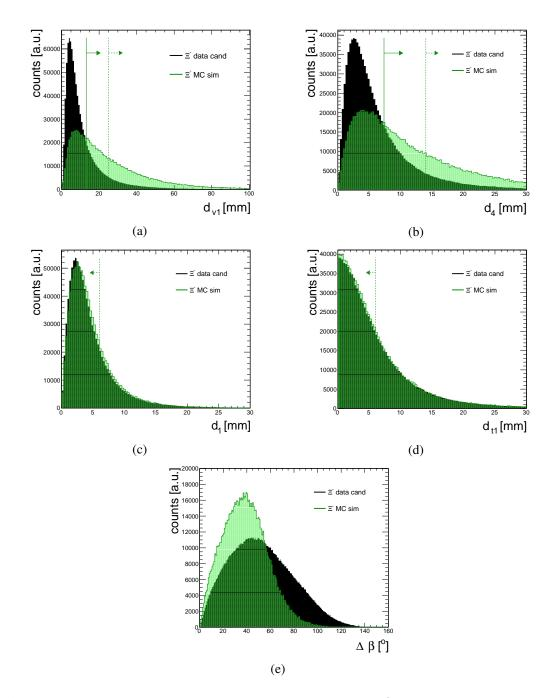


**Figure 4.41:** Topology parameter distributions for all identified  $\Lambda$ - $\pi^-$  pairs in data (black) and for  $\Xi^-$  hyperons generated in a MC simulation (green). This comparison can be used to estimate the region where a cut on a topology parameter can be applied in order to suppress more background than signal in experimental data. The solid lines indicate where the distribution from simulation starts to be enhanced over the one from data whereas the dashed lines indicate the actually used cut in the later analysis. The distributions from simulation are normalized to the integral of the distribution in data. The arrows indicate the region of accepted values.

	$\Lambda$ from $\Xi^-$ decay			$\Xi^-$ decay			
	default	loose	tight		default	loose	tight
$d_{\mathrm{v2}}$ [mm]	> 55	> 45	> 65	$d_{\rm v1}$ [mm]	> 14	> 12	> 16
$d_5 \text{ [mm]}$	< 6	< 7	< 5	$d_1 \text{ [mm]}$	< 6	< 7	< 5
$d_2 \text{ [mm]}$	> 21	> 19	> 23	$d_4 \; [mm]$	> 8	>7	> 9
$d_3 [{ m mm}]$	> 5	> 4	> 6	$d_{\mathrm{t1}}$ [mm]	< 6	< 7	< 5
$d_{\mathrm{t2}}$ [mm]	< 6	< 7	< 5				

**Table 4.8:** Overview of topology cuts variations used in the analysis of  $\Xi$  hyperons to test the robustness of the acceptance and efficiency correction of the upper limit.

# Chapter 5

# **Experimental Results**

In the following, the results of the investigation on the weakly decaying strange hadrons  $\Lambda$  and  $K_s^0$  as well as the doubly-strange  $\Xi^-$  hyperon are presented. The  $\Lambda$  and  $K_s^0$  reconstruction and the extraction of the differential count rates as well as the search for the Cascade have been described in chapter 4.

After correcting the differential yields (see section 4.2.2.6) for acceptance and efficiency of the spectrometer (see section 4.3), the transverse mass spectra are obtained. The corrected number of counts N per transverse mass  $m_t$  and per unit in rapidity y, divided by the transverse mass squared  $m_t^2$ , are plotted as a function of reduced transverse mass  $m_t - m_0$ , such that the Boltzmann relation [256] of the following form

$$\frac{1}{m_t^2} \frac{d^2 M}{dm_t dy_{\rm cm}} = C(y_{\rm cm}) \, \exp\left(-\frac{(m_t - m_0)c^2}{T_B(y)}\right) \tag{5.1}$$

can be applied to fit the data points. The Boltzmann equation describes statistical (particle) emission assuming a thermal source where the Boltzmann temperature  $T_B$  is given by the rapidity-dependent inverse slope of the spectrum<sup>1</sup>. The inverse slope for thermally emitted particles reaches a maximum at mid-rapidity  $y_{mid}$  which is referred to as effective temperature  $T_{eff}$  and which can be related to the kinetic freeze-out temperature  $T_{kin}$  in a thermalized system as follows:

$$T_{\rm kin} = \frac{T_{\rm eff}}{\cosh(y_{\rm cm})}.$$
(5.2)

The fit to data can be used to extrapolate the measured yield to the transverse mass region which is not covered by the acceptance of the detector. Analytic integration of equation 5.1 over  $m_t$  in the interval  $[m_0, +\infty]$  gives the rapidity-differential yield:

$$\left. \frac{dN}{dy} \right|_{y_i} = C(y_i) [(m_0 c^2)^2 T_{\rm B}(y_i) + 2m_0 c^2 T_{\rm B}^2(y_i) + 2T_{\rm B}^3(y_i)],$$
(5.3)

<sup>&</sup>lt;sup>1</sup> The basic assumption here is that the kinematic spectra of particles produced in a heavy-ion collision follow the emission pattern of a source in thermal equilibrium (Maxwell-Boltzmann distribution) based on the concept of a classical ideal gas [257, 258].

which is a function of the nominal mass  $m_0$  of the particle, an integration constant  $C(y_i)$ and the inverse slope  $T_B(y_i)$ . The resulting rapidity density distribution  $dN/dy(y_i)$  is symmetric around mid-rapidity  $y_{\text{mid}}$  for symmetric collisions systems and integration of measured data plus an extrapolation to the unmeasured rapidity regions provides the total particle production yield in full phase space. The width  $\sigma_y$  of the rapidity density distribution dN/dy, assuming a purely thermal scenario neglecting flow contributions, can be approximated by:

$$\sigma_y = \sqrt{\frac{T_{\text{eff}}}{m_0 c^2}}.$$
(5.4)

The same procedure is conducted as a function of centrality C according to the four centrality classes from most central (0 - 10%) to semi-peripheral (30 - 40%) collisions, which were estimated in [233].

In the following, the resulting transverse mass spectra and rapidity density distributions are presented for  $\Lambda$  hyperons in section 5.1 and  $K_s^0$  mesons in section 5.2. Correspondingly, the evaluation of statistical and systematic uncertainties to the rapidity density and inverse slope distributions and the extraction of the total yield will be explained in detail.

# **5.1** $\Lambda$ **Production**

In the following the results for  $\Lambda$  hyperons corrected for acceptance and reconstruction efficiency are presented and systematic uncertainties estimated. The reconstructed  $\Lambda$  hyperon yield always includes a contribution of  $\Sigma^0$  hyperons, which decay electromagnetically exclusively into  $\Lambda$  and a  $\gamma$ -photon (BR $\approx 100\%$ ). The latter one cannot be detected with the current experimental setup. Thus in the following, when referring to  $\Lambda$  production, this actually has to be understood as  $\Lambda + \Sigma^0$  production.

## 5.1.1 Transverse Mass Spectra

The transverse mass spectra for  $\Lambda$  hyperons are presented in figure 5.1 (a) integrated over the 40% most central events ranging from backward-rapidities (filled symbols) starting at y = 0.09 and ending in the forward-rapidity region (open symbols) at y = 0.89 in rapidity steps of  $\Delta y = 0.1$ . Displayed is the number of produced particles per event, per transverse mass and per unit rapidity normalized to the transverse mass squared  $m_t^2$ .

The statistical errors on the data points are determined as described in section 4.2.2.4. Figure 5.1 (b) shows the ratio of data points to the Boltzmann fit for three different rapidities corresponding to very backward-, mid-backward- and mid-rapidity. A description assuming a Boltzmann-like behavior with reduced transverse mass  $m_t - m_0$  seems reasonable within statistical uncertainties. Hence, in order to determine the full yield per unit rapidity, the measured data points plus the fit function in the unmeasured phase space are integrated.

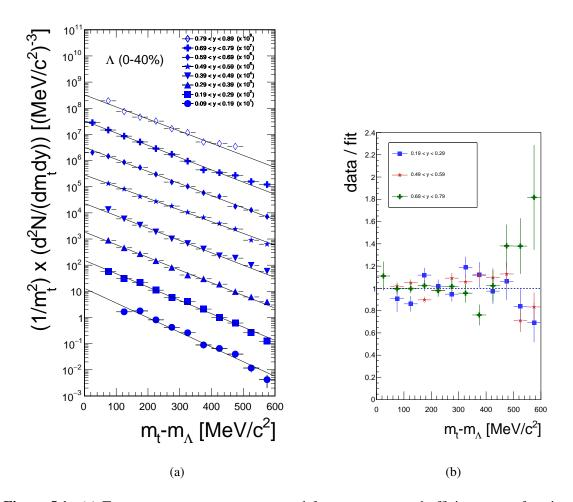


**Figure 5.1:** (a) Transverse mass spectra corrected for acceptance and efficiency as a function of rapidity for  $\Lambda$  hyperons for the 40% most central data. For better visibility, the spectra are scaled as indicated in the legend. Filled symbols refer to data measured in the backward-rapidity hemisphere and at mid-rapidity, open symbols to data at forward-rapidities. (b) Ratio of data to the corresponding Boltzmann fit for three different rapidities. The experimental data points indicate fluctuations slightly exceeding statistical uncertainties with respect to the Boltzmann parametrization.

## 5.1.2 Rapidity Density and Inverse Slope Distributions

Figure 5.2 (a) shows the rapidity density distribution obtained by integration of the transverse mass spectra, normalized to the number of events as a function of center-of-mass rapidity  $y_{\rm cm}$ . The filled circles indicate the measured 40% most central data whereas the open symbols are the same data points reflected around mid-rapidity. To derive the total particle production yield of  $Mult_{\rm tot} = (3.97 \pm 0.06^{\rm stat} \pm 0.06^{\rm sys}_{\rm Cut} \pm 0.04^{\rm sys}_{\rm Extrapol}) \times 10^{-2}$ , a Gaussian distribution is fitted to data and can be used to estimate the yield outside the acceptance. The assumption of a Gaussian-shaped rapidity density distribution is tested and will be discussed later in this section.

In figure 5.2 (b) the inverse slope  $T_{\rm B}$  is depicted as a function of center-of-mass rapidity  $y_{\rm cm}$ . The distribution can be described by an inverse *cosh* dependence as a function of rapidity y according to eq. 5.2. The measured value at mid-rapidity is defined as the effective temperature and amounts to  $T_{\rm eff} = (93 \pm 2^{\rm stat} \pm 4^{\rm sys})$  MeV. The indicated statistical and systematic (boxes) uncertainties on the rapidity density and the inverse slope distributions will be described in detail in the following section.

#### 5.1.2.1 Systematic Uncertainties on Rapidity Density and Inverse Slope Distributions

Systematic uncertainties are measurement errors which are not due to statistical fluctuations in real or simulated data samples [255]. The potential sources for systematic uncertainties are numerous and have to be either tested for an impact on the analysis outcome or, if possible, identified and then eliminated or bypassed. Typical sources for systematic uncertainties, having an impact on the results of analysis exceeding statistical uncertainties, were found to be:

- 1. particle identification,
- 2. topology cuts,
- 3. background determination,
- 4. uncertainty due to underlying theoretical models used for acceptance and efficiency correction.

A systematic bias has been found when identifying the charged decay products by using graphical cuts for the specific velocity-momentum dependence of particle species (for a detailed description of the method, see section 3.6.1.1). This bias was found to be negligible for charged tracks emitted from or close to the primary vertex [37] and appears to be restricted to the secondary vertex analysis. The reconstructed momentum and hence the calculated velocity of charged particles are determined under the assumption that the production occurs in the target. Since this is not the case for particles originating from a long-lived massive hadron, their velocity is underestimated and hence the mass shifted towards higher values. Due to their lower mass, this effect will have a stronger impact on pions relative to protons.

Figure 5.3 shows the significant discrepancy for the resulting rapidity density distributions for  $\Lambda$  hyperons indicating a strong bias of about 10% towards lower values for an identification based on the velocity-momentum information. The source for this one-sided bias could not

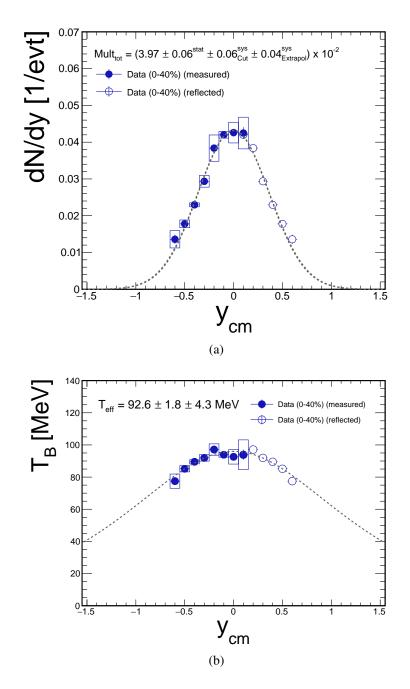
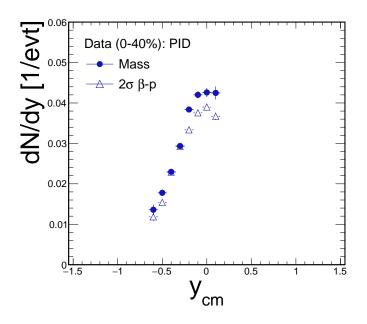


Figure 5.2: (a) Rapidity density distribution dN/dy for  $\Lambda$  hyperons as a function of center-of-mass rapidity normalized to the number of events for 40% most central data (filled circles). The measured data is reflected at mid-rapidity  $y_{\text{mid}}$  (open circles). A Gaussian distribution is fitted to the measured data points and can be used to determine the yield in the region of unmeasured rapidities. Adding this contribution to the measured yield gives the full  $\Lambda + \Sigma^0$  multiplicity  $Mult_{\text{tot}}$ . (b) Inverse slope parameter  $T_B$  for  $\Lambda$  hyperons as a function of center-of-mass rapidity as extracted from a fit of equation 5.1 to the transverse mass spectra. The distribution can be described by an equation of type 5.2 and the inverse slope at mid-rapidity gives the effective temperature  $T_{\text{eff}}$ .

yet be identified and hence must be circumvented by using a looser constraint which is given by the selection on the mass using cuts in a wide mass window  $0 < m_{\pi} < 300 \text{ MeV/c}^2$  and  $700 < m_{p} < 1200 \text{ MeV/c}^2$  around the expected pion and proton mass respectively.



**Figure 5.3:** Rapidity density distribution for  $\Lambda$  hyperons when using an identification for the daughter hadrons based on either loose mass cuts (filled circles) or on the  $\beta$ -p information (open triangles) according to section 3.6.1.1.

It is in particular the interplay between item 2 and 3 in the above list which gives the largest contribution to the remaining overall systematic uncertainty. On the one hand, the topology cuts give a significant reduction of the underlying background to the signal and hence its uncertainty, whereas on the other hand any tight constraint in analysis may increase the uncertainty of the result arising from discrepancies in simulation compared to data distributions. The decay curve measurements extracting the lifetimes described in 4.3.3 provide a solid ground for the acceptance and efficiency correction when using cuts on the decay topology. Furthermore, the robustness of the correction has been tested on the derived lifetimes when varying these cuts, as presented in table 4.5. The impact of the same three sets of cut values on the rapidity density distribution is shown in figure 5.4 (a).

The topology cut values have been varied such that in one case more background from uncorrelated daughter pairs is rejected by requiring stronger constraints (*tight* cuts), whereas in the other case the selection windows are widened (*loose* cuts) leading to a deterioration of the signalto-background ratio in the invariant mass spectra. The impact on the rapidity density distribution is visible, however, not exceeding 7% around mid-rapidity at  $-0.05 < y_{cm} < -0.15$  which may partly also be attributed to a change in the S/B ratio. Only at the edge of acceptance in the backward-rapidity hemisphere ( $-0.65 < y_{cm} < -0.55$ ) a stronger deviation by about 23% is observed. A discrepancy of maximum 2% in the region from  $-0.55 < y_{cm} < -0.15$ , where the S/B ratio is the highest (see 4.32), is found to be negligible when comparing to the statistical uncertainties. Figure 5.4 (b) shows the effect of widening the region of background normalization (see 4.2.2.4) on the dN/dy spectrum varying up to 10% at most of the negative rapidities. At the edges of acceptance a deviation of 13% at forward rapidity and 20% at backward rapidity is ob-

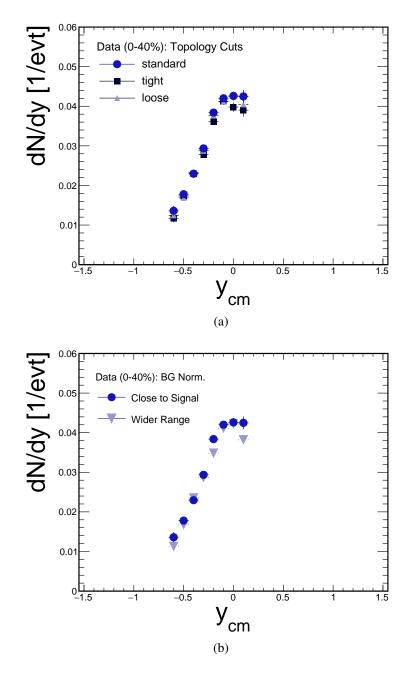


**Figure 5.4:** (a) Rapidity density distribution for  $\Lambda$  hyperons for different sets of topology cuts as indicated in table 4.6. The alternative cut values are either stronger (dark black squares) or looser (light blue triangles) than the cut values used as standard (blue circles). Their absolute deviation from the data points are taken as systematic uncertainty symmetrically around the values used as standard. (b) Rapidity density distribution for  $\Lambda$  hyperons using different regions for background normalization as indicated in figure 4.22. The background is normalized either in small (blue circles) or wider (light blue) sidebands close to the signal (in both cases at least  $3\sigma$  away from the mean). Their absolute deviation from the data points are taken as systematic uncertainty symmetrically around the values used as default.

served. In general, larger systematic uncertainties are found at forward- and mid-rapidity which can be related to the worse reconstruction efficiency at low polar angles for forward boosted  $\Lambda$  hyperons and hence the reconstructed final-state protons.

The two investigated sources of uncertainty are strongly correlated and complicated to disentangle. Furthermore, the studied variations are not independent since a reduced data set due to tighter cuts is fully contained in the default sample which again is a subset of the enlarged data set when loosening the cuts. On the other hand, choosing independent sets of cut values would reduce the statistics tremendously such that the statistical uncertainty would exceed systematic ones and would hamper any conclusions on systematic errors. However, in both cases, the variations do not seem to uncover a systematic bias to the obtained results. The overall systematic uncertainty is estimated point-to-point as the absolute maximum deviation of all investigated variations symmetric around the default value. The systematic uncertainties on the inverse slopes  $T_{\rm B}$  as a function of center-of-mass rapidity have been determined by applying the same variations.

The reconstruction efficiencies and purity of particle identification strongly depend on the track multiplicities reached in an event. The detector efficiencies depend on the occupancies in each sub-system and with it also the reconstruction efficiency including tracking and particle identification. Therefore, the particles are generated in a MC simulation and then embedded into a realistic event-by-event environment modeling the multiplicities which are present in Au+Au collisions. In this analysis two approaches are investigated: embedding into events either from the same recorded data set or as generated in UrQMD simulations. A systematic discrepancy of about 15% around mid-rapidity between both approaches was observed and the source for the problem could not yet be identified which is an on-going investigation. For the analysis of single pions or protons, the deviation between both methods does not exceed few percent. Up to now, the embedding of the simulated hadrons into events generated with UrQMD was tested in more detail (e.g. lifetime measurements) and is hence preferred.

#### 5.1.2.2 Statistical and Systematic Uncertainties on Total Yield

The total particle production yield per event (*multiplicity*) can be determined by integrating the measured data points in the rapidity density distribution which is depicted in figure 5.2 for  $\Lambda$  hyperons. The yields per unit rapidity can be considered to be symmetric with respect to midrapidity and hence the reflected data points can be integrated in the region where no measured points are available. The data can be fitted with a Gaussian showing a reasonable matching with the measured data points. This fit can be used to estimate, first, the yield in the phase space region not covered by the detector acceptance and, secondly, the statistical uncertainty on the total yield which is about  $\Delta N_{\text{tot}}^{\text{stat}} \approx 2\%$ .

However, the shape of the rapidity density distribution is of complex nature and strongly depends on the kinematics of the reaction involving stopping and energy redistribution in the dense medium, hence its determination is no trivial task. Therefore, the assumption of a Gaussian distribution is nothing more than an educated guess and the extrapolated yield has to be investigated in more detail. Figure 5.5 shows the dN/dy distribution assuming besides a Gaussian-like shape (gray dashed line) also a rapidity density distribution as obtained from the UrQMD (orange),

#### 5.1. $\Lambda$ PRODUCTION

HSD (green) and IQMD (purple) simulations which are normalized to the integral of measured data points. In case of a Gaussian distribution the extrapolated yield covers  $\approx 7.5\%$  of the total multiplicity. In case of the transport models the yield fractions range from  $\approx 5\%$  to 8% of the total multiplicity. For the estimation of the uncertainty in the extrapolation, for each model prediction the fraction of the yield in the region of unmeasured phase space to the integrated yield is calculated. The difference of this fraction to the one obtained by assuming a Gaussian distribution is then determined and averaged over the three models yielding in  $\Delta N_{\rm Extrapol}^{\rm sys} \approx 1\%$ . The uncertainty on the extrapolation is moderate as the rapidity density distribution is rather narrow.

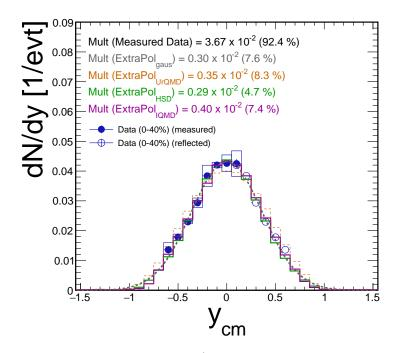


**Figure 5.5:** Rapidity density distribution for  $\Lambda$  hyperons as a function of center-of-mass rapidity normalized to the number of events for 40% most central data (filled circles). The measured data is reflected at mid-rapidity  $y_{\text{mid}}$  (open circles). For an extrapolation of the multiplicity to unmeasured phase space either a Gaussian fit to data (gray dashed line) or predictions of the dN/dy distribution by the UrQMD, HSD and IQMD transport models (orange, green and purple) are assumed. Therefore, the model predictions are normalized to the integral of measured data points. For each model distribution, the fraction of the yield in the region of unmeasured phase space to the corresponding fully integrated yield is calculated and then the difference to the fraction obtained by assuming a Gaussian distribution is determined. The average deviation is taken as the systematic uncertainty which is estimated to roughly 1.5%. Including the reflected data points, more than 90% of the total yield is within the acceptance.

Anyhow, a closer look reveals that the shape obtained with UrQMD is rather flat around mid-rapidity and is slightly broadened towards beam- and target rapidity, which can be attributed to an incomplete stopping. This kinematic observable is quite sensitive to the centrality of the collision which suggests a centrality-differential comparison involving further transport models, which is also conducted within this investigation and will be discussed in chapter 6, section 6.3.

For the estimation of the systematic uncertainty arising from the cut variations according to the previous subsection 5.1.2.1, a Gaussian distribution is fitted to the data points assuming point-to-point errors as indicated by the boxes in the dN/dy distribution. This gives an additional contribution of  $\Delta N_{\text{Cut}}^{\text{sys}} \approx 1.5\%$  to the overall uncertainty.

### 5.1.3 Centrality-differential Analysis

The high statistic data set allows for an analysis as a function of centrality for the 0 - 40% most central events in steps of 10%. Therefore, the very same steps undertaken in the previous subsections 5.1.1 and 5.1.2 to obtain the transverse mass spectra and rapidity density distributions are conducted in four centrality classes from most central (0 - 10%) to semi-peripheral (30 - 40%) collisions. The rapidity density distributions for  $\Lambda$  hyperons are presented in figure 5.6 each described by a Gaussian parametrization. In the two more central classes of 0 - 10% and 10 - 20%, measured data ranges only up to mid-rapidity which can be attributed to a lower reconstruction efficiency for protons due to higher track densities in particular at forward-rapidity.

The total yields are determined for each centrality class identically as for data integrated over 0 - 40% and are summarized in table 5.1 together with the effective temperatures  $T_{\rm eff}$ . As anticipated, the multiplicity rises when going from semi-peripheral (yellow circles) to most central (blue stars) data, where the system size and hence the number of participating nucleons  $A_{\rm part}$  is much larger. In order to look beyond this rather trivial dependence the yields are normalized to  $A_{\rm part}$  and hence the volume of the collision zone. Figure 5.7 (a) shows the dependence of the  $\Lambda$  multiplicity per mean number of participating nucleons  $Mult/\langle A_{\rm part}\rangle$  per centrality class as a function of  $\langle A_{\rm part} \rangle$ . The systematic errors on  $Mult/\langle A_{\rm part} \rangle$ , indicated as boxes, are obtained by adding the statistical and systematic uncertainties of the multiplicity in quadrature whereas the uncertainties on the x-axis for  $\langle A_{\rm part} \rangle$  are taken from [233] and listed in table 3.2.

A rise is observed with increasing centrality indicating a sensitivity of the  $\Lambda$  hyperon production to multi-particle interactions. In order to get a more quantitative estimation on this rise, a parametrization of the type  $M \propto \langle A_{part} \rangle^{\alpha}$  is fitted to data. A linear increase of multiplicity Multwith centrality, as it is e.g. the case for negative pions  $\pi^-$  in this Au+Au system as demonstrated in [37], will give a value for the exponent  $\alpha$  at unity, hence values above unity indicate a rise stronger than linear. The fit of the parametrization to data gives a value of  $\alpha = 1.37 \pm 0.1$ .

Figure 5.7 (b) shows the rise of the effective temperature  $T_{\text{eff}}$  as a function of  $\langle A_{\text{part}} \rangle$ . The data points indicate an increase of  $T_{\text{eff}}$  with centrality. The data points are parametrized by a simple first-order polynomial function giving a slope of  $m = 0.12 \pm 0.02$  MeV.

The width assuming a Gaussian-like rapidity density distribution as a function  $\langle A_{\text{part}} \rangle$  is depicted in figure 5.7 (c), where no indication for a rise is observed with increasing centrality. As no clear trend with increasing centrality can be observed, the mean of the widths for the four centrality classes is given by  $\langle \sigma_{\text{Gauss}} \rangle = 0.35 \pm 0.01$ . The systematic uncertainty of the width is determined as the variation of the width when fitting a Gaussian parameterization to the rapidity density distribution assuming the given point-to-point systematic uncertainties, as indicated by the boxes in figure 5.2.

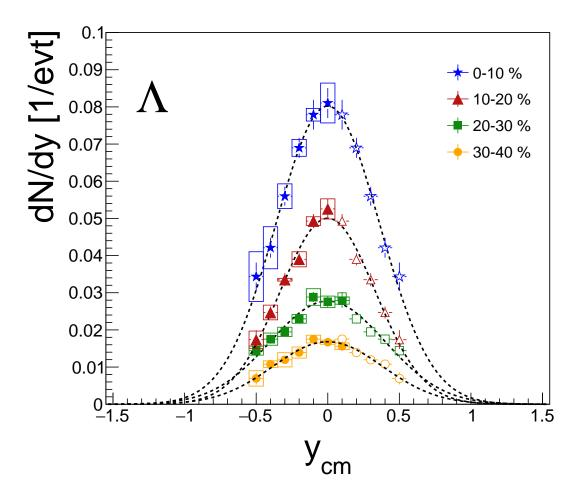


**Figure 5.6:** Rapidity density distributions of  $\Lambda$  hyperons as a function of four different centrality classes from most central 0 - 10% to semi-peripheral 30 - 40% collisions normalized to the number of events per class. The classes have been determined in [233]. The corresponding impact parameter distributions have been shown in section 3.4.3.

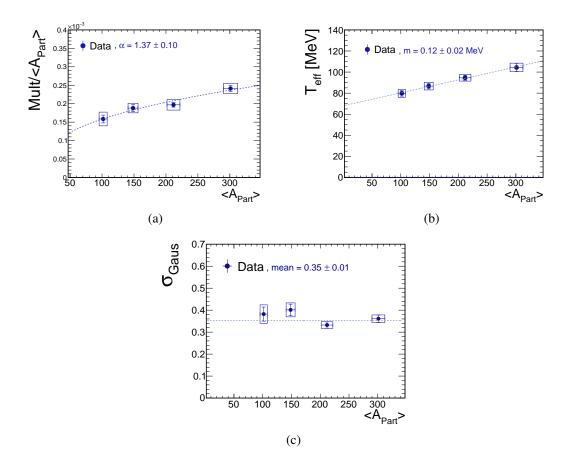


Figure 5.7: (a)  $\Lambda$  hyperon multiplicity normalized to the mean number of participants per centrality class  $Mult/\langle A_{part}\rangle$  as a function of  $\langle A_{part}\rangle$ , which is proportional to centrality. The data points are fitted with a parametrization of the type  $M \propto \langle A_{part}\rangle^{\alpha}$  which gives a value for the exponent of  $\alpha = 1.37 \pm 0.1$ . (b) Effective temperatures  $T_{\rm eff}$ , as extracted from the inverse slope distributions, as a function of centrality. The data points show a reasonable agreement with a linear parametrization giving a slope of  $m = 0.12 \pm 0.01$  MeV. (c) Gaussian width  $\sigma_{\rm Gauss}$  of the rapidity density distribution as a function of  $\langle A_{\rm part} \rangle$  indicating no significant dependence on centrality. The mean width is determined to  $\langle \sigma_{\rm Gauss} \rangle = 0.35 \pm 0.01$ .

# **5.2** $K_s^0$ **Production**

In the following the results on the same observables as for the  $\Lambda$  hyperons are shown for  $K_s^0$  mesons. Due to its similarities in both analysis, the systematic uncertainties are estimated as described in the previous section 5.1, if not stated otherwise.

## 5.2.1 Transverse Mass Spectra

Figure 5.8 (a) shows the transverse mass spectra for  $K_s^0$  mesons integrated over the 40% most central events ranging from backward-rapidities (filled symbols) at y = 0.09 and ending in the forward-rapidity region (open symbols) at y = 1.49 in rapidity steps of  $\Delta y = 0.1$ . Displayed is the number of produced particles per event, per transverse mass and per unit rapidity normalized to the transverse mass squared  $m_t^2$  as a function of reduced transverse mass  $m_t - m_0$ . A strikingly larger coverage is observed for  $K_s^0$  mesons compared to  $\Lambda$  hyperons in the region at forwardrapidities ( $y > y_{mid} = 0.74$ ) for reasons discussed in subsection 4.2.2.2.

In this representation the data can be parametrized by a Boltzmann function of type eq. 5.1 and used to extrapolate the yield to the unmeasured reduced transverse mass region by analytic integration according to eq. 5.3.

Figure 5.8 (b) shows the ratio of data points to the fit of the Boltzmann parametrization for three selected rapidities at backward-, mid- and forward-rapidity. A description assuming a Boltzmann-like behavior with reduced transverse mass  $m_t - m_0$  seems reasonable within statistical uncertainties. In order to determine the full yield in  $m_t - m_0$ , the measured data points plus the fit function in the unmeasured phase space region are integrated.

### 5.2.2 Rapidity Density and Inverse Slope Distributions

Figure 5.9 (a) shows the rapidity density distribution, obtained by integration of the transverse mass spectra, normalized to the number of events as a function of center-of-mass rapidity  $y_{\rm cm}$ . The filled circles indicate the measured 40% most central data whereas the open symbols in the forward-rapidity region are the data points at backward-rapidities reflected at mid-rapidity giving an impression of the symmetry of the measured data points. The acceptance of the spectrometer for  $K_s^0$  mesons is almost identical for forward- and backward rapidities, however, with slightly larger systematic uncertainties in the region at very forward-rapidities. To derive the total particle production yield of  $Mult_{tot} = (1.54 \pm 0.03^{stat} \pm 0.05^{sys}_{Cut} \pm 0.15^{sys}_{Extrapol}) \times 10^{-2}$ , a Gaussian distribution is fitted to data and can be used to estimate the yield outside the acceptance.

In figure 5.9 (b) the inverse slope  $T_B$  is depicted as a function of center-of-mass rapidity  $y_{\rm cm}$ . The distribution can be described by an inverse *cosh* dependence as a function of rapidity y according to eq. 5.2. The measured value at mid-rapidity is defined as the effective temperature and gives  $T_{\rm eff} = (97.5 \pm 0.7^{\rm stat} \pm 2.6^{\rm sys})$  MeV.

The indicated statistical and systematic (boxes) uncertainties on the rapidity density and the inverse slope distributions will be described in detail in the following section.

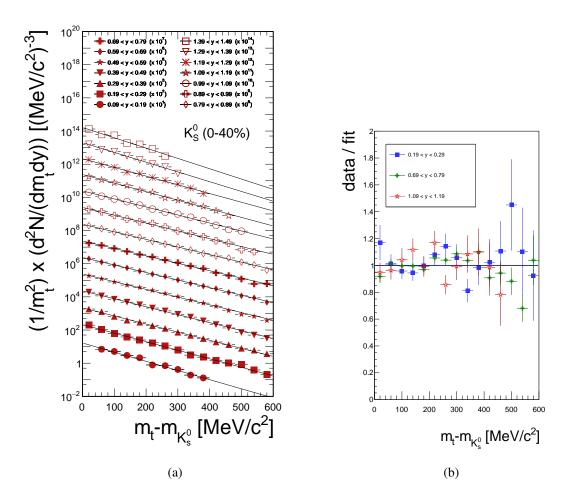


**Figure 5.8:** (a) Transverse mass spectra corrected for acceptance and efficiency as a function of rapidity for  $K_s^0$  mesons for the 40% most central data. For better visibility, the spectra are scaled as indicated in the legend. Filled symbols refer to data measured in the backward-rapidity hemisphere and at mid-rapidity, open symbols to data at forward-rapidities. (b) Ratio of data to the corresponding Boltzmann fit at backward-, forward- and mid-rapidity. Within statistical uncertainties the Boltzmann parametrization provides a satisfactory description of experimental data.

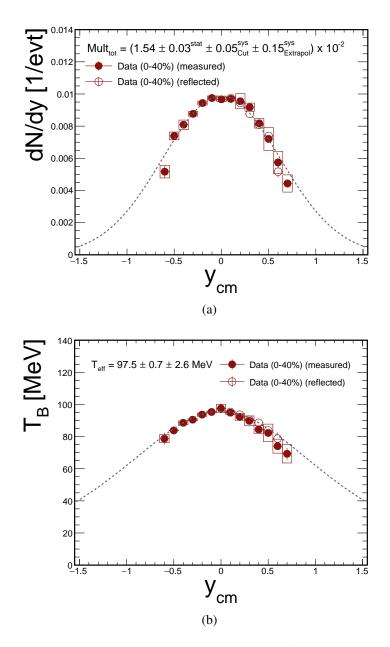


**Figure 5.9:** (a) Rapidity density distribution dN/dy for  $K_s^0$  mesons as a function of center-of-mass rapidity normalized to the number of events for 40% most central data (filled circles). The measured data is reflected at mid-rapidity  $y_{mid}$  (open circles). A Gaussian distribution is fitted to the measured data points and can be used to determine the yield in the region of unmeasured rapidities. Adding this contribution to the measured yield gives the full  $K_s^0$  production yield per event  $Mult_{tot}$ . (b) Inverse slope parameter  $T_B$  for  $K_s^0$  mesons as a function of center-of-mass rapidity as extracted from a fit of equation 5.1 to the transverse mass spectra. The distribution can be described by an equation of type 5.2 and the inverse slope at mid-rapidity gives the effective temperature  $T_{eff}$ .

#### 5.2.2.1 Systematic Uncertainties on Rapidity Density and Inverse Slope Distribution

The systematic bias found when identifying the charged decay products by using graphical cuts for the specific velocity-momentum dependence of particle species was discussed in section 5.1.2.1. Since this bias was found to be more severe for pions than the much heavier protons, this effect will emerge more significantly in the  $K_s^0$  spectra involving two pions in the final state. Figure 5.10 shows the significant difference for the resulting rapidity density distributions for  $K_s^0$  mesons indicating a strong bias towards lower values for an identification based on the velocity-momentum information. Compared to  $\Lambda$  hyperons, a looser cut of only  $3\sigma$  around the expected velocity-momentum curve was used for charged pions, anyhow, showing a stronger bias of about 15 - 25%.

The deterioration in signal-to-background ratio when using a rather loose selection on the mass spectra cutting in a window of  $0 < m_{\pi} < 300 \text{ MeV/c}^2$  can be compensated by applying stronger topology cuts.

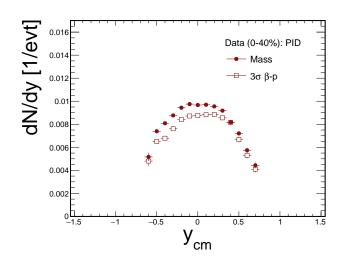


**Figure 5.10:** (a) Rapidity density distribution for  $K_s^0$  mesons when using an identification for the daughter pions based on either loose mass cuts (filled circles) or on the  $\beta$ -p information (open squares) according to 3.6.1.1. A strong bias towards lower values is observed when using the much stronger graphical cut located  $3\sigma$  around the calculated pion curves in the  $\beta$ -p plane. This systematic bias is avoided by using cuts in a wide mass window  $0 < m < 300 \text{ MeV/c}^2$  around the expected pion mass.

The impact of the topology cuts on the systematic uncertainty of the corrected  $K_s^0$  yields has been investigated by decay curve measurements, see section 4.3.3. The direct contribution to the rapidity density distribution was tested by comparing the outcome for the three different cut sets listed in table 4.6, pursuing the same strategy as for  $\Lambda$  hyperons of tightening and loosening the default cut values. The result is demonstrated in figure 5.11 (a). A deviation of maximum 13% is observed, however, at the very edges of acceptance at forward rapidity. For most of the phase space only small deviations of about 2 - 5% are obtained.

Figure 5.11 (b) shows that the contribution from a background variation has only slight influence on the differential rates which does not exceed statistical fluctuations. This is in particular striking as the alternative normalization of the mixed-event background to the invariant mass spectrum of  $K_s^0$  candidates involves the full phase space region, see section 4.2.2.4. This observation points to a precise determination of the background from uncorrelated charged pions to the  $K_s^0$  mass spectrum via the mixed-event method.

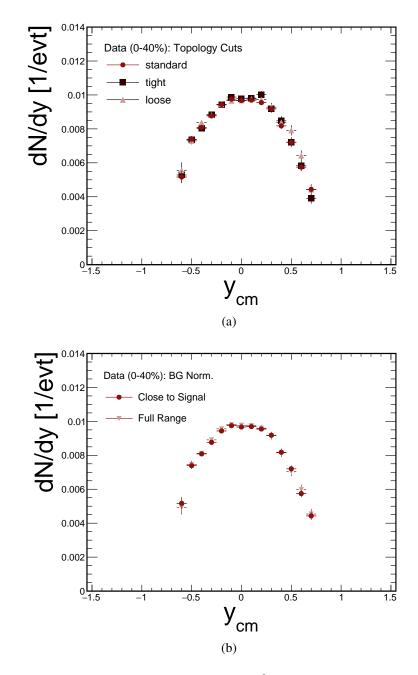


**Figure 5.11:** (a) Rapidity density distribution for  $K_s^0$  mesons for different sets of topology cuts as indicated in table 4.6. The alternative cut values are either stronger (dark red squares) or looser (light red triangles) than the cut values used as standard (red circles). Their absolute deviation from the data points are taken as systematic uncertainty symmetrically around the values used as standard. (b) Rapidity density distribution for  $K_s^0$  mesons using different regions for background normalization as indicated in figure 4.22. The background is normalized either in small sidebands close to the signal (red circles) or in the full range (light red) excluding the signal region (in both cases at least  $3\sigma$  away from the mean). Their absolute deviation from the data points are taken as systematic uncertainty symmetrically around the values systematic uncertainty symmetrically around the values at least  $3\sigma$  away from the mean). Their absolute deviation from the data points are taken as systematic uncertainty symmetrically around the values used as standard.

The influence on the rapidity density distribution, due to assumptions made when correcting data for acceptance and efficiency of the spectrometer, is also tested for  $K_s^0$  mesons. Similar to the  $\Lambda$  analysis, a systematic discrepancy of about 15% around mid-rapidity between both approaches was observed and the source for the problem was not yet found. The investigations are on-going.

#### 5.2.2.2 Statistical and Systematic Uncertainties on Total Yield

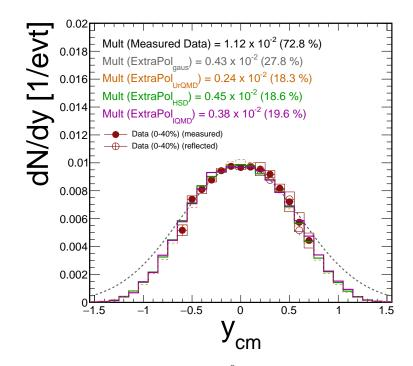
The total particle production yield per event (*multiplicity*) can be determined by integrating the measured data points (filled circles) in the rapidity density distribution which is depicted in figure 5.9 for  $K_s^0$  mesons. The data can be fitted with a Gaussian showing a reasonable agreement within systematic uncertainties. The Gaussian can be used to estimate, first, the yield in the phase space region not covered by the detector acceptance and, secondly, the statistical uncertainty on the total yield which is below  $\Delta N_{\text{tot}}^{\text{stat}} < 1\%$ . More than in case of the  $\Lambda$  hyperon, a deviation from a Gaussian is observed for the shape of the rapidity density distribution, indicating a shift away from mid-rapidity resulting in a flattening at  $y_{\text{cm}} = 0$ .

Figure 5.12 shows the dN/dy distribution assuming besides a Gaussian-like shape (gray dashed line) also a rapidity density distribution as obtained from UrQMD (orange), HSD (green) and IQMD (purple) simulations which are normalized to the integral of measured data points. In case of a Gaussian distribution the extrapolated yield covers  $\approx 27.2\%$ , in case of a comparison with the transport models about  $\approx 19\%$  of the total yield. Though the acceptance is much higher for  $K_s^0$  mesons than for  $\Lambda$  hyperons, the uncertainty from the extrapolation is higher due to the larger width of the spectrum. For the estimation of the uncertainty in the extrapolation, for each model prediction the fraction of the yield in the region of unmeasured phase space to the integrated yield is calculated. The difference of this fraction to the one obtained by assuming a Gaussian distribution is then determined and averaged over the three models yielding in  $\Delta N_{\rm Extrapol}^{\rm sys} \approx 9\%$ . In this particular case, the transport models do not differ significantly, however, when performing a centrality-differential analysis, the models show stronger deviations in their predictions on the shape of the rapidity density distribution from one centrality class to the next. By calculating the average, a smoother estimate on the uncertainty of the extrapolation can be guaranteed.

For the estimation of the systematic uncertainty arising from the cut variations according to the previous subsection 5.2.2.1, a Gaussian distribution is fitted to the data points assuming point-to-point errors as indicated by the boxes in the dN/dy distribution. This gives an additional contribution of  $\Delta N_{\text{Cut}}^{\text{sys}} \approx 3\%$  to the overall uncertainty.

## 5.2.3 Centrality-differential Analysis

The high statistic data set allows for an analysis as a function of centrality for the 0 - 40% most central events in steps of 10%, according to section 3.4.3. Therefore, the very same steps undertaken in the previous subsections 5.2.1 and 5.2.2 to obtain the transverse mass spectra and rapidity density distributions are conducted in four centrality classes from most central (0 - 10%) to semi-peripheral (30 - 40%) collisions. The rapidity density distributions for  $K_s^0$  mesons are



**Figure 5.12:** Rapidity density distribution for  $K_s^0$  mesons as a function of center-of-mass rapidity normalized to the number of events for 40% most central data (filled circles). The measured data is reflected at mid-rapidity  $y_{mid}$  (open circles). For an extrapolation of the multiplicity to unmeasured phase space either a Gaussian fit to data (gray dashed line) or a prediction of the dN/dy distribution by the UrQMD, HSD and IQMD transport models (orange, green and purple) are assumed. Therefore, the model predictions are normalized to the integral of measured data points. For each model distribution, the fraction of the yield in the region of unmeasured phase space to the corresponding integrated yield is calculated and then the deviation to the fraction obtained by assuming a Gaussian distribution is determined. The average deviation is taken as the systematic uncertainty which is estimated to roughly 10%. Including the reflected data points, more than 70% of the total yield is within the acceptance.

presented in figure 5.13 each fitted with a Gaussian parametrization. The obtained systematic uncertainties are comparable going from semi-central to most central collisions and of the order of maximum 5% at mid-rapidity. Same as for data integrated over 0 - 40% most central collisions, the uncertainty increases strongly in the region of positive center-of-mass rapidities due to the much lower reconstruction efficiencies, which was discussed in section 4.3, reaching up to 35% for 30 - 40% and 20% for 0 - 10% most central data. Furthermore, a slight shift of the acceptance towards backward rapidity is observed for most-central compared to semi-peripheral events where the charged particle reconstruction is more stable and the signal-to-background ratio higher. However, on the other hand this may be compensated by an overall decrease of the S/B ratio towards more central events.

The multiplicities per centrality class are summarized in table 5.1 together with the effective temperatures  $T_{\text{eff}}$ . Figure 5.14 (a) shows the dependence of the  $K_s^0$  multiplicity per mean number of participating nucleons per centrality class  $Mult/\langle A_{\text{part}}\rangle$  as a function of  $\langle A_{\text{part}}\rangle$ . The systematic errors on  $Mult/\langle A_{\text{part}}\rangle$ , indicated as boxes, are obtained by adding the corresponding statistical and systematic uncertainties of the multiplicity in quadrature whereas the uncertainties on the x-axis for  $\langle A_{\text{part}}\rangle$  are taken from [233].

A similar rise is observed with increasing centrality as for the  $\Lambda$  hyperon multiplicity per  $\langle A_{\text{part}} \rangle$ . Fitting a parametrization of type  $M \propto \langle A_{\text{part}} \rangle^{\alpha}$  gives an exponent of  $\alpha = 1.24 \pm 0.12$  indicating a more than linear increase with centrality agreeing within uncertainties with the same parameter obtained for  $\Lambda$  hyperons.

Figure 5.14 (b) shows the rise of the effective temperature  $T_{\text{eff}}$  as a function of  $\langle A_{\text{part}} \rangle$ . The data points show an increase of  $T_{\text{eff}}$  which is parametrized by a simple first-order polynomial function in order to quantify the rise which is given by a slope of  $m = 0.12 \pm 0.01$  MeV.

The width assuming a Gaussian-like rapidity density distribution as a function  $\langle A_{\text{part}} \rangle$  is depicted in figure 5.7 (c), where no indication for a rise is observed with increasing centrality. Again, no clear trend, hence the mean of the widths for the four centrality classes is determined to  $\langle \sigma_{\text{Gauss}} \rangle = 0.55 \pm 0.02$ . The systematic uncertainty of the width is determined as the variation of the width when fitting a Gaussian parametrization to the rapidity density distribution assuming the given point-to-point systematic uncertainties, as indicated by the boxes in figure 5.9.

# **5.3** Upper Limit on $\Xi^-$ Production

As described in section 4.4, the strategy for the reconstruction of the doubly-strange Cascade hyperon is to search for a significant correlation in the invariant mass spectrum of its decay products  $\pi^-$  and  $\Lambda$  whereas the latter one has to be reconstructed via its charged decay products  $\pi^-$  and proton, following almost an identical strategy as in the  $\Lambda$  hyperon analysis. The resulting invariant mass distribution of all  $\Lambda$ - $\pi^-$  candidates after applying decay topology cuts, as discussed in section 4.4.2, is presented in figure 5.15.

The mass distribution (black points) does not hint at any signal which would be expected to emerge at around  $M_{inv} = 1321 \text{ MeV/c}^{2.2}$  The background is estimated via the mixed-event

<sup>&</sup>lt;sup>2</sup> A slight shift of the measured mass was contemplated, as it was e.g. observed for the Cascade measurement in the p+Nb collision system. Such a shift may be attributed to effects like energy-loss in the detector material.

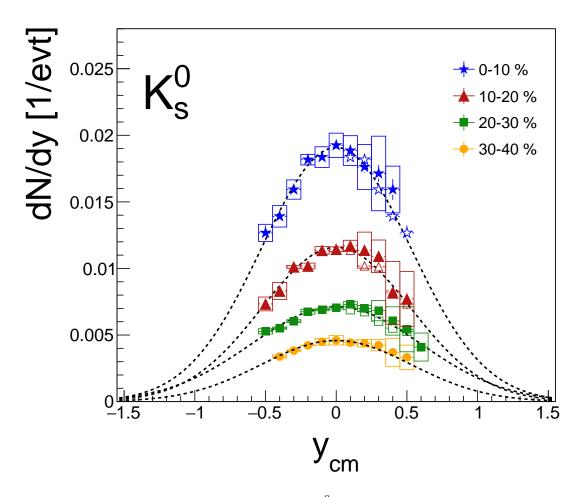


**Figure 5.13:** Rapidity density distributions of  $K_s^0$  mesons as a function of four different centrality classes from most central 0 - 10% to semi-peripheral 30 - 40% collisions normalized to the number of events per class. The classes have been determined in [233]. The corresponding impact parameter distributions have been shown in section 3.4.3.

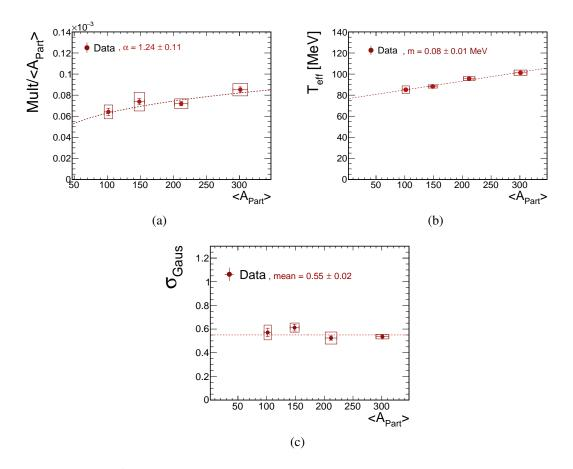


**Figure 5.14:** (a)  $K_s^0$  meson multiplicity normalized to the mean number of participants per centrality class  $Mult/\langle A_{part}\rangle$  as a function of  $\langle A_{part}\rangle$  which is proportional to centrality. The data points are fitted with a parametrization of the type  $M \propto \langle A_{part}\rangle^{\alpha}$  which gives a value for the exponent of  $\alpha = 1.24 \pm 0.12$ . (b) Effective temperatures  $T_{\rm eff}$  per centrality class as extracted from the inverse slope distributions as a function of centrality. The data points show a reasonable agreement with a linear parametrization giving a slope of  $m = 0.08 \pm 0.01$  MeV. (c) Gaussian width  $\sigma_{\rm Gauss}$  of the rapidity density distribution as a function of  $\langle A_{\rm part} \rangle$  indicating no significant dependence on centrality. The mean width is determined to  $\langle \sigma_{\rm Gauss} \rangle = 0.55 \pm 0.02$ .

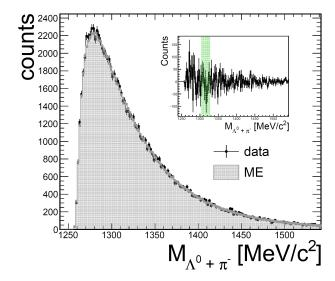


Figure 5.15: Invariant mass distribution of  $\Lambda$ - $\pi^-$  pairs (black points). The shape of the background is well reproduced by the mixed-event method (gray area). The inlet shows the invariant mass spectrum after subtraction of the background. The mass region, where the doubly-strange  $\Xi^$ hyperon is expected ( $M_{inv} = 1321 \pm 12$ MeV/c<sup>2</sup>), is indicated (green area) showing no significant correlation.

method and shows a satisfactory agreement. Also after subtraction, no sign of a signal is revealed in the spectrum in the indicated mass region (inlet, green area).

The range of cuts on the decay topology, track quality parameters and particle identification has been varied largely, anyhow, still not unraveling any indication for a peak-like structure. An alternative strategy of loosening topology cuts widely to maintain high statistics was not found to be successful either, hampered by the huge combinatorics resulting in a bad signal-to-background ratio which cannot be compensated within the precision of background determination.

However, observing this null result, an upper limit on the  $\Xi^-$  production can be determined. This limit is derived by using the Feldman-Cousins approach [259], which is purely based on the statistics of the selected data sample. The invariant mass distribution displayed in figure 5.15 as well as the underlying mixed-event background are therefore integrated in a  $\pm 3\sigma_{\text{Gauss}}^3$  interval around the mean value where the signal is expected ( $M_{\text{inv}} = 1321 \text{ MeV/c}^2$ ). The confidence interval is chosen to include 99.7% (corresponding to  $3\sigma$ ) of the hypothetical signal providing an upper limit of  $M_{\text{FC}} = (1.29 \pm 0.1_{\text{BG}}^{\text{sys}} \pm 1.33_{\text{Cuts}}^{\text{sys}}) \times 10^{-3}$ . The fraction of detectable  $\Xi^-$  hyperons due to the acceptance  $\epsilon_{\text{acc}}$  and the reconstruction efficiency  $\epsilon_{\text{rec}}$  were determined in simulations to  $\epsilon_{\text{acc}} \cdot \epsilon_{\text{rec}} = 0.012\%$ .

The first error is calculated by varying the region where the mixed-event background is normalized to the integral of the mass spectrum. By default, this normalization is done in sidebands around the expected signal at  $1280 - 1309 \text{ MeV/c}^2$  and  $1335 - 1400 \text{ MeV/c}^2$ , whereas the variations involve either a normalization in the first or the second band. Furthermore, topology cut values are varied as listed in table 4.8, resulting in a rather strong discrepancy for the obtained yields. However, same as in the analysis for  $K_s^0$  and  $\Lambda$ , this variation cannot be solely traced back to discrepancies in data and simulation when applying topology cuts but also to larger systematic uncertainties due to a mismatching background. A tightened cut set will reduce the systematic uncertainty from the background and vice versa. Therefore, the uncertainties are added in quadrature.

 $<sup>\</sup>sigma_{\text{Gauss}} = 4 \text{ MeV/c}^2$ , width taken from measurement in Ar+KCl collision system.

Since we calculate an upper limit, the positive uncertainties are added to the deduced multiplicity  $M_{\rm FC}$  finally yielding in a limiting value of  $M_{\rm FC} < 2.32 \text{ x} 10^{-3}$  per event.

Figure 5.16 shows the same invariant mass spectrum zoomed into the region where the  $\Xi^-$  signal is expected. Additionally, a Cascade peak is depicted assuming the derived upper limit to be the actual multiplicity sitting on top of the background obtained by a fit to the mixed-event spectrum. The peak is assumed to be distributed Gaussian-like with a width taken from the signal measured in the Ar+KCl collision system [218].

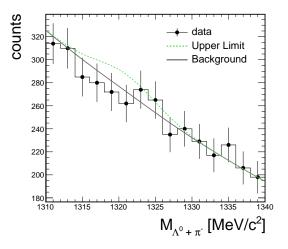


**Figure 5.16:** Invariant mass distribution of  $\Lambda$ - $\pi^-$  pairs (black points) zoomed into the expected  $\Xi^-$  mass region. The background is obtained by fitting a second-order polynomial function to the mixed-event background (gray solid line). Also indicated is the signal corresponding to the upper limit which is assumed to be the actual multiplicity following a Gaussian with a width of  $\sigma_{\text{Gauss}} = 3\sigma$ . The width ( $\sigma = 4$  MeV/c<sup>2</sup>) is an educated guess based on the  $\Xi^-$  measurement in Ar+KCl at 1.76A GeV.

## 5.4 Summary of Investigated Particle Production in Au+Au

The obtained results on the total yields and effective temperature, centrality-dependent as well as integrated over the 40% most central events, are summarized in table 5.1 for  $\Lambda$  hyperons and  $K_s^0$  mesons. Furthermore, the upper limit estimated for the  $\Xi^-$  production is listed.

$K_s^0$	yield $\times 10^{-2}$ [1/ evt]	$T_{\rm eff}$ [MeV]	
0 - 40%	$1.54 \pm 0.03 \pm 0.05 \pm 0.15$	$97\pm1\pm2$	
0 - 10%	$2.56 \pm 0.08 \pm 0.13 \pm 0.09$	$101\pm1\pm4$	
10 - 20%	$1.52 \pm 0.04 \pm 0.07 \pm 0.04$	$96\pm1\pm2$	
20 - 30%	$1.10 \pm 0.04 \pm 0.03 \pm 0.11$	$88\pm1\pm1$	
30 - 40%	$0.65 \pm 0.04 \pm 0.03 \pm 0.04$	$85\pm1\pm2$	
Λ	yield $\times 10^{-2}$ [1/ evt]	$T_{\rm eff}$ [MeV]	
0 - 40%	$3.97 \pm 0.06 \pm 0.06 \pm 0.04$	$93\pm2\pm4$	
0 - 10%	$7.26 \pm 0.24 \pm 0.34 \pm 0.26$	$104\pm1\pm1$	
10 - 20%	$4.17 \pm 0.13 \pm 0.17 \pm 0.19$	$95\pm1\pm4$	
20 - 30%	$2.79 \pm 0.14 \pm 0.12 \pm 0.09$	$87\pm1\pm4$	
30 - 40%	$1.61 \pm 0.11 \pm 0.13 \pm 0.07$	$80\pm1\pm4$	
Ξ-	upper limit: yield $\times 10^{-2}$ [1/ evt]		
0 - 40%	< 0.232		

**Table 5.1:**  $K_s^0$  and  $\Lambda$  multiplicities in full phase space and inverse slopes at mid-rapidity  $T_{\text{eff}}$ . The first given error corresponds always to the statistical, the second to the systematic error within the rapidity range covered by HADES and the last one to the extrapolation uncertainty to full phase space, see text for details. If the second or third error is not given, it was found to be well below the statistical error and is hence neglected. In case of the Cascade, an upper limit was estimated.

# Chapter 6

# Discussion

As already motivated in the introduction, in the Au+Au collision system measured with HADES at a kinetic beam energy of 1.23 GeV per nucleon all hadrons containing strangeness are produced below their elementary production threshold. Hence, the required energy is not available in binary NN collisions but must be provided by the system e.g. through multi-particle interactions or medium effects. Thus, a high sensitivity to these medium effects is expected in the investigated system. Possible mechanisms enabling a sub-threshold production have been discussed in section 1.2.2. The different production thresholds of strange hadrons as well as the corresponding negative excess energies<sup>1</sup>, which need to be provided by the system to enable a production, are summarized in table 1.1 in the introduction.

The combination of sub-threshold production and a high-statistic data set containing a few billion analyzed events makes this large collision system particularly suitable to study the mechanism of strangeness production and propagation in the dense medium created in such collisions. For a conclusive understanding, the production yields of all hadrons, strange or non-strange, have been analyzed in three dimensions: transverse mass  $m_t$ , rapidity y and centrality C. Whereas the investigation with respect to the first two variables enable an investigation of the kinematics and the determination of (differential) production yields, the latter one provides further insight in the system size dependence of particle production.

The production of protons, negative pions, charged kaons and  $\phi$  mesons has been analyzed in [37] and is complemented by the strange hadrons  $\Lambda$  and  $K_s^0$  as well as the doubly-strange  $\Xi^$ hyperon within this thesis.

Based on the results presented in the previous chapter 5, the questions introduced at the end of the first chapter in section 1.5.4 can be addressed in the following<sup>2</sup>. First, the particle yields of  $\Lambda$  and  $K_s^0$  are compared to the other strange hadrons reconstructed in the Au+Au system and to data from other experiments, in order to obtain a more comprehensive picture.

Being sensitive to multi-particle interactions in sub-threshold strangeness production, the results are then compared to transport models to test their predictive power and to investigate whether conclusions can be drawn on in-medium potentials or not.

<sup>&</sup>lt;sup>1</sup> The excess energy is defined as the difference between available beam energy and energy for particle production in NN collisions.

<sup>&</sup>lt;sup>2</sup> The question with respect to the  $\phi/K^-$  production ratio has been addressed in [37].

Furthermore, a comparison to a statistical hadronization models (SHM) may provide information on the degree of equilibration reached in the reaction volume. The complete reconstruction of hadrons combined with a multi-differential analysis also enables a detailed comparison of the kinetic and chemical freeze-out conditions.

In the end, having a null result for the cascade production, the derived upper limit on the  $\Xi^-$  yield is compared to model predictions and world data.

### 6.1 Ensemble of Reconstructed Strange Hadrons in Au+Au

Figure 6.1 shows the multiplicity normalized to  $\langle A_{\text{part}} \rangle$  for pions and all strange hadrons measured with HADES in the Au+Au system as a function of  $\langle A_{\text{part}} \rangle$ , which is proportional to the centrality of the collision. A clear hierarchy is indicated when comparing the hadron multiplicities which directly reflects the different elementary production thresholds. Therefore, the much more abundant negative pions had to be scaled down, the rarely produced  $\phi$  and  $K^-$  mesons scaled up, in order to allow for a comparison to  $K_s^0$ ,  $\Lambda$  and  $K^+$ .

The systematic errors on  $Mult/\langle A_{part}\rangle$ , indicated as boxes, are obtained by adding the corresponding statistical and systematic uncertainties of the multiplicity in quadrature whereas the uncertainties on  $\langle A_{part}\rangle$  are taken from [233].

The multiplicity is normalized to the number of participating nucleons, which is in leading order proportional to the volume of the collision zone, in order to become sensitive to a rise of particle production independent of the considered system size and hence to look beyond the rather trivial relation of an increasing particle multiplicity in larger systems. The strength of this rise is proportional to the amount of energy that the medium provides with increasing density, folded with the energy excitation function of the given particle yield in NN collisions. The latter one is measured [5] and included in microscopic models, hence such models can be used to extract further properties of the created system.

A parametrization of the type  $M \propto \langle A_{\text{part}} \rangle^{\alpha}$ , where the  $\alpha$  exponent can be considered as a parameter quantifying the rise of  $Mult / \langle A_{\text{part}} \rangle$  with the centrality of the collision, is fitted to data for strange hadrons simultaneously. This simultaneous fit implies the hypothesis that all particles experience the same rise with centrality. The fit gives a common value for the  $\alpha$ parameter of  $1.35 \pm 0.07$  which agrees within systematic uncertainties with data on all strange hadrons. A linear increase of multiplicity with centrality would correspond to a horizontal line in this representation with an  $\alpha$  value of  $\approx 1$ , as observed for negative pions [37] and which is in line with transport model calculations [136], whereas values greater than unity indicate a more than linear rise of the multiplicity with centrality.

A different approach would be to fit the parametrization  $M \propto \langle A_{\text{part}} \rangle^{\alpha}$  individually to each hadron species. The result of this investigation is shown in figure A.5 in the appendix. As the strange and antistrange quarks, which are contained in the  $\Lambda$  and  $K_s^0$  respectively, are produced in pairs due to strangeness conservation, one expects both particles to exhibit a similar rise<sup>3</sup>, which is indeed observed.

<sup>&</sup>lt;sup>3</sup> The same holds true for positive kaons  $K^+$ , which are produced with a  $\Lambda$  hyperon as well.

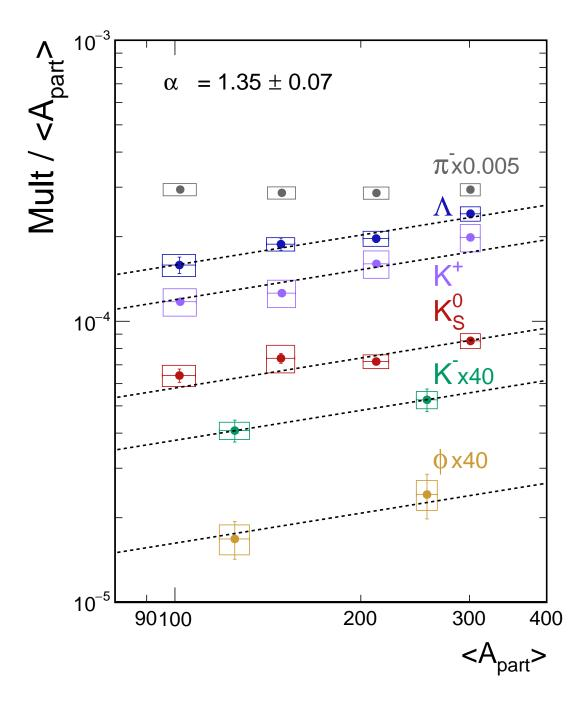


**Figure 6.1:** Multiplicity normalized to  $\langle A_{\text{part}} \rangle$  as a function of  $\langle A_{\text{part}} \rangle$  for negative pions and strange hadrons reconstructed in the Au+Au collision system at  $E_{\text{beam}} = 1.23$ A GeV measured with HADES. Pions, charged kaons and the  $\phi$  meson have been investigated in [37]. The points are fitted simultaneously with a parametrization of the type  $M \propto \langle A_{\text{part}} \rangle^{\alpha}$  in order to quantify the rise of the data with increasing centrality of the collision which is then given by the  $\alpha$  exponent. The extracted value for  $\alpha = 1.35 \pm 0.07$  agrees within the systematic uncertainties of all strange hadrons.

Within the uncertainties of  $\alpha$ , an agreement is observed for all strange hadrons measured in this collision system. The mentioned hierarchy concerning the elementary production threshold is not found to be reflected in the rise of  $Mult/\langle A_{part} \rangle$  with centrality. This may be a surprise, when considering that particles produced even deeper below NN threshold, such as  $\phi$  and  $K^$ mesons, are expected to benefit more from local secondary processes where energy is accumulated via multi-step processes enabling their formation<sup>4</sup>. Also a comparison to results from the Ni+Ni collision system at  $E_{beam} = 1.93$ A GeV measured by the FOPI collaboration indicate a similar behavior of the normalized yields with centrality, i.e.  $\alpha_{K_s^0} = 1.20 \pm 0.25$  for neutral kaons and  $\alpha_{\Lambda} = 1.34 \pm 0.16$  for  $\Lambda$  hyperons [229], compared to  $\alpha_{K_s^0} = 1.24 \pm 0.12$  and  $\alpha_{\Lambda} = 1.37 \pm 0.1$ as obtained in this investigation. Again, this may not be expected considering a classical picture of multi-step processes where the strength of the rise is sensitive to the excess energy. It could be explained by a common threshold for  $s\bar{s}$  production while the observed final states are the results of complicated propagation processes which go beyond simple strangeness exchange reactions like e.g.  $\pi\Lambda \to Kp$  as otherwise the  $\phi$  does not fit into the picture.

In any case, the argument that the probability for secondary processes is expected to increase with density and the lifetime of a system, which are both predicted to be relatively high in the SIS energy regime [34], is strengthened by the observation of  $\alpha$  values greater than unity. Such a sensitivity to multi-particle interactions suggests a deeper investigation with respect to transport models, which follows up in section 6.3.

Furthermore, the effective temperatures  $T_{\text{eff}}$  as a function of  $\langle A_{\text{part}} \rangle$  can be compared for  $\Lambda$  hyperons and  $K_s^0$  mesons, as depicted in figure 6.2. The data points are parametrized by a first-order polynomial function of the form:

$$T_{\rm eff} = m \cdot \langle A_{\rm part} \rangle + b. \tag{6.1}$$

According to the fit, the increase of the effective temperatures  $T_{\text{eff}}$  with centrality for  $\Lambda$  hyperons, which is characterized by the fit parameter m, is with a value of  $m = 0.12 \pm 0.01$  MeV slightly higher than for neutral kaons with  $m = 0.08 \pm 0.01$  MeV, yet, taking the systematic uncertainties into account, a similar slope is observed. Within uncertainties, the rise of the effective temperature agrees with the one extracted for positive kaons  $K^+$  with a value of  $m = 0.10 \pm 0.01$  [37].

Also previous data by KaoS for positive kaons observed the same trend with increasing centrality, which was explained by an increasing number of scattered kaons and could be fairly reproduced by the transport models IQMD and HSD [136]. This is also in line with observations of higher inverse slopes in heavy compared to light collision systems [29].

In figure 6.3 (a), the widths of the measured rapidity density distributions (see figures 5.2 and 5.9 in chapter 5) as a function of  $\langle A_{\text{part}} \rangle$  are compared for  $\Lambda$  hyperons (blue) and  $K_s^0$  mesons (red). The widths are obtained assuming a Gaussian distribution. A significantly broader distribution is observed for  $K_s^0$  mesons in all centrality classes. For both hadrons, data points do not indicate a dependence of the widths on centrality. Hence, for a better comparison, the mean width

<sup>&</sup>lt;sup>4</sup> This is true under the assumption that density increases with centrality and such local multi-step processes become more likely.

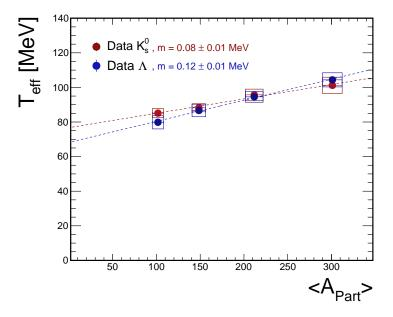


**Figure 6.2:** Effective temperature  $T_{\text{eff}}$  as a function of  $\langle A_{\text{part}} \rangle$  for  $\Lambda$  hyperons (blue) and  $K_s^0$  mesons (red). The data points are parametrized by a linear function of type  $T_{\text{eff}} = m \cdot \langle A_{\text{part}} \rangle + b$ . The rise m with centrality does not differ significantly when considering systematic uncertainties.

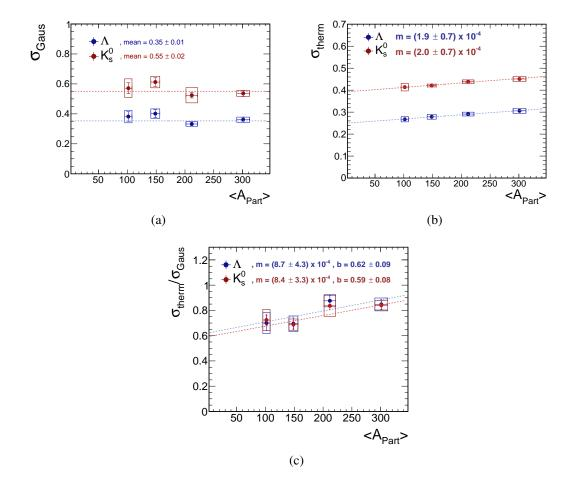
is estimated to be  $\langle \sigma_{\text{Gauss}} \rangle = 0.35 \pm 0.01$  for  $\Lambda$  indicating significantly narrower distributions than the ones for  $K_s^0$  showing a mean value of  $\langle \sigma_{\text{Gauss}} \rangle = 0.55 \pm 0.02$ .

Figure 6.3 (b) shows the thermal widths  $\sigma_y$ , which are calculated according to equation 5.4, as a function of centrality. The strength of the rise is directly proportional to the rise of the inverse slopes  $T_{\rm eff}$  with centrality (see figure 6.2) which is trivial, as the only parameter the thermal width depends on is  $T_{\rm eff}$  and the particle mass  $m_0$ . The latter one is a constant and dictates the difference in the absolute values of  $\sigma_y$  between  $\Lambda$  and  $K_s^0$ . Consequently, similar as  $T_{\rm eff}$  as a function of  $\langle A_{\rm part} \rangle$ , the rise agrees within uncertainties. A linear function was used to quantify the rise, giving  $m = 1.9 \pm 0.7 \times 10^{-4}$  for  $\Lambda$  hyperons and  $m = 2.0 \pm 0.7 \times 10^{-4}$  for  $K_s^0$  mesons.

Furthermore, the thermal widths  $\sigma_y$  are normalized to the experimental widths  $\sigma_{Gauss}$  which is shown in figure 6.3 (c), again as a function of  $\langle A_{part} \rangle$ . The data points for  $\Lambda$  and  $K_s^0$  indicate a striking agreement for the normalized widths  $\sigma_y/\sigma_{Gauss}$ . This can be interpreted in a naive picture such that both particles reach a similar degree of equilibration along the z-axis. Thus, an agreement between baryons and mesons may indicate a scenario, where freeze-out conditions could be similar among the different strange hadron species, independent on the number of containing quarks. It seems like  $K_s^0$  and  $\Lambda$  have lost to a very similar degree the memory of their collision history. Under the assumption that the measured widths  $\sigma_{Gauss}$  are constant as a function of  $\langle A_{part} \rangle$ , a slight increase of  $\sigma_y/\sigma_{Gauss}$  is observed with centrality approaching values at unity, which can be interpreted as a higher degree of thermalization<sup>5</sup>. However, when calculating

 $<sup>\</sup>overline{}^{5}$  The rise is driven by the increase of  $T_{\rm eff}$  with centrality, as presented in figure 6.2.

the rise assuming a linear fit function, the large uncertainties of 49% for  $\Lambda$  and 40% for  $K_s^0$  soften this statement. The fit gives a slope of  $m = 8.7 \pm 4.3 \text{ x } 10^{-4}$  for  $\Lambda$  and  $8.4 \pm 3.3 \text{ x } 10^{-4}$  for  $K_s^0$ .



**Figure 6.3:** (a) Width of rapidity density distribution of  $\Lambda$  hyperons (blue) and  $K_s^0$  mesons (red), assuming a Gaussian parametrization, as a function of  $\langle A_{part} \rangle$ . The data points do not suggest a dependence of the width on centrality. The mean width of neutral kaons lies with  $\langle \sigma_{Gauss} \rangle = 0.55 \pm 0.02$  significantly above the one observed for  $\Lambda$  hyperons with  $\langle \sigma_{Gauss} \rangle = 0.35 \pm 0.01$ . (b) Thermal width  $\sigma_y$ , as calculated via equation 5.4, as a function of  $\langle A_{part} \rangle$ . A similar rise for  $K_s^0$  and  $\Lambda$  is observed with centrality. As the effective temperatures for both particles were found to agree within uncertainties (figure 6.2), the different absolute values can be solely attributed to the difference in particle mass. (c) Thermal width  $\sigma_y$  normalized to the Gaussian width  $\sigma_{Gauss}$  of  $\Lambda$  hyperons (blue) and  $K_s^0$  mesons (red) as a function of centrality showing a striking agreement within uncertainties.

# **6.2** Comparison of $K_s^0$ and $\Lambda$ Production Yields to World Data

The excitation functions of the mid-rapidity yields of both particles for central Au+Au and Pb+Pb collisions as function of  $\sqrt{s}$  are displayed in figure 6.4. While the data on neutral kaon production

(red symbols) are scarce [85, 260, 261, 262], for the  $\Lambda$  hyperon (blue symbols) more measurements over a wide range of energies are available [263, 264, 265, 230, 232, 261, 266, 267, 268, 269]. Their yields show a strong, almost linear rise with increasing energy up to  $\sqrt{s} \approx 5$  GeV and flattens out at higher energies. In case of  $\Lambda$  hyperons, AGS data points (open triangles) indicate a steep drop towards low energies. The HADES data point (blue filled circle, left) lines up with respect to this trend. In case of  $K_s^0$  mesons, however, world data is scarce and the HADES point (red filled circle, left) gives strong constraints on the low energy behavior.

The comparison of experimental yields to transport models has been considered to be a reasonable tool to deduce the existence and size of in-medium potentials as they directly affect production thresholds [57, 270]. The behaviour of data at energies below  $\sqrt{s} \approx 5$  GeV indicates a strong sensitivity to production yields with decreasing excess energy, hence the Au+Au system can be considered to be an appropriate system to study such potentials. Additionally, both hadrons are in particular well suited for these studies as they do not undergo Coulomb interactions.

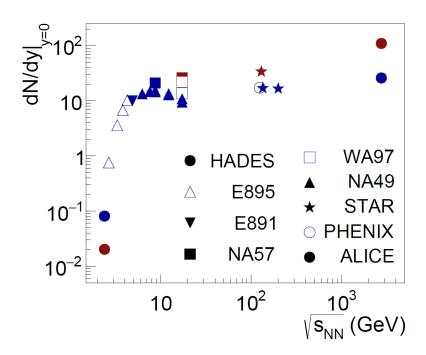


Figure 6.4: Yield per unit rapidity per event at mid-rapidity of  $\Lambda$  hyperons (blue symbols) and  $K_s^0$  mesons (red symbols) measured in central Au+Au or Pb+Pb systems (at maximum 10% most central data) from LHC beam energies over SPS and RHIC down to the SIS energy regime. Data on  $\Lambda$  production from AGS (open triangles) indicate a steep drop of the excitation function towards its elementary production threshold ( $\sqrt{s} \approx 2.56$  GeV). The  $\Lambda$  yield obtained with HADES (blue filled circle, left) for 0 - 10% most central data follows this trend. Data on  $K_s^0$  measurements in heavy systems are scarce over the full range of energies, hence the HADES data point (red filled circle, left) gives strong constraints on the trend at low beam energies close to threshold.

## 6.3 Comparison to Transport Model Calculations

In the following, the experimental data are compared to predictions from three hadronic transport models, the Isospin Quantum Molecular Model IQMD (version c8), the Hadron String Dynamics HSD (version 711n) and the Ultra-relativistic Quantum Molecular Dynamics model UrQMD (version 3.4). All three are semi-classical models simulating HIC on an event-by-event basis. While UrQMD produces particles at SIS energies in two-step processes via intermediate resonance excitations, in HSD and IQMD also direct production via two-to-three particle processes are included. In the chosen version of UrQMD, neither mean field NN-potentials nor explicit K-/ $\Lambda$ -N potentials are included. As the treatment of a many-body problem is complex, in transport models the potentials are reduced to a one-body problem where e.g. kaons or hyperons are propagated in a mean field, generated by all surrounding nucleons. Such potentials depend on the density of the system and modify the phase space distributions of a particle<sup>6</sup> and hence cross-sections of particle production. A more detailed description of transport models and the mean field treatment was given in section 1.4.1 and 1.3.3, respectively. In IQMD and HSD the K-N mean field potential is implemented with a strength of 40 MeV at ground state density  $\rho_0$ and increasing linearly with density whereas for the  $\Lambda$ -N potential, both models scale the mean field NN potential by 2/3, motivated by the additive quark model<sup>7</sup>. In contrast to UrQMD, they include only  $\Delta$  resonances, hence these codes are in this mode not applicable for energies > 2A GeV<sup>8</sup>, but it is very well tested in the SIS18 energy regime. HSD allows for propagation of off-shell particles in addition, however, this is more relevant for antikaon production. Further information can be found in [180, 186, 271].

The comparison to microscopic models give access to e.g. the extraction of particle specific properties of neutral kaons and  $\Lambda$  hyperons like the K-N and  $\Lambda$ -N potential which affect both, their production and propagation in the medium. For the time being, it is assumed that all three models reproduce the bulk properties sufficiently well in order to investigate the microscopic properties of  $K_s^0$  and  $\Lambda$ .

### **6.3.1** Particle Production Yields and Centrality Dependence

First, a comparison of the integrated yield for a given centrality class and the centrality dependence of the yield is made, as can be seen in figure 6.5 for  $\Lambda$  hyperons and 6.6 for  $K_s^0$  mesons respectively.

An overshoot of the yield by a large factor compared to data is found for all models without implementation of a KN potential (figure 6.5 and 6.6 (a)). For neutral kaons, also the rise with  $\langle A_{part} \rangle$  is mostly over-predicted, especially in case of UrQMD. For both hadrons, HSD matches

<sup>&</sup>lt;sup>6</sup> Such an effect may be observed as e.g. a redshift for attractive or blueshift for repulsive potentials in the momentum distribution.

<sup>&</sup>lt;sup>7</sup> Assuming a simple SU(3) flavor picture, this scaling is motivated by the reduced non-strange quark content. Mean field calculations for hyper nuclei [145, 146, 147] show a rough agreement with such a scaling. The inclusion of a  $\Lambda$ -N potential results in an additional shift of the production threshold.

<sup>&</sup>lt;sup>8</sup> At higher energies above few GeV, particle production in the HSD and UrQMD model is described by string fragmentation which is not available in IQMD.

the rise with centrality within uncertainties. The observed overshoot for the  $\alpha$  exponent in case of UrQMD might be due to a higher level of energy redistribution for particles produced via excitation of intermediate resonances, which are not implemented in IQMD and HSD. An additional uncertainty is certainly introduced by the experimentally not well constrained production cross sections of these resonances and their decay branches. Hence, they strongly rely on the used effective parametrization of the cross sections<sup>9</sup>. The differences among the models amount to roughly 30%, which can be considered as the minimal systematic uncertainty when comparing experimental yields and model predictions.

If the above mentioned K-N potential is enabled, the  $K_s^0$  curves come much closer to data and also the  $\alpha$  parameter is reduced as indicated in figure 6.6 (b). The IQMD predictions are, with a deviation of the yields of the order 30 - 45% and an agreement almost within errors of the extracted  $\alpha$  exponent, the closest to the data. The reduction of the yield and  $\alpha$  values can be understood qualitatively by an effective shift in production threshold of the kaons. As this shift increases with density, it is more pronounced for central events, hence also the rise is reduced.

Figure 6.5 (b) shows the effect on  $\Lambda$  yields when including the K-N potential. Due to the associated production of kaons and  $\Lambda$  hyperons, also the  $\Lambda$  yields are strongly reduced, yet, still overpredicted by about 40-65% whereas the parameter  $\alpha$  agrees within uncertainties. Note, that in the UrQMD model no  $\Lambda$ -N potential is implemented, while both versions of HSD and IQMD include a  $\Lambda$ -N potential with a strength scaled by 2/3 with respect to the N-N potential, which also affects the  $\Lambda$  and  $K_s^0$  yield.

### 6.3.2 Rapidity Density Distribution

Next, the shapes of the rapidity distributions are compared and therefore the model curves are normalized to the area of the experimental ones, which is depicted for the 0 - 10% most-central collisions in figure 6.7 (a) for  $\Lambda$  hyperons and figure 6.8 (a) for  $K_s^0$  mesons. To allow for a better comparison, the ratios of the distributions in model calculations to experimental data are plotted in the lower parts of the figures.

This observable is in particular sensitive to the stopping of baryons in the collision zone and the ability of the system to redistribute energy. This effect may occur in form of a redistribution of kinetic energy either by elastic scattering, transferring collective into random motion, or by intrinsic excitation of resonances, which is both expected to be more likely with increasing density.

Repulsive potentials influence the shape of the distribution in addition by pushing the particles away from the bulk of matter at mid-rapidity. By looking at the ratio, the shape seems to be rather well reproduced for  $\Lambda$  hyperons, in particular in case of the UrQMD model. The modification in HSD and IQMD when using a KN potential (solid lines/filled circles) does not affect the shape of the distributions of  $\Lambda$  hyperons. A significant broadening is observed for the rapidity density distributions of neutral kaons when implementing the KN potential.

<sup>&</sup>lt;sup>9</sup> For detailed discussions on the parametrization of elementary cross sections of some of the high-mass resonances implemented in UrQMD, the reader is referred to [186][187].

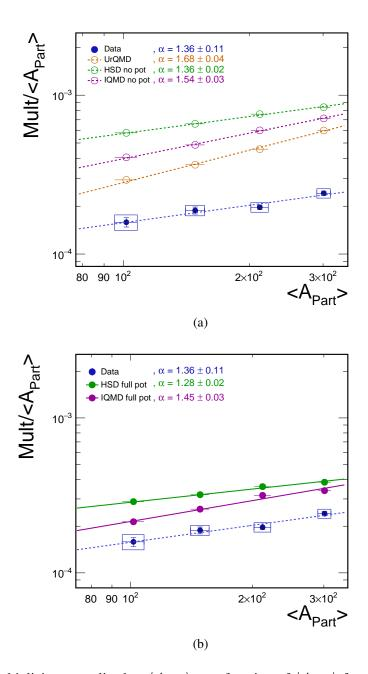


**Figure 6.5:** Multiplicity normalized to  $\langle A_{part} \rangle$  as a function of  $\langle A_{part} \rangle$  for  $\Lambda$  hyperons compared to the three transport models HSD (green), IQMD (purple) and UrQMD (orange) without (a) and involving (b) a repulsive K-N potential of 40 MeV at ground-state density. The repulsive K-N potential affects the  $\Lambda$  production yield through an effective increase of the kaon in-medium mass, which enhances the corresponding threshold of the coupled kaon- $\Lambda$  production. In all cases the yield is strongly overshot, the best agreement is obtained with IQMD including a potential, however, still deviating by 40% to 65%. All three models show a different rise with centrality which is given by the  $\alpha$  parameter. Whereas the  $\alpha$  parameter for HSD and IQMD agree with data within uncertainties, UrQMD over-predicts the rise. The inclusion of a K-N potential slightly reduces the rise with  $\langle A_{part} \rangle$ .

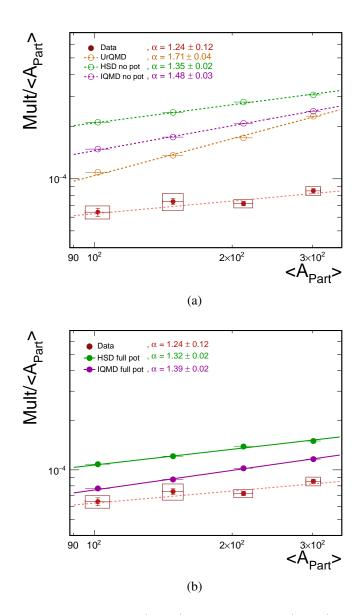


**Figure 6.6:** Multiplicity normalized to  $\langle A_{part} \rangle$  as a function of  $\langle A_{part} \rangle$  for  $K_s^0$  mesons compared to the three transport models HSD (green), IQMD (purple) and UrQMD (orange) without (a) and involving (b) a repulsive K-N potential of 40 MeV at ground-state density. The repulsive K-N potential significantly reduces the production cross-section. Similar as for  $\Lambda$ , in all cases the yield is strongly overshot, whereas the best agreement is obtained with IQMD including a potential, yet, still deviating by 25% to 45%. All three models show a different rise with centrality which is given by the  $\alpha$  parameter. Whereas the  $\alpha$  parameter for HSD and IQMD agree with data within uncertainties, UrQMD over-predicts the riseThe inclusion of a K-N potential slightly reduces the rise with  $\langle A_{part} \rangle$ .

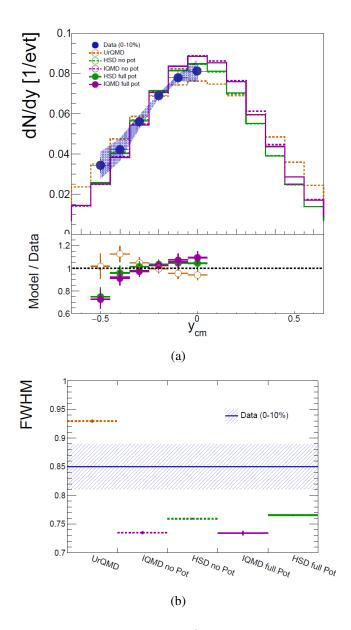


**Figure 6.7:** (a) Rapidity density distribution for  $\Lambda$  in most central collisions (0 - 10%) compared to three transport models HSD (green), IQMD (purple) and UrQMD (orange), which are normalized to the integral of experimental data. The model calculations including a K-N potential are indicated as solid lines. An overall fair agreement with data for all implementations is observed. The strongest deviation of about 25% is observed for HSD and IQMD at very backward rapidities at around  $y_{\rm cm} \approx -0.5$  which can be seen from the lower plot indicating the ratio between model and experimental data. The influence of the K-N potential on the shape is negligible. (b) Full width at half maximum of the dN/dy spectra assuming a Gaussian-like distribution. The FWHM for the distribution of data is indicated by the continuous blue line and its statistical uncertainty as a blue band. The uncertainties for all distributions are taken from the width  $\sigma$  as obtained from the Gaussian fit. The distribution in UrQMD is broader than the ones obtained from IQMD and HSD as well as from experimental data.

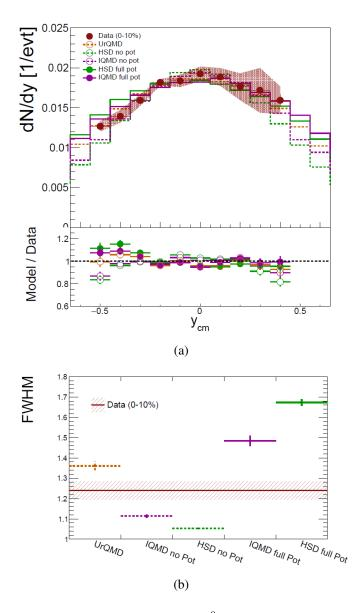


**Figure 6.8:** (a) Rapidity density distribution for  $K_s^0$  in most central collisions (0 - 10%) compared to three transport models HSD (green), IQMD (purple) and UrQMD (orange), which are normalized to the integral of experimental data. The model calculations including a K-N potential are indicated as solid lines. An overall fair agreement with data for all implementations is observed. The strongest deviations of about 15% are observed for HSD and IQMD at very backward and very forward rapidities at around  $y_{\rm cm} \approx -0.5$  and  $\approx +0.4$  which can be seen from the lower plot indicating the ratio between model and experimental data. The repulsive K-N potential induces a rapidity shift away from mid-rapidity. (b) Full width at half maximum of the dN/dy spectra assuming a Gaussian-like distribution. The FWHM for the distribution of data is indicated by the continuous red line and its statistical uncertainty as a red band. The uncertainties for all distributions are taken from the width  $\sigma$  as obtained from the Gaussian fit. An impact of the K-N potential on the shape of the distribution is clearly visible.

Although, an agreement between model and experimental data is observed when investigating the ratio, a clear distinction between the different scenarios with and without potential and also with respect to UrQMD can be made. To get a more quantitative handle when comparing the shape of the rapidity density distributions, each model as well as experimental data are fitted with a Gaussian and, from the extracted widths  $\sigma_{Gauss}$ , the full width at half maximum FWHM was deduced<sup>10</sup>. The FWHM obtained for the five implementations HSD (green) and IQMD (purple) with (solid) and without (dashed) potential as well as UrQMD (orange) are shown in figure 6.7 (b) for  $\Lambda$  hyperons and figure 6.8 (b) for  $K_s^0$  mesons. The experimental widths for 0-10% most-central data are indicated as a continuous line with the statistical error (displayed as colored band) as extracted from the fit of the Gaussian parametrization to data. For both particles UrQMD predicts a broader distribution than IQMD and HSD without potential. Whereas no effect on the kinematics is observed for  $\Lambda$  hyperons when implementing a KN potential, the values for the FWHM obtained for  $K_s^0$  mesons become significantly larger indicating a push of the particles away from mid-rapidity.

Since the shape of the rapidity density distributions may be sensitive to the density of the system and hence the centrality of the collision, the comparison is also conducted for semiperipheral collisions (30-40%) which is depicted in figure 6.9 for  $\Lambda$  hyperons and figure 6.10 for  $K_s^0$  mesons. For both particles, IQMD and HSD are well reproducing the shape, independently of involving a potential or not. The UrQMD calculation, on the other hand, overpredicts the width of the distribution for  $\Lambda$  hyperons which was already observed for most-central reactions. This effect, again, might hint to an overestimation of energy redistribution in the system due to a more dominant role of resonant production in UrQMD compared to HSD and IQMD.

### 6.3.3 Transverse Momentum Spectra

Finally, the shape of transverse momentum distributions at mid-rapidity for the most central event class are compared<sup>11</sup>, which is presented in figure 6.11 (a) for  $\Lambda$  hyperons and (b) for  $K_s^0$  mesons. Besides the production mechanism [272] and the radial expansion velocity of the system, the low transverse momentum part is particularly sensitive to the K/ $\Lambda$ -N potentials [137] and hence the impact of a red- or blueshift will be most pronounced. Therefore, the spectra obtained from transport model calculations are normalized to data in the high transverse momentum part (700 <  $p_t < 1000$  MeV/c and  $600 < p_t < 900$  MeV/c respectively).

Clearly, in case of neutral kaons, the data favor calculations including a potential, the IQMD prediction describes the shape rather well whereas HSD misses by about 20 - 50%. However, again, UrQMD without any potential shows a completely different behavior at low  $p_t$  compared to the two other calculations, being 40 - 60% below data indicating that in the UrQMD model a much larger fraction of particles are produced with high  $p_t$  compared to low  $p_t$  than in HSD or IQMD calculations.

<sup>&</sup>lt;sup>10</sup> The width of a Gaussian is related to the full width at half maximum by FWHM<sub>Gauss</sub>  $\approx 2.35\sigma_{Gauss}$ .

<sup>&</sup>lt;sup>11</sup> From simple kinematical considerations, the impact of in-medium potentials on particle spectra will be most pronounced at mid-rapidity, at least when assuming a system where also the nucleon emission is dominant at mid-rapidity [57].

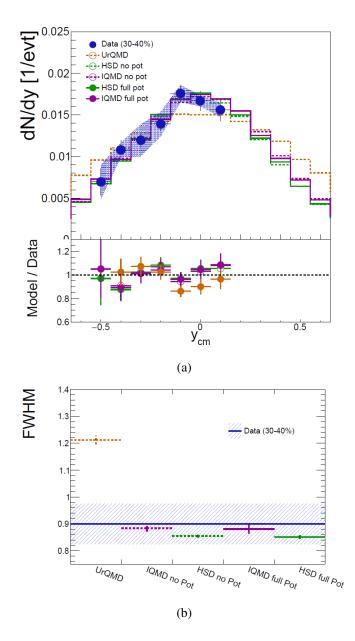


**Figure 6.9:** (a) Rapidity density distribution for  $\Lambda$  in semi-peripheral collisions (30-40%) compared to three transport models HSD (green), IQMD (purple) and UrQMD (orange), which are normalized to the integral of experimental data. The model calculations including a K-N potential are indicated as solid lines. An agreement within statistical uncertainties for all implementations is observed as can be seen from the lower part of the plot indicating the ratio between model calculations and experimental data. The influence of the K-N potential on the shape is negligible. (b) Full width at half maximum of the dN/dy spectra assuming a Gaussian-like distribution. The FWHM for the distribution of data is indicated by the continuous blue line and its statistical uncertainty as a blue band. The uncertainties for all distributions are taken from the width  $\sigma$  as obtained from the Gaussian fit. Whereas the FWHM of the distributions from HSD and IQMD agree within the statistical uncertainty of data, the distribution in UrQMD is much broader.

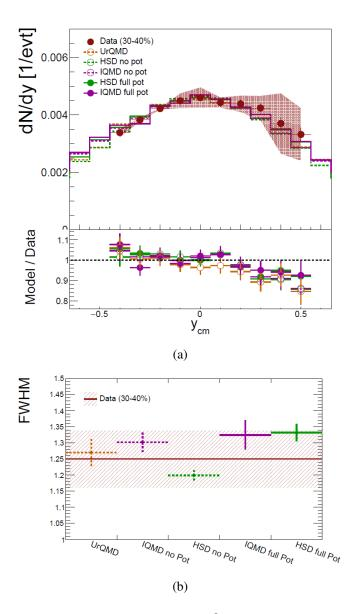


**Figure 6.10:** (a) Rapidity density distribution for  $K_s^0$  in semi-peripheral collisions (30 - 40%) compared to three transport models HSD (green), IQMD (purple) and UrQMD (orange), which are normalized to the integral of experimental data. The model calculations including a K-N potential are indicated as solid lines. An overall fair agreement with data for all implementations is observed not exceeding 15% at very forward rapidities which can be seen from the lower plot indicating the ratio between the model calculation and experimental data. Same as for most central collisions, the repulsive K-N potential induces a rapidity shift away from mid-rapidity which, however, seems to be weaker in semi-peripheral reactions. (b) Full width at half maximum of the dN/dy spectra assuming a Gaussian-like distribution. The FWHM for the distribution of data is indicated by the continuous red line and its statistical uncertainty as a red band. The uncertainty for all distributions is taken from the width  $\sigma$  as obtained from the Gaussian fit. An impact of the K-N potential on the shape of the distribution is barely visible.

In addition, UrQMD offers the best description of the  $\Lambda$  transverse momentum spectra agreeing within uncertainties of experimental data, whereas HSD and IQMD fail to describe the shape at low  $p_t$  by about 50 – 80%. However, in contrast to the UrQMD model, IQMD and HSD include an attractive  $\Lambda$ -N potential and hence the momentum spectra experience an additional redshift<sup>12</sup>.

The observed discrepancy between the models might again be related to the dominant role of resonant particle production in UrQMD where in particular the high-mass resonances seemingly affect the high  $p_t$  tails of the spectra significantly. On the other hand, the production in HSD and IQMD via the direct two-to-three body channel  $NN \rightarrow N\Lambda K$  may lead to an enhancement of kaons and/or hyperons at low over high  $p_t$ . This brings us back to the ambiguities of observables, where different microscopic effects can compensate each other. The uncertainty in particle production between 2 to 3 body interactions and the production in two step processes via intermediate resonances can (over-)mimic the effect of a potential.

### 6.3.4 What can be concluded from comparisons to transport models?

This brings us back to the question addressed at the end of the introduction (see 1.5.4).

The investigated transport models can be divided in two relevant groups: on one side, the HSD and IQMD transport models with a K-N potential of 40 MeV at nuclear ground state density  $\rho_0$  increasing linearly with density as well as a  $\Lambda$ -N potential which scales with 2/3 of the strength of the N-N potential.

On the other side there is the UrQMD code involving higher-lying  $\Delta$  and  $N^*$  resonances but neither including a repulsive K-N nor an attractive N-/ $\Lambda$ -N potential. Table 6.1 summarizes whether the presented transport models provided satisfactory (•) descriptions of the investigated observables or not ( $\circ$ ).

Certainly, such a classification is rough as the level of agreement for a given observable between data and transport model is difficult to quantify and rather subjective, yet, an impression is given on their consistency. No model describes all observables simultaneously, it was also shown that no observable can be described unambiguously by all models.

They all fail to reproduce the production yields. Though the shape of the rapidity density distributions is indicated as agreeing with experimental measurements, the models show clear distinctions in the widths of the distributions with respect to each other. Results from the HSD and IQMD transport models may give the impression that a repulsive K-N potential is necessary to describe particle kinematics ( $p_t$  spectra), yet, at least partially UrQMD calculations can (over)compensate the effect of the potential via particle production through intermediate resonances but fails to reproduce the scaling of the yields with centrality. On the other hand,  $\Lambda p_t$  spectra are best described by the UrQMD model. On closer inspection, the success of approaching kaon data when including a K-N potential in HSD and IQMD is not too surprising, as these models have a longer history examining observables at SIS energies, particularly data for positive [53, 136] but also neutral kaons [137, 211].

<sup>&</sup>lt;sup>12</sup> The K-N potential does not affect the  $\Lambda$  kinematics.

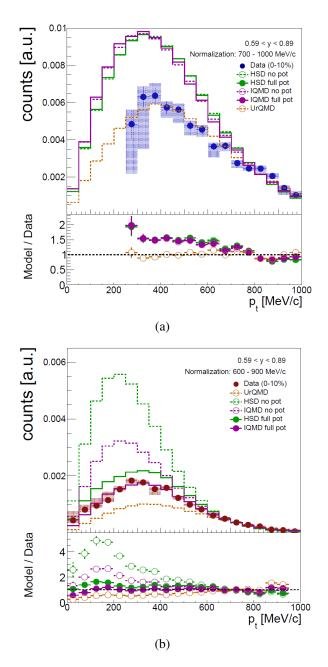


**Figure 6.11:** Transverse momentum spectra of (a)  $\Lambda$  (blue) and (b)  $K_s^0$  (red) at mid-rapidity (0.59 < y < 0.89) for most-central collisions (0-10%) compared to three models HSD (green), IQMD (purple) and UrQMD (orange). The model spectra are normalized to the integral of experimental data in the tails at high  $p_t$  in order to compare the shape at low transverse momenta, where a stronger sensitivity to a K/ $\Lambda$ -N potential is expected. For a better comparison, the ratio of model to experimental data is plotted in the lower part of each figure. Whereas IQMD and HSD without implementation of a K-N potential (dashed lines) miss the shape at low  $p_t$ , the inclusion of a K-N potential (solid lines) shows a rather well agreement for  $K_s^0$ , in particular for the IQMD model. In case of  $\Lambda$ , this potential does not have any significant effect on the distribution and fails to model the shape. Strikingly, UrQMD, which contains neither K- nor  $\Lambda$ -N potentials, reproduces the shape of the  $\Lambda p_t$  spectra, yet, misses the behaviour at low  $p_t$  for  $K_s^0$  mesons.

model		HSD (no pot)	IQMD (no pot)	UrQMD	HSD (pot)	IQMD (pot)
$K_s^0$	mult	0	0	0	0	0
	rise $\alpha$	•	0	0	•	•
	dN/dy	•	•	•	•	•
	$p_t$	0	0	0	0	•
Λ	mult	0	0	0	0	0
	rise $\alpha$	•	•	0	•	•
	dN/dy	•	•	•	•	•
	$p_t$	0	0	•	0	0

**Table 6.1:** Level of agreement between investigated observables in data and as obtained from transport model calculations. The two transport models HSD (green) and IQMD (purple) include the option of implementing a repulsive kaon-nucleon potential (*pot*) with a strength of 40 MeV at nuclear ground state density  $\rho_0$ , linearly increasing with density. The UrQMD model (orange), on the other hand, contains a more extended set of higher-lying  $\Delta$  and  $N^*$  resonances. The experimental data for  $\Lambda$  hyperons and  $K_s^0$  mesons have been compared to transport models with respect to four different observables: multiplicity (*mult*), rise of multiplicity with centrality (*rise*  $\alpha$ ) as well as the shape of the rapidity density (*dN/dy*) and transverse momentum ( $p_t$ ) distribution after normalizing the models to data. The level of agreement refers to experimental uncertainties and is roughly classified either as satisfactory ( $\bullet$ ) or not ( $\circ$ ).

A steady and systematic comparison for different collision systems between data and transport models, which rely on numerous input parameters, is mandatory to approach a more sophisticated prediction power<sup>13</sup>. Ambiguities in three out of four observables for each investigated particle are observed, hence, no common picture emerges. Before making sole conclusions on the K-N potential, more model-to-data comparison on additional observables are important to rule out further ambiguities.

Furthermore, an investigation of dynamical properties of strange hadrons, e.g. flow patterns, have been proposed to be a promising probe to draw conclusions on in-medium potentials [273, 274, 275] as they are free from uncertainties of total production yields. In the future, the study of such observables in the Au+Au collision system in the strangeness sector will deepen our understanding.

It will also be interesting to see how well the different models predict pion production in the same system as they are particularly sensitive to intermediate resonance production and hence the difference in the model descriptions may be pinned down more precisely.

<sup>&</sup>lt;sup>13</sup> Discrepancies in their predictions on physical observables may occur due to different model input such as crosssections, but, the type of model (e.g. QMD vs (semi-)classical treatment) or technical implementation should not influence the outcome.

### Are local two-body collisions an appropriate picture when describing HIC at high densities?

For both investigated hadrons  $\Lambda$  and  $K_s^0$ , as well as for  $K^+$ ,  $K^-$  and  $\phi$  mesons investigated in [37], a rise of the multiplicity stronger than linear with the number of participating nucleons  $\langle A_{part} \rangle$  was observed, as expected from simple threshold arguments. The rise was found to agree within uncertainties and hence to be independent on the clear hierarchy of their elementary production thresholds. This may not be expected considering a simple picture of multi-step processes where the strength of the rise is sensitive to the excess energy. However, this depends strongly on the defining picture and hence the degrees of freedom which one assumes to be relevant for particle production in a highly compressed system and whether quantum-mechanical processes play a role or not.

Considering, that the formation time  $\Delta \tau_f$  for a hadronic state is of the order of 1 fm/c and that the collisions rates  $\Delta f_{coll}^{-1}$  of hadrons can reach a few collisions per fm/c in transport models [136, 223], it follows that a violation of energy conservation in the order of approximately  $\hbar/\Delta f_{coll} \approx 200 - 500$  MeV, according to Heisenberg's equation 1.1 occurs. Hence a relevant question with respect to strangeness production in a transport model ansatz is whether NN thresholds can play a decisive role with such high uncertainties in energy reached during the interaction phase.

Many of the production mechanisms introduced in section 1.2.1 are based on hadronic degrees of freedom and neglecting quantum effects. An alternative picture is offered by the cloudy bag model, which was discussed in section 1.3.5 and at the end of section 1.2.2, giving reasonable explanations of e.g. enhancement of strange and in particular multi-strange hadron yields observed in HIC too. In this model, the properties of hadrons are described by the dynamics of their containing quarks confined inside a bag which is surrounded by a meson cloud. According to [164], an interesting implication of cloud sizes of roughly 0.8 - 1.1 fm would be that nucleons already at ground state density overlap in a nucleus and quark degrees of freedom become relevant. One can roughly estimate the lifetime of an  $s\bar{s}$  state to  $\Delta t_{
m life}pprox 1$  fm/c when using Heisenberg's uncertainty relation considering a mass of a strange quark of  $m_s \approx 100 \text{ MeV/c}^2$ . If one assumes a locally and temporally fusion of several hadrons to one large bag and that such a system may live long enough to establish a deep fermi sea of light quarks, the probability might be enhanced, that these quarks can interact with such a  $s\bar{s}$  state from the meson cloud and enable the formation of a (multi-)strange hadron. Another consequence could be that an  $s\bar{s}$  state propagating in the meson cloud could gain sufficient energy through scattering with light quarks from the bag to be lifted onto the mass shell.

An observation consistent with such a picture is the similar  $\langle A_{part} \rangle$  dependence of all strange hadrons. Another argument may be the enhancement of multi-strange particle production below the elementary threshold like e.g. the observed  $\Xi^-$  yield in the Ar+KCl collision system which could be reproduced only in two models up to now. It will be interesting to see whether more observables can be found to verify or falsify this scenario.

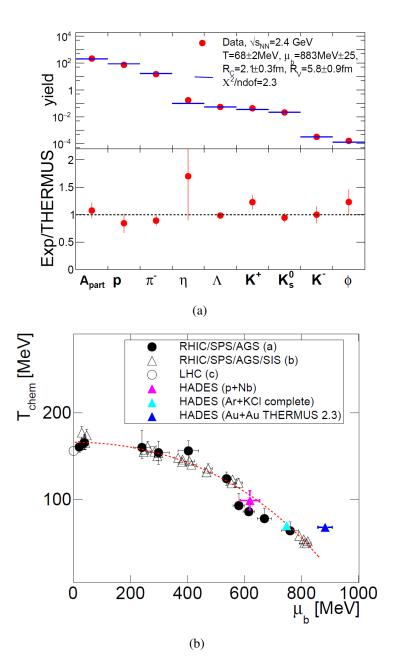


**Figure 6.12:** (a) Upper plot: Fit of the hadron yields at chemical freeze-out in the statistical hadronization model SHM (blue bars) to the measured yields (red points) for 0 - 20% most central data. Lower plot: Yield ratio of experimental data to SHM. The minimization shows a reasonable agreement with a  $\chi^2/n_{dof}$  of 2.3 giving the three macroscopic parameters temperature  $T_{chem} = 68 \pm 2$  MeV, baryo-chemical potential  $\mu_B = 883 \pm 25$  MeV and a radius of the fireball volume of  $R_V = 5.8 \pm 0.9$  fm. The correlation radius  $R_C$  is determined to  $2.1 \pm 0.3$  fm. (b) Comparison of the extracted chemical freeze-out point from Au+Au (dark blue) to data from other experiments in the T- $\mu_B$  plane. The red dashed line indicates a parametrization corresponding to a constant energy density  $\frac{\langle E \rangle}{\langle N \rangle}$  of 1 GeV. The colored data points refer to previous measurements by HADES, i.e. from Ar+KCl at 1.76A GeV (light blue) and p+Nb at 3.5 GeV (magenta).

## 6.4 Comparison to Statistical Hadronization Model

A different type of model introduced in chapter 1 are the statistical hadronization models (SHM). Here, particles are assumed to be produced probabilistic at chemical freeze-out emitted from a thermal source in equilibrium. In contrast to transport theory, for the description of particle yields the static SHM only depends on a few macroscopic parameters characterizing the system: temperature T, baryo-chemical potential  $\mu_B$  and volume V. These models have been found to successfully describe experimental particle production yields from top energies at LHC even down to the SIS18 energy regime [44, 276], where the underlying assumption of global and even local equilibrium is questionable. HADES demonstrated that a statistical model fit to elementary and p+Nb data gives results of at least same quality as in heavier systems [36], which leaves the question if or to which extent the fit quality sheds light on the degree of thermalization of the reaction.

Combining the results from this thesis with the investigations performed in [37] and [241], the SHM using the THERMUS software (version 2.3 [41]) can be fitted to the measured hadron yields for the 0 - 20% most central Au+Au collisions. The broad data set includes protons, negative pions, charged and neutral kaons,  $\eta$  mesons,  $\Lambda$  hyperons and  $\phi$  mesons<sup>14</sup>, as well as the mean number of participants  $\langle A_{part} \rangle$ . The SHM is treated in a strangeness canonical approach, i.e. strangeness has to be conserved exactly within a reduced volume of radius  $R_C$  which is smaller than the fireball volume<sup>15</sup>.

Figure 6.12 (a) shows the result of this fit indicating a fair agreement giving a  $\chi^2/n_{dof}$  of 2.3. The temperature at chemical freeze-out is determined to  $T_{chem} = 68 \pm 2$  MeV and the baryochemical potential to  $\mu_B = 883 \pm 25$  MeV with a fireball radius of  $R_V = 5.8 \pm 0.9$  fm. The fit provides a strangeness correlation radius of  $R_C = 2.1 \pm 0.3$  fm. The yield ratio of experimental data to SHM in the lower plot indicates a fair agreement within statistical uncertainties.

The obtained freeze-out parameters can now be compared to points from previous experiments in the T- $\mu_B$  plane, as depicted in figure 6.12 (b). Whereas the other data points seem to line up on a universal freeze-out curve (red dashed line) assuming a constant energy density  $\frac{\langle E \rangle}{\langle N \rangle}$ of 1 GeV, the new values of T and  $\mu_B$  obtained for Au+Au (dark blue) differ significantly with respect to this parametrization. At the same time, points extracted from an SHM fit to HADES data in smaller systems (Ar+KCl in light blue, p+Nb in magenta) show a better agreement. The temperature is comparable to the one obtained for the light collision system Ar+KCl but the baryo-chemical potential is roughly 10% higher than suggested by the freeze-out curve as well as further data points from Au+Au systems at low energies taken at AGS and SIS (open triangles). However, these data sets contained only few hadrons and the extracted parameters are therefore not well constrained. The impact of the number of hadrons included in an SHM fit has been studied recently in [36] for the Ar+KCl collision system.

In the future, it will be also important to compare the fireball radius at chemical freeze-out as obtained from the SHM fit to the HBT radii extracted from a femtoscopy measurements of pions [277].

<sup>&</sup>lt;sup>14</sup> The statistical and systematic uncertainties of the experimental hadron yields have been added in quadrature.

<sup>&</sup>lt;sup>15</sup> By definition, the  $\phi$  meson yield is not affected by such a suppression as strangeness conservation is immanent in an  $s\bar{s}$  state.

## 6.5 Chemical vs. Kinetic Freeze-out Temperatures

For a deeper investigation of thermal properties of the system, the effective temperatures  $T_{\rm eff}$  extracted for the hadrons investigated in [37] for  $\pi^-$ , proton, positive kaons and  $\phi$  mesons as well as in this thesis for  $\Lambda$  and  $K_s^0$  can be compared to the chemical freeze-out properties obtained by the SHM fit. Figure 6.13 shows the inverse slopes at mid-rapidity  $T_{\rm eff}$  as a function of mass of these hadrons<sup>16</sup> for 0 - 20% most central Au+Au data.

In a purely thermal system, the effective temperatures extracted from the transverse mass distributions can be considered as the kinetic freeze-out temperature of the particle. Strikingly, the effective temperatures for all hadrons<sup>17</sup> lie all above the chemical freeze-out temperature  $T_{\rm chem}$ . In an expanding system which cools down, the kinetic occurs by definition after the chemical freeze-out, hence an opposite ordering is expected for the temperatures, i.e.  $T_{\rm kin} < T_{\rm chem}$ , however, only when assuming a pure thermal system without additional collective effects.

As the momentum spectra are also affected by a collective expansion of the system, the effective temperature additionally contains a radial flow component. This collective motion with an average velocity  $\langle \beta_t \rangle$  depends on the mass of the particles and has to be added to the thermal temperature component giving the measured effective temperature as follows [29]:

$$T_{\rm eff} = T_{\rm kin} + m \left\langle \beta_t \right\rangle^2. \tag{6.2}$$

The momentum dependence is reflected in the significantly higher effective temperatures  $T_{\rm eff}$  extracted for protons compared to e.g. the much lighter pions leading to a distortion of their momentum spectra when comparing to Boltzmann spectra. The above equation is described by a Siemens-Rasmussen parametrization which can be fitted to the experimental transverse mass spectra, as it was done for protons [37], for which a higher sensitivity to the second term is expected than for pions or kaons. From this fit, the kinetic freeze-out temperature can be determined to  $T_{\rm kin}^{\rm SR} = 70 \pm 4$  MeV and the radial flow velocity to  $\beta_{\rm r}^{\rm SR} = 0.43 \pm 0.01$ . The value for  $T_{\rm kin}^{\rm SR}$  can be compared to the temperature obtained in the limit of zero masses, when assuming a linear increase of  $T_{\rm eff}$  with increasing mass as it is indicated by the data points for  $\pi^-$ , p and  $K^+$  giving a value of  $T_{\rm kin}^{\rm fit} = 71.5 \pm 4.2$  and a slope of  $\beta_{\rm r}^{\rm SR} = 0.28 \pm 0.09$ . These temperatures are within uncertainties of the same order as the chemical freeze-out temperature  $T_{\rm chem} = 68 \pm 2$  MeV as extracted from the SHM fit.

On the other hand, strange hadrons do not seem to experience a similar mass dependence on the effective temperature but rather show similar values within uncertainties among each other, as was already discussed when comparing the effective temperatures of  $K_s^0$  and  $\Lambda$ . This observation, that the much more massive  $\Lambda$  shows a similar  $T_{\text{eff}}$  as the neutral kaons, was already found in former measurements at similar beam energies by HADES [44] and by FOPI [229], however, in much lighter collision systems. A detailed investigation on flow observables of strange hadrons will give a more comprehensive insight to their collective behavior. In the future, it will also be

<sup>&</sup>lt;sup>16</sup> The negative kaons are not included. The analysis performed in [37] indicate a similar temperature as for positive kaons when correcting for the  $\phi$  feed-down.

<sup>&</sup>lt;sup>17</sup> Except for pions which are dominantly produced via resonance decays corresponding to the slope at low transverse momenta (indicated by the lower open circle at the pion mass).

interesting to see how the light nuclei deuterons, tritons or <sup>3</sup>He can contribute which will strongly constrain this picture due to their much higher mass. Additionally, a global blast wave fit [278], which is applied to all particle species simultaneously may give further insight on the thermal properties of the system.

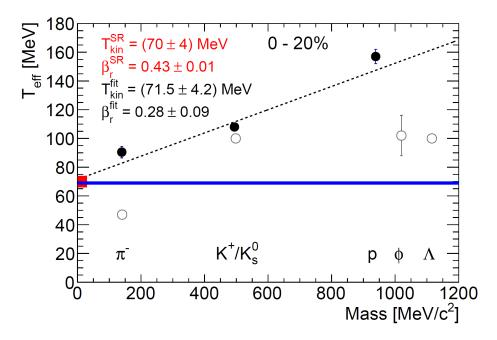


**Figure 6.13:** Effective temperatures  $T_{\text{eff}}$ , as extracted in this analysis for  $\Lambda$  and  $K_s^0$  as well as in the analysis within [37] for  $\pi^-$ , proton,  $K^+$  and  $\phi$ , as a function of hadron mass for the 0 - 20% most central events. The blue line indicates the chemical freeze-out temperature  $T_{\text{chem}} = 68 \pm 2$  MeV as obtained from the SHM fit to hadron yields, see previous section. The filled circles mark the data points of  $\pi^-$ ,  $K^+$  and protons to which a first-order polynomial function is fitted (dashed line) in order to extrapolate to zero masses and to extract the kinetic freeze-out temperature  $T_{\text{kin}}^{\text{fit}} = 71.5 \pm 4.2$  MeV and the radial flow velocity  $\beta_r^{\text{fit}} = 0.28 \pm 0.09$ . The red square indicates the kinetic freeze-out temperature stracted with a fit of a Siemens-Rasmussen parametrization to the  $m_t - m_0$  spectra of protons giving  $T_{\text{kin}}^{\text{SR}} = 74 \pm 4$  MeV [37].

# 6.6 Comparison of the Upper Production Limit of Ξ<sup>−</sup> to World Data

Figure 6.14 displays the invariant mass distribution of  $\Lambda^0$ - $\pi^-$  pairs showing no clear indication of a  $\Xi^-$  signal. As already presented in section 5.3, a Gaussian peak with a count rate of 157 and a width of  $\sigma = 4 \text{ MeV/c}^2$  is implemented (green dashed line), corresponding to the upper limit assumed to be the actual multiplicity, sitting on top of a second-order polynomial function (gray continuous line) fitted to the mixed-event background<sup>18</sup>.

<sup>&</sup>lt;sup>18</sup> A fit was chosen over ME data to improve visibility.

### 6.6. COMPARISON OF THE UPPER PRODUCTION LIMIT OF $\Xi^-$ TO WORLD DATA 197

The upper limit is compared to a UrQMD prediction of the  $\Xi^-$  yield (orange dashed line). A tuned version of the UrQMD transport model was one among two transport codes able to reproduce the observed cascade yield in the Ar+KCl system [108, 222]. An additional peak comprising 32 counts according to the UrQMD prediction for the  $\Xi^-$  yield in the Au+Au system is seen on top of the background being a factor 5 below the determined upper limit. The signal is deduced from a predicted  $\Xi^-/(\Lambda + \Sigma^0)$  [222] ratio of =  $3.5 \times 10^{-3}$ , multiplied with the measured  $\Lambda$  multiplicity of  $Mult_{tot} = 39.4 \times 10^{-3}$ , the number of events in this data set ( $N_{evts} = 1.98 \times 10^9$ ) folded with the acceptance and reconstruction efficiency ( $\epsilon_{acc} \propto \epsilon_{rec} = 1.2 \times 10^{-4}$ ) when applying the topology cuts listed in table 4.7.

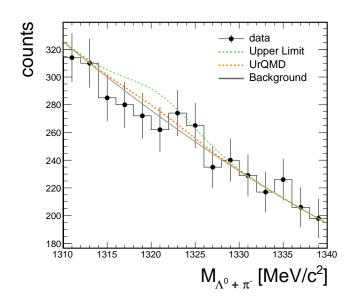
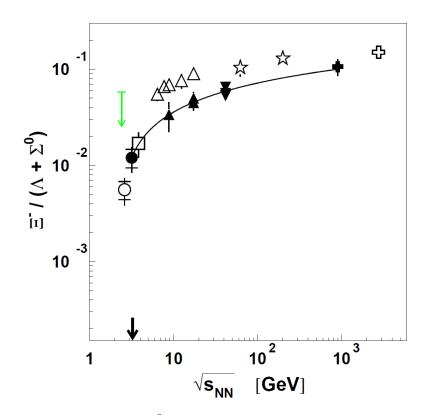


Figure 6.14: Invariant mass distribution of  $\Lambda$ - $\pi^-$  pairs (black points) zoomed into the expected  $\Xi^-$  mass region. Also indicated is the signal corresponding to the upper limit assumed to be the actual multiplicity following a Gaussian distribution on top of a second-order polynomial function (gray) fitted to the mixedevent background. The width ( $\sigma = 4$  $MeV/c^2$ ) is an educated guess based on the  $\Xi^-$  measurement in Ar+KCl at 1.76A GeV. A signal corresponding to a prediction by the UrQMD transport model is shown as well being a factor 5 below the upper limit.

Considering the upper production limit estimated in section 5.3, a maximum boundary on the ratio of  $\Xi^-$  to  $(\Lambda + \Sigma^0)$  hyperons is derived to be  $N_{\Xi^-}/N_{\Lambda+\Sigma^0} < 5.8 \times 10^{-2}$ . This limit is compared to world data in figure 6.15 which is in agreement with the sensitivity of the experimental setup estimated from former HADES measurements.

The relatively high upper limit indicates that HADES is not sensitive to a  $\Xi^-$  measurement in this system due to a significant increase in combinatorics. An enhanced yield of at least a factor 10 would be required compared to the measurement in the Ar+KCl collision system (open circle), which was already roughly a factor 10 above the SHM prediction.

However, the improvement in the track finding algorithm for secondary vertex decays in the new generation of data may significantly enhance the efficiency for the investigated decay channel. It will be also interesting to see, whether the  $\Xi^-$  is produced at slightly higher energies in the Ag+Ag system, which is on the agenda of upcoming beam times to be measured with HADES.



**Figure 6.15:** Yield ratio  $\Xi^-/(\Lambda + \Sigma^0)$  as a function of  $\sqrt{s_{\rm NN}}$ . The black arrow indicates the elementary production threshold of  $\Xi^-$  hyperons. The upper limit (green arrow) determined in this thesis is compared to data from symmetric heavy-ion reactions (open symbols) taken at LHC [263, 279] (cross), RHIC [280, 264] (stars), SPS [265, 281] (triangles), AGS [282] (square), and SIS18 [218] (circle). The filled symbols indicate data from p+A at SPS and DESY (upward and downward triangles), or elementary reactions at LHC (cross). The filled circle corresponds to the ratio obtained from p+Nb reactions at 3.5 GeV [110], the open circle from Ar+KCl at 1.76A GeV [218], both measured with HADES. The curve is a parameterization of the form  $f(\sqrt{s}) = C[1 - (D/\sqrt{s})^G]^H$  fitted to the data points indicated by filled symbols. Figure taken from [110, 283].

# Summary

### Sub-threshold Production of Strange Hadrons

Ab-initio calculations of quantum chromodynamics cannot be performed rigorously on the lattice at finite baryo-chemical potentials due to the fermion sign problem, hence effective descriptions have to be used in order to model properties of dense systems and the involved particles. The unique tool to constrain the input to such effective models at densities exceeding nuclear ground state density  $\rho_0$  experimentally are relativistic heavy-ion collisions (HIC). It is in particular the behavior of hadrons containing strangeness, i.e. kaons,  $\Lambda$  and multi-strange hyperons, in the dense medium which may has severe implications on astrophysical objects and processes.

At a beam energy of  $\sqrt{s_{\rm NN}} = 2.4$  GeV in the investigated Au+Au collision system all strange hadrons are produced below their individual elementary production threshold, hence a production in binary collisions is not possible and must be enabled by the surrounding medium in multi-step processes or by modification of their properties. The strange hadrons produced in this system can therefore be considered to be promising messengers for the high-density phase as in this phase a high sensitivity to such processes is expected. As the coupling of kaons containing an  $\bar{s}$  quark to baryons via formation of hyperons is suppressed, they have been in particular focus of numerous investigations e.g. trying to extract the equation of state (EOS) of nuclear matter as well as the attempt to determine the strength of the kaon-nucleon (KN) potential, both by comparing data to microscopic models. The latter one was studied using various different approaches, e.g. chiral Lagrangians, OBE models, the Nambu-Jona-Lasinio model or coupled-channel treatments finding a broad consent on a repulsive KN potential of increasing strength with rising density. Comparisons of experimental data to transport models seem to support this scenario, however, so far still no model provides a consistent picture of all kaon observables simultaneously.

The properties of  $\Lambda$  and multi-strange hyperons such as  $\Xi^-$  in a dense multi-nucleon environment has influence on the EOS itself and their appearance in the core of neutron stars via the weak interaction may lead to a significantly softening of these objects. Their occurrence seemingly conflicts recent findings on the maximum mass of neutron stars, however, the degree of softening strongly depends on the strength of the attractive  $\Lambda$ -nucleon ( $\Lambda$ N) potential at densities exceeding nuclear ground state density  $\rho_0$ , which is yet barely constrained. According to e.g. the  $\omega$ - $\sigma$  model this potential is even predicted to be repulsive above three times  $\rho_0$ .

As mentioned above, relativistic HIC provide the opportunity to study the in-medium potentials of strange hadrons at supra-normal densities when comparing to microscopic transport models. Up to now, not much data on neutral kaons and  $\Lambda$  hyperons are available from heavy collision systems close to the NN threshold. These two electromagnetically uncharged strange hadrons are in particular well suited to study their potential in a dense nucleon-dominated environment as their kinematic spectra are not affected by Coulomb interactions. Furthermore, the production of the doubly-strange  $\Xi^-$  hyperon has never been investigated thus far below its elementary production threshold (-840 MeV). Already the observation in the Ar+KCl collision system with HADES could up to now only be predicted by two theoretical models and required a reconsideration of (multi-)strange particle production processes in the dense medium. According to many scenarios, the much larger Au+Au collision system may provide an even more beneficial environment to catalyze the Cascade production, on the other hand, the strong increase of combinatorics and hence the deterioration of the signal-to-background ratio presents a challenge for its reconstruction via three final state particles.

# Reconstruction of $\Lambda$ and $K^0_s$ in Au+Au Collisions with HADES

In April and May 2012 data on Au+Au collisions at beam energies of  $E_{\rm kin} = 1.23$ A GeV were recorded with the High Acceptance Di-Electron Spectrometer, which is located at the GSI Helmholtz Center for Heavy Ion Research in Darmstadt, Germany. The charged-particle spectrometer consists of a six-coil toroidal magnet centered around the beam axis and six trapezoidal sectors covering almost the full azimuthal angle. Each of these sectors contains in the indicated order a Ring-Imaging Cherenkov (RICH) detector, four planes of Mini-Drift Chambers (MDC), two in front of and two behind the superconducting magnet (ILSE), followed by a scintillator hodoscope (TOF) and Resistive Plate Chambers (RPC) respectively in the back of the setup. Whereas the RICH detector is mainly used for  $e^+/e^-$  identification purposes, the drift chambers MDC in combination with the magnet serve as tracking detectors and TOF/RPC are used for time-of-flight measurements together with a diamond-based  $t_0$  detector, located in front of the 15-fold segmented gold target, to determine the start time of the collision. The polar angle  $\theta$  is covered from 18° to 45° by the RPC and from 45° to 85% by the TOF walls. A forward hodoscope  $(0.3^{\circ} < \theta < 7.3^{\circ})$  is completing the setup which can be used for the event plane determination.

After an elaborate event cleaning procedure, in total 2.1 x  $10^9$  Au+Au events were analyzed containing the 0 - 40% most central events. The investigated strange hadrons  $\Lambda$  and  $K_s^0$  are identified via their weak decays into  $p \cdot \pi^-$  (BR $\approx 63.9\%$ ) and  $\pi^+ \cdot \pi^-$  (BR $\approx 69.2\%$ ) respectively. Therefore, loose cuts on the reconstructed mass of pions and protons as well as their track quality parameters is applied. The relatively large mean decay lengths of 7.89 and 2.68 cm enable an analysis based on constraints on the decay topology which allows to distinguish between the decay and the primary vertex in order to suppress combinatorial background to the invariant mass spectrum. The remaining uncorrelated background is reproduced via the mixed-event technique and subtracted. The remaining signal is parametrized by a Gaussian and integrated in a  $3\sigma$  region around the mean of the distribution. For the 0 - 40% most central collisions, this gives in total 95000  $K_s^0$  mesons and 71000  $\Lambda$  hyperons with signal-to-background ratios of 0.5 - 7 and 0.5 - 4 respectively. The data is analyzed multi-differentially as a function of rapidity y, transverse mass  $m_t$  and four centrality classes in steps of 10%. The extracted raw signal counts are corrected for limited acceptance and efficiency of the spectrometer individually for each phase space cell. The

#### SUMMARY

correction factors are based on particles generated in a Monte Carlo simulation with PLUTO, which are subjected to a realistic detector response and acceptance simulation in GEANT and finally propagated through the full analysis chain as used for experimental data. By this method, combined acceptance and efficiency correction factors of 0.4 - 1.9% for  $K_s^0$  and 0.2 - 1.4% for  $\Lambda$  are obtained.

## **Results and Discussion**

The corrected yields N per transverse mass  $m_t$  and rapidity y are normalized to the transverse mass squared  $m_t^2$  and plotted as a function of reduced transverse mass  $m_t - m_0$ , as can be seen in figure 6.16, such that the Boltzmann relation in the following representation

$$\frac{1}{m_t^2} \frac{d^2 M}{dm_t dy_{\rm cm}} = C(y_{\rm cm}) \, \exp\left(-\frac{(m_t - m_0)c^2}{T_B(y)}\right) \tag{6.3}$$

can be applied to fit the data points. The Boltzmann equation describes statistical (particle) emission assuming a thermal source where the Boltzmann temperature  $T_B$  is given by the rapidity-dependent inverse slope of the spectrum. The inverse slope for thermally emitted particles reaches a maximum at mid-rapidity  $y_{\rm mid}$  which is referred to as effective temperature  $T_{\rm eff}$  and which can be related to the kinetic freeze-out temperature  $T_{kin}$ . The rapidity density distributions shown in figure 6.17 are obtained by integration of data points of the transverse mass spectra and the yield in the unmeasured phase space is determined by using the extrapolation assuming the Boltzmann parametrization. In order to end up with the total particle production yield  $Mult_{tot}$ , a Gaussian distribution is fitted to data and can be used to estimate the yield outside the acceptance. The systematic uncertainties are estimated by varying the region of normalization for the mixed-event background and the values used for the topology cuts. For the 0-40% most central collisions multiplicities of  $Mult_{tot} = (3.97 \pm 0.06^{stat} \pm 0.06^{sys}_{Cut} \pm 0.04^{sys}_{Extrapol}) \times 10^{-2}$  for  $\Lambda$  hyperons and of  $Mult_{tot} = (1.54 \pm 0.03^{stat} \pm 0.05^{sys}_{Cut} \pm 0.15^{sys}_{Extrapol}) \times 10^{-2}$  for  $K_s^0$  mesons were determined. The inverse slope parameters at mid-rapidity  $T_{eff}$  of  $93\pm2\pm4$  for  $\Lambda$  and  $97\pm1\pm2$  for  $K_s^0$  $K_s^0$  agree within uncertainties. The analysis is repeated as a function of four centrality bins in steps of 10% from most central 0 - 10% to semi-peripheral 30 - 40% events following the very same strategy as for the integrated yields obtained for 0 - 40% most central collisions. For both particles a more than linear rise of the mean multiplicity is observed with centrality which is in agreement with measurements by former experiments at higher energies. This indicates that the strength of the rise is only weakly proportional to the excess energy.

The experimental data are compared to predictions from three hadronic transport models: IQMD (c8), HSD (711n) and UrQMD (3.4). All three are semi-classical models simulating HIC on an event-by-event basis. While UrQMD produces particles at SIS energies in two-step processes via intermediate resonance excitations, in HSD and IQMD also direct production via two-to-three particle processes are included. In the presented version of UrQMD, neither mean field NN-potentials nor explicit K/ $\Lambda$ -N potentials are included. As the treatment of a many-body problem is complex, in transport models the potentials are reduced to a one-body problem where e.g. kaons or hyperons are propagated in a mean field, generated by all surrounding nucleons.

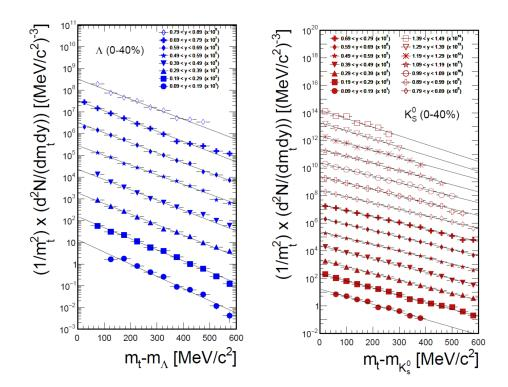


**Figure 6.16:** Transverse mass spectra corrected for acceptance and efficiency as a function of rapidity for  $\Lambda$  (left) and  $K_s^0$  (right) for the 40% most central data normalized to the transverse mass squared  $m_t^2$ . A Boltzmann function can be used to determine the yield in unmeasured phase space regions and to extract the inverse slope  $T_{\rm B}$ .

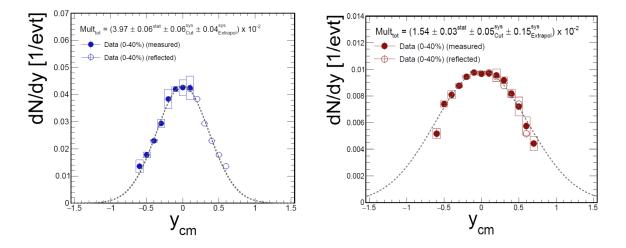


**Figure 6.17:** (a) Rapidity density distribution dN/dy for  $\Lambda$  (left) and  $K_s^0$  (right) as a function of center-of-mass rapidity normalized to the number of events for 40% most central data (filled circles). The measured data is reflected at mid-rapidity  $y_{mid}$  (open circles). A Gaussian distribution is fitted to the measured data points and can be used to determine the yield in the region of unmeasured rapidities.

### SUMMARY

Such potentials depend on the density of the system and modify the kinematics and hence crosssections of particle production.

The investigated transport models can be grouped in two relevant fractions: on one side, the HSD and IQMD transport models with a K-N potential of 40 MeV at nuclear ground state density  $\rho_0$  increasing linearly with density as well as a  $\Lambda$ N potential which scales with 2/3 of the strength of the NN potential. On the other side there is the UrQMD code which employs higher-lying  $\Delta$  and  $N^*$  resonances but neither includes a repulsive KN nor an attractive N/ $\Lambda$ N potential. Table 6.2 summarizes whether the presented transport models provided satisfactory (•) descriptions of the investigated observables or not ( $\circ$ ). It is shown, that no model describes all observables at once and that no observable can be described unambiguously by all models.

Results from the HSD and IQMD transport models may give the impression that a repulsive K-N potential is necessary to describe particle kinematics ( $p_t$  spectra), yet, at least partially UrQMD calculations can (over)compensate the effect of the potential via particle production through intermediate resonances but fails to reproduce the scaling of the yields with centrality. On the other hand,  $\Lambda p_t$  spectra are best described by UrQMD. The ambiguities in three out of four observables for each investigated particle hamper conclusions on the K/ $\Lambda$ N potential and more model-to-data comparison on additional observables are important to rule out ambiguities.

model		HSD (no pot)	IQMD (no pot)	UrQMD	HSD (pot)	IQMD (pot)
$K_s^0$	mult	0	0	0	0	0
	rise $\alpha$	•	0	0	•	•
	dN/dy	•	•	•	•	•
	$p_t$	0	0	0	0	•
Λ	mult	0	0	0	0	0
	rise $\alpha$	•	•	0	•	•
	dN/dy	•	•	•	•	•
	$p_t$	0	0	•	0	0

**Table 6.2:** Level of agreement between investigated observables in experimental data and as obtained from calculations by the transport models HSD, IQMD each with and w/o potential and UrQMD. The comparisons were made with respect to four different observables: multiplicity (*mult*), rise of multiplicity with centrality (*rise*  $\alpha$ ) as well as the shape of the rapidity density (*dN/dy*) and transverse momentum ( $p_t$ ) distribution after normalizing the models to data. The level of agreement refers to experimental uncertainties and is roughly classified either as satisfactory ( $\bullet$ ) or not ( $\circ$ ).

Observing a null result within the attempt to reconstruct the multi-strange  $\Xi^-$  hyperon, an upper limit on the production yield can be determined. This limit is derived by using the Feldman-Cousins approach, which is purely based on the statistics of the selected data sample. The confidence interval is chosen to include 99.7% of the hypothetical signal providing an upper limit of  $M_{\rm FC} < 2.32 \text{ x} 10^{-3}$ , being in agreement with former  $\Xi^-$  measurements and transport predictions. Considering the upper production limit, a maximum boundary on the ratio of  $\Xi^-$  to  $(\Lambda + \Sigma^0)$  hyperons is derived to be  $N_{\Xi^-}/N_{\Lambda+\Sigma^0} < 5.8 \text{ x} 10^{-2}$ .

# Zusammenfassung

### Produktion von Seltsamkeit unterhalb der NN-Schwelle

Relativistische Schwerionenkollisionen (HIC) erlauben die Erzeugung hadronischer Materie mit bis zu dreifacher Grundzustandsdichte  $\rho_0$ , wie sie beispielsweise im Inneren von Neutronensternen auftreten könnte. Da diese Zustände mit Hilfe der Theorie der starken Wechselwirkung, der Quantenchromodynamik (QCD), bei endlichen Dichten nicht präzise berechnet werden können, muss auf effektive Beschreibungen dichter Systeme und der darin befindlichen Teilchen zurückgegriffen werden. Diese effektiven Modelle liefern Vorhersagen für Schwerionenexperimente und dienen umgekehrt der weiteren Präzisierung dieser theoretischen Beschreibungen und deren Anfangsbedingungen. Im Speziellen das Verhalten Seltsamkeit-enthaltender Teilchen wie Kaonen ( $K^{+/-}$ ,  $K_s^0$ ) und Hyperonen ( $\Lambda$ ,  $\Xi^-$ ) in dichter Materie könnte weitreichende Konsequenzen für astrophysikalische Prozesse sowie Objekte und deren Struktur haben.

Bei einer Strahlenergie im untersuchten Au+Au-Kollisionssystem von  $\sqrt{s} = 2,4$  GeV läuft die Produktion aller Seltsamkeit-enthaltenden Hadronen unterhalb ihrer individuellen Nukleon-Nukleonschwelle ab, was eine Produktion in binären Kollisionsprozessen unmöglich macht und daher indirekt durch das sie umgebende Medium bewerkstelligt werden muss. Die unter diesen Bedingungen produzierten Hadronen eignen sich daher besonders, um die Hochdichtephase des Systems zu untersuchen, da die Produktion in dieser Phase maximal sensitiv auf sekundäre Produktionsprozesse ist. Insbesondere Kaonen, die im Gegensatz zu Antikaonen aufgrund ihres  $\bar{s}$ -Quarkinhalts nicht stark an Baryonen über die Erzeugung von Hyperonresonanzen koppeln, propagieren relativ ungestört in dichter Materie und waren daher im Fokus zahlreicher Untersuchungen einschließlich dem Versuch der Formulierung der Zustandsgleichung (EOS) von Kernmaterie sowie der Bestimmung des Kaon-Nukleon (KN) Potentials mit Hilfe von Transportmodellen. Letzteres kann mit Hilfe effektiver theoretischer Modelle wie u.a. chiralen Lagrangians oder dem Nambu-Jona-Lasinio-Modells beschrieben werden, überwiegend mit dem Ergebnis eines repulsiven KN Potentials, dessen Stärke mit steigender Dichte zunimmt. Der Vergleich experimenteller Daten mit mikroskopischen Transportmodellen scheint dieses Szenario zu bekräftigen, jedoch ist es bislang keinem dieser Modelle gelungen eine konsistente, simultane Beschreibung aller Kaon-Observablen zu liefern.

Weiterhin hätte das Verhalten der  $\Lambda$  sowie  $\Xi^-$  Hyperonen in dichten Vielteilchensystemen entscheidenden Einfluss auf die Steifigkeit der EOS. Ihr Vorkommen im Innersten von Neutronensternen würde zu einer signifikanten Reduktion der Steifigkeit solcher Objekte führen, was in scheinbarem Widerspruch zu jüngsten Messungen der maximalen Masse von Neutronensternen steht. Der Grad der Steifigkeit der EOS hängt jedoch stark von der Größe des attraktiven AN Potentials ab, dessen Dichteabhängigkeit abseits der Grundzustandsdichte  $\rho_0$  kaum bekannt und gemäß einiger Modelle sogar repulsiv oberhalb 3 x  $\rho_0$  ist.

Wie oben erwähnt bieten relativistische HIC die einzige Möglichkeit das Potential seltsamer Teilchen in Materie oberhalb der Grundzustandsdichte zu untersuchen, indem experimentelle Daten mit Transportmodellen verglichen werden. Die Datenlage um neutrale Kaonen und  $\Lambda$  Hyperonen, die in Schwerionenkollisionen unterhalb der elementaren Schwelle produziert werden, ist bis heute rar. Diese beiden elektrisch neutralen seltsamen Hadronen eignen sich insbesondere um das Potential in dichter Nukleon-dominierter Umgebung zu untersuchen, da ihre kinematischen Spektren nicht durch Coulomb-Wechselwirkung überlagert werden. Weiterhin wurde das  $\Xi^-$  Hyperon, welches zwei seltsame Quarks enthält, bislang nicht derart weit unterhalb seiner NN-Schwelle (-840 MeV) nachgewiesen. Bereits die Messung im Ar+KCl-Kollisionssystem mit HADES wurde bis zum heutigen Zeitpunkt nur von zwei theoretischen Modellen beschrieben und führte zu einem Überdenken der zugrundeliegenden Produktionsprozesse. Auf der einen Seite bietet gemäß vieler Vorhersagen das wesentlich größere Au+Au-Kollisionssystem eine günstigere Umgebung zur Katalysation der  $\Xi^-$  Produktion. Auf der anderen Seite stellt der immense Anstieg an Kombinatorik und somit die gravierende Verschlechterung des Signal-zu-Untergrund Verhältnisses eine Herausforderung in der Rekonstruktion über die drei geladenen Hadronen im Endzustand dar.

# **Rekonstruktion von** $\Lambda$ , $K_s^0$ und $\Xi^-$ in Au+Au mit HADES

Im April und Mai 2012 nahm das in Darmstadt am SIS18 befindliche High Acceptance Di-Electron Spectrometer Daten von Au+Au-Kollisionen bei einer Strahlenergie von  $E_{kin} = 1,23A$ GeV auf. Das Spektrometer zum Nachweis geladener Teilchen besteht aus einem sechsspuligen Toroidalmagneten in rotationssymmetrischer Anordnung um die Strahlachse und sechs trapezoidalen Sektoren, die annähernd den vollen Azimuthalwinkel abdecken. Jeder dieser Sektoren umfasst in angegebener Reihenfolge einen Ring-Imaging Cherenkov (RICH) Detektor, vier Ebenen von Mini-Drift Chambers (MDC), wovon sich zwei vor und zwei hinter dem supraleitenden Magneten (ILSE) befinden, gefolgt von einem Szintillatorhodoskop (TOF) sowie einer Resistive Plate Chamber (RPC) im hinteren Teil des Spektrometers. Während der RICH Detektor hauptsächlich zur Identifizierung von  $e^+$ - $e^-$ -Paaren dient, eignen sich die Vieldrahtdriftkammern MDC in Kombination mit dem Magneten als Spurrekonstruktionsdetektoren. Die TOFbzw. RPC-Wände werden zusammen mit einem Startzeitdetektor, der sich vor dem 15-fach segmentierten Goldtarget befindet, zur Flugzeitmessung verwendet. Der Aufbau deckt einen Polarwinkelbereich von  $18^{\circ}$  bis  $45^{\circ}$  im RPC- und von  $45^{\circ}$  bis  $85^{\circ}$  im TOF-Bereich ab. Ein Vorwärtshodoskop zur Bestimmung der Reaktionsebene schliesst das Spektrometer im niedrigen Polarwinkelbereich  $(0, 3^{\circ} \text{ bis } 7, 3^{\circ})$  ab.

Nach einer sorgfältigen Ereignisselektion wurden insgesamt 2,1 x  $10^9$  Au+Au-Reaktionen analysiert, welche die 0 - 40% zentralsten Ereignisse enthalten. Die untersuchten seltsamen Hadronen  $\Lambda$  und  $K_s^0$  werden über ihre schwachen Zerfälle in p- $\pi^-$  (BR  $\approx 63, 9\%$ ) bzw.  $\pi^+$ - $\pi^-$ (BR  $\approx 69, 2\%$ ) nachgewiesen. Diese geladenen Hadronen wiederum werden über ihre rekon-

struierte Masse sowie über Spurrekonstruktionsparameter ausgewählt. Die relativ großen mittleren Zerfallslängen von 7,89 bzw. 2,68 cm ermöglichen eine Analyse basierend auf deren Zerfallstopologie. Hierbei kann der Reaktions- vom Zerfallsvertex unterschieden und zur Unterdrückung des kombinatorischen Untergrunds zum invarianten Massenspektrum verwendet werden. Der unkorrelierte Untergrund kann über die Mixed-Event Methode wiedergegeben und vom Massenspektrum abgezogen werden. Das resultierende Signalspektrum wird durch eine Gauß-Funktion parametrisiert und anschließend in einem  $3\sigma$ -Bereich um den Mittelwert  $\mu$  integriert. Dies ermöglicht den Nachweis von 95000  $K_s^0$  Mesonen und 71000  $\Lambda$  Hyperonen mit einem Signal-zu-Untergrund Verhältnis von 0, 5-7 bzw. 0, 5-4 für die 0-40% zentralsten Ereignisse. Die Daten werden daraufhin differentiell als Funktion der Rapidität, reduzierten transversalen Masse  $m_t - m_0$  sowie in vier Zentralitätsklassen in Schritten von 10% analysiert. Die extrahierten Signalzählraten werden im Anschluss auf die eingeschränkte Akzeptanz und Effizienz des Spektrometers individuell in jeder Phasenraumzelle korrigiert. Die Korrektur basiert auf in Monte-Carlo Simulationen generierten Teilchen, die anschließend einer realistischen Simulation des Detektoransprechverhaltens sowie der Akzeptanz mit Hilfe von GEANT unterzogen werden. Daraufhin durchlaufen die Teilchen dieselbe Analysekette wie die experimentellen Daten. Die auf diese Weise gefundenen Werte für die kombinierte Akzeptanz und Effizienz reichen von 0, 4 - 1, 9% für  $K_s^0$  und 0, 2 - 1, 4% für  $\Lambda$ . Die Effizienzen für die  $\Lambda$ -Rekonstruktion sind niedriger aufgrund stärkerer Einschränkung der Topologieparameter bedingt durch eine größere Kombinatorik der Hadronen im Endkanal.

### **Resultate und Diskussion**

Die korrigierten Zählraten N pro transversale Masse  $m_t$  und Rapidität y werden auf  $m_t^2$  normiert und als Funktion der reduzierten transversalen Masse  $m_t - m_0$  aufgetragen, wie in Abbildung 6.18 zu sehen ist, sodass die Boltzmann-Beziehung in folgender Darstellung

$$\frac{1}{m_t^2} \frac{d^2 M}{dm_t dy_{\rm cm}} = C(y_{\rm cm}) \, \exp\left(-\frac{(m_t - m_0)c^2}{T_B(y)}\right) \tag{6.4}$$

an die Datenpunkte angepasst werden kann. Die Boltzmann-Gleichung beschreibt die statistische Teilchenemission durch eine thermischen Quelle, wobei die Boltzmann-Temperatur  $T_B$ durch den rapiditätsabhängigen, inversen Steigungsparameter des Spektrums gegeben ist. Dieser Steigungsparameter für thermisch emittierte Teilchen erreicht sein Maximum bei Midrapidität, der an dieser Stelle auch als effektive Temperatur  $T_{eff}$  bezeichnet wird und von der kinetischen Ausfriertemperatur  $T_{kin}$  abhängt. Die Rapiditätsdichtespektren, dargestellt in Abbildung 6.19, werden durch Integration der Datenpunkte der transversalen Massenspektren und durch Integration der Boltzmann-Parametrisierung zur Bestimmung der extrapolierten Zählraten bestimmt. Zur Ermittlung der totalen Produktionsrate Mult<sub>tot</sub> werden einerseits die Datenpunkte der Dichteverteilungen integriert. Andererseits, zur Bestimmung der Multiplizität außerhalb der Akzeptanz, wird die Verteilung mit einer Gauß-Funktion angepasst, welche anschließend in diesem Bereich integriert werden kann. Die systematischen Unsicherheiten werden über Variation der Analyseparameter, nämlich der Zerfallstopologiegrößen und des Normalisierungsbere-

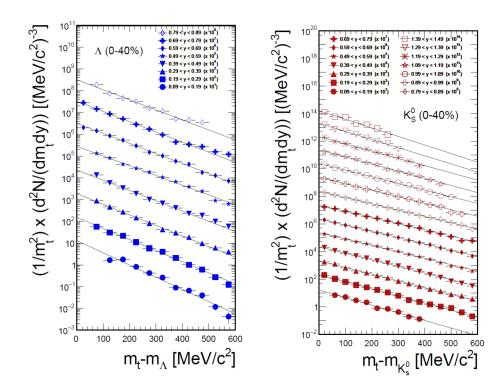


**Figure 6.18:** Transversale Massenspektren korrigiert auf Akzeptanz und Effizienz des Spektrometers und normiert auf  $m_t^2$  als Funktion der Rapidität für  $\Lambda$  (links) und  $K_s^0$  (rechts). Durch Anpassung einer Boltzmann-Funktion an die Daten kann die korrigierte Zählrate in Bereichen außerhalb der Akzeptanz sowie der inverse Steigungsparameter  $T_{\rm B}$  bestimmt werden.

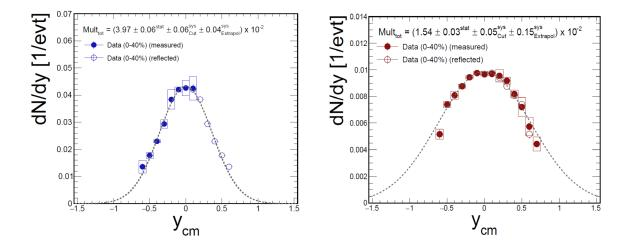


**Figure 6.19:** Rapiditätsdichteverteilungen dN/dy für  $\Lambda$  (links) und  $K_s^0$  (rechts) als Funktion der Schwerpunktsrapidität normiert auf die Anzahl der 40% zentralsten Ereignisse (gefüllte Kreise). Die gemessenen Daten werden um Midrapidität  $y_{mid} = y_{cm}(0)$  gespiegelt (offene Kreise). Eine Gauß-Verteilung wird an die Daten angepasst, um die Multiplizität außerhalb der Akzeptanz zu bestimmen.

iches der Mixed-Event-Spektren, bestimmt. Es wurden Multiplizitäten für die 0 - 40% zentralsten Kollisionen von  $Mult_{tot} = (3,97 \pm 0,06^{stat} \pm 0,06^{sys}_{Cut} \pm 0,04^{sys}_{Extrapol}) \times 10^{-2}$  für  $\Lambda$  Hyperonen und von  $Mult_{tot} = (1,54 \pm 0,03^{stat} \pm 0,05^{sys}_{Cut} \pm 0,15^{sys}_{Extrapol}) \times 10^{-2}$  für  $K_s^0$  Mesonen ermittelt. Die inversen Steigungsparameter bei Midrapidität  $T_{eff}$  von  $93\pm2\pm4$  für  $\Lambda$  und  $97\pm1\pm2$  für  $K_s^0$  stimmen innerhalb der Unsicherheiten miteinander überein. Die genannten Schritte werden für die vier Zentralitätsklassen wiederholt. Für beide Teilchen wird ein mehr als linearer Anstieg der Produktionsrate mit zunehmender Anzahl der Partizipanten, und somit der Zentralität, beobachtet. Dieser Anstieg ist in Übereinstimmung mit den Ergebnissen früherer Experimente bei höheren Energien, was den Schluss nahe legt, dass die Stärke des Anstiegs nur eine schwache Abhängigkeit von der Exzessenergie aufweist.

Im Anschluss werden die experimentellen Daten mit Vorhersagen dreier State-of-the-Art-Transportmodelle verglichen: IQMD (c8), HSD (711n) und UrQMD (3.4). Bei diesen Modellen handelt sich um semi-klassische Beschreibungen, die der Simulation von Schwerionenkollisionen auf Event-by-Event-Basis dienen. Während UrQMD im SIS18-Energiebereich Teilchen ausschließlich in Zwei-Schritt-Prozessen über intermediäre Resonanzanregung erzeugt, sind in HSD und IQMD auch die direkte Produktion von zwei Teilchen im Ausgangs- zu drei Teilchen im Endkanal möglich. Da sich die Behandlung von Vielteilchensystemen als äußerst komplex darstellt, wird in Transportmodellen das Potential auf die Beschreibung eines Einteilchenproblems reduziert, in der z.B. Kaonen oder Hyperonen in mittleren Feldpotentialen propagieren, die durch alle sie umgebenden Nukleonen erzeugt wird. Solche Potentiale hängen stark von der Dichte des Systems ab und können großen Einfluss auf die Wirkungsquerschnitte und Kinematik (Rot- für attraktive, Blauverschiebung für repulsive Potentiale) von Teilchen haben. Die untersuchten Transportmodelle lassen sich grob in zwei Gruppen unterteilen: Auf der einen Seite stehen die Modelle HSD und IQMD mit einem repulsiven KN Potential von 40 MeV bei Grundzustandsdichte  $\rho_0$  und linearem Anstieg mit zunehmender Dichte, sowie einem attraktiven AN Potential, das mit 2/3 relativ zur Stärke des NN Potentials skaliert. Auf der anderen Seite befindet sich UrOMD, welches in der verwendeten Version weder mittlere NN Potentiale noch KN/AN Potentiale beinhaltet. Tabelle 6.3 zeigt einen Überblick, ob das präsentierte Modell eine befriedigende (•) oder weniger befriedigende (0) Beschreibung der untersuchten Observablen liefert, gemessen anhand der Übereinstimmung im Rahmen der experimentellen Unsicherheiten. Es zeigt sich, dass kein Modell in der Lage ist, alle Observablen simultan zu beschreiben und keine Observable übereinstimmend von allen Modellen beschrieben werden kann.

Die Ergebnisse der HSD und IQMD Transportmodelle legen nahe, dass ein repulsives KN Potential notwendig ist, um die Teilchenkinematik ( $p_t$ -Spektren) wiederzugeben, jedoch ist UrQMD zumindest teilweise in der Lage diesen Effekt des Potentials durch die Produktion über Zwischenresonanzen zu kompensieren. Gleichzeitig scheitert es daran, den Anstieg der Multiplizitäten mit steigender Zentralität zu beschreiben. Eine auffällig gute Beschreibung liefert letzteres Modell bei der Beschreibung der  $p_t$ -Spektren der  $\Lambda$  Hyperonen. Die Uneindeutigkeit der Vorhersagen (für je drei von vier Observablen pro Teilchen) macht den weiteren Versuch der Extraktion von KN bzw.  $\Lambda$ N Potentialen unmöglich.

Die Beobachtung eines Nullresultats beim Versuch der Rekonstruktion des  $\Xi^-$  Hyperons veranlasste die Bestimmung einer oberen Produktionsgrenze. Diese Grenze wird mit Hilfe der Feldman-Cousins Methode, welche rein auf der Statistik der vorliegenden Datenprobe basiert,

#### ZUSAMMENFASSUNG

model		HSD (no pot)	IQMD (no pot)	UrQMD	HSD (pot)	IQMD (pot)
K0	mult	0	0	0	0	0
	rise $\alpha$	•	0	0	٠	•
$K_s^0$	dN/dy	•	•	•	•	•
	$p_t$	0	0	0	0	•
Λ	mult	0	0	0	0	0
	rise $\alpha$	•	•	0	•	•
	dN/dy	•	•	•	٠	•
	$p_t$	0	0	•	0	0

**Table 6.3:** Übereinstimmung der untersuchten Observablen experimenteller Daten mit Vorhersagen dreier Transportmodelle HSD, IQMD (je mit Option mit/ohne KN Potentials) und UrQMD. Der Vergleich wurde in Bezug auf folgende Observablen durchgeführt: Multiplizität (*mult*), Anstieg der Multiplizität mit Zentralität der Kollision (*rise*  $\alpha$ ) sowie die Form der Verteilungen der Rapiditäts-(*dN/dy*) und transversalen Impulsspektren (*p*<sub>t</sub>). Der Grad der Übereinstimmung bezieht sich hierbei auf experimentelle Unsicherheiten und is grob eingeteilt in befriedigend (•) und weniger befriedigend ( $\circ$ ).

ermittelt. Hierfür wird ein Konfidenzintervall gewählt, das 99,7% (entsprechend  $3\sigma$  einer Normalverteilung) des hypothetischen Signals umfasst, was zu einer oberen Grenze von  $M_{\rm FC}$  < 2,32 x  $10^{-3}$  führt. Das Resultat stimmt mit früheren Untersuchungen zur Rekonstruktionsfähigkeit von HADES sowie mit Vorhersagen des UrQMD-Transportmodells überein. Unter der Annahme der ermittelten oberen Produktionsgrenze lässt sich weiterhin ein maximales Verhältnis von  $\Xi^-$  zu  $\Lambda + \Sigma^0$  Hyperonen von  $N_{\Xi^-}/N_{\Lambda+\Sigma^0} < 5,8 \times 10^{-2}$  bestimmen.

# Appendix A

### **Supplemental Material**

#### **Graphical Identification using Time-of-Flight**

As explained in section 3.6.1.1, charged particles can be separated by plotting the velocity  $\beta$  as a function of the reconstructed momentum p over charge q. In order to determine quantitatively similar selection regions in data and simulation the graphical cuts are calculated for each particle separately for data and simulation as follows:

- Due to the different time resolutions of TOF and RPC the  $\beta p$  distributions are considered separately.
- The momentum is projected in slices of  $\Delta p = 40 MeV/c^2$  on the beta axis as shown in figure A.1.
- Each momentum-differential  $\beta$  distribution of the respective particle is fitted with a Gaussian distributionFrom this fit the two moments of the distribution mean  $\mu$  and standard deviation  $\sigma$  are extracted which is presented in figure A.2.
- The cut is located in  $\pm n \cdot \sigma$  around the mean  $\mu$  with n = [1, 3.5] in steps of  $\Delta n = 0.5$ .
- The same procedure is repeated for the Monte-Carlo simulation.

The graphical selections for pions and protons obtained following this procedure are shown in figure A.3 and A.4 for the TOF and RPC walls separately. However, the assumption of an underlying Gaussian distribution is not fully justified in particular in the region of low momenta p since the distribution has a non-linear relation between  $\beta$  and p. Therefore the projection has a one-sided non-Gaussian tail for small momenta.

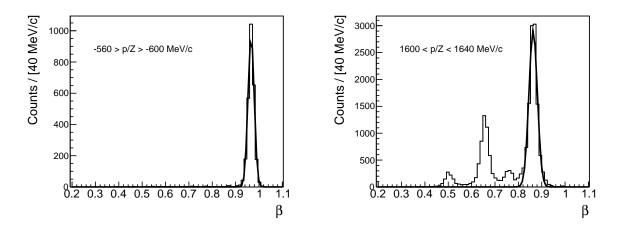


**Figure A.1:** Left:  $\beta$  distribution in a momentum/charge range from -600 to -560 MeV/c in the RPC detector. A peak close to unity is observed which can be attributed to negative pions. The distribution is parametrized by a Gaussian. The extracted width  $\sigma$  is then located around the theoretically calculated curve for negative pions in the  $\beta$ -p plane. Right:  $\beta$  distribution in a momentum/charge range from 1600 to 1640 MeV/c. A peak close to unity is observed which can be attributed to protons. Also visible are the peaks for the slower fragments <sup>3</sup>He, deuterons and tritons.

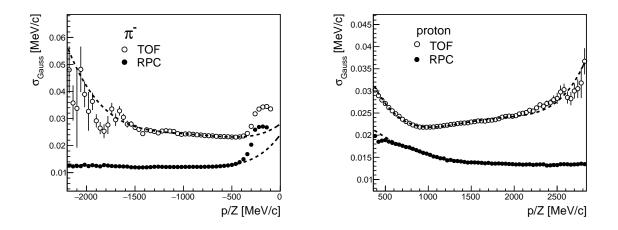


**Figure A.2:** Extracted width of a Gaussian fit to pion (left) and proton (right) signals in the  $\beta$  distribution as a function of momentum over charge in TOF (open circles) and RPC (filled circles). The widths are then located around the theoretically expected curves for the corresponding charged particles in the  $\beta$ -p plane. Due to the non-linear relation between  $\beta$  and p particularly at low momenta, the projection gives an asymmetric distribution with longer tails towards smaller  $\beta$  which is not well described by a Gaussian anymore. This leads to an increase of the width in this region especially for pions. Therefore, the distribution is fitted with a fourth-order polynomial and the values of this parametrization are taken in this region.

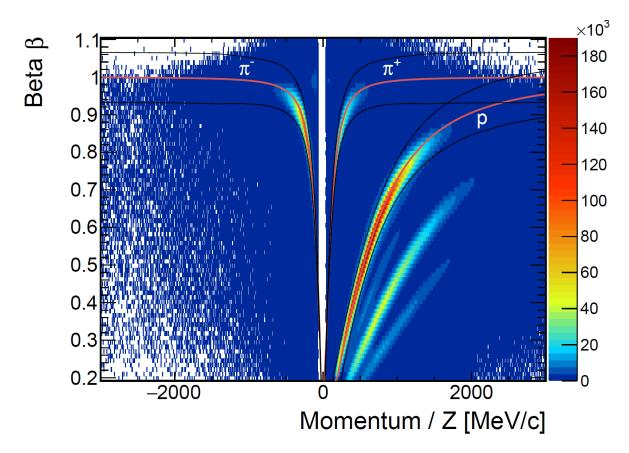


**Figure A.3:** Velocity  $\beta$  as a function of momentum p over charge q for charged particles in the TOF wall. The red lines indicate the theoretically calculated curves for each particle species. The black boxes enclose the final selection region for the corresponding charged particles as determined by the procedure described in the text.

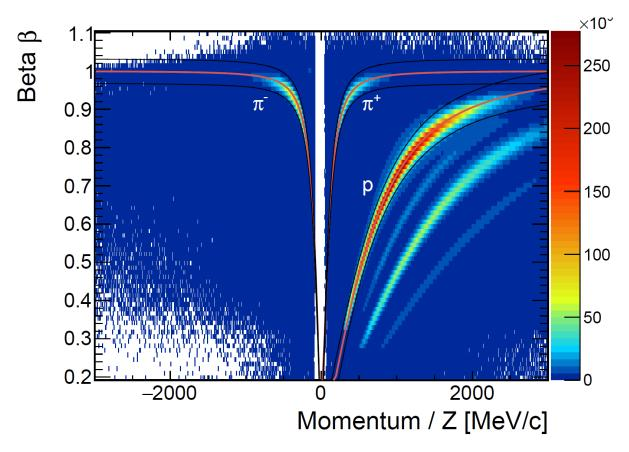


**Figure A.4:** Velocity  $\beta$  as a function of momentum p over charge q for charged particles in the RPC wall. The red lines indicate the theoretically calculated curves for each particle species. The black boxes enclose the final selection region for the corresponding charged particles as determined by the procedure described in the text.

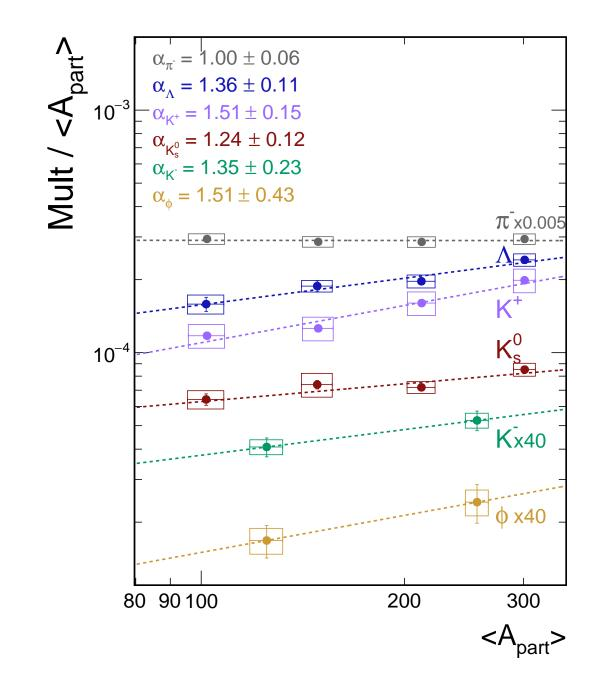


**Figure A.5:** Multiplicity normalized to  $\langle A_{\text{part}} \rangle$  as a function of  $\langle A_{\text{part}} \rangle$  for negative pions and strange hadrons reconstructed in the Au+Au collision system at  $E_{\text{beam}} = 1.23$ A GeV measured with HADES. Pions, charged kaons and the  $\phi$  meson have been investigated in [37]. Due to a higher production threshold,  $\phi$  and  $K^-$  are less abundant, hence only two instead of four data points could be determined which had to be scaled up in order to compare to  $\Lambda$ ,  $K_s^0$  and  $K^+$ . The points are fitted with a parametrization of the type  $M \propto \langle A_{\text{part}} \rangle^{\alpha}$  in order to quantify the rise of the data with increasing centrality of the collision which is then given by the  $\alpha$  exponent. Whereas the pions show a linear increase ( $\alpha \approx 1$ ), all strange particles rise more than linear with  $\langle A_{\text{part}} \rangle$ , showing within uncertainties a similar rise among each other.

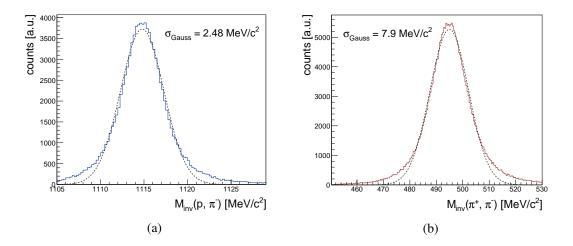


**Figure A.6:** Invariant mass distribution as obtained from Monte-Carlo simulations for  $\Lambda$  (a) and  $K_s^0$  (b). The distributions are parametrized by a Gaussian function in order to extract the measured width  $\sigma_{\text{Gauss}}$  which is dominated by the detector resolution.

# **List of Figures**

1.1	Phase diagram of QCD	3
1.2	Stages of a heavy-ion collision in the SIS18 energy regime	5
1.3	Evolution of a heavy-ion collision in $T$ - $\mu_B$ plane	7
1.4	Phase diagram of QCD mapped with statistical hadronization model	7
1.5	Internal energy per nucleon as a function of compression of nuclear matter	9
1.6	Gravitational mass to radius relation for neutron stars calculated with QMC model	10
1.7	Symmetry energy as a function of relative baryon density	11
1.8	Excitation function of charged pions and strange hadrons in heavy systems	16
1.9	Sketch of three different scenarios for a hadronic system in the cloudy bag model	17
1.10	Time evolution of macroscopic observables T, $\rho_{\rm eff}/\rho_0$ and $\mu_{\pi}$ in Au+Au at 1.23A	
	GeV calculated with UrQMD coarse-graining approach	19
1.11	In-medium kaon energy normalized to nominal kaon mass $E_K/m_K$ as a function	
	of density relative to nuclear ground-state density $\rho/\rho_0$	22
1.12	Feynman diagram of antikaons coupling to hyperon resonance through nucleon-	
	hole excitation	24
1.13	Sketch of balance of forces in the MIT bag model	25
1.14	Region of validity of transport models as a function of center-of-mass energy	28
1.15	In-medium spectral functions for kaons and antikaons from coupled channel cal-	
	culations for different momenta	30
1.16	Results from the KaoS Collaboration on negative to positive kaon yield ratio as	
	a function of $A_{\text{part}}$ and their inverse slope parameter for different systems $\ldots$ .	36
1.17	Comparison of experimental yields from Ar+KCl at 1.76A GeV to THERMUS	
	calculations	38
2.1	Exploded view of the HADES setup	41
2.2	Schematic cross-section of HADES showing the detector components	43
2.3	Schematic view of the magnetic spectrometer	44
2.4	Schematic description of the six layers of one MDC sector	44
2.5	Schematic view of a charged particle traversing an MDC cell	45
2.6	Technical drawing of the ironless, superconducting toroidal electromagnet ILSE .	47
2.7	Schematic design of scintillator array of the time-of-flight wall TOF	47
2.8	Technical drawing of one sector of resistive plate chambers RPC	48
2.9	Multi-strip diamond start detector	49

#### LIST OF FIGURES

2.10	Scheme of the start and veto system	50
2.11	Front view of the 15-fold segmented gold target	50
	Front layout of forward hodoscope	51
	Schematic cross section of the RICH detector	52
2.14	Recorded data volume for different HADES beam times	53
3.1	Mean count rate of identified negative pions per event and per sector as a function	
	of beam time for calendar day 109	58
3.2	Reconstructed reaction vertices in the x-z plane	59
3.3	Relative loss for number of events after requiring event cleaning criteria	60
3.4	Sketch of two colliding nuclei and impact parameter distribution	62
3.5	Flow chart of the track and momentum reconstruction	64
3.6	Schematic view of the segment finding process in the four MDC planes and ex-	
	ample of clusters found in projection plane	66
3.7	Scheme of improving projection resolution when using the measured drift time	
	information	67
3.8	Schematic view of secondary vertex finding routine	69
3.9	Effect of secondary vertex track finder algorithm on track reconstruction effi-	
	ciency of charged pions from $K_s^0$ decays in simulation as a function of momentum	70
3.10	Effect of secondary vertex track finder algorithm on track reconstruction effi-	
	ciency of negative pions and protons from $\Lambda$ decays in simulation as a function	
	of momentum	70
	Distance $dx$ of extrapolated Runge-Kutta tracks to hits in META detectors	72
3.12	Scheme of reconstructed tracks extrapolated to META detector to visualize META	
	matching quality	73
3.13	Sectional drawing of the magnetic spectrometer and the deflection of a particle	
	experienced by the magnetic field	74
	Schematic view of particle tracks reconstructed with three different methods	76
3.15	Velocity $\beta$ as a function of momentum $p$ over charge $q$ for charged particles in	
	RPC and TOF	78
	Mass spectrum of charged particles normalized to the charge $q$	78
3.17	Mean energy loss in the mini-drift chambers for charged particles as a function	
	of momentum normalized to charge	79
	Stopping power for positive muons in copper as a function of $\beta \gamma = p/Mc$	80
	Flow chart of analysis scheme from data taking to corrected particle spectra	83
3.20	Time over threshold in inner MDCs before applying time cut	85
3.21	Number of reconstructed segments in MDCI in data and simulation with and	
	without MDC time cuts	86
	Technical drawing of $\delta$ -electron shield $\ldots \ldots \ldots$	87
3.23	Time over threshold as a function of drift time in MDCI before and after event	
	cleaning procedure	88
3.24	MDCI hit distribution in six sectors	88

#### LIST OF FIGURES

3.25	Wire efficiency as a function of cell number for one layer compared between data and simulation	. 89
4.1	Hit multiplicity distributions in TOF and RPC in data and simulation for $0-40\%$	
	most central collisions	. 93
4.2	Number of inner and outer track segments per event for data and simulation	. 94
4.3	Sketch of four combinations of ambiguously assigning the three track compo-	
	nents inner/outer segment and META hit	. 94
4.4	Probability density distributions of shared segments and META hits for track candidates compared for data and simulation	. 95
4.5	Probability density distributions of shared segments and META hits for selected	
	track candidates compared for data and simulation	. 97
4.6	Mass distribution of selected and rejected track candidates	
4.7	Ratio of simulation to data in $x$ - $y$ coordinates of the intersection point of a re-	
	constructed inner track segment with two layers of each drift chamber plane	. 98
4.8	Runge-Kutta $\chi^2$ distribution for charged particles in data and simulation	
4.9	Track candidate distribution in data and simulation before and after track selec-	• • • •
		. 100
4.10	Mass over charge distribution from $-400$ to 0 MeV/c <sup>2</sup> and 0 to 500 MeV/c <sup>2</sup> for	. 100
	charged particles in data and simulation	. 103
4.11	Mass over charge spectra from 500 to 1400 MeV/ $c^2$ in data and simulation	
	Invariant mass spectra of $p-\pi^-$ and $\pi^+-\pi^-$ pairs w/o applying topology cuts	
	Two-dimensional sketch of the $\Lambda$ hyperon decay topology	
	$d_v$ distribution with and without topology cuts applied for $p-\pi^-$ pairs	
	Opening angle and $\theta$ distribution between decay products of $\Lambda$ and $K_s^0$ generated	
		. 108
	Sketch of decay vertex resolution dependence on opening angle and momentum	. 109
4.17	Topology parameter distributions for all $p$ - $\pi^-$ pairs in data and for $\Lambda$ hyperons	
	generated in Pluto	. 112
4.18	Topology parameter distributions for all $\pi^+$ - $\pi^-$ pairs in data and for $K_s^0$ mesons	
	generated in Pluto	
	Invariant mass spectra of $p$ - $\pi^-$ and $\pi^+$ - $\pi^-$ pairs with topology cuts applied	
	Invariant mass distribution of $p$ - $\pi^-$ pairs after applying DCA selections	. 115
4.21	Invariant mass spectra for $\Lambda$ hyperons and $K_s^0$ mesons after applying final topol-	
	ogy cuts	. 116
4.22	Invariant mass spectra of $p$ - $\pi^-$ and $\pi^+$ - $\pi^-$ pairs and mixed-event spectra normal-	
	ized in two different regions	. 118
4.23	Topology parameter distributions for all $p$ - $\pi^-$ pairs compared between data and	
	simulation	. 120
4.24	Track quality parameter distributions for all $p$ - $\pi^-$ pairs compared between data	
	and simulation	. 121
4.25	Topology parameter distributions for all $\pi^+$ - $\pi^-$ pairs compared between data and	
	simulation	. 122

4.26	Track quality parameter distributions for all $\pi^+$ - $\pi^-$ pairs compared between data and simulation	123
	Relative loss of signal counts in experimental and simulated data for $\Lambda$ hyperon as a function of varying selection values for topology parameters $\ldots$ $\ldots$ $\ldots$	124
4.28	Relative loss of signal counts in experimental and simulated data for $K_s^0$ meson as a function of varying selection values for topology parameters	125
4.29	Invariant mass distributions for $p-\pi^-$ pairs at mid-rapidity as a function of reduced transverse mass	127
4.30	Invariant mass distributions for $\pi^+$ - $\pi^-$ pairs at mid-rapidity as a function of reduced transverse mass	128
4.31	Raw signal counts as a function of reduced transverse mass and rapidity for $\Lambda$ hyperons and $K_s^0$ mesons	129
4.32	Signal-to-background ratio as a function of reduced transverse mass and rapidity for $\Lambda$ hyperons and $K_s^0$ mesons	131
4.33	Signal-to-background ratio as a function of reduced transverse mass, rapidity and centrality for $\Lambda$ hyperons	
4.34	Signal-to-background ratio as a function of reduced transverse mass, rapidity and centrality for $K_s^0$ mesons	
4.35	Fraction of accepted tracks as a function of reduced transverse mass and rapidity estimated in GEANT	
4.36	Detector and reconstruction efficiency as a function of reduced transverse mass and rapidity for accepted $\Lambda$ and $K_s^0$	
4.37	Decay time distributions for $\Lambda$ hyperons	
	Decay time distributions for $K_s^0$ mesons $\ldots \ldots \ldots \ldots \ldots \ldots \ldots \ldots \ldots$	
	Two-dimensional sketch of the $\Xi^-$ hyperon decay topology	
4.41	Topology parameter distributions for all $\Lambda$ - $\pi^-$ pairs in data and for $\Xi^-$ hyperons	
	generated in Pluto	143
5.1	Transverse mass spectra corrected for acceptance and efficiency as a function of rapidity for $\Lambda$ hyperons for the 40% most central data	149
5.2	Rapidity density and inverse slope parameter distribution for $\Lambda$ hyperons as a function of center-of-mass rapidity normalized to the number of events for 40%	
	most central data	151
5.3	Rapidity density distribution for $\Lambda$ hyperons using different PID methods of charged daughter particles	152
5.4	Rapidity density distribution for $\Lambda$ hyperons for different selection of topology cuts and background normalization	153
5.5	Rapidity density distribution for $\Lambda$ hyperons for $40\%$ most central data and as obtained from three transport models used for extrapolation	155

#### LIST OF FIGURES

5.6	Rapidity density distributions of $\Lambda$ hyperons as a function of four different centrality classes from most central $0 - 10\%$ to semi-peripheral $30 - 40\%$ collisions
	normalized to the number of events per class
5.7	$Mult/\langle A_{part}\rangle$ , $T_{eff}$ and $\sigma_{Gauss}$ as a function of $\langle A_{part}\rangle$ for $\Lambda$ hyperons
5.8	Transverse mass spectra corrected for acceptance and efficiency as a function of
	rapidity for $K_s^0$ mesons for the 40% most central data
5.9	Rapidity density and inverse slope parameter distribution for $K_s^0$ mesons as a
	function of center-of-mass rapidity normalized to the number of events for $40\%$
	most central data
5.10	Rapidity density distribution for $K_s^0$ mesons using different PID methods of
	charged daughter particles
5.11	Rapidity density distribution for $K_s^0$ mesons for different selections of topology
0.111	cuts and background normalization
5.12	Rapidity density distribution for $K_s^0$ mesons for 40% most central data and as
5.12	obtained from three transport models used for extrapolation $\ldots$ $\ldots$ $\ldots$ $\ldots$ 165
5 13	Rapidity density distributions of $K_s^0$ mesons as a function of four different cen-
5.15	trality classes from most central $0 - 10\%$ to semi-peripheral $30 - 40\%$ collisions
	normalized to the number of events per class
5 14	$Mult/\langle A_{part}\rangle$ , $T_{eff}$ and $\sigma_{Gauss}$ as a function of $\langle A_{part}\rangle$ for $K_s^0$ mesons
	Invariant mass distribution of $\Lambda$ - $\pi$ <sup>-</sup> pairs
	Invariant mass distribution of $\Lambda^+\pi^-$ pairs 200 med into expected $\Xi^-$ mass region . 170
5.10	$\frac{1}{10000000000000000000000000000000000$
6.1	Multiplicity normalized to $\langle A_{part} \rangle$ as a function of $\langle A_{part} \rangle$ for negative pions and
6.1	
6.1 6.2	Multiplicity normalized to $\langle A_{\text{part}} \rangle$ as a function of $\langle A_{\text{part}} \rangle$ for negative pions and strange hadrons simultaneously fitted with a parametrization of type $M \propto \langle A_{\text{part}} \rangle^{\alpha} 175$ Effective temperature $T_{\text{eff}}$ as a function of $\langle A_{\text{part}} \rangle$ for $\Lambda$ hyperons and $K_s^0$ mesons 177
	strange hadrons simultaneously fitted with a parametrization of type $M\propto \langle A_{\rm part} angle^{lpha}$ 175
6.2	strange hadrons simultaneously fitted with a parametrization of type $M \propto \langle A_{\text{part}} \rangle^{\alpha} 175$ Effective temperature $T_{\text{eff}}$ as a function of $\langle A_{\text{part}} \rangle$ for $\Lambda$ hyperons and $K_s^0$ mesons 177
6.2	strange hadrons simultaneously fitted with a parametrization of type $M \propto \langle A_{\text{part}} \rangle^{\alpha} 175$ Effective temperature $T_{\text{eff}}$ as a function of $\langle A_{\text{part}} \rangle$ for $\Lambda$ hyperons and $K_s^0$ mesons 177 Thermal and experimental width of rapidity density distribution of $\Lambda$ and $K_s^0$ as
6.2 6.3	strange hadrons simultaneously fitted with a parametrization of type $M \propto \langle A_{\text{part}} \rangle^{\alpha} 175$ Effective temperature $T_{\text{eff}}$ as a function of $\langle A_{\text{part}} \rangle$ for $\Lambda$ hyperons and $K_s^0$ mesons 177 Thermal and experimental width of rapidity density distribution of $\Lambda$ and $K_s^0$ as a function of $\langle A_{\text{part}} \rangle$
6.2 6.3	strange hadrons simultaneously fitted with a parametrization of type $M \propto \langle A_{\text{part}} \rangle^{\alpha} 175$ Effective temperature $T_{\text{eff}}$ as a function of $\langle A_{\text{part}} \rangle$ for $\Lambda$ hyperons and $K_s^0$ mesons 177 Thermal and experimental width of rapidity density distribution of $\Lambda$ and $K_s^0$ as a function of $\langle A_{\text{part}} \rangle$
6.2 6.3 6.4	strange hadrons simultaneously fitted with a parametrization of type $M \propto \langle A_{\text{part}} \rangle^{\alpha} 175$ Effective temperature $T_{\text{eff}}$ as a function of $\langle A_{\text{part}} \rangle$ for $\Lambda$ hyperons and $K_s^0$ mesons 177 Thermal and experimental width of rapidity density distribution of $\Lambda$ and $K_s^0$ as a function of $\langle A_{\text{part}} \rangle$
6.2 6.3 6.4	strange hadrons simultaneously fitted with a parametrization of type $M \propto \langle A_{\text{part}} \rangle^{\alpha} 175$ Effective temperature $T_{\text{eff}}$ as a function of $\langle A_{\text{part}} \rangle$ for $\Lambda$ hyperons and $K_s^0$ mesons 177 Thermal and experimental width of rapidity density distribution of $\Lambda$ and $K_s^0$ as a function of $\langle A_{\text{part}} \rangle$
<ul><li>6.2</li><li>6.3</li><li>6.4</li><li>6.5</li></ul>	strange hadrons simultaneously fitted with a parametrization of type $M \propto \langle A_{\text{part}} \rangle^{\alpha} 175$ Effective temperature $T_{\text{eff}}$ as a function of $\langle A_{\text{part}} \rangle$ for $\Lambda$ hyperons and $K_s^0$ mesons 177 Thermal and experimental width of rapidity density distribution of $\Lambda$ and $K_s^0$ as a function of $\langle A_{\text{part}} \rangle$
<ul><li>6.2</li><li>6.3</li><li>6.4</li><li>6.5</li></ul>	strange hadrons simultaneously fitted with a parametrization of type $M \propto \langle A_{\text{part}} \rangle^{\alpha} 175$ Effective temperature $T_{\text{eff}}$ as a function of $\langle A_{\text{part}} \rangle$ for $\Lambda$ hyperons and $K_s^0$ mesons 177 Thermal and experimental width of rapidity density distribution of $\Lambda$ and $K_s^0$ as a function of $\langle A_{\text{part}} \rangle$
<ul> <li>6.2</li> <li>6.3</li> <li>6.4</li> <li>6.5</li> <li>6.6</li> </ul>	strange hadrons simultaneously fitted with a parametrization of type $M \propto \langle A_{\text{part}} \rangle^{\alpha} 175$ Effective temperature $T_{\text{eff}}$ as a function of $\langle A_{\text{part}} \rangle$ for $\Lambda$ hyperons and $K_s^0$ mesons 177 Thermal and experimental width of rapidity density distribution of $\Lambda$ and $K_s^0$ as a function of $\langle A_{\text{part}} \rangle$
<ul> <li>6.2</li> <li>6.3</li> <li>6.4</li> <li>6.5</li> <li>6.6</li> </ul>	strange hadrons simultaneously fitted with a parametrization of type $M \propto \langle A_{\text{part}} \rangle^{\alpha} 175$ Effective temperature $T_{\text{eff}}$ as a function of $\langle A_{\text{part}} \rangle$ for $\Lambda$ hyperons and $K_s^0$ mesons 177 Thermal and experimental width of rapidity density distribution of $\Lambda$ and $K_s^0$ as a function of $\langle A_{\text{part}} \rangle$
<ul> <li>6.2</li> <li>6.3</li> <li>6.4</li> <li>6.5</li> <li>6.6</li> <li>6.7</li> </ul>	strange hadrons simultaneously fitted with a parametrization of type $M \propto \langle A_{\text{part}} \rangle^{\alpha} 175$ Effective temperature $T_{\text{eff}}$ as a function of $\langle A_{\text{part}} \rangle$ for $\Lambda$ hyperons and $K_s^0$ mesons 177 Thermal and experimental width of rapidity density distribution of $\Lambda$ and $K_s^0$ as a function of $\langle A_{\text{part}} \rangle$
<ul> <li>6.2</li> <li>6.3</li> <li>6.4</li> <li>6.5</li> <li>6.6</li> <li>6.7</li> </ul>	strange hadrons simultaneously fitted with a parametrization of type $M \propto \langle A_{\text{part}} \rangle^{\alpha} 175$ Effective temperature $T_{\text{eff}}$ as a function of $\langle A_{\text{part}} \rangle$ for $\Lambda$ hyperons and $K_s^0$ mesons 177 Thermal and experimental width of rapidity density distribution of $\Lambda$ and $K_s^0$ as a function of $\langle A_{\text{part}} \rangle$
<ul> <li>6.2</li> <li>6.3</li> <li>6.4</li> <li>6.5</li> <li>6.6</li> <li>6.7</li> <li>6.8</li> </ul>	strange hadrons simultaneously fitted with a parametrization of type $M \propto \langle A_{\text{part}} \rangle^{\alpha}$ 175 Effective temperature $T_{\text{eff}}$ as a function of $\langle A_{\text{part}} \rangle$ for $\Lambda$ hyperons and $K_s^0$ mesons 177 Thermal and experimental width of rapidity density distribution of $\Lambda$ and $K_s^0$ as a function of $\langle A_{\text{part}} \rangle$
<ul> <li>6.2</li> <li>6.3</li> <li>6.4</li> <li>6.5</li> <li>6.6</li> <li>6.7</li> <li>6.8</li> <li>6.9</li> </ul>	strange hadrons simultaneously fitted with a parametrization of type $M \propto \langle A_{\text{part}} \rangle^{\alpha}$ 175 Effective temperature $T_{\text{eff}}$ as a function of $\langle A_{\text{part}} \rangle$ for $\Lambda$ hyperons and $K_s^0$ mesons 177 Thermal and experimental width of rapidity density distribution of $\Lambda$ and $K_s^0$ as a function of $\langle A_{\text{part}} \rangle$
<ul> <li>6.2</li> <li>6.3</li> <li>6.4</li> <li>6.5</li> <li>6.6</li> <li>6.7</li> <li>6.8</li> <li>6.9</li> </ul>	strange hadrons simultaneously fitted with a parametrization of type $M \propto \langle A_{\text{part}} \rangle^{\alpha}$ 175 Effective temperature $T_{\text{eff}}$ as a function of $\langle A_{\text{part}} \rangle$ for $\Lambda$ hyperons and $K_s^0$ mesons 177 Thermal and experimental width of rapidity density distribution of $\Lambda$ and $K_s^0$ as a function of $\langle A_{\text{part}} \rangle$
<ul> <li>6.2</li> <li>6.3</li> <li>6.4</li> <li>6.5</li> <li>6.6</li> <li>6.7</li> <li>6.8</li> <li>6.9</li> <li>6.10</li> </ul>	strange hadrons simultaneously fitted with a parametrization of type $M \propto \langle A_{\text{part}} \rangle^{\alpha}$ 175 Effective temperature $T_{\text{eff}}$ as a function of $\langle A_{\text{part}} \rangle$ for $\Lambda$ hyperons and $K_s^0$ mesons 177 Thermal and experimental width of rapidity density distribution of $\Lambda$ and $K_s^0$ as a function of $\langle A_{\text{part}} \rangle$

6.12	Fit of the hadron yields at chemical freeze-out in the statistical hadronization
	model to the measured yields for $0 - 20\%$ most central data and comparison of
	the extracted chemical freeze-out point from Au+Au to world data 193
6.13	Effective temperatures $T_{\rm eff}$ for $\Lambda$ , $K_s^0$ , $\pi^-$ , proton, $K^+$ and $\phi$ as a function of
	hadron mass for the $0 - 20\%$ most central events $\ldots \ldots 196$
6.14	Invariant mass distribution of $\Lambda$ - $\pi^-$ pairs including upper limit on $\Xi^-$ production 197
6.15	Yield ratio $\Xi^-/(\Lambda + \Sigma^0)$ as a function of $\sqrt{s_{\rm NN}}$ compared to world data $\ldots$ 198
A.1	Velocity distribution in RPC detector
A.2	Width of pion and proton signals in the velocity distribution as a function of
	momentum over charge in TOF and RPC
A.3	Velocity as a function of momentum over charge for charged particles in TOF 213
A.4	Velocity as a function of momentum over charge for charged particles in RPC 214
A.5	Multiplicity normalized to $\langle A_{part} \rangle$ as a function of $\langle A_{part} \rangle$ for negative pions and
	strange hadrons reconstructed in the Au+Au collision system at $E_{\text{beam}} = 1.23$ A
	GeV
A.6	Line shape of $\Lambda$ and $K_s^0$ simulated with Pluto $\ldots \ldots \ldots$

## **List of Tables**

1.1	Production channels and thresholds of strange particles in NN collisions 14
2.1	Overview of HADES beam times
3.1	Overview of beam time characteristics in Au(1.23A GeV) on Au $\ldots \ldots \ldots 56$
3.2	Summary of the four centrality classes for $0 - 40\%$ most central collisions in steps of $10\%$
4.1	Overview of characteristics of analyzed hadrons $\Lambda$ , $K_s^0$ and $\Xi^-$
4.2	Overview of selections used for identification of charged particles
4.3	Overview of selection values for topology parameters for $\Lambda$ and $K_s^0$
4.4	Overview of differential phase space bins used for $\Lambda$ and $K_s^0$
4.5	Mean lifetimes estimated from decay curves of $\Lambda$ and $K_s^0$
4.6	Overview of variations of selection values for topology parameters applied in the
	analysis of $\Lambda$ and $K_s^0$
4.7	Overview of topology parameter values applied in the analysis of $\Xi$ hyperons 143
4.8	Overview of topology cut variations used in the analysis of $\Xi$ hyperons 146
5.1	Overview of experimental results on $K_s^0$ , $\Lambda$ and $\Xi^-$ production
6.1	Level of agreement between investigated observables in data and as obtained from transport model calculations

### **Bibliography**

- [1] Kenneth G. Wilson. Confinement of quarks. Phys. Rev. D, 10:2445-2459, Oct 1974. 1
- [2] M. Plümer, S. Raha, and R. M. Weiner. How free is the Quark-Gluon-Plasma? Nuclear Physics A, 418:549–557, April 1984. 2, 5
- W. A. Zajc. The Fluid Nature of Quark-Gluon Plasma. *Nuclear Physics A*, 805:283–294c, June 2008. 2
- [4] Henrik Bohr and H.B. Nielsen. Hadron production from a boiling quark soup: A thermodynamical quark model predicting particle ratios in hadronic collisions. *Nuclear Physics B*, 128(2):275–293, 1977. 2, 5
- [5] K. A. Olive et al. Review of Particle Physics. *Chin. Phys.*, C38:090001, 2014. 2, 32, 80, 104, 115, 139, 140, 174
- [6] Private communication T. Galatyuk. 3, 25
- [7] E. Y. Loh, J. E. Gubernatis, R. T. Scalettar, S. R. White, D. J. Scalapino, and R. L. Sugar. Sign problem in the numerical simulation of many-electron systems. *Phys. Rev. B*, 41:9301–9307, May 1990. 2
- [8] Mikhail A. Stephanov. QCD phase diagram and the critical point. *Prog. Theor. Phys. Suppl.*, 153:139–156, 2004. [Int. J. Mod. Phys.A20,4387(2005)]. 2
- [9] A. Barducci, R. Casalbuoni, G. Pettini, and L. Ravagli. A NJL-based study of the QCD critical line. *Phys. Rev.*, D72:056002, 2005. 2
- [10] A. Barducci, R. Casalbuoni, S. De Curtis, Raoul Gatto, and Giulio Pettini. Chiral Phase Transitions in QCD for Finite Temperature and Density. *Phys. Rev.*, D41:1610, 1990. 2
- [11] Lokesh Kumar. Review of Recent Results from the RHIC Beam Energy Scan. Mod. Phys. Lett., A28:1330033, 2013. 3, 8
- [12] M. M. Aggarwal et al. An Experimental Exploration of the QCD Phase Diagram: The Search for the Critical Point and the Onset of De-confinement. 2010. 3
- [13] Gordon Baym. Neutron stars and quark matter. AIP Conf. Proc., 892:8–14, 2007.
   [,8(2006)]. 3

- [14] Feryal Ozel, Dimitrios Psaltis, Tolga Guver, Gordon Baym, Craig Heinke, and Sebastien Guillot. The Dense Matter Equation of State from Neutron Star Radius and Mass Measurements. Astrophys. J., 820(1):28, 2016. 3
- [15] M. Baldo. The Nuclear Equation of State and Neutron Star Structure. Ser. Adv. Quant. Many Body Theor., 5:119–126, 2001. 3
- [16] Sanjay Reddy. Matter at Extreme Density and its Role in Neutron Stars and Supernova. Ser. Adv. Quant. Many Body Theor., 9:146–155, 2006. 3
- [17] Daniel L. Whittenbury. Hadrons and Quarks in Dense Matter: From Nuclear Matter to Neutron Stars. PhD thesis, Adelaide U., 2015. 3
- [18] A. W. Thomas, D. L. Whittenbury, J. D. Carroll, K. Tsushima, and J. R. Stone. Equation of State of Dense Matter and Consequences for Neutron Stars. *EPJ Web Conf.*, 63:03004, 2013. 3, 10, 40
- [19] B. P. Abbott et al. Observation of Gravitational Waves from a Binary Black Hole Merger. *Phys. Rev. Lett.*, 116(6):061102, 2016. 3
- [20] https://home.cern/. [Online; accessed 14-January-2017]. 4
- [21] K. Aamodt et al. The ALICE experiment at the CERN LHC. JINST, 3:S08002, 2008. 4
- [22] ATLAS Collaboration, G. Aad, E. Abat, J. Abdallah, A. A. Abdelalim, A. Abdesselam, O. Abdinov, B. A. Abi, M. Abolins, H. Abramowicz, and et al. The ATLAS Experiment at the CERN Large Hadron Collider. *Journal of Instrumentation*, 3:S08003, August 2008.
   4
- [23] S. Chatrchyan et al. The CMS experiment at the CERN LHC. JINST, 3:S08004, 2008. 4
- [24] http://lhc.web.cern.ch/lhc/. [Online; accessed 10-July-2016]. 4
- [25] http://www.bnl.gov/rhic/. [Online; accessed 10-July-2016]. 4
- [26] https://www.bnl.gov/world/. [Online; accessed 14-January-2017]. 4
- [27] http://www.star.bnl.gov/. [Online; accessed 14-January-2017]. 4
- [28] http://www.phenix.bnl.gov/. [Online; accessed 14-January-2017]. 4
- [29] N. Herrmann, Johannes P. Wessels, and Thomas Wienold. Collective Flow in Heavy-Ion Collisions. Annual Review of Nuclear and Particle Science, 49(1):581–632, 1999. 4, 6, 176, 195
- [30] Christoph Hartnack. *Dissertation*. PhD thesis, Johann Wolfgang Goethe Universität, 1992.5

- [31] Simon Hands. The phase diagram of QCD. *Contemporary Physics*, 42(4):209–225, 2001. 5
- [32] Sergei A. Voloshin, Arthur M. Poskanzer, and Raimond Snellings. Collective phenomena in non-central nuclear collisions. 2008. 5
- [33] A. Andronic. Elliptic flow and equation of state in heavy ion collisions at SIS energies. *Nuclear Physics A*, 661(1–4):333 336, 1999. 5
- [34] Tetyana Galatyuk, Paul M. Hohler, Ralf Rapp, Florian Seck, and Joachim Stroth. Thermal Dileptons from Coarse-Grained Transport as Fireball Probes at SIS Energies. *Eur. Phys.* J., A52(5):131, 2016. 6, 7, 18, 19, 176
- [35] Stephan Endres, Hendrik van Hees, Janus Weil, and Marcus Bleicher. Coarse-graining approach for dilepton production at energies available at the CERN Super Proton Synchrotron. *Phys. Rev.*, C91(5):054911, 2015. 6
- [36] G. Agakishiev et al. Statistical model analysis of hadron yields in proton-nucleus and heavy-ion collisions at SIS 18 energies. 2015. 7, 37, 38, 194
- [37] Heidi Schuldes. Charged Kaon and φ Reconstruction in Au+Au Collisions at 1.23 AGeV. PhD thesis, Johann Wolfgang Goethe Universität, 2016. 7, 37, 71, 78, 89, 91, 119, 141, 150, 156, 173, 174, 175, 176, 192, 194, 195, 196, 215
- [38] Bernd-Jochen Schaefer, Jan M. Pawlowski, and Jochen Wambach. The Phase Structure of the Polyakov–Quark-Meson Model. *Phys. Rev.*, D76:074023, 2007. 7, 25
- [39] Talk at CPOD 2016 in Wroclaw F. Seck. 7
- [40] A. Andronic, P. Braun-Munzinger, and J. Stachel. Hadron production in central nucleusnucleus collisions at chemical freeze-out. *Nucl. Phys.*, A772:167–199, 2006. 6, 7
- [41] S. Wheaton and J. Cleymans. THERMUS: A Thermal model package for ROOT. Comput.Phys.Commun., 180:84–106, 2009. 7, 194
- [42] J. Cleymans, H. Oeschler, K. Redlich, and S. Wheaton. Comparison of chemical freezeout criteria in heavy-ion collisions. *Phys.Rev.*, C73:034905, 2006. 7, 8
- [43] X. Lopez et al. Subthreshold production of  $\Sigma(1385)$  baryons in Al+Al collisions at 1.9A GeV. *Phys. Rev. C*, 76:052203, Nov 2007. 7
- [44] G. Agakishiev et al. Hyperon production in Ar+KCl collisions at 1.76A GeV. Eur.Phys.J., A47:21, 2011. 7, 37, 38, 40, 194, 195
- [45] J. Cleymans and K. Redlich. Unified Description of Freeze-Out Parameters in Relativistic Heavy Ion Collisions. *Phys. Rev. Lett.*, 81:5284–5286, Dec 1998. 8

- [46] P Braun-Munzinger and J Stachel. Particle ratios, equilibration and the QCD phase boundary. *Journal of Physics G: Nuclear and Particle Physics*, 28(7):1971, 2002. 8
- [47] V. Magas and H. Satz. Conditions for confinement and freeze-out. *The European Physical Journal C Particles and Fields*, 32(1):115–119, 2003. 8
- [48] J. Cleymans, H. Oeschler, K. Redlich, and S. Wheaton. Transition from baryonic to mesonic freeze-out. *Physics Letters B*, 615(1–2):50 – 54, 2005. 8
- [49] Deog Ki Hong, Stephen D. H. Hsu, and Francesco Sannino. Supernovae, hypernovae and color superconductivity. *Phys. Lett.*, B516:362–366, 2001. 8
- [50] Masakiyo Kitazawa, Tomoi Koide, Teiji Kunihiro, and Yukio Nemoto. Chiral and color superconducting phase transitions with vector interaction in a simple model. *Prog. Theor. Phys.*, 108:929–951, 2002. 8
- [51] Bogdan Povh, Klaus Rith, Christoph Scholz, and Frank Zetsche. *Teilchen und Kerne. Eine Einführung in die physikalischen Konzepte*. Springer-Verlag GmbH, sixth edition, 2004. 8, 12
- [52] R. Stock. Particle Production in High-Energy Nucleus Nucleus Collisions. Phys. Rept., 135:259–315, 1986. 9
- [53] A. Förster, F. Uhlig, I. Bottcher, D. Brill, M. Debowski, et al. Production of K+ and of K- Mesons in Heavy-Ion Collisions from 0.6 to 2.0-A-GeV Incident Energy. *Phys.Rev.*, C75:024906, 2007. 9, 23, 35, 36, 40, 189
- [54] Ch. Hartnack, H. Oeschler, and Jorg Aichelin. Hadronic matter is soft. *Phys.Rev.Lett.*, 96:012302, 2006. 9, 40
- [55] Zhigang Xiao, Bao-An Li, Lie-Wen Chen, Gao-Chan Yong, and Ming Zhang. Circumstantial Evidence for a Soft Nuclear Symmetry Energy at Suprasaturation Densities. *Phys. Rev. Lett.*, 102:062502, Feb 2009. 9
- [56] J. Aichelin and Che Ming Ko. Subthreshold Kaon Production as a Probe of the Nuclear Equation of State. *Phys. Rev. Lett.*, 55:2661–2663, Dec 1985. 9
- [57] Christian Fuchs. Kaon Production in heavy ion reactions at intermediate energies. *Prog.Part.Nucl.Phys.*, 56:1–103, 2006. 9, 12, 20, 21, 22, 23, 29, 30, 40, 179, 186
- [58] G. Stoicea et al. Azimuthal Dependence of Collective Expansion for Symmetric Heavy-Ion Collisions. *Phys. Rev. Lett.*, 92:072303, Feb 2004. 9
- [59] A. Andronic et al. Directed flow in Au+Au, Xe+CsI, and Ni+Ni collisions and the nuclear equation of state. *Phys. Rev. C*, 67:034907, Mar 2003. 9
- [60] A. Andronic et al. Excitation function of elliptic flow in Au + Au collisions and the nuclear matter equation of state. *Physics Letters B*, 612(3–4):173 – 180, 2005. 9

- [61] J. R. Oppenheimer and G. M. Volkoff. On Massive neutron cores. *Phys. Rev.*, 55:374–381, 1939. 9
- [62] Paul Demorest, Tim Pennucci, Scott Ransom, Mallory Roberts, and Jason Hessels. Shapiro Delay Measurement of A Two Solar Mass Neutron Star. *Nature*, 467:1081–1083, 2010. 9, 10, 35, 40
- [63] John Antoniadis et al. A Massive Pulsar in a Compact Relativistic Binary. *Science*, 340:6131, 2013. 9, 10, 35, 40
- [64] C. Fuchs, Amand Faessler, E. Zabrodin, and Yu-Ming Zheng. Probing the nuclear equation of state by K+ production in heavy ion collisions. *Phys.Rev.Lett.*, 86:1974–1977, 2001. 9, 40
- [65] H.A. Bethe and M.B. Johnson. Dense baryon matter calculations with realistic potentials. *Nuclear Physics A*, 230(1):1 58, 1974. 9, 40
- [66] V.R. Pandharipande. Hyperonic matter. *Nuclear Physics A*, 178(1):123 144, 1971. 9, 40
- [67] N. K. Glendenning and S. A. Moszkowski. Reconciliation of neutron-star masses and binding of the Λ in hypernuclei. *Phys. Rev. Lett.*, 67:2414–2417, Oct 1991. 9, 40
- [68] Shmuel Balberg and Avraham Gal. An Effective equation of state for dense matter with strangeness. *Nucl. Phys.*, A625:435–472, 1997. 9, 40
- [69] Pierre A. M. Guichon, Anthony W. Thomas, and Kazuo Tsushima. Binding of hypernuclei in the latest quark-meson coupling model. *Nucl. Phys.*, A814:66–73, 2008. 10
- [70] C. Fuchs and H. H. Wolter. Modelization of the EOS. *Eur. Phys. J.*, A30:5–21, 2006. 10, 11
- [71] W. Reisdorf et al. Nuclear Stopping from 0.09A to 1.93A GeV and Its Correlation to Flow. *Phys. Rev. Lett.*, 92:232301, Jun 2004. 10
- [72] F. Rami et al. Isospin Tracing: A Probe of Nonequilibrium in Central Heavy-Ion Collisions. *Phys. Rev. Lett.*, 84:1120–1123, Feb 2000. 10
- [73] Lie-Wen Chen. Nuclear matter symmetry energy and the symmetry energy coefficient in the mass formula. *Phys. Rev. C*, 83:044308, Apr 2011. 11
- [74] X. Lopez et al. Isospin dependence of relative yields of K<sup>+</sup> and K<sup>0</sup> mesons at 1.528A GeV. *Phys. Rev. C*, 75:011901, Jan 2007. 11
- [75] C. Sfienti et al. Isotopic Dependence of the Nuclear Caloric Curve. *Phys. Rev. Lett.*, 102:152701, Apr 2009. 12

- [76] G. Ferini, T. Gaitanos, M. Colonna, M. Di Toro, and H.H. Wolter. Isospin effects on sub-threshold kaon production at intermediate energies. *Phys.Rev.Lett.*, 97:202301, 2006. 12
- [77] T. Gaitanos, M. Colonna, M. Di Toro, and H.H. Wolter. Stopping and isospin equilibration in heavy ion collisions. *Physics Letters B*, 595(1–4):209 215, 2004. 12
- [78] Bao-An Li, Gao-Chan Yong, and Wei Zuo. Near-threshold pion production with radioactive beams. *Phys. Rev. C*, 71:014608, Jan 2005. 12
- [79] Che Ming Ko. Effect of final state interactions on subthreshold K- production in heavy-ion collisions. *Physics Letters B*, 138(5):361 – 364, 1984. 15
- [80] Ch. Hartnack, H. Oeschler, and J. Aichelin. Erratum: What Determines the K<sup>-</sup> Multiplicity at Energies around (1-2)A GeV? [Phys. Rev. Lett. 90, 102302 (2003)]. *Phys. Rev. Lett.*, 93:149903, Sep 2004. 15, 35
- [81] E. L. Bratkovskaya, W. Cassing, and U. Mosel. Analysis of kaon production at SIS energies. *Nucl. Phys.*, A622:593–604, 1997. 15
- [82] D.B. Kaplan and A.E. Nelson. Strange Goings on in Dense Nucleonic Matter. *Phys.Lett.*, B175:57–63, 1986. 15, 21
- [83] Matthias F. M. Lutz, A. Steiner, and W. Weise. Kaons in baryonic matter. Nucl. Phys., A574:755–787, 1994. 15, 22, 40
- [84] Ann E. Nelson and David B. Kaplan. Strange Condensate Realignment in Relativistic Heavy Ion Collisions. *Phys.Lett.*, B192:193, 1987. 15, 21
- [85] C. Blume and C. Markert. Strange hadron production in heavy ion collisions from SPS to RHIC. *Prog. Part. Nucl. Phys.*, 66:834–879, 2011. 16, 179
- [86] I. G. Bearden et al. Charged Meson Rapidity Distributions in Central Au + Au Collisions at  $\sqrt{s_{NN}} = 200$  GeV. *Phys. Rev. Lett.*, 94:162301, Apr 2005. 16
- [87] P. Chung et al. Near-Threshold Production of the Multistrange  $\Xi^-$  Hyperon. *Phys. Rev. Lett.*, 91:202301, Nov 2003. 16
- [88] B. B. Back et al. Production of  $\phi$  mesons in Au + Au collisions at 11.7*A* GeV. *Phys. Rev. C*, 69:054901, May 2004. 16
- [89] L. Ahle et al. Kaon production in Au+Au collisions at 11.6AGeV/c. Phys. Rev. C, 58:3523–3538, Dec 1998. 16
- [90] L. Ahle et al. An Excitation function of K- and K+ production in Au + Au reactions at the AGS. *Phys.Lett.*, B490:53–60, 2000. 16

- [91] L. Ahle et al. Particle production at high baryon density in central Au+Au reactions at 11.6A GeV/c. Phys. Rev. C, 57:R466–R470, Feb 1998. 16
- [92] J. L. Klay et al. Charged pion production in 2A to 8A GeV central Au + Au Collisions. Phys. Rev. C, 68:054905, Nov 2003. 16
- [93] C. Alt et al.  $\Omega^-$  and  $\overline{\Omega}^+$  Production in Central Pb + Pb collisions at 40 and 158A GeV. *Phys. Rev. Lett.*, 94:192301, May 2005. 16
- [94] C. Alt et al. Energy dependence of  $\phi$  meson production in central Pb + Pb collisions at  $\sqrt{s_{NN}} = 6$  to 17 GeV. *Phys. Rev. C*, 78:044907, Oct 2008. 16
- [95] C. Alt et al. Energy dependence of Λ and Ξ production in central Pb + Pb collisions at 20A,30A,40A,80A, and 158A GeV measured at the CERN Super Proton Synchrotron. *Phys. Rev. C*, 78:034918, Sep 2008. 16
- [96] S. V. Afanasiev et al. Energy dependence of pion and kaon production in central Pb+Pb collisions. *Phys. Rev. C*, 66:054902, Nov 2002. 16
- [97] C. Alt et al. Pion and kaon production in central Pb + Pb collisions at 20-A and 30-A-GeV: Evidence for the onset of deconfinement. *Phys.Rev.*, C77:024903, 2008. 16
- [98] S. Theberge, Anthony William Thomas, and Gerald A. Miller. The Cloudy Bag Model. 1. The (3,3) Resonance. *Phys. Rev.*, D22:2838, 1980. [Erratum: Phys. Rev.D23,2106(1981)]. 16, 26
- [99] Anthony William Thomas, S. Theberge, and Gerald A. Miller. The Cloudy Bag Model of the Nucleon. *Phys. Rev.*, D24:216, 1981. 16, 25, 26
- [100] Gerald A. Miller, Anthony William Thomas, and S. Theberge. Pion Nucleon Scattering in the Cloudy Bag Model. *Phys. Lett.*, B91:192–195, 1980. 16, 26
- [101] Kolymbari/Crete J. Stroth at ICNFP 2015. 17
- [102] Jorgen Randrup and Jean Cleymans. Maximum freeze-out baryon density in nuclear collisions. *Phys. Rev.*, C74:047901, 2006. 17
- [103] A. M. Gasparyan, J. Haidenbauer, and C. Hanhart. Scattering lengths of strangeness S=-2 baryon-baryon interactions. *Phys. Rev.*, C85:015204, 2012. 18, 38
- [104] E. L. Kryshen. QCD sum rules for the baryon octet in nuclear matter. *Phys. Rev. C*, 84:055205, Nov 2011. 18, 38
- [105] A. Valcarce, H. Garcilazo, and T.F. Caramés. Strangeness-2 two-baryon systems. *Physics Letters B*, 693(3):305 309, 2010. 18, 38
- [106] E. E. Kolomeitsev, B. Tomasik, and D. N. Voskresensky. Strangeness Balance in HADES Experiments and the  $\Xi^-$  Enhancement. *Phys. Rev.*, C86:054909, 2012. 18

- [107] B. Tomásik and E.E. Kolomeitsev. Acta Phys. Pol., B, proc. suppl., 5:201, 2012. 18
- [108] Feng Li, Lie-Wen Chen, Che Ming Ko, and Su Houng Lee. Contributions of hyperonhyperon scattering to subthreshold cascade production in heavy ion collisions. *Phys. Rev. C*, 85:064902, Jun 2012. 18, 31, 38, 197
- [109] C.H. Li and C.M. Ko. Cascade production from antikaon induced reactions on lambda and sigma. *Nuclear Physics A*, 712(1):110 130, 2002. 18, 31
- [110] G. Agakishiev et al. Subthreshold  $\Xi^-$  Production in Collisions of p(3.5 GeV)+Nb. *Phys. Rev. Lett.*, 114(21):212301, 2015. 18, 37, 39, 198
- [111] R. Subedi et al. Probing Cold Dense Nuclear Matter. Science, 320(5882):1476–1478, 2008. 18
- [112] O. Hen et al. Momentum sharing in imbalanced Fermi systems. *Science*, 346(6209):614–617, 2014.
- [113] P. Braun-Munzinger, J. Cleymans, H. Oeschler, and K. Redlich. Maximum relative strangeness content in heavy ion collisions around 30-GeV/A. *Nucl. Phys.*, A697:902– 912, 2002. 18
- [114] V. Metag. Near threshold particle production: A Probe for resonance matter formation in relativistic heavy ion collisions. *Prog. Part. Nucl. Phys.*, 30:75–88, 1993. 18
- [115] P. Senger and H. Strobele. Hadronic particle production in nucleus-nucleus collisions. J. Phys., G25:R59–R131, 1999. 18
- [116] Ralf Rapp. Dilepton Spectroscopy of QCD Matter at Collider Energies. Adv. High Energy Phys., 2013:148253, 2013. 18
- [117] Volker Koch. Introduction to chiral symmetry. 1995. 20
- [118] Steven Weinberg. Nonlinear realizations of chiral symmetry. *Phys.Rev.*, 166:1568–1577, 1968. 21
- [119] Steven Weinberg. Effective chiral Lagrangians for nucleon pion interactions and nuclear forces. Nucl. Phys., B363:3–18, 1991. 21
- [120] M.F.M. Lutz and E.E. Kolomeitsev. Relativistic chiral SU(3) symmetry, large-Nc sum rules and meson–baryon scattering. *Nuclear Physics A*, 700(1):193 308, 2002. 21, 23
- [121] Guangjun Mao, P. Papazoglou, S. Hofmann, S. Schramm, H. Stöcker, and W. Greiner. Kaon effective mass and energy from a novel chiral SU(3)-symmetric Lagrangian. *Phys. Rev. C*, 59:3381–3385, Jun 1999. 21
- [122] Matthias Lutz. Nuclear kaon dynamics. *Physics Letters B*, 426(1–2):12 20, 1998. 21

- [123] T. Wass, M. Rho, and W. Weise. Effective kaon mass in dense baryonic matter: role of correlations. *Nuclear Physics A*, 617(4):449 – 463, 1997. 21, 24
- [124] T. Waas, N. Kaiser, and W. Weise. Effective kaon masses in dense nuclear and neutron matter. *Physics Letters B*, 379(1):34 – 38, 1996. 21
- [125] Norbert Kaiser, P. B. Siegel, and W. Weise. Chiral dynamics and the low-energy kaon nucleon interaction. *Nucl. Phys.*, A594:325–345, 1995. 21, 23
- [126] G.E. Brown and Mannque Rho. Chiral restoration in hot and/or dense matter. *Physics Reports*, 269(6):333 380, 1996. 21, 22
- [127] G.E. Brown, Kuniharu Kubodera, Mannque Rho, and Vesteinn Thorsson. A novel mechanism for kaon condensation in neutron star matter. *Physics Letters B*, 291(4):355 – 362, 1992. 21
- [128] G. E. Brown, Chang-Hwan Lee, Mannque Rho, and Vesteinn Thorsson. From kaon nuclear interactions to kaon condensation. *Nucl. Phys.*, A567:937–956, 1994. 21
- [129] S. J. Dong, J. F. Lagaë, and K. F. Liu.  $\pi N\sigma$  term,  $\overline{ss}$  in the nucleon, and the scalar form factor: A lattice study. *Phys. Rev. D*, 54:5496–5500, Nov 1996. 22
- [130] Bugra Borasoy, Randy Lewis, and Pierre-Philippe A. Ouimet. Baryon magnetic moments and sigma terms in lattice regularized chiral perturbation theory. *Phys. Rev.*, D65:114023, 2002. 22
- [131] T. Inoue, V. E. Lyubovitskij, Th. Gutsche, and Amand Faessler. Updated analysis of meson-nucleon  $\sigma$  terms in the perturbative chiral quark model. *Phys. Rev. C*, 69:035207, Mar 2004. 22
- [132] B. Borasoy. Sigma terms in heavy baryon chiral perturbation theory revisited. *Eur. Phys.* J., C8:121–130, 1999. 22
- [133] G.E Brown and Mannque Rho. From chiral mean field to Walecka mean field and kaon condensation. *Nuclear Physics A*, 596(3–4):503 – 514, 1996. 22
- [134] C.J. Batty, E. Friedman, and A. Gal. Strong interaction physics from hadronic atoms. *Physics Reports*, 287(5):385 – 445, 1997. 22, 40
- [135] K. Tsushima, K Saito, A.W Thomas, and S.V Wright. In-medium kaon and antikaon properties in the quark-meson coupling model. *Physics Letters B*, 429(3–4):239 – 246, 1998. 22
- [136] Christoph Hartnack, Helmut Oeschler, Yvonne Leifels, Elena L. Bratkovskaya, and Jörg Aichelin. Strangeness production close to the threshold in proton–nucleus and heavy-ion collisions. *Physics Reports*, 510(4–5):119 – 200, 2012. 23, 31, 32, 38, 40, 174, 176, 189, 192

- [137] G. Agakishiev et al. In-medium effects on K<sup>0</sup> mesons in relativistic heavy-ion collisions. *Phys. Rev. C*, 82:044907, Oct 2010. 23, 37, 40, 186, 189
- [138] M. L. Benabderrahmane et al. Measurement of the In-Medium  $K^0$  Inclusive Cross Section in  $\pi^-$ -Induced Reactions at 1.15 GeV/c. *Phys. Rev. Lett.*, 102:182501, May 2009. 23, 36, 40
- [139] G. Agakishiev et al. Medium effects in proton-induced  $K^0$  production at 3.5 GeV. *Phys. Rev. C*, 90:054906, Nov 2014. 23, 37, 40
- [140] A. Mishra, E. L. Bratkovskaya, J. Schaffner-Bielich, S. Schramm, and H. Stöcker. Kaons and antikaons in hot and dense hadronic matter. *Phys. Rev. C*, 70:044904, Oct 2004. 23, 40
- [141] Subrata Pal, C. M. Ko, Ziwei Lin, and Bin Zhang. Antiflow of kaons in relativistic heavy ion collisions. *Phys. Rev. C*, 62:061903, Nov 2000. 23, 40
- [142] V. Zinyuk et al. Azimuthal emission patterns of  $K^+$  and of  $K^-$  mesons in Ni+Ni collisions near the strangeness production threshold. *Phys. Rev.*, C90(2):025210, 2014. 23, 40
- [143] V. M. Belyaev and B. L. Ioffe. Determination of Baryon and Baryonic Resonance Masses from QCD Sum Rules. 1. Nonstrange Baryons. *Sov. Phys. JETP*, 56:493–501, 1982. [Zh. Eksp. Teor. Fiz.83,876(1982)]. 23, 31
- [144] Xue-min Jin, Marina Nielsen, Thomas D. Cohen, R. J. Furnstahl, and David K. Griegel. QCD Sum rules for nucleons in nuclear matter. 3. *Phys. Rev.*, C49:464–477, 1994. 23, 31
- [145] N. K. Glendenning, D. Von-Eiff, M. Haft, H. Lenske, and M. K. Weigel. Relativistic mean-field calculations of  $\Lambda$  and  $\Sigma$  hypernuclei. *Phys. Rev. C*, 48:889–895, Aug 1993. 23, 180
- [146] C. M. Keil, F. Hofmann, and H. Lenske. Density dependent hadron field theory for hypernuclei. *Phys. Rev. C*, 61:064309, May 2000. 23, 180
- [147] K. Tsushima, K. Saito, J. Haidenbauer, and A.W. Thomas. The quark-meson coupling model for  $\Lambda$ ,  $\Sigma$  and  $\Xi$  hypernuclei. *Nuclear Physics A*, 630(3):691 718, 1998. 23, 180
- [148] Z. S. Wang, C. Fuchs, Amand Faessler, and T. Gross-Boelting. Kaon squeeze-out in heavy ion reactions. *Eur. Phys. J.*, A5:275–283, 1999. 23
- [149] G. Q. Li, C. M. Ko, and W. S. Chung.  $K^+$  production in baryon-baryon and heavy-ion collisions. *Phys. Rev. C*, 57:434–437, Jan 1998. 23
- [150] V. Bernard, N. Kaiser, and Ulf-G. Meißner. Aspects of chiral pion-nucleon physics. Nuclear Physics A, 615(4):483 – 500, 1997. 23
- [151] E. E. Kolomeitsev, Burkhard Kampfer, and D. N. Voskresensky. Kaon polarization in nuclear matter. *Nucl. Phys.*, A588:889–917, 1995. 23, 40

- [152] A. Ramos and E. Oset. The properties of  $\overline{K}$  in the nuclear medium. *Nuclear Physics A*, 671(1–4):481 502, 2000. 23, 24
- [153] Johann Rafelski, Jean Letessier, and Giorgio Torrieri. Erratum: Strange hadrons and their resonances: A diagnostic tool of quark-gluon plasma freeze-out dynamics [Phys. Rev. C 64, 054907 (2001)]. Phys. Rev. C, 65:069902, Jun 2002. 23, 24
- [154] Laura Tolos, Angels Ramos, Artur Polls, and Thomas T. S. Kuo. Partial wave contributions to the anti-kaon potential at finite momentum. *Nucl. Phys.*, A690:547–566, 2001. 23, 24
- [155] Volker Koch.  $K^-$ -proton scattering and the  $\Lambda$  (1405) in dense matter. *Physics Letters B*, 337(1):7 13, 1994. 24
- [156] Evgeni E. Kolomeitsev and Dmitri N. Voskresensky. Negative kaons in dense baryonic matter. *Phys. Rev. C*, 68:015803, Jul 2003. 24
- [157] M. Lutz, S. Klimt, and W. Weise. Meson properties at finite temperature and baryon density. *Nuclear Physics A*, 542(4):521 – 558, 1992. 24
- [158] Murray Gell-Mann, R.J. Oakes, and B. Renner. Behavior of current divergences under SU(3) x SU(3). *Phys. Rev.*, 175:2195–2199, 1968. 25
- [159] John F. Donoghue and K. Johnson. The pion and an improved static bag model. *Phys. Rev. D*, 21:1975–1985, Apr 1980. 25
- [160] R. D. Carlitz, S. D. Ellis, and R. Savit. Why the neutron isn't all neutral. *Physics Letters* B, 68:443–446, July 1977. 25
- [161] Anthony W. Thomas. Chiral symmetry and the bag model. *Nuclear Physics A*, 416:69 86, 1984. 25
- [162] Leo Lagerkvist. Glueball mass spectrum using the MIT bag-model. Bachelor thesis, Royal Institute of Technology, 2015. 25
- [163] Hideki Yukawa. On the Interaction of Elementary Particles. I. Proceedings of the Physico-Mathematical Society of Japan. 3rd Series, 17:48–57, 1935. 26
- [164] G. A Miller. The Cloudy Bag Model of Hadrons. In *Quarks and Nuclear Structure Bad Honnef, Germany, June 13-16, 1983*, pages 150–171, 1983. 26, 192
- [165] I. G. Aznauryan and V. D. Burkert. Electroexcitation of nucleon resonances. Prog. Part. Nucl. Phys., 67:1–54, 2012. 26
- [166] F. Myhrer. Nucl. Phys, A362:377, 1981. 26
- [167] A. W. Schreiber, P. J. Mulders, A. I. Signal, and A. W. Thomas. Pion cloud of the nucleon and its effect on deep-inelastic structure. *Phys. Rev. D*, 45:3069–3078, May 1992. 26

- [168] W. Koepf, L. L. Frankfurt, and M. Strikman. The Nucleon's virtual meson cloud and deep inelastic lepton scattering. *Phys. Rev.*, D53:2586–2598, 1996. 26
- [169] F. S. Navarra, M. Nielsen, and S. Paiva. Strangeness production in the meson cloud model. 56:3041–3045, September 1997. 26
- [170] Höchst 2014 J. Weil at HADES Winter School. 28
- [171] P. Danielewicz. Quantum Theory of Nonequilibrium Processes. II. Application to Nuclear Collisions. Annals Phys., 152:305–326, 1984. 29
- [172] H. S. Köhler. Memory and correlation effects in nuclear collisions. *Phys. Rev. C*, 51:3232– 3239, Jun 1995. 29
- [173] W. Cassing, L. Tolos, E.L. Bratkovskaya, and A. Ramos. Antikaon production in A+A collisions at SIS energies within an off-shell G-matrix approach. *Nuclear Physics A*, 727(1):59 94, 2003. 29
- [174] O. Buss, T. Gaitanos, K. Gallmeister, H. van Hees, M. Kaskulov, O. Lalakulich, A. B. Larionov, T. Leitner, J. Weil, and U. Mosel. Transport-theoretical Description of Nuclear Reactions. *Phys. Rept.*, 512:1–124, 2012. 29, 31
- [175] W. Cassing and S. Juchem. Semiclassical transport of particles with dynamical spectral functions. *Nucl. Phys.*, A665:377–400, 2000. 29, 31
- [176] Carsten Greiner and Stefan Leupold. Stochastic interpretation of Kadanoff-Baym equations and their relation to Langevin processes. *Annals Phys.*, 270:328–390, 1998. 29
- [177] J. Lehr, M. Effenberger, H. Lenske, S. Leupold, and U. Mosel. Transport theoretical approach to the nucleon spectral function in nuclear matter. *Physics Letters B*, 483(1–3):324 330, 2000. 29
- [178] W. Cassing and S. Juchem. Semiclassical transport of hadrons with dynamical spectral functions in a+a collisions at sis/ags energies. *Nuclear Physics A*, 672(1):417 – 445, 2000. 29
- [179] Joerg Aichelin. Quantum molecular dynamics dynamical microscopic n-body approach to investigate fragment formation and the nuclear equation of state in heavy ion collisions. *Physics Reports*, 202:233 – 360, 1991. 29
- [180] C. Hartnack, Rajeev K. Puri, J. Aichelin, J. Konopka, S.A. Bass, et al. Modeling the many body dynamics of heavy ion collisions: Present status and future perspective. *Eur.Phys.J.*, A1:151–169, 1998. 29, 180
- [181] Heinz Sorge, Horst Stöcker, and Walter Greiner. Poincaré invariant Hamiltonian dynamics: Modelling multi-hadronic interactions in a phase space approach. *Annals of Physics*, 192(2):266 – 306, 1989. 29

- [182] S. A. Bass et al. Microscopic models for ultrarelativistic heavy ion collisions. Prog. Part. Nucl. Phys., 41:255–369, 1998. 29, 32
- [183] K. Tsushima, S.W. Huang, and Amand Faessler. The role of the  $\Delta$  (1920) resonance for kaon production in heavy ion collisions. *Physics Letters B*, 337(3):245 253, 1994. 30, 31
- [184] K Tsushima, S W Huang, and A Faessler. Resonance model of pi Delta to YK for kaon production in heavy-ion collisions. *Journal of Physics G: Nuclear and Particle Physics*, 21(1):33, 1995. 30
- [185] Guo-Qiang Li, C. H. Lee, and G. E. Brown. Kaons in dense matter, kaon production in heavy ion collisions, and kaon condensation in neutron stars. *Nucl. Phys.*, A625:372–434, 1997. 30
- [186] S.A. Bass et al. Microscopic models for ultrarelativistic heavy ion collisions. *Progress in Particle and Nuclear Physics*, 41:255 369, 1998. 30, 32, 180, 181
- [187] M. Bleicher et al. Relativistic hadron-hadron collisions in the ultra-relativistic quantum molecular dynamics model. *Journal of Physics G: Nuclear and Particle Physics*, 25(9):1859, 1999. 30, 32, 181
- [188] R. W. Bland, M. G. Bowler, J. L. Brown, J. A. Kadyk, G. Goldhaber, S. Goldhaber, V. H. Seeger, and G. H. Trilling. The k-plus p interaction from 864 to 1585 MeV/c cross sections and mass distributions. *Nucl. Phys.*, B13:595–621, 1969. 30
- [189] Christian Sturm. K<sup>+</sup>-Produktion in Schwerionenreaktionen als Sonde für die Inkompressibilität von Kernmaterie. PhD thesis, Technische Universität Darmstadt, 2001. 30
- [190] Andreas Lang, Wolfgang Cassing, Ulrich Mosel, and Klaus Weber. Covariant calculation of K+ production in nucleus-nucleus collisions at SIS-energies. *Nuclear Physics A*, 541(3):507 – 524, 1992. 30
- [191] X.S. Fang, C.M. Ko, and Y.M. Zheng. Rescattering effects on kaon energy spectra in heavy-ion collisions. *Nuclear Physics A*, 556(3):499 – 508, 1993. 30
- [192] X. S. Fang, C. M. Ko, Guo-Qiang Li, and Y. M. Zheng. The Relativistic transport model description of subthreshold kaon production in heavy ion collisions. *Nucl. Phys.*, A575:766–790, 1994. 30
- [193] Jurgen Schaffner, Jakob Bondorf, and Igor N. Mishustin. In-medium production of kaons at the mean field level. *Nucl.Phys.*, A625:325–346, 1997. 31, 40
- [194] J. Weil et al. Particle production and equilibrium properties within a new hadron transport approach for heavy-ion collisions. *Phys. Rev.*, C94(5):054905, 2016. 31

- [195] W. Cassing, E. L. Bratkovskaya, and S. Juchem. Excitation functions of hadronic observables from SIS to RHIC energies. *Nucl. Phys.*, A674:249–276, 2000. 31
- [196] Bengt Friman, Claudia Hohne, Jorn Knoll, Stefan Leupold, Jorgen Randrup, Ralf Rapp, and Peter Senger. The CBM physics book: Compressed baryonic matter in laboratory experiments. *Lect. Notes Phys.*, 814:pp.1–980, 2011. 31
- [197] Kazuo Tsushima, Alexander Sibirtsev, Anthony William Thomas, and G. Q. Li. Resonance model study of kaon production in baryon baryon reactions for heavy ion collisions. *Phys. Rev.*, C59:369–387, 1999. [Erratum: Phys. Rev.C61,029903(2000)]. 31
- [198] P. Danielewicz and G.F. Bertsch. Production of deuterons and pions in a transport model of energetic heavy-ion reactions. *Nuclear Physics A*, 533(4):712 748, 1991. 31, 32
- [199] W. Cassing and E. L. Bratkovskaya. Parton-Hadron-String Dynamics: an off-shell transport approach for relativistic energies. *Nucl. Phys.*, A831:215–242, 2009. 32
- [200] Microscopic models for ultrarelativistic heavy ion collisions. 32
- [201] M. Berenguer, H. Sorge, and W. Greiner.  $\phi$  meson production in ultrarelativistic heavy ion collisions. *Physics Letters B*, 332(1):15 19, 1994. 32
- [202] R. Averbeck, R. Holzmann, V. Metag, and R. S. Simon. Neutral pions and eta mesons as probes of the hadronic fireball in nucleus-nucleus collisions around 1-A-GeV. *Phys. Rev.*, C67:024903, 2003. 34
- [203] F. Becattini, M. Gazdzicki, A. Keranen, J. Manninen, and R. Stock. Chemical equilibrium in nucleus nucleus collisions at relativistic energies. *Phys. Rev.*, C69:024905, 2004. 34
- [204] Peter Braun-Munzinger, Krzysztof Redlich, and Johanna Stachel. Particle production in heavy ion collisions. 2003. 34
- [205] J. Cleymans, H. Oeschler, K. Redlich, and S. Wheaton. Comparison of chemical freezeout criteria in heavy-ion collisions. *Phys. Rev.*, C73:034905, 2006. 34
- [206] A. Andronic et al. Hadron Production in Ultra-relativistic Nuclear Collisions: Quarkyonic Matter and a Triple Point in the Phase Diagram of QCD. *Nucl. Phys.*, A837:65–86, 2010. 34
- [207] H. Oeschler, J. Cleymans, and K. Redlich. Strange particle production from SIS to LHC. *Pramana*, 60:1039–1044, 2002. 34
- [208] Edward V. Shuryak. The multibody production at mediate energy. *Phys. Lett.*, B42:357– 360, 1972. 34
- [209] Jean Letessier, Ahmed Tounsi, and Johann Rafelski. Hot hadronic matter and strange anti-baryons. *Phys. Lett.*, B292:417–423, 1992. 34

- [210] P. Senger et al. The kaon spectrometer at SIS. Nuclear Instruments and Methods in Physics Research Section A: Accelerators, Spectrometers, Detectors and Associated Equipment, 327(2):393 – 411, 1993. 35
- [211] D. Miskowiec, W. Ahner, R. Barth, M. Cieslak, M. Debowski, et al. Observation of enhanced subthreshold K+ production in central collisions between heavy nuclei. *Phys.Rev.Lett.*, 72:3650–3653, 1994. 35, 189
- [212] W. Reisdorf et al. Systematics of azimuthal asymmetries in heavy ion collisions in the 1A GeV regime. *Nuclear Physics A*, 876:1 – 60, 2012. 36
- [213] W. Reisdorf et al. Systematics of central heavy ion collisions in the 1A GeV regime. Nuclear Physics A, 848(3):366 – 427, 2010. 36
- [214] Olaf N. Hartmann. Studying Strange Meson Production with FOPI. *International Journal* of Modern Physics A, 24(02n03):271–278, 2009. 36
- [215] A. Mangiarotti et al. Sub-threshold phi-meson yield in central 58Ni+58Ni collisions. Nucl.Phys., A714:89–123, 2003. 36
- [216] K. Piasecki et al. Influence of  $\phi$  mesons on negative kaons in Ni+Ni collisions at 1.91A GeV beam energy. 2014. 36
- [217] P. Gasik et al. Strange meson production in Al+Al collisions at 1.9A GeV. 2015. 36
- [218] G. Agakishiev et al. Deep Subthreshold Ξ<sup>−</sup> Production in Ar+KCl Reactions at 1.76A GeV. Phys. Rev. Lett., 103:132301, Sep 2009. 37, 170, 198
- [219] G. Agakishiev et al. Phi decay: A Relevant source for K- production at SIS energies? *Phys.Rev.*, C80:025209, 2009. 37
- [220] M. Lorenz. Reviewing hadron production at SIS energies featuring the new HADES Au + Au data. *Nucl.Phys.*, A931:785–789, 2014. 37
- [221] E.E. Kolomeitsev and B. Tomasik. Catalytic phi meson production in heavy-ion collisions. *J.Phys.*, G36:095104, 2009. 38
- [222] Jan Steinheimer and Marcus Bleicher. Sub-threshold  $\phi$  and  $\Xi^-$  production by high mass resonances with UrQMD. 2015. 38, 197
- [223] J. Stroth. Rare signals from dense baryonic matter. Nuclear Physics A, 862:205 211, 2011. 39, 192
- [224] C. Sturm et al. Evidence for a Soft Nuclear Equation-of-State from Kaon Production in Heavy-Ion Collisions. *Phys. Rev. Lett.*, 86:39–42, Jan 2001. 40
- [225] W Cassing, E.L Bratkovskaya, U Mosel, S Teis, and A Sibirtsev. Kaon versus antikaon production at sis energies. *Nuclear Physics A*, 614(3):415 – 432, 1997. 40

- [226] Michael Buballa et al. EMMI rapid reaction task force meeting on quark matter in compact stars. *J. Phys.*, G41(12):123001, 2014. 40
- [227] S. Weissenborn, D. Chatterjee, and J. Schaffner-Bielich. Hyperons and massive neutron stars: The role of hyperon potentials. *Nuclear Physics A*, 881:62 77, 2012. 40
- [228] Z. S. Wang, Amand Faessler, C. Fuchs, and T. Waindzoch. Lambda collective flow in heavy ion reactions. *Nucl. Phys.*, A645:177–188, 1999. [Erratum: Nucl. Phys.A648,281(1999)]. 40
- [229] M. Merschmeyer et al.  $K^0$  and  $\Lambda$  production in Ni+Ni collisions near threshold. *Phys. Rev. C*, 76:024906, Aug 2007. 40, 176, 195
- [230] C. Pinkenburg. Production and collective behavior of strange particles in Au+Au collisions at 2–8 AGeV. *Nuclear Physics A*, 698(1):495 498, 2002. 40, 179
- [231] P. Chung et al. Directed Flow of  $\Lambda$  Hyperons in (2–6) $\Lambda$  GeV Au + Au Collisions. *Phys. Rev. Lett.*, 86:2533–2536, Mar 2001. 40
- [232] S. Albergo et al.  $\Lambda$  Spectra in 11.6AGeV/c Au-Au Collisions. *Phys. Rev. Lett.*, 88:062301, Jan 2002. 40, 179
- [233] Behruz Kardan. Centrality Determination at 1.23 AGeV Gold-Gold Collision and Readout-Electronics for the HADES Electromagnetic Calorimeter. Master's thesis, Diploma thesis, Johann Wolfgang Goethe Universität, 2015. 42, 62, 63, 148, 156, 157, 166, 167, 174
- [234] G. Agakishiev et al. The High-Acceptance Dielectron Spectrometer HADES. *Eur.Phys.J.*, A41:243–277, 2009. 42, 45, 53, 72, 73, 74, 75
- [235] Jochen Markert. Untersuchung Ansprechverhalten der Vieldraht-Driftkammern niedriger Massenbelegung des HADES-Experimentes. PhD thesis, Johann Wolfgang Goethe Universität, 2005. 45, 68, 85
- [236] Private communication G. Kornakov. 48, 82
- [237] J. Pietraszko, L. Fabbietti, and W. Koenig. Diamonds as timing detectors for MIP: The HADES proton-beam monitor and start detectors. *Nucl. Instrum. Meth.*, A618:121–123, 2010. 49
- [238] HADES internal reports. 51, 53, 57, 62, 85, 87, 88, 98
- [239] Jan Michel. Development and Implementation of a New Trigger and Data Acquisition System for the HADES Detector. PhD thesis, Johann Wolfgang Goethe Universität, 2012. 54, 56
- [240] Alexander Schmah. Produktion von Seltsamkeit in Ar+KCl Reaktionen bei 1.756 AGeV mit HADES. PhD thesis, Technische Universität Darmstadt, 2009. 57

- [241] Claudia Behnke. Reconstruction of neutral mesons via conversion in Au+Au Collisions at 1.23 AGeV with the HADES. PhD thesis, Johann Wolfgang Goethe Universität, 2017. To be published. 57, 194
- [242] Patrick Sellheim. *Backtracking algorithm for dilelectron reconstruction with HADES*. PhD thesis, Johann Wolfgang Goethe Universität, 2017. To be published. 57, 58, 82
- [243] M. Alvioli, H.J. Drescher, and M. Strikman. A Monte Carlo generator of nucleon configurations in complex nuclei including nucleon nucleon correlations. *Physics Letters B*, 680(3):225 – 230, 2009. 62
- [244] G. Agakishiev. W. Pechenov. HADES internal reports, December 2001. 66
- [245] Private communication V. Pechenov. 67, 68
- [246] V. Pechenov at HADES Collaboration Meeting XXVI Prag. 68
- [247] V. Pechenov at HADES Collaboration Meeting XXXII Paris. 70
- [248] J. Markert at HADES Collaboration Meeting XXXI Darmstadt. 72, 86, 88, 89
- [249] Carina Ungethüm. Searching for the Dark Photon. Bachelor thesis, Technische Universität Darmstadt, 2015. 71
- [250] Private communication H. Schuldes. 79
- [251] Manuel Lorenz. Vector meson production in p+Nb reactions and statistical particle production. PhD thesis, Johann Wolfgang Goethe Universität, 2012. 81
- [252] Stefano Spataro. Characterization of the HADES spectrometer in pp collisions at 2.2 GeV: elastic scattering and exclusive eta reconstruction. PhD thesis, Università degli studi di Catania, 2005. 82
- [253] I. Frohlich, T. Galatyuk, R. Holzmann, J. Markert, B. Ramstein, et al. Design of the Pluto Event Generator. J.Phys.Conf.Ser., 219:032039, 2010. 84
- [254] J. Markert at HADES Collaboration Meeting XXX Lissabon. 87
- [255] Olaf Behnke, Kevin Kröninger, Thomas Schörner-Sadenius, and Gregory Schott, editors. *Data analysis in high energy physics*. Wiley-VCH, Weinheim, Germany, 2013. 117, 150
- [256] P. Cerulus and E. Hagedorn. A Monte-Carlo method to calculate multiple phase space integrals — I. Il Nuovo Cimento (1955-1965), 9(2):646–658, 1958. 147
- [257] J. Clerk Maxwell. On the Dynamical Theory of Gases. *Philosophical Transactions of the Royal Society of London*, 157:49?88, 1867. 147
- [258] Frederick Reif. *Fundamentals of Statistical and Thermal Physics*. Waveland Pr Inc;, 56946th edition, December 2008. 147

- [259] Gary J. Feldman and Robert D. Cousins. Unified approach to the classical statistical analysis of small signals. *Phys. Rev. D*, 57:3873–3889, Apr 1998. 169
- [260] F. Antinori et al. Rapidity distributions around mid-rapidity of strange particles in Pb-Pb collisions at 158-A-GeV/c. J. Phys., G31:1345–1357, 2005. 179
- [261] E. Andersen et al. Strangeness enhancement at mid-rapidity in Pb–Pb collisions at 158 A GeV/c. *Physics Letters B*, 449(3–4):401 – 406, 1999. 179
- [262] C. Adler et al. Kaon production and kaon to pion ratio in Au + Au collisions at  $\sqrt{s_{NN}}$ =130 GeV. *Physics Letters B*, 595(1–4):143 150, 2004. 179
- [263] B. Abelev et al.  $K_S^0$  and  $\Lambda$  Production in Pb-Pb Collisions at  $\sqrt{s_{NN}}=2.76$  TeV. *Phys. Rev. Lett.*, 111:222301, Nov 2013. 179, 198
- [264] J. Adams et al. Scaling Properties of Hyperon Production in Au+Au Collisions at  $\sqrt{s_{NN}}$ = 200 GeV. *Phys. Rev. Lett.*, 98:062301, Feb 2007. 179, 198
- [265] F Antinori et al. Energy dependence of hyperon production in nucleus-nucleus collisions at {SPS}. *Physics Letters B*, 595(1–4):68 – 74, 2004. 179, 198
- [266] S. Ahmad et al. Λ production by 11.6 A GeV/c Au beam on Au target. *Physics Letters B*, 382(1):35 – 39, 1996. 179
- [267] F. Antinori et al. Enhancement of hyperon production at central rapidity in 158-A-GeV/c Pb-Pb collisions. J. Phys., G32:427–442, 2006. 179
- [268] C. Adler et al. Midrapidity  $\Lambda$  and  $\overline{\Lambda}$  Production in Au + Au Collisions at  $\sqrt{s_{NN}} = 130$  GeV. *Phys. Rev. Lett.*, 89:092301, Aug 2002. 179
- [269] K. Adcox et al. Measurement of  $\Lambda$  and  $\overline{\Lambda}$  Particles in Au + Au Collisions at  $\sqrt{s_{NN}} = 130$  GeV. *Phys. Rev. Lett.*, 89:092302, Aug 2002. 179
- [270] X. S. Fang, C. M. Ko, G. Q. Li, and Y. M. Zheng. Medium effects on subthreshold kaon production in heavy-ion collisions. *Phys. Rev. C*, 49:R608–R611, Feb 1994. 179
- [271] W. Cassing and E. L. Bratkovskaya. Hadronic and electromagnetic probes of hot and dense nuclear matter. *phys rep*, 308:65–233, January 1999. 180
- [272] J. Steinheimer and M. Bleicher. Hadron resonance production and final state hadronic interactions with UrQMD at LHC. *EPJ Web Conf.*, 97:00026, 2015. 186
- [273] G. Q. Li, C. M. Ko, and Bao-An Li. Kaon Flow as a Probe of the Kaon Potential in Nuclear Medium. *Phys. Rev. Lett.*, 74:235–238, Jan 1995. 191
- [274] Guo-Qiang Li and C. M. Ko. Kaon flow in heavy ion collisions. Nucl. Phys., A594:460– 482, 1995. 191

- [275] Guo-Qiang Li and G. E. Brown. K<sup>+</sup> versus lambda flow in relativistic heavy ion collisions. *Nucl. Phys.*, A636:487–506, 1998. 191
- [276] J Stachel, A Andronic, P Braun-Munzinger, and K Redlich. Confronting LHC data with the statistical hadronization model. *Journal of Physics: Conference Series*, 509(1):012019, 2014. 194
- [277] R. Kotte at HADES Collaboration Meeting XXXII Paris. 194
- [278] Ekkard Schnedermann, Josef Sollfrank, and Ulrich Heinz. Thermal phenomenology of hadrons from 200 A GeV S+S collisions. *Phys. Rev. C*, 48:2462–2475, Nov 1993. 196
- [279] B. Abelev et al. Multi-strange baryon production at mid-rapidity in Pb–Pb collisions at  $\sqrt{s_{NN}} = 2.76$  TeV. *Physics Letters B*, 728:216 227, 2014. 198
- [280] M. M. Aggarwal et al. Strange and multistrange particle production in Au + Au collisions at  $\sqrt{s_{NN}} = 62.4$  GeV. *Phys. Rev. C*, 83:024901, Feb 2011. 198
- [281] C. Alt et al. Energy dependence of Λ and Ξ production in central Pb+Pb collisions at 20A, 30A, 40A, 80A, and 158A GeV measured at the CERN Super Proton Synchrotron. *Phys. Rev. C*, 78:034918, Sep 2008. 198
- [282] P. Chung et al. Near-Threshold Production of the Multistrange  $\Xi^-$  Hyperon. *Phys. Rev. Lett.*, 91:202301, Nov 2003. 198
- [283] Private communication R. Kotte. 198

## Rechtliches

Die vorliegende Druckfassung enthält kleinere, inhaltlich nicht relevante Änderungen, gegenüber der dem Promotionsbüro vorgelegten Version.

### Danksagung

An allererster Stelle gebührt ein großes Dankeschön meinem Doktorvater Prof. Dr. Joachim Stroth für die Möglichkeit in seiner Arbeitsgruppe nach der Bachelor- und Masterarbeit auch promovieren zu dürfen. Seine Leidenschaft, sein Engagement und seine Identifikation mit der Physik und im Speziellen der HADES-Gruppe, sind beispielhaft. Insbesondere seine strukturierte Denkweise und die Fähigkeit bei großer Detailtreue stets den Überblick über komplexe Sachverhalte zu behalten und diese mit einer scheinbaren Leichtigkeit anzugehen, werden mir als Vorbild dienen.

Weiterhin gilt ein riesiger Dank meinem Mentor und Freund Dr. Manuel 'Rick Grimes' Lorenz. Ich habe unschätzbar viel von dir gelernt und vermittelt bekommen. Die mittlerweile 7 Jahre andauernde Zusammenarbeit möchte ich nicht missen und werde mit Freude an Diskussionen über Physik, Datenanalyse, Seltsamkeit, Fußball, Filme/Serien (und die damit verbundenen mittelmäßigen Imitationen und inakkuraten Zitate), Country-Musik, Walton Goggins, Dinosaurier sowie die Zeit in Utrecht und an Jessie's gemalte Bilder zurückdenken. Auf dass du diesen Ohrwurm nie mehr los wirst. Möge dir deine pragmatische Arbeitsweise erhalten bleiben und ich hoffe, dein Rasierapparat gibt nicht so bald den Geist auf.

Ich danke Prof. Dr. Carsten Greiner für seine Verfügbarkeit als externer, theoretischer Supervisor und dass er sich regelmäßig Zeit für die PhD-Komitteesitzungen nahm, sowie für die anschauliche und didaktisch wertvolle Einführung in die theoretische Physik (Mechanik I+II) vor nunmehr über 10 Jahren.

Ich danke Jochen Markert für die zuverlässige Hilfe bei sämtlichen Fragen bezüglich Softwareund Programmierproblemen, die fortwährende Verbesserung der Qualität der Daten, sowie für Unterhaltungen zu wirklich sämtlichen Themen angefangen bei politischem Alltag, über den Verfall der Sprache unter Jugendlichen bis hin zur japanischen Version des Films Thor. Weiterhin möchte ich auch Vladimir und Olga Pechenov danken, ohne deren ständige Verbesserungen im Bereich des Trackings eine derart hohe Qualität der Datenauswertung nicht möglich gewesen wäre. Außerdem danke ich Jan Michel für die effiziente Lösung bei Netzwerkproblemen und sonstigen Fragen rund um Rechenmaschinen.

Für die Hilfe bei physikbezogenen Anliegen danke ich der ganzen Kollaboration und insbesondere folgenden HADESianern: Romain Holzmann, dessen fundierte Erklärungen v.a. durch Präzision und Verständlichkeit bestechen, sowie für das Korrekturlesen meiner Arbeit. Christoph Blume, der bei Problemen zur Methodik in der Datenanalyse immer einen guten Rat hatte, und Herbert Ströbele insbesondere für seine kreativen Ideen abseits der gängigen Vorgehensweisen und dass er seine umfangreiche Erfahrung in dem Forschungsfeld immernoch regelmäßig und mit Leidenschaft teilt. Weiterhin danke ich Roland Kotte als aufmerksamen Experten für Strangenessbelange, besonders bei der  $\Xi$ -Analyse. Ein Dankeschön gilt auch Piotr Salabura mit seiner durchdringenden, motivierenden Art, dessen leidenschaftliche, rege Beteiligung an allen Analysen mich stets beeindruckte. Tetyana Galatyuk danke ich u.A. für ihren wertschätzenden und einbeziehenden Umgang im wissenschaftlichen Dialog, egal ob mit jung oder alt, Bachelor oder Postdoc. Ebenso danke ich Christian Müntz, Detailteufel, Allrounder und Stimmungsmacher, sowie Christian Wendisch u.A. für das Korrekturlesen. Ilse & Wolfgang Koenig danke ich neben ihrer Expertise und Hilfsbereitschaft für nette Anekdoten aus fast 25 Jahren HADES.

Ich danke Yvonne Leifels, E. Bratkovskaya und C. Hartnack für die Bereitstellung von Rechnungen theoretischer Transportmodelle und anregenden Diskussionen, sowie Onkel Jan Steinheimer als Ansprechpartner für sämtliche theoretische Belange.

Weiterhin gilt ein Dank meinen studentischen (Ex-)Mitstreitern innerhalb und außerhalb der Kollaboration, namentlich Claudia, Bachelor, Heidi, Erik, Behruz, Jacek, Theo, Flo S., Pascuale sowie Laura R. und Katharina G. Für ein fantastisches Arbeitsklima an der GSI/Uni sorgten über die Jahre ausserdem die Dileptonen-Guys, Melanie, Michael W., Adrian, Gosia, Georgy, Erwin und Burkhard. Bei Florian Uhlig möchte ich mich für die kontinuierliche Bereitstellung von Kaffee und sauren Leckerlis bedanken. Ein dickes Extra-Dankeschön gilt Riga Putschemui, sowie den ALICE-Kickern.

Ein riesengroßes Dankeschön gilt Marianne Frey für den uneingeschränkten, ständigen Einsatz und ihre Zuverlässigkeit. Sie ist eine absolute Konstante und ohne sie hätten meine organisatorischen Defizite um ein Vielfaches mehr Schaden angerichtet.

Ich danke dem gesamten HGS-Hire Team für die hervorragenden Rahmenbedingungen, vor allem das Engagement und die reibungslose Organisation sämtlicher Veranstaltungen und die Möglichkeit für einen Aufenthalt an der Universität der wunderschönen Stadt Utrecht. In diesem Zusammenhang danke ich außerdem Raimond Snellings für die vorübergehende, reibungslose Aufnahme in seiner Gruppe sowie Redmer Bertens in seinem prächtigen Büro mit der etwas eigenwilligen Jalousie.

Zu guter Letzt gebührt ein großer Teil meines Danks Alexandra Cleve, ihrer beispiellosen Geduld sowie Aufopferungsbereitschaft und dass sie alles Erdenkliche unternommen hat, um mich zu jeder Zeit zu unterstützen. Ich freue mich darauf, bald einen neuen Lebensabschnitt mit dir beginnen zu können.

# Timo Scheib

Curriculum Vitae



### Personal Details

born January 3rd 1986 in Offenbach am Main citizenship German

#### **Studies**

#### PhD in Experimental Physics

since $11/2012$	Goethe-University Frankfurt am Main/Germany
04/2015 - 07/2015	HGS-HIRe Abroad at the Utrecht University, Utrecht/Netherlands
title of thesis	$\Lambda$ and $K^0_s$ Production in Au+Au-Collisions at $E_{lab}=1.23A~GeV$ with HADES
supervisor	Prof. Dr. Joachim Stroth
	Master of Science in Physics, Grade: 1.1
10/2009 - 03/2010	Université Pierre et Marie Curie in Paris/France
04/2010 - 06/2012	Goethe-University Frankfurt am Main/Germany
28.06.2012	Masterthesis, Grade: 1.3
title	Hypertriton Reconstruction in Ar+KCl-Collisions at $E_{lab} = 1.76A$ GeV with HADES
supervisor	Prof. Dr. Joachim Stroth
	Bachelor of Science in Physics, Grade: 1.7
10/2006 - 09/2009	Goethe-University Frankfurt am Main/Germany
13.06.2009	Bachelorthesis, Grade: 1.7
title	Exclusive Production of $\omega$ -Mesons in pp-Collisions at $E_{lab} = 3.5$ GeV with HADES
supervisor	Prof. Dr. Joachim Stroth